LITHOSPHERIC STRUCTURE OF PAMPEAN FLAT SLAB (LATITUDE 30-33°S) AND NORTHERN COSTA RICA (LATITUDE 9-11°N) SUBDUCTION ZONES

by

Lepolt Linkimer Abarca

A Dissertation Submitted to the Faculty of the

DEPARTMENT OF GEOSCIENCES

In Partial Fulfillment of the Requirements
For the Degree of

DOCTOR OF PHILOSOPHY

In the Graduate College

THE UNIVERSITY OF ARIZONA

2011

THE UNIVERSITY OF ARIZONA
GRADUATE COLLEGE

As members of the Dissertation Committee, we certify that we have read the dissertation

prepared by Lepolt Linkimer Abarca

entitled Lithospheric Structure of the Pampean Flat Slab (Latitude 30-33°S) and Northern Costa Rica (Latitude 9-11°N) Subduction Zones

and recommend that it be accepted as fulfilling the dissertation requirement for the

Degree of Doctor of Philosophy

_____ Date: July 26, 2011
Susan Beck

_____ Date: July 26, 2011
George Zandt

_____ Date: July 26, 2011
Richard Bennett

_____ Date: July 26, 2011
Roy Johnson

_____ Date: July 26, 2011
Clement Chase

Final approval and acceptance of this dissertation is contingent upon the candidate's submission of the final copies of the dissertation to the Graduate College.

I hereby certify that I have read this dissertation prepared under my direction and recommend that it be accepted as fulfilling the dissertation requirement.

_____ Date: July 26, 2011
Dissertation Director: Susan Beck

STATEMENT BY AUTHOR

This dissertation has been submitted in partial fulfillment of requirements for an advanced degree at the University of Arizona and is deposited in the University Library to be made available to borrowers under rules of the Library.

Brief quotations from this dissertation are allowable without special permission, provided that accurate acknowledgment of source is made. Requests for permission for extended quotation from or reproduction of this manuscript in whole or in part may be granted by the head of the major department or the Dean of the Graduate College when in his or her judgment the proposed use of the material is in the interests of scholarship. In all other instances, however, permission must be obtained from the author.

SIGNED: Lepolt Linkimer Abarca

ACKNOWLEDGMENTS

I would like to thank the members of my committee, especially Susan and George. My dissertation would not have been possible without financial support through the University of Arizona, its Department of Geosciences, the University of Costa Rica, and grants awarded to my advisers through the National Science Foundation.

Special thanks to Patricia Alvarado, Kiriaki Xiluri, C. Berk Biryol, Ivonne Arroyo, and Lina Patiño. Thanks to Goran Buble, Andy Frassetto, Suncana Laketa, Ryan Porter, Christine Gans, Facundo Fuentes, Zerkan Arca, Josh Calkins, and the GSAT group. Thanks to my friends Ivonne Arroyo, Maria Andrea Carvajal, Guaria Cardenes, Natalia Zamora, Helga Arroyo, Paulo Hidalgo, Linda Sjöbohm, Michael Sand. Special thanks to Russell Ronnebaum. Thanks to family: Maria Elena Abarca, Lepolt Linkimer, Silja Linkimer, Madai Linkimer, Mildred Linkimer, Ana Catalina Ramirez, and Robert Utsman. Thanks to Jennifer Hoefle, Glenn Matchett-Morris, Martie van der Voort, the Office LGBTQ Affairs and the LGBTQ Support Group of U of A.

Gracias a todos por hacerme sentir allá con ustedes y por estar aquí conmigo.

TABLE OF CONTENTS

TABLE OF CONTENTS - *Continued*

TABLE OF CONTENTS - *Continued*

LIST OF ILLUSTRATIONS

ABSTRACT

The Pampean flat slab subduction in west-central Argentina (latitude 30-33°S) and the steeply dipping Northern Costa Rica subduction zone (latitude 9-11°N) show significant along-trench variations in both the subducting and overriding plates. This dissertation contains the results of three seismological studies using broadband instruments conducted in these subduction zones, with the aim of understanding the structure of the lithosphere and the correlation between the variability observed in the downgoing and the overriding plates. In the Costa Rica region, by analyzing teleseismic receiver functions we investigate the variability in the hydration state of the subducting Cocos Plate and the nature of three distinct crustal terranes within the overriding Caribbean Plate: the Nicoya and Chorotega terranes that display an oceanic character, and the Mesquito Terrane, which is more compatible with continental crust.

In the Pampean region of Argentina, we apply a regional-scale double-difference tomography algorithm to earthquake data recorded by the SIEMBRA (2007-2009) and ESP (2008-2010) broadband seismic networks to obtain high-resolution images of the South America lithosphere. We find that most of the upper mantle has seismic properties consistent with a depleted lherzolite or harzburgite, with two anomalous regions above the flat slab: a higher Vp/Vs ratio anomaly consistent with up to 10% hydration of mantle peridotite and a localized lower Vp/Vs ratio anomaly consistent with orthopyroxene enrichment. In addition, we study the geometry and brittle deformation of the subducting Nazca Plate by determining high-quality earthquake locations, slab contours, and focal mechanisms. Our results suggest that the subduction of the incoming Juan Fernandez

Ridge controls the slab geometry and that ridge buoyancy and slab pull are key factors in the deformation of the slab. The spatial distribution of the slab seismicity suggests variability in the hydration state of the subducting Nazca Plate and/or in strain due to slab bending. These observations support the hypothesis that the along-trench variability in bathymetric features and hydration state of the incoming plate has profound effects in the subducting slab geometry and the upper plate structure in both flat and steeply dipping subduction zones.

INTRODUCTION

Subduction zones are the regions of the Earth where slabs of lithosphere created at mid-ocean ridges dive into the mantle inducing convection in the mantle wedge. Subduction zones are also our planet's largest recycling system [Stern, 1992]. They are termed the "subduction factory", where the raw materials entering the process are the components of the oceanic plate, including sediments, the oceanic crust, and serpentinized oceanic mantle; which eventually "generate" melting, volatiles, and continental crust. In addition to their role on the planet's current configuration, subduction zones profoundly impact civilization. The largest earthquakes, volcanic eruptions, slumps, and tsunamis occur in subduction zones. Additionally, these regions contain most of the mineral resources of the planet [Stern, 1992]. Research on subduction zones, therefore, not only enriches our understanding of the Earth, but also provides knowledge that could improve the lives of millions of people.

Subduction zones are defined by the inclined array of earthquakes known as the Wadati-Benioff Zone (WBZ). The mechanism responsible for the WBZ seismicity has been a subject of discussion since its existence was revealed [Wadati, 1928; 1935; Benioff, 1955]. At depths greater than ~30 km, the lithostatic pressure is so great that it should prevent brittle failure [Scholz, 1990]. The intermediate-depth seismicity is commonly explained by dehydration embrittlement [Kirby et al., 1996, Hacker et al., 2003b]. According to this hypothesis, as the slab sinks, metamorphic reactions liberate fluids from hydrous phases, which increase pore pressure, reducing the normal stress enough to bring the system into the brittle regime. Thermal modeling shows that

seismicity within the subducting slab is distributed in a narrow belt of pressure-temperature conditions, which coincides with the breakdown of high-pressure hydrous phases [e.g., Abers et al., 2006]. However, the exact relationship between dehydration and earthquake nucleation is not yet well understood.

WBZ earthquakes could be generated by dehydration embrittlement creating new faults [Zhang, J. et al., 2004] or reactivating pre-existing weak zones [Peacock, 2001; Warren et al., 2008]. It has been noted for the Middle America and Chile subduction zones that higher rates of intra-slab seismicity are associated with segments with more pervasive trench faulting. This suggests that most of the intra-slab seismicity is related to reactivation of faults rather than formation of new ones [Ranero et al., 2005]. According to the conceptual model of Ranero et al. [2005], the intermediate-depth seismicity starts between 60-80 km, when dehydration of oceanic crust causes a concentration of earthquakes on the upper part of slab. Deeper than ~100 km, eclogitization of the oceanic crust is completed; here or slightly deeper dehydration of slab mantle occurs generating seismicity within the subducting oceanic mantle.

Petrologic models [e.g., Kirby et al., 1996; Hacker et al., 2003a,b] predict a casual connection between intra-slab earthquakes and a hydrated mantle above the subducting slab. The addition of water to the mantle produces serpentinization under certain pressure and temperature conditions. Antigorite is the main serpentine mineral in ultramafic rocks metamorphosed under moderate temperatures and is stable to temperatures of 620-720°C at depths between 30 and 150 km [Ulmer and Trommsdorff, 1995]. Hacker et al. [2003a] support the idea that seismic velocities and Vp/Vs ratios indicate that mantle wedges

locally reach 60-80% hydration. Very high (> 50%) serpentinization values have been reported in several subduction zones such as central Japan [Kamiya and Kobayashi, 2000] and the Cascades [Bostock et al., 2002].

Bathymetric highs such as aseismic oceanic ridges, seamounts, plateaus, and rises are common features of the ocean floor. In the context of plate tectonics, these oceanic features are expected to be either subducted or accreted at some point in geologic history. In fact, the subduction of oceanic ridges is a widespread phenomenon occurring worldwide and has been strongly correlated to shallow and flat subduction regions that represent about 10% of modern convergent margins [Gutscher, et al., 2000a,b]. The subduction of bathymetric highs represents a deviation of "normal" or steeply dipping subduction in which smooth constant-age ocean floor is subducted [McCann and Habermann, 1989].

Contrasts in lithospheric bulk density of < 0.10 g/cm^3 between the subducting and overriding plates are the difference between whether subduction is nearly inevitable, as for oceanic crust; or whether subduction is greatly resisted, as for thick ancient continents [Cloos, 1993]. Because subduction metamorphisms make the crust more dense, even basaltic plateaus as thick as 17 km are subductable and only Hawaii-sized, > 8-km high seamount chains may caused an orogenic collision [Cloos, 1993]. Since very few plume-related features are the size of the Hawaii chain Islands, most of the aseismic oceanic ridges worldwide are subductable. Once an aseismic oceanic ridge is subducted it produces a perturbation in the normal "steady-state" subduction process [McCann and Habermann, 1989]. The higher buoyancy of plume generated oceanic ridges, plateaus,

and seamounts, is thought to facilitate flat subduction because the extra compositional buoyancy could prohibit the slab from sinking into the mantle [van Hunen et al., 2002]. Other proposed contributing factors for flat subduction includes: subduction below a trenchward moving overthrusting continent, slab suction forces in the mantle wedge, the hydrous weakening of the mantle wedge region, the subduction of young slabs, and a delay in the basalt to eclogite transition due to cool thermal structure [e.g., Gutscher et al., 2000a, b; van Hunen et al., 2002, 2004].

Several major effects in the upper plate are attributed to the subduction of oceanic ridges and the shallow-flat subduction process. One of the main impacts is the extinction or migration of arc volcanism, which is explained by the disappearance of the mantle wedge with decreasing dip angle and the absence of contact between the hydrated subducting crust with the hot asthenosphere, which prevents partial melting [e.g., van Hunen et al., 2002]. Flat subduction also completely alters the thermal structure of the margin, bringing cold oceanic lithosphere where typically hot asthenosphere is usually present [Gutscher, et al., 2000b]. Above subducting oceanic ridges, a much higher elevation than the segments located both sides of the subducted path has been reported in the arc region [e.g., Yáñez et al., 2002]. In fore arc region normal faulting is expected as well as initial uplift in response to the underthrusting of a seamount followed by subsidence after the seamount is subducted [e.g., Cloos, 1993; Fisher et al., 1998].

Above flat slab segments interplate coupling is highest [Gutscher, et al., 2000b]. Consequently, seismic energy release is higher by 3 to 5 times than above steep slab segments [Gutscher, et al., 2000b; Alvarado et al., 2007]. Increased interplate coupling

together with the stronger rheology of a cooled upper lithosphere, allow stress deformation to be transferred several hundred kilometers into the heart of the upper plate, as can be seen in the form of block fault uplifts such as the Sierras Pampeanas in Argentina [Gutscher, et al., 2000b; Alvarado et al., 2007].

Seamounts chains, submarine ridges, and other bathymetric highs on oceanic plates will in general migrate along the active margin, unless they are parallel to the convergent direction [Hampel, 2002]. Migration of the ridge-trench intersection with time produces a pulse deformation at the lower slope of the trench as well as uplift and later subsidence of the inner wall [MacCann and Habermann, 1989; Hampel, 2002]. One interesting effect of subducting bathymetry highs is the decrease in the trench-axis sediment supply, which may enhance subduction erosion and also facilitate accretion of detached fragments of the incoming seamounts that become accreted into the lower trench slope [Cloos, 1993].

Seismology is a valuable tool to investigate subduction zones. The improvement of instrumentation and infrastructure allows for temporary deployments of seismometers enabling robust analysis of specific regions or questions. In this dissertation, several earthquake datasets are carefully examined to study two subduction zones (Fig. 1): Northern Costa Rica (latitude 9-11°N) where normal subduction of the Cocos Plate occurs beneath the Caribbean Plate and South-Central Argentina (latitude 30-33°S) where flat subduction of the Nazca Plate occurs beneath the South American Plate.

To study the Northern Costa Rica subduction zone (Appendix A) we used 20 broadband stations of the CRSEIZE (December 1999 to December 2001), Pocosol (April

2005 to July 2006), and Corisubmod (February 2005 to February 2007) experiments, as well as stations JTS and HDC from the Global Seismology Network and the Geoscope Project, respectively. To study the Pampean flat slab (Appendixes B and C), we used data from two temporary broadband seismic deployments: SIEMBRA and ESP. The author assisted in collecting the data on these deployments.

The SIerras pampeanas Experiment using a Multicomponent BRoadband Array (SIEMBRA, which in Spanish means *crop*) was deployed between December 2007 and November 2009 and consisted of 40 broadband seismometers, an unprecedented number of stations above this flat slab. SIEMBRA is a NSF-funded project that involves faculty and students from the University of Arizona, and the National University of San Juan and Instituto Nacional de Prevención Sísmica (INPRES) in Argentina. The Eastern Sierras Pampeanas (ESP) experiment was deployed between August 2008 and August 2010 and consisted of 12 stations and involved faculty and students from Purdue University, Colorado College, and the National University of San Juan. Instrumentation for the SIEMBRA deployment was provided by the Program for Array Seismic Studies of the Continental Lithosphere (PASSCAL) of the Incorporated Research Institutions for Seismology (IRIS) and for the ESP deployment by Purdue University and Colorado College.

Although both the Costa Rican and Argentinean regions have been sites of numerous geological and geophysical studies and much progress has been made towards understanding the lithospheric structure and tectonics, there are still many unconstrained aspects. For example, the crust in Northern Costa Rica displays a continental character

even though it is presumably composed of terranes of oceanic origin. In addition, there is no consensus on the location of the boundary between blocks and terranes. In Argentina, above the flat slab, arc magmatism migrated progressively eastward, completely shutting off in the Main Cordillera and Precordillera between 7 and 11 Ma [Kay et al., 1988]. It is however unknown where slab volatiles go once this happens, and why the flat slab finally rolls over to descend steeply into the mantle further east. The lack of seismic evidence of hydration above the region of high seismicity in the flat slab is another unresolved question.

Constraining the lithospheric structure in the Costa Rica and Argentina regions is relevant as it gives insights into understanding tectonic history and provides a velocity structure that directly improves earthquake location models. The study of the Pampean Flat Slab region of Argentina is particularly significant for understanding the geologic history of the western United States as it is considered a modern analogue of the Laramide deformation when a proposed aseismic ridge on the Farallon Plate was subducted beneath the North America Plate [Jordan and Allmendinger, 1986].

The seismic data acquired using the aforementioned seismic networks were analyzed using several robust seismological methods. In Costa Rica, we calculate receiver functions for P- and PP- waves from teleseismic earthquakes (Appendix A). In Argentina, we applied a regional-scale double-difference tomography algorithm (Appendix B) and calculated earthquake locations and focal mechanisms for intermediate-depth earthquakes (Appendix C).

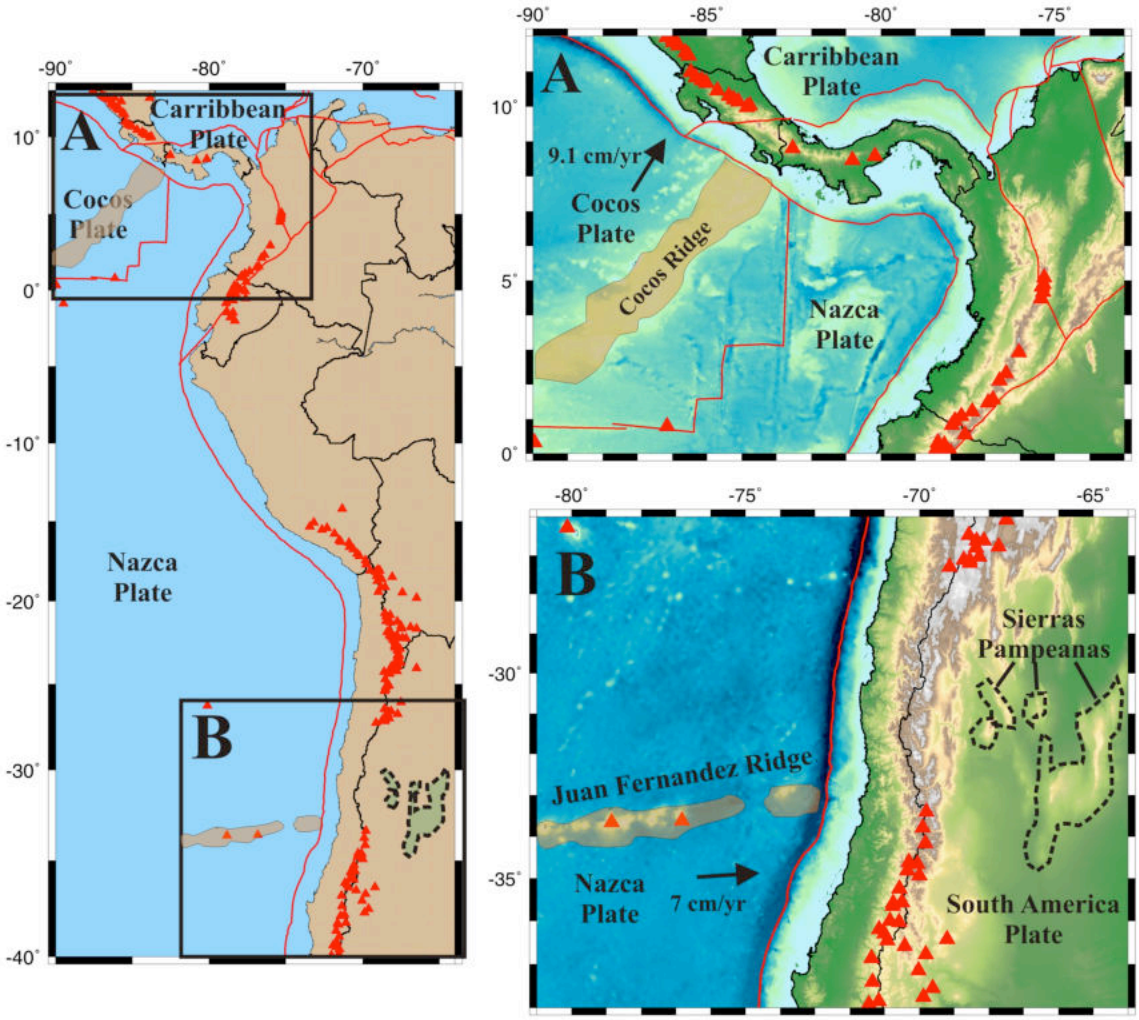

Figure 1. Location map of study areas **A.** Costa Rica **B.** South-Central Andes and Sierras Pampeanas of Argentina. Red triangles indicate Holocene volcanoes.

PRESENT STUDY

The methods, results, and conclusions of these three studies are presented in three manuscripts appended to this dissertation. The following is a summary of the most important findings of each study.

In the steeply dipping Northern Costa Rica subduction zone (Appendix A) we used the method of receiver function analysis to investigate the variability in the hydration state of the subducting Cocos Plate and the nature of crustal terranes within the overriding Caribbean Plate (Fig. 2). Receiver function analysis is a method used to provide constraints on lithospheric structure by isolating P to S conversions (Ps) and its multiples (i.e., PpPs, PsPs, and PpSs) produced at interfaces beneath a three-component receiver [Langston, 1979]. This is accomplished by deconvolving the vertical P-wave energy from the horizontal components. The deconvolution procedure removes both source effects and instrument response, resulting in a time series that is sensitive only to the lithospheric interfaces beneath the seismic station where Ps occur [Langston, 1979]. In this study, receiver functions were calculated by applying an iterative time domain deconvolution approach [Ligoría and Ammon, 1999]. We calculate high-quality P- and PP- wave receiver functions using broadband data of the Global Seismology Network, Geoscope Project, and the CRSEIZE, Pocosol, and Corisubmod experiments. In addition, we estimate the depth (H) and vertically averaged Vp/Vs (κ) to Moho and present a sensitivity study to explore the effects of a dipping interface on receiver functions and the H and κ estimates.

The Central American subduction zone in Northern Costa Rica shows along-strike variations in both the incoming and overriding plates. In the incoming Cocos Plate, there is along-trench variability in the number and size of bathymetric features, outer-rise fault patterns, and crustal age [e.g., von Huene et al., 2000; Barckhausen et al., 2001]. Outer-rise faults are thought to create pathways for seawater to hydrate the uppermost mantle; therefore, heterogeneity in outer-rise fault patterns may control the hydration and thermal state of the Cocos Plate segments [e.g., Ranero et al., 2005; Ivandic et al., 2008]. Our results are consistent with a drier oceanic mantle subducting beneath the southernmost part of the Nicoya Peninsula, as compared to a serpentinized oceanic mantle subducting beneath the northern part. In the Caribbean Plate, we describe the nature of the Mesquito, Nicoya, and Chorotega terranes by integrating new and published Vp/Vs estimates. Both the Nicoya and Chorotega terranes display high Vp/Vs (1.80-1.92) consistent with their oceanic character. In contrast, the oceanic Mesquito Terrane mostly displays lower Vp/Vs (1.62-1.80) more compatible with continental crust. We conclude that the low to moderate Vp/Vs in the fore arc and volcanic arc regions, together with the record of voluminous silicic magmatism, seismic velocities, and crustal thickness, may indicate that the midcrust and upper crust have been profoundly modified by emplacement of silicic melts. Our estimates show that the deepest upper plate Moho (~42 km) is observed in the volcanic arc region whereas the shallowest (~27-33 km) is observed in parts of the fore-arc and back-arc regions (Fig. 2).

In the Pampean flat slab region of Argentina (Fig. 3) we applied a double-difference tomography algorithm (Appendix B) and determine earthquake locations and

focal mechanisms (Appendix C) to earthquake data recorded from the SIEMBRA and ESP broadband deployments. In this region, the flat subduction of the Nazca Plate including the Juan Fernandez Ridge is spatially correlated in the overriding South America Plate with a gap in the arc volcanism and the thick-skinned, basement-cored uplifts of the Sierras Pampeanas.

In Appendix B we study the lithospheric structure of the South America Lithosphere above the flat slab (Fig. 4). We show results of earthquake locations and a detailed three-dimensional model of the subduction zone velocity structure in west-central Argentina (latitude 30-32°S and longitude 64-70°W). We used a regional-scale double-difference (DD) tomography algorithm [tomoFDD; Zhang et al., 2004; Zhang and Thurber, 2006] that is based on the DD location method of Waldhauser and Ellsworth [2000]. This algorithm is designed to solve jointly for 3D velocity structure and earthquake locations using a combination of absolute arrival times and differential times. This leads to a substantially higher resolution in the source region compared to that obtained via conventional tomography [Zhang and Thurber, 2007]. In addition, we present results from a series of careful tests to investigate the sensitivity of our results to many parameters, such as the inter-event distance for calculating the differential times, the starting model, the starting locations, parameterization, and the influence of random error in the data.

For this tomography study, we built a large earthquake data set composed of 40,729 P-wave and 25,183 S-wave absolute times and 170,241 P-wave and 92,325 and S-wave differential times from 1,157 earthquakes recorded at 55 sites. Our model shows the

subducting Nazca Plate as a mostly continuous band of increased (2-6%) P- and S- wave velocities (Vp and Vs). The lithospheric mantle of the South America Plate appears to be heterogeneous but mostly characterized by Vp of 8.0-8.2 km/s, Vs of 4.5-4.7 km/s and Vp/Vs ratio of 1.75-1.78, which is consistent with either a depleted lherzolite or a chlorite harzburgite. We observe a region of higher Vp/Vs ratio (1.78-1.80) that we correlated with up to 10% hydration of mantle peridotite above the flat slab. In addition, we observe localized regions of lower Vp/Vs ratio (1.71-1.73) in the mantle above the westernmost part of the flat slab, which suggests orthopyroxene enrichment. Our results from both the 1D and 3D inversions are consistent with a thicker South America crust in the Western Sierras Pampeanas than in the Eastern Sierras Pampeanas. Our model shows the middle-to-upper crust in the Precordillera as a lower Vp and Vs compared to that of the Cuyania and Pampia terranes. In addition, the Vp/Vs is generally higher in the Cuyania Terrane compared to the Pampia Terrane. These observations are consistent with the presence of Paleozoic carbonate rocks in the Precordillera and the differences in composition for the Sierras Pampeanas basement: a more mafic composition for Cuyania Terrane in the west and a more felsic composition for the Pampia Terrane in the east. The greater variability in the Vp/Vs ratio in the Cuyania Terrane is also in agreement with a more complex structure for this region. The relocated slab earthquakes illuminate the slab geometry and suggest that the flat slab region is broader than the width of Juan Fernandez Ridge offshore.

In Appendix C we study the geometry of the Wadati-Benioff Zone and deformation of the subducting Nazca Plate by determining earthquake locations, slab

contours, and focal mechanisms (Fig. 5). We present high quality earthquake locations from four different methods: single event location [e.g., Lienert et al., 1986], Minimum 1D model [Kissling et al., 1995], double difference [Waldhauser and Ellsworth, 2000], and a regional-scale double difference tomography [Zhang et al., 2004; Zhang and Thurber, 2006] and we compare our new determinations to past studies, especially the results from the CHARGE experiment. Determination of hypocentral parameters is a typical inverse problem, where the location and origin time of earthquakes are estimated from observed travel-times. In our study we used earthquake location algorithms that are based on some form the methodology of Geiger [1912], the linearization of the travel time equation in a first order Taylor series that relates the difference between the observed and predicted travel time to unknown adjustments in the hypocentral coordinates through the partial derivatives of the travel time with respect to the unknowns.

Additionally, we determine high-quality focal mechanism solutions from P-wave first motion polarities by using the program FOCMEC [Snoke et al., 1984]. A focal mechanism is the result of an analysis of waveforms generated by an earthquake and recorded by a number of seismographs. On average, 33 P-wave polarities were used per event and the search for solutions was controlled by a grid-search every five degrees to find zero polarity errors. Our new locations are determined using a higher density network than previous studies, thus allows for a more thorough study of the variations in depth of seismicity across the flat slab region and the determination of a larger number of higher quality focal mechanisms.

Our new, more detailed contours show that the top of the WBZ of the Nazca Plate is nearly flat at ~100 km depth approximately within the region between latitude 28°S and 32°S and longitude 70°W and 68.5°W. Our earthquake locations show a 100 km-wide region of increased seismicity that coincides with the subducted path of the Juan Fernandez Ridge between longitude 70ºW and 68ºW, a seismicity gap along the projected path of Juan Fernandez Ridge to the northeast of longitude 68.5ºW, and the two arms of descending seismicity on both sides of the seismicity gap. This non-uniform spatial distribution of the slab seismicity may reflect the variability in the hydration state of the subducting Nazca Plate with greater release of water from the subducted ridge region. We determine that WBZ is a single layer of seismicity with thickness of 10-15 km and may correspond to dehydration of the oceanic mantle of the Nazca Plate. The abrupt decrease of earthquakes to the northeast of 68.5ºW may indicate that the upper mantle is completely de-serpentinized at this longitude perhaps after the Nazca Plate was intensively dehydrated in the region of the greatest concentration of seismicity. We found that the flat slab region is wider (~240 km) than the Juan Fernandez Ridge offshore (~100 km), and together with the shape of the slab contours may reflect the response of the geometry of the slab to the southward migration of the buoyant ridge. Focal mechanisms suggest that the slab is mostly under extension in the flat slab area. There is a region of mixed T-axis trends near where the slab descends abruptly to the south and northeast which suggests that slab pull and ridge buoyancy may be key factors in the deformation of the slab.

The results of the three seismological studies presented in this dissertation support the hypothesis that the along-trench variability in bathymetric features and the hydration state of the incoming plate has profound effects on the subducting slab geometry and the upper plate structure in both flat and steeply dipping subduction zones.

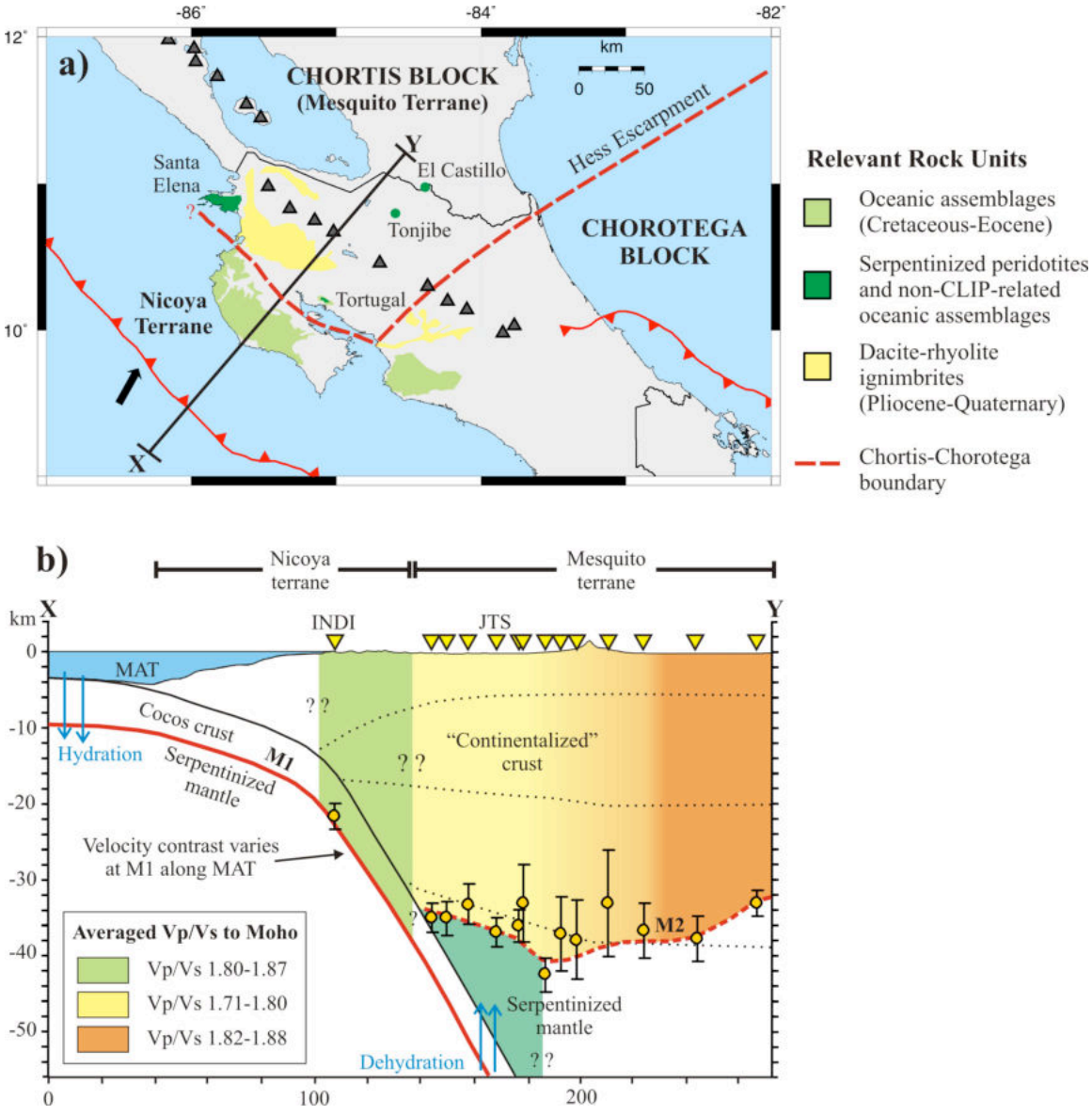

Figure 2. Generalized interpretation of terrane boundaries integrating receiver function results for Northern Costa Rica.

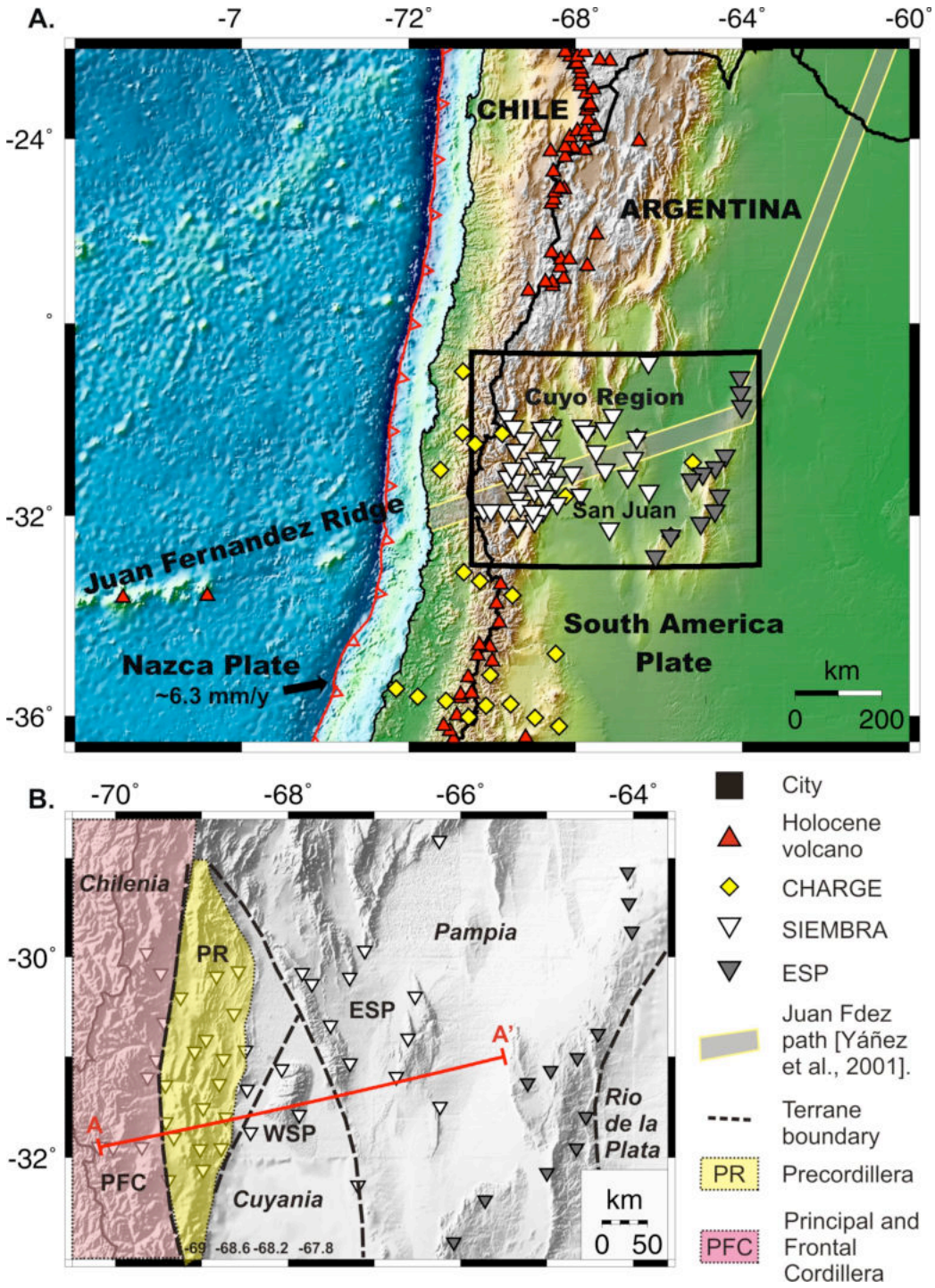

Figure 3. A. Location Map of the Pampean flat slab region **B.** Morphotectonic units and terrane boundaries [Ramos et al., 2002; Rapela et al., 2007] and location of profile shown in Figures 4. ESP, Eastern Sierras Pampeanas; WSP, Western Sierras Pampeanas.

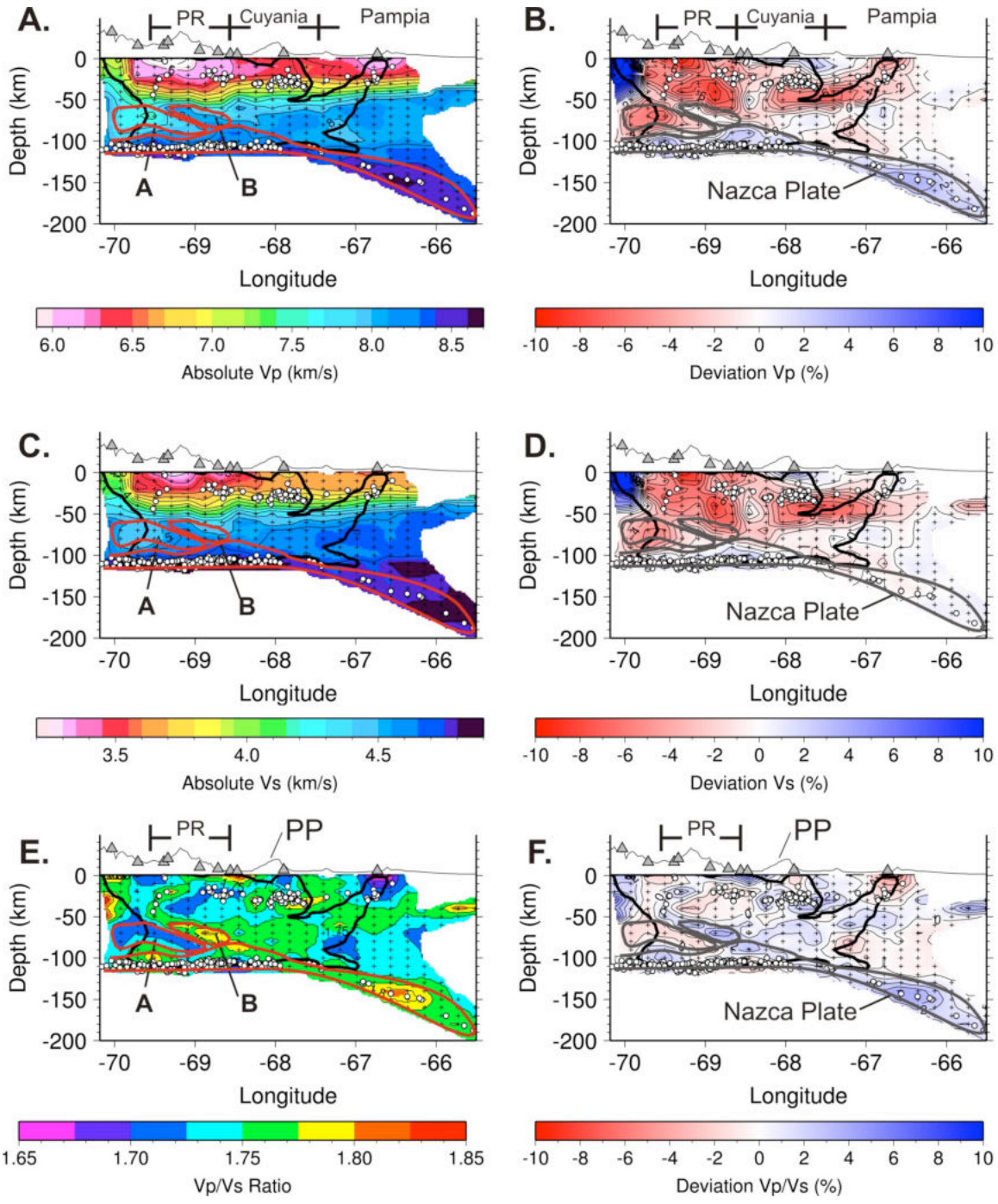

Figure 4. Vertical depth A-A' cross-section (Fig. 3) along the Pampean Flat Slab region for Vp, Vs, and Vp/Vs Ratio. Color bars are indicated below each plot. Marked anomalies are discussed in the text of Appendix B.

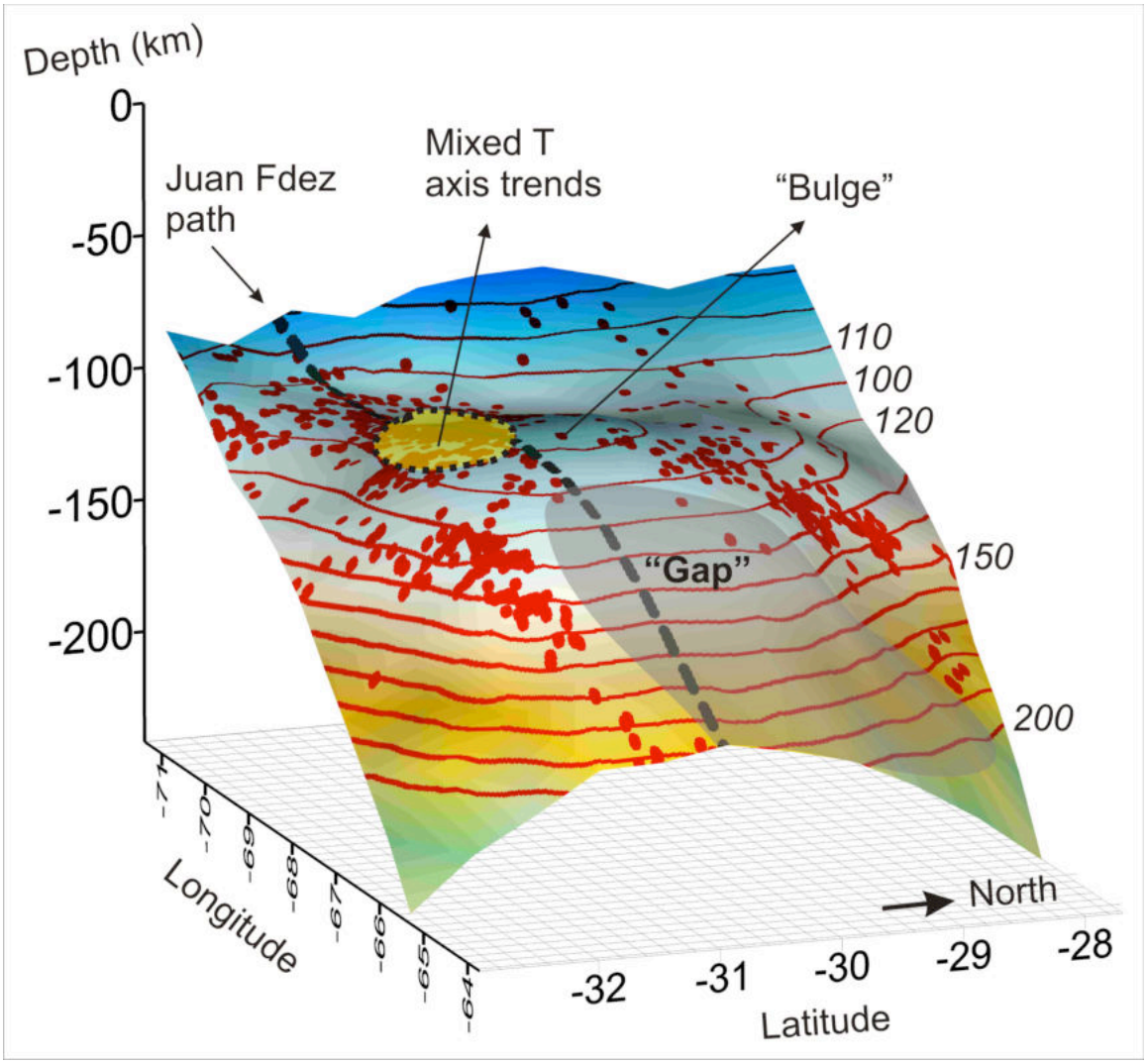

Figure 5. Summary figure using a 3D diagram showing the surface of the top of the Wadati Benioff Zone as view from the southeast.

REFERENCES

Abers, G.A., van Keken, P.E., Kneller, E.A., Ferris, A. & Stachnik, J.C., 2006. The thermal structure of subduction zones constrained by seismic imaging: Implications for slab dehydration and wedge flow, *Earth Planet. Sci. Lett.,* **241,** 387-397, doi:doi: 10.1016/j.epsl.2005.11.055.

Alvarado, P., Beck, S. & Zandt, G., 2007. Crustal structure of the south-central Andes Cordillera and backarc region from regional waveform modelling, *Geophys. J. Int.,* **170,** 858-875, doi:10.1111/j.1365-246X.2007.03452.x.

Barckhausen, U., Ranero, C.R., von Huene, R., Cande, S.C. & Roeser, H.A., 2001. Revised tectonic boundaries in the Cocos Plate off Costa Rica: Implications for the segmentation of the convergent margin and for plate tectonic models, *J. Geophys. Res.,* **106,** 19207-19220, doi:10.1029/2001jb000238.

Benioff, H., 1955. Seismic evidence for crustal structure and tectonic activity, *Spec. Pap. - Geol. Soc. Am.,* **62,** 61-74.

Bostock, M.G., Hyndman, R.D., Rondenay, S. & Peacock, S.M., 2002. An inverted continental Moho and serpentinization of the forearc mantle, *Nature,* **417,** 536-538, doi:10.1038/417536a.

Cloos, M., 1993. Lithospheric buoyancy and collisional orogenesis: Subduction of the oceanic plateaus, continental margins, island arcs, spreading ridges, and seamounts, *Geol. Soc. Am. Bull.,* **105,** 715-737, doi:10.1130/0016-7606(1993)105<0715:LBACOS>2.3.CO;2.

Fisher, D.M., Gardner, T.W., Marshall, J.S., Sak, P.B. & Protti, M., 1998. Effect of subducting sea-floor roughness on fore-arc kinematics, Pacific coast, Costa Rica,

Geology, **26,** 467-470, doi:10.1130/0091-7613(1998)026<0467:EOSSFR>2.3.CO;2.

Geiger, L., 1912. Probability method for the determination of earthquake epicenters from the arrival time only, *Bull. St. Louis Univ.,* **8,** 60-71.

Gutscher, M.-A., Maury, R., Eissen, J.-P. & Bourdon, E., 2000a. Can slab melting be caused by flat subduction?, *Geology,* **28,** 535-538, doi:10.1130/0091-7613(2000)28<535:CSMBCB>2.0.CO;2.

Gutscher, M.-A., Spakman, W., Bijwaard, H. & Engdahl, E.R., 2000b. Geodynamics of flat subduction: Seismicity and tomographic constraints from the Andean margin, *Tectonics,* **19,** 814-833, doi:10.1029/1999tc001152.

Hacker, B.R., Abers, G.A. & Peacock, S.M., 2003a. Subduction factory 1. Theoretical mineralogy, densities, seismic wave speeds, and H2O contents, *J. Geophys. Res.,* **108,** 2029, doi:10.1029/2001jb001127.

Hacker, B.R., Peacock, S.M., Abers, G.A. & Holloway, S.D., 2003b. Subduction factory 2. Are intermediate-depth earthquakes in subducting slabs linked to metamorphic dehydration reactions?, *J. Geophys. Res.,* **108,** 2030, doi:10.1029/2001jb001129.

Hampel, A., 2002. The migration history of the Nazca Ridge along the Peruvian active margin: a re-evaluation, *Earth Planet. Sci. Lett.,* **203,** 665-679, doi:doi: 10.1016/S0012-821X(02)00859-2.

Ivandic, M., Grevemeyer, I., Berhorst, A., Flueh, E.R. & McIntosh, K., 2008. Impact of bending related faulting on the seismic properties of the incoming oceanic plate offshore of Nicaragua, *J. Geophys. Res.,* **113,** B05410, doi:10.1029/2007jb005291.

Jordan, T.E. & Allmendinger, R.W., 1986. The Sierras Pampeanas of Argentina; a modern

analogue of Rocky Mountain foreland deformation, *Am. J. Sci.,* **286,** 737-764, doi:10.2475/ajs.286.10.737.

Kamiya, S.i. & Kobayashi, Y., 2000. Seismological evidence for the existence of serpentinized wedge mantle, *Geophys. Res. Lett.,* **27,** 819-822.

Kay, S.M., Maksaev, V., Moscoso, R., Mpodozis, C., Nasi, C. & Gordillo, C.E., 1988. Tertiary andean magmatism in Chile and Argentina between 28°S and 33°S: Correlation of magmatic chemistry with a changing Benioff zone, *J. South Am. Earth Sci.,* **1,** 21-38, doi:10.1016/0895-9811(88)90013-2|.

Kirby, S., Engdahl, E.R. & Denlinger, R., 1996. Intermediate-depth intraslab earthquakes and arc volcanism as physical expressions of crustal and uppermost mantle metamorphism in subducting slabs (Overview), *in Subduction from Top to Bottom*, pp. 195-215, eds. Bebout, G. E., Scholl, D. W., Kirby, S. H. & Platt, J. P., American Geophysical Union Geophysical Monograph.

Kissling, E., Kradolfer, U. & Maurer, H., 1995. *VELEST User's Guide-short Introduction*, Institute of Geophysics & Swiss Seismological Service ETH Zurich.

Langston, C.A., 1979. Structure Under Mount Rainier, Washington, Inferred From Teleseismic Body Waves, *J. Geophys. Res.,* **84,** 4749-4762, doi:10.1029/JB084iB09p04749.

Lienert, B.R., Berg, E. & Frazer, L.N., 1986. HYPOCENTER: An earthquake location method using centered, scaled, and adaptively damped least squares, *Bull. Seismol. Soc. Am.,* **76,** 771-783.

Ligorría, J.P. & Ammon, C.J., 1999. Iterative deconvolution and receiver-function estimation,

Bull. Seismol. Soc. Am., **89,** 1395-1400.

McCann, W.R. & Habermann, R.E., 1989. Morphologic and geologic effects of the subduction of bathymetric highs, *Pure Appl. Geophys.,* **129,** 41-69-69, doi:10.1007/bf00874624.

Peacock, S.M., 2001. Are the lower planes of double seismic zones caused by serpentine dehydration in subducting oceanic mantle?, *Geology,* **29,** 299-a-302, doi:10.1130/0091-7613(2001)029<0299:ATLPOD>2.0.CO;2.

Ramos, V.A., Cristallini, E.O. & Pérez, D.J., 2002. The Pampean flat-slab of the Central Andes, *J. South Am. Earth Sci.,* **15,** 59-78, doi:10.1016/S0895-9811(02)00006-8.

Ranero, C.R., Villaseñor, A., Phipps Morgan, J. & Weinrebe, W., 2005. Relationship between bend-faulting at trenches and intermediate-depth seismicity, *Geochem., Geophys., Geosyst.,* **6,** Q12002, doi:10.1029/2005gc000997.

Rapela, C.W., Pankhurst, R.J., Casquet, C., Fanning, C.M., Baldo, E.G., González-Casado, J.M., Galindo, C. & Dahlquist, J., 2007. The Río de la Plata craton and the assembly of SW Gondwana, *Earth-Sci. Rev.,* **83,** 49-82, doi:10.1016/j.earscirev.2007.03.004.

Scholz, C.H., 1990. *The mechanics of earthquakes and faulting*, pp. 439, Cambridge University Press, New York.

Snoke, J.A., Munsey, J.W., Teague, A.C. & Bollinger, G.A., 1984. A program for focal mechanism determination by combined use of polarity and *SV-P* amplitude ratio data, *Earthquake Notes,* **55,** 15.

Stern, R.J., 2002. Subduction zones, *Rev. Geophys.,* **40,** 1012, doi:10.1029/2001rg000108.

Ulmer, P. & Trommsdorff, V., 1995. Serpentine Stability to Mantle Depths and Subduction-

Related Magmatism, *Science,* **268,** 858-861, doi:10.1126/science.268.5212.858.

van Hunen, J., van den Berg, A.P. & Vlaar, N.J., 2002. On the role of subducting oceanic plateaus in the development of shallow flat subduction, *Tectonophysics,* **352,** 317-333, doi:10.1016/S0040-1951(02)00263-9.

van Hunen, J., van den Berg, A.P. & Vlaar, N.J., 2004. Various mechanisms to induce present-day shallow flat subduction and implications for the younger Earth: a numerical parameter study, *Phys. Earth Planet. Inter.,* **146,** 179-194, doi:10.1016/j.pepi.2003.07.027.

von Huene, R., Ranero, C.R., Weinrebe, W. & Hinz, K., 2000. Quaternary convergent margin tectonics of Costa Rica, segmentation of the Cocos Plate, and Central American volcanism, *Tectonics,* **19,** 314-334, doi:10.1029/1999tc001143.

Wadati, K., 1928. Shallow and deep earthquakes, *Geophys. Mag.,* **1,** 162-202.

Wadati, K., 1935. On the activity of deep-focus earthquakes in the Japan islands and neighbourhoods, *Geophys. Mag.,* **8,** 305-325.

Waldhauser, F. & Ellsworth, W.L., 2000. A Double-Difference Earthquake Location Algorithm: Method and Application to the Northern Hayward Fault, California, *Bull. Seismol. Soc. Am.,* **90,** 1353-1368, doi:10.1785/0120000006.

Warren, L.M., Langstaff, M.A. & Silver, P.G., 2008. Fault plane orientations of intermediate-depth earthquakes in the Middle America Trench, *J. Geophys. Res.,* **113,** B01304, doi:10.1029/2007jb005028.

Yáñez, G., Cembrano, J., Pardo, M., Ranero, C. & Selles, D., 2002. The Challenger-Juan Fernández-Maipo major tectonic transition of the Nazca-Andean subduction system at

33-34°S: geodynamic evidence and implications, *J. South Am. Earth Sci.,* **15,** 23-38, doi:10.1016/S0895-9811(02)00004-4.

Yáñez, G.A., Ranero, C.R., von Huene, R. & Díaz, J., 2001. Magnetic anomaly interpretation across the southern central Andes (32°-34°S): The role of the Juan Fernández Ridge in the late Tertiary evolution of the margin, *J. Geophys. Res.,* **106,** 6325-6345, doi:10.1029/2000jb900337.

Zhang, H. & Thurber, C., 2006. Development and Applications of Double-difference Seismic Tomography, *Pure Appl. Geophys.,* **163,** 373-403-403, doi:10.1007/s00024-005-0021-y.

Zhang, H. & Thurber, C.H., 2007. Estimating the model resolution matrix for large seismic tomography problems based on Lanczos bidiagonalization with partial reorthogonalization, *Geophys. J. Int.,* **170,** 337-345, doi:10.1111/j.1365-246X.2007.03418.x.

Zhang, H., Thurber, C.H., Shelly, D., Ide, S., Beroza, G.C. & Hasegawa, A., 2004. High-resolution subducting-slab structure beneath northern Honshu, Japan, revealed by double-difference tomography, *Geology,* **32,** 361-364, doi:10.1130/G20261.2.

Zhang, J., Green, H.W., Bozhilov, K. & Jin, Z., 2004. Faulting induced by precipitation of water at grain boundaries in hot subducting oceanic crust, *Nature,* **428,** 633-636, doi:10.1038/nature02475.

APPENDIX A: NATURE OF CRUSTAL TERRANES AND THE MOHO IN NORTHERN COSTA RICA FROM RECEIVER FUNCTION ANALYSIS

Lepolt Linkimer and Susan L. Beck

Department of Geosciences, University of Arizona, Gould-Simpson Building 77, Tucson, AZ 85721, USA (linkimer@email.arizona.edu)

Susan Y. Schwartz

Department of Earth and Planetary Sciences, University of California, Santa Cruz, CA 95064, USA.

George Zandt

Department of Geosciences, University of Arizona, Gould-Simpson Building 77, Tucson, AZ 85721, USA

Vadim Levin

Department of Earth and Planetary Sciences, Rutgers University, Piscataway, NJ 08854, USA

Permission to reprint from copyright holder

Citation: Linkimer, L., S. L. Beck, S. Y. Schwartz, G. Zandt, and V. Levin (2010), Nature of crustal terranes and the Moho in northern Costa Rica from receiver function analysis, *Geochem. Geophys. Geosyst.*, 11, Q01S19, doi:10.1029/2009GC002795.

****

We are pleased to grant permission for the use of the material requested for inclusion in your thesis. The following non-exclusive rights are granted to AGU authors:

- All proprietary rights other than copyright (such as patent rights).
- The right to present the material orally.
- The right to reproduce figures, tables, and extracts, appropriately cited.
- The right to make hard paper copies of all or part of the paper for classroom use.
- The right to deny subsequent commercial use of the paper.

Further reproduction or distribution is not permitted beyond that stipulated. The copyright credit line should appear on the first page of the article or book chapter. The following must also be included, "Reproduced by permission of American Geophysical Union." To ensure that credit is given to the original source(s) and that authors receive full credit through appropriate citation to their papers, we recommend that the full bibliographic reference be cited in the reference list. The standard credit line for journal articles is: "Author(s), title of work, publication title, volume number, issue number,

Program Manager

American Geophysical Union

202-7770-7365

mconnolly@agu.org

****

Abstract

The Central American subduction zone in northern Costa Rica shows along-strike variations in both the incoming and overriding plates. By analyzing the subducting oceanic Moho (M1) and the upper plate Moho (M2) with receiver functions, we investigate the variability in the hydration state of the subducting Cocos Plate and the nature of crustal terranes within the overriding Caribbean Plate. We calculate high-quality *P*- and *PP*- wave receiver functions using broadband data of the Global Seismology Network, Geoscope Project, and the CRSEIZE, Pocosol, and Corisubmod

experiments. In addition, we estimate the depth (*H*) and vertically averaged *Vp/Vs* (κ) to Moho and present a sensitivity study to explore the effects of a dipping interface on receiver functions and the *H* and κ estimates. Our results are consistent with a drier oceanic mantle subducting beneath the southernmost part of the Nicoya Peninsula, as compared to a serpentinized oceanic mantle subducting beneath the northern part. In the Caribbean Plate, we describe the nature of the Mesquito, Nicoya, and Chorotega terranes by integrating new and published *Vp/Vs* estimates. Both the Nicoya and Chorotega terranes display high *Vp/Vs* (1.80-1.92) consistent with their oceanic character. In contrast, the oceanic Mesquito Terrane mostly displays lower *Vp/Vs* (1.62-1.80) more compatible with continental crust, which may indicate that subduction zone magmatism is modifying the crust to display continental character. Our estimates show that the deepest M2 (~42 km) is observed in the volcanic arc region whereas the shallowest M2 (~27-33 km) is observed in parts of the fore-arc and back-arc regions.

1. Introduction

The Central American subduction zone in Costa Rica shows along-strike variations that are useful for understanding subduction zone processes. In the incoming Cocos Plate, there is along-trench variability in the number and size of bathymetric features, outer-rise fault patterns, and crustal age [e.g., *von Huene et al*., 2000; *Barckhausen et al*., 2001]. Outer-rise faults are thought to create pathways for seawater to hydrate the uppermost mantle; therefore, heterogeneity in outer-rise fault patterns may control the hydration and thermal state of the Cocos Plate segments [e.g., *Ranero et al*.,

2005; *Ivandic et al.*, 2008]. In northern Costa Rica, the trenchward location of the Nicoya Peninsula over the fore arc makes it ideal to study the hydration state of the subducting Cocos Plate using on-land geophysical experiments.

In the upper plate, the modern volcanic arc is built upon the Chorotega and Chortis blocks. In Costa Rica, the Chortis Block consists of the oceanic Mesquito (or Siuna) Terrane [e.g., *Rogers et al.*, 2007; *Baumgartner et al.*, 2008]. In addition, the Nicoya Peninsula has been described as a separate Nicoya Terrane [*Di Marco et al*, 1995]. There is no consensus on the location of the boundary between these blocks and terranes (Figure 1). The Chorotega-Chortis boundary has been suggested to lie in southern Nicaragua [*MacKenzie et al.*, 2008], along the Costa Rica-Nicaragua border [e.g., *Dengo*, 1985; *Rogers et al.*, 2007], and near the Nicoya Gulf [*Hauff et al.*, 2000], and has also been interpreted as a broad region, where both blocks coexist at depth, bounded to the south by the southwestward projection of the Hess Escarpment into central Costa Rica [*Baumgartner et al.*, 2008].

One of the intriguing aspects of the crust in northern Costa Rica is that it displays a continental character even though it is presumably composed of terranes of oceanic origin. There are large-volume silicic pyroclastic flows and ignimbrites associated with the volcanic arc [*Vogel et al.*, 2004; 2006] and the velocity structure and crustal thickness have been suggested as indicators of continental crust [e.g., *Drummond et al.*, 1995; *Sallarès et al.*, 2001; *Vogel et al.*, 2004; *MacKenzie et al.*, 2008].

Costa Rica has been the site of numerous geological and geophysical studies and much progress has been made towards understanding the lithospheric structure and

tectonics [e.g., *Sallarès et al.*, 2001; *DeShon et al.*, 2006; *MacKenzie et al.*, 2008; *Baumgartner et al.*, 2008]. In this study, we build upon previous work and analyze a larger data set of receiver functions at stations in northern Costa Rica. The main goals of this paper are to describe the amplitude and azimuthal variation of converted waves from both the subducting oceanic Moho (M1) and the upper plate Moho (M2) and to calculate the depth (H) and vertically averaged Vp/Vs (κ) to these interfaces. Our intention is to use this information to investigate the variation in the hydration state of the subducting Cocos Plate. By integrating our new receiver function estimates with published geological data and the receiver function estimates from *MacKenzie et al.* [2008], we describe the nature of crustal blocks and terranes (Mesquito, Nicoya, and Chorotega) within the overriding Caribbean Plate and reexamine the previously proposed boundaries between them.

We present evidence of a drier oceanic mantle subducting beneath the southernmost part of the Nicoya Peninsula, as compared to a serpentinized oceanic mantle subducting beneath the central and northern parts. We also document a moderate to low Vp/Vs in the fore arc and volcanic arc of northern Costa Rica similar to the Vp/Vs of continental-crust regions. In addition, by computing synthetic receiver functions for simple velocity models, we examine the bias that might be introduced in the H and κ estimates by a dipping interface and study the azimuthal variation in P- to S- wave conversions (Ps) and reverberations expected above the subducting Cocos Plate in the Nicoya Peninsula.

2. Tectonic Framework

Central America has been traditionally divided into two main tectonic blocks (Figure 1). The Chortis Block, to the north, is mostly underlain by Paleozoic continental basement and/or accreted oceanic rocks [*Rogers et al.*, 2007]. The Chorotega Block, to the south, has no crystalline Paleozoic basement but instead consists of a ~20-km-thick oceanic plateau known as the Caribbean Large Igneous Province (CLIP), which formed ~88-91 Ma during a period of extreme volcanism related to the initiation of the Galapagos hotspot [*Sinton et al.*, 1998; *Hauff et al.*, 2000].

The Chortis Block has been traditionally described as continental [i.e., *Dengo*, 1985]. However, recent studies have described it as composed of terranes of both oceanic and continental origins [*Rogers et al.*, 2007]. The Central Chortis Terrane, largely restricted to Honduras, is strictly continental (Figure 1). But, the southernmost part of the Chortis Block, known as Siuna Terrane in Nicaragua [*Rogers et al.*, 2007], or Mesquito Oceanic Composite Terrane from El Salvador to northern Costa Rica [*Baumgartner et al.*, 2008], includes both deformed rocks of Ocean Island Basalt (OIB) and island-arc affinities that were accreted to the edges of the Central and Eastern Chortis Terranes during Late Cretaceous [*Rogers et al.*, 2007; *Baumgartner et al.*, 2008].

The Nicoya Peninsula has been described as a separate Nicoya Terrane [*Di Marco et al*, 1995], where the Nicoya Complex is exposed (Figure 2a). The Nicoya Complex represents a set of Cretaceous plateaus that intruded Jurassic–Early Cretaceous radiolarites between 139 and 83 Ma and has been interpreted as fragments of the CLIP [*Denyer and Gazel,* 2009, and references therein] as well as Pacific pre-CLIP plateaus

[*Baumgartner et al.*, 2008]. Along the Pacific coast, to the south of the Nicoya Peninsula, there are exposures of younger (Late Cretaceous to Tertiary) igneous complexes that consist of portions of seamounts and aseismic ridges uplifted and/or accreted to the margin but are related to the activity of the Galapagos hotspot after the formation of the CLIP [*Hoernle et al.*, 2002].

Costa Rica is located at the southern end of the Middle America Trench (MAT) in a tectonic setting controlled by the interaction of the Cocos, Caribbean, and Nazca plates. The Cocos Plate is subducting to the northeast underneath the Caribbean Plate at a rate of ~83 mm/yr in northwestern Costa Rica [*DeMets et al.*, 1994]. The volcanic arc is located ~150 km to the northeast of the MAT. Extensive silicic magmatism, dominated by rhyolitic ignimbrites, has occurred in the central and northern parts of Costa Rica between ~6 and 0.32 Ma. The ignimbrite deposits in the Guanacaste region (Figure 2a) represent the most voluminous (> 200 km^3) silicic volcanic deposits in Costa Rica [*Vogel et al.*, 2004].

In the incoming Cocos Plate, off the coast of the Nicoya Peninsula, two different segments have been identified (Figure 1). The northern segment is characterized by a ~5-km-thick oceanic crust [e.g., *Grevemeyer et al.,* 2007] that was created at the East Pacific Rise (EPR). The oceanic crust is 24 Ma [*Barckhausen et al*., 2001] at the trench, has exceptionally low heat flow [~14 mW/m^2, *Langseth and Silver*, 1996], and displays pervasive normal faulting that presumably extends through the entire oceanic crust and facilitates the hydration of the uppermost mantle [*Ranero et al.*, 2003]. Furthermore, the oceanic-mantle rocks show anomalously low *P*-wave velocities in tomographic images,

suggesting 12-17 % serpentinization [*Ivandic et al.*, 2008]. The segment located off the coast of southern Nicoya is characterized by ~7-km-thick oceanic crust created at an ancient Cocos-Nazca Spreading Center (CNS1), has relatively high heat flow (~110 mW/m^2), displays only a few small-offset faults in the outer rise, and exhibits age variability along the margin, from 21 to 23 Ma [*von Huene et al.*, 2000; *Barckhausen et al.*, 2001; *Ranero et al.*, 2003].

3. Previous Geophysical Studies

A simplified picture of the margin in northern Costa Rica has been constructed from local tomography [e.g., *Sallarès et al.*, 2000; *Husen et al.*, 2003; *DeShon et al.*, 2006; *Syracuse et al.*, 2008], receiver functions [*DeShon and Schwartz*, 2004; *MacKenzie et al.*, 2008], and reflection and refraction studies [e.g., *Ye et al.*, 1996; *Christeson et al.*, 1999; *Sallarès et al.*, 1999, 2001; *Bullock et al.*, 2007; *Grevemeyer et al.*, 2007]. The upper plate has been divided into three levels tied to velocity gradients instead of first-order velocity contrasts [*Sallarès et al.*, 2001]. The margin wedge has been imaged as a region of high velocities compared to those expected for an accretionary prism and has been interpreted as the seaward extension of the Nicoya Complex [e.g., *Ye et al.*, 1996; *Christeson et al.*, 1999]. The uppermost mantle beneath the fore arc displays reduced velocities (6.8-7.2 km/s) and has been interpreted as evidence for 15-25 % serpentinization [*Sallarès et al.*, 2001; *DeShon and Schwartz*, 2004; *DeShon et al.*, 2006].

The upper plate Moho (M2) has been identified at a depth range of 27 to 43 km, based on Pn and Pg travel times [*Matumoto et al.*, 1977; *Quintero and Kulhánek,* 1998], seismic refraction [*Sallarès et al.*, 1999, 2001], and receiver functions [*DeShon and*

Schwartz, 2004; *MacKenzie et al.*, 2008]. M2 has been imaged as a region of low-velocity contrast in the fore arc [*DeShon et at.*, 2006; *Arroyo et al.*, 2009] and interpreted as a transition zone [*Sallarès et al.*, 2001]. Using receiver functions, which are sensitive to discontinuities, *MacKenzie et al.* [2008] were able to image M2 as a relatively strong velocity contrast (~0.5-1.0 km/s) beneath both the volcanic arc and back-arc regions and describe a more complicated signal in the fore-arc region. The intersection of the subducting Cocos Plate with M2 (Figure 2a) occurs at depths of 30-34 km beneath the western part of the Nicoya Peninsula [*Sallarès et al.*, 1999; *DeShon et al.*, 2006].

The subducting Cocos Plate has been recognized from Wadati-Benioff Zone (WBZ) seismicity [e.g., *Protti et al.*, 1994; *Newman et al.*, 2002; *DeShon et al.*, 2006], seismic refraction [e.g., *Christeson et al.*, 1999; *Sallarès et al.*, 2001], and seismic tomography [e.g., *Husen et al.*, 2003; *DeShon et al.*, 2006; *Syracuse et al.*, 2008], but has not been previously imaged using receiver functions. A narrow zone of low velocities paralleling the top of the high-velocity subducting Cocos Plate was recognized by *Husen et al*. [2003] and linked to a cold and highly hydrated Cocos oceanic crust that is subducting beneath northern Costa Rica.

4. Data and Methodology

Receiver function analysis is a method used to provide constraints on lithospheric structure by isolating Ps and its multiples (i.e., PpPs, PsPs, and PpSs, Figure 3a) produced at interfaces beneath a three-component receiver. This is accomplished by deconvolving the vertical *P*-wave energy from the horizontal components under the assumption that very little converted energy appears on the vertical component for steeply incident rays

(distances > 30º). The deconvolution procedure removes both source effects and instrument response, resulting in a time series that is sensitive only to the lithospheric interfaces beneath the seismic station where Ps occur [*Langston*, 1979]. In this study, receiver functions were calculated by applying an iterative time domain deconvolution approach. This estimation is a least-squares minimization of the difference between the observed horizontal seismogram and a predicted signal generated by the convolution of an iteratively-updated spike train with the vertical component seismogram [*Ligoría and Ammon*, 1999].

P- and *PP*- wave receiver functions were calculated using teleseismic events recorded by stations of the CRSEIZE Experiment from December 1999 to December 2001, Pocosol Network from April 2005 to July 2006, and Corisubmod Project from February 2005 to February 2007, as well as Geoscope Project station HDC from March 1997 to December 2005 and Global Seismology Network station JTS from April 1995 to May 2008 (Figure 2b). The majority of these stations were equipped with Streckeisen STS-2, Guralp CMG3T and 40T, and Trillium seismometers.

We calculated a total of 615 high-quality receiver functions from 22 broadband stations. The number of events for individual stations varies from 1 to 111, depending on the length and quality of recording. Stations HDC and JTS have the largest number of high-quality receiver functions documented for a single station in Costa Rica, with 85 and 111, respectively. We do not show results for stations with less than nine high-quality receiver functions (CRCZ, HOJA, VCR, and LCH0) and stations HATA, CDL, and SAN, where shallow structures and/or sedimentary basin reverberations precluded

interpretation. In order to increase the number of traces and improve the signal-to-noise ratio, stations close to each other were stacked, such as PAPA and COND, PNCB and MOSD, and JOC and TIR (Table 1, Figure 2b).

Earthquake locations were selected from the US Geological Survey National Earthquake Information Center (NEIC) with magnitude > 5.5 and a distance range from 30° to 90° for calculating *P*-wave receiver functions and with magnitude > 6.0 from 90° and 180° for calculating *PP*-wave receiver functions. Our data are mostly composed of events clustered in backazimuths of 140-340°, especially from South America and the South Pacific regions (Figure 3b).

4.1. Data Processing

Each earthquake recorded on the Z, E-W, and N-S components was band-pass-filtered (0.1-3 Hz and 0.2-3 Hz) and the horizontal components were rotated to the radial and tangential directions of the great circle path, based on the NEIC hypocentral locations. For the receiver function calculation we applied an iterative time domain deconvolution approach [*Ligoría and Ammon*, 1999] on a time window of 120 s for each record, starting 20 s before *P*- or *PP*- wave onset (Figure 3c) and applied Gaussian-filter width factors of 1.0 and 2.5 to remove high-frequency noise [e.g., *Cassidy*, 1992].

For each event-station pair, we examined four different receiver functions using a combination of the aforementioned band-pass and Gaussian filters, and selected the combination with the best signal-to-noise ratio. For stations in the Nicoya Peninsula, a band-pass filter of 0.2-3 Hz and a Gaussian of 2.5 was preferred. For the remaining stations, we used a band-pass filter of 0.1-3 Hz and a Gaussian of 2.5. Also, both

absolute-amplitude and normalized-to-the-maximum-amplitude receiver functions were calculated for the above combination of parameters. To analyze the highest quality results, we rejected events with less than 80% match between the predicted and observed waveforms produced via a comparison of the radial (or tangential) component seismogram with a convolution of the vertical component seismogram and the receiver function (i.e., variance reduction less than 80%).

4.2. Depth and *Vp/Vs* Calculations

The depth (*H*) and vertically averaged *Vp/Vs* (κ) estimates to Moho were obtained using a stacking algorithm that maps in the *H*-κ domain the weighted sum of the radial receiver function amplitudes of each phase [*Zhu and Kanamori*, 2000]. The radial receiver function stack $s(H,\kappa)$ is given by the equation:

$$s(H,\kappa) = \omega_{Ps} r(t_{Ps}) + \omega_{PpPs} r(t_{PpPs}) - \omega_{PpSs+PsPs} r(t_{PpSs+PsPs})$$

where ω is the weight associated with the radial receiver function r(t) of the Ps, PpPs, and PpSs+PsPs phases (Figure 3a). The arrival times (t_{Ps}, t_{PpPs}, and $t_{PpSs+PsPs}$) are predicted from the ray parameter (p) and the depth and velocity structure to Moho. During stacking, ω is assigned to each of the three phases such that the sum of ω equals 1.0. We tested several weighting schemes but we present the results obtained from one that gives equal weight to the three phases (ω_{Ps}= 1/3 ω_{PpPs}= 1/3 $\omega_{PpSs+PsPs}$= 1/3) to ensure equal importance to each phase independent of their actual amplitude.

Receiver functions were stacked for depth and *Vp/Vs* ranges from 10 to 70 km and 1.6 to 2.1, respectively. A point of maximum amplitude or "bulls-eye" occurs when the

three phases are stacked coherently and it denotes the most likely solution for H and κ. In order to constrain the confidence in our results, we estimated uncertainties based on the variance of the $s(H,\kappa)$ stack and the flatness at the maximum, as proposed by *Zhu and Kanamori* [2000].

Since the time delay equations for Ps and multiples hold for flat interfaces, we estimated H and κ to Moho using this algorithm only at stations where the receiver function azimuthal behavior suggests flat layers. For the dipping Cocos Plate, H and κ were approximated by applying a post-stack correction to H and κ based on synthetic data (see Section 5.2).

Receiver functions were stacked assuming that a standard Vp represents a reasonable average-crustal-wave speed (Table 1). A crustal Vp of either 6.0 or 6.3 km/s was used for stations in the Nicoya region based on *DeShon and Schwartz* [2004]. A higher Vp of 6.3 km/s and 6.5 km/s was used for JTS and Pocosol stations, respectively, based on *Sallarès et al*. [2001]. For stations LCH0 and HDC we used a Vp of 6.0 and 6.3 km/s, respectively, based on *Syracuse et al*. [2008]. We do not expect deviations from the assumed Vp to significantly affect our results (see Section 5.3).

To discriminate between Ps and multiples (PpPs, and PpSs+PsPs) we plotted the moveout of phase arrivals as a function of ray parameter. Ps arrivals exhibit positive moveout with respect to the direct *P*-wave arrival with increasing ray parameter, while the ray geometry of multiples produces a negative moveout. Thus, we compare expected and observed moveout on receiver functions in order to verify that the arrival of Ps phases and multiple reverberations are produced at particular depths.

5. Sensitivity Tests

By knowing the dip direction (~N40ºE) and dip angle (~13-35°) of the subducting Cocos Plate beneath the Nicoya Peninsula [*DeMets et al.*, 1994; *Christeson et al., 1999*; *Sallarès et al.,* 2001], we examined the receiver function sensitivity to a dipping interface as a function of backazimuth and amount of dip, as well as the assumed Vp. This analysis was performed by calculating synthetic receiver functions with no noise. Synthetic seismograms were generated using RAY3D [*Owens*, 1984], a 3-D ray tracing code based on *Langston* [1977]. The *P*- and *S*- wave velocities, density, strike, dip angle, and thickness were specified for each layer in the model. Synthetic vertical, radial, and tangential seismograms were generated by specifying a backazimuth and ray parameter for an incident *P* wave at the base of the model. Synthetic receiver functions were computed by applying the deconvolution procedure (Section 4.1) on the synthetic responses.

5.1. Sensitivity to Backazimuth

In the presence of a dipping interface, stacking to create an average receiver function risks misinterpretation of the structure as Ps and multiples may show a strong azimuthal variation in timing, amplitude, and polarity [e.g., *Cassidy*, 1992; *Hayes and Furlong*, 2007; Figure 4]. We analyzed the azimuthal behavior of synthetic receiver functions to search for the direction at which the complications are minimized. We performed this analysis by creating synthetic receiver functions using a dipping interface with the appropriate orientation for our study region. We found that receiver functions along the strike of the dipping interface are similar to a flat interface case, particularly for

the Ps phase and the absence of PpPp phases that are observed at other backazimuths (Figure 4a). In addition, the Ps amplitude of receiver functions along the strike is not very sensitive to changes in the dip angle (Figure 4b). These observations motivated us to stack our observed receiver functions along the strike of the subducting Cocos Plate for individual stations located in the Nicoya Peninsula, in order to compare the Ps amplitude between stations.

5.2. *H*-κ Sensitivity to Dip Angle

Rossi et al. [2006] and *Hayes and Furlong* [2007] developed a new method to estimate depth and *Vp/Vs* to dipping interfaces by stacking receiver functions. We chose to use an alternative approach to this problem by investigating the potential bias introduced by a dipping interface in the *H*-κ stacking algorithm, similar to that presented by *Lombardi et al.* [2008] for the Alps. We stacked synthetic receiver functions calculated from models with varying interface depth and dip angle and created a map of the differences between the apparent results for *H* and *κ* and the true model values, which are referred hereafter as "bias in depth" and "bias in *Vp*/*Vs*". The biases given in Figure 5a are representative of receiver functions from all backazimuths and ray parameter of 0.06 whereas those in Figure 5b are representative of the ray parameter and azimuthal coverage of our data set.

We found that when dealing with a dipping interface, calculations are biased towards shallower depths and higher *Vp/Vs* than true model parameters. In the case of a full and evenly-distributed azimuthal coverage (Figure 5a), the depth bias is small (< 1 km) for an interface dipping < 12º. The bias in the *Vp/Vs* estimate could be as high as

0.08 for a 10- to 40 km-depth interface dipping 12º. If the interface depth varies from 40 km to 60 km and the interface dips < 12º, the *Vp/Vs* bias is < 0.02. We recommend using the *H*-κ stacking algorithm with caution when the dip angle is known to be greater than 12º, as the bias in *Vp/Vs* could be geologically significant, especially if the interface depth is > 35 km.

Beneath the Nicoya Peninsula, the depth to the top of the ~7 km-thick Cocos crust varies from 15 to 35 km [*DeShon et al.*, 2006] and its dip angle is 13° beneath the coastline [*Christeson et al.*, 1999; *Sallarès et al.*, 1999, 2001]. For the ray parameter and azimuthal coverage of our data set (Figure 5b) and within the 10-35 km depth range, the bias is likely to be < 4 km in depth and < 0.08 in *Vp/Vs* for an interface dipping < 14º. For a 13º dipping oceanic Moho at 22 km depth, as expected beneath the coastline in central Nicoya [*Christeson et al.*, 1999], the bias is on the order of 2 km in depth and -0.05 in *Vp/Vs*. We used these values as a correction that we applied to our *H* and κ estimates for the coastal stations INDI, MARB, and PNCB. Similarly, we applied a correction for station GRAN (3 km and -0.09).

For stations BANE, GUAI, and JUDI the expected M1 depth and dip angle may be > 30 km and > 30º, respectively. We think that the *H*-κ stacking algorithm should not be used for these sites as biases predicted from synthetic data are too large (> 8 km in depth and < -0.20 in *Vp/Vs*), although our calculations suggested that *Vp/Vs* may be higher than 1.80 for all three sites. Similarly, high *Vp/Vs* (1.80-1.89) is suggested if we accept the M1 depth based on previous studies [*Christeson et al.*, 1999; *Sallarès et al.*, 2001; *DeShon et al.*, 2006] and determine the *Vp/Vs* by migrating the Ps time of the

receiver functions along the strike of the subducting Cocos Plate. Unfortunately, we cannot reliably estimate the *Vp/Vs* in this way, as synthetic tests for a layer dipping >30º predicted that the *Vp/Vs* could 0.08 higher than the one estimated from the Ps time only.

5.3. *H*-κ Sensitivity to the Assumed Vp

The sensitivity of the *H*-κ stacking algorithm to the assumed Vp is examined by creating a map of the bias for both the depth and *Vp/Vs* estimates for a range of Vp values and interface depths. We found that the *H*-κ stacking algorithm is not particularly sensitive to Vp. If the Vp deviation is < 0.4 km/s from the correct input value (i.e., Vp in the model is 6.3 km/s and a value of 6.3±0.4 km/s is used instead in the *H*-κ algorithm, Figure 6) the *Vp/Vs* estimate differs from the initial model by < ±0.02 in *Vp/Vs* and < ±3 km in depth, for models with interface depths in the range from 10 to 45 km. A larger bias in the depth estimate is expected for models with interface depths > 45 km. In this study, we do not expect the assumed crustal Vp (Table 1) to significantly affect the overall findings, as deviations greater than ±0.4 km/s in the assumed Vp are unlikely.

6. Results and Discussion

6.1 The Subducting Cocos Plate beneath the Nicoya Peninsula

We detected M1 in the Nicoya Peninsula region as a clear positive Ps at delay times from 3 to 5 s in the radial receiver functions (Figures 7 and 8). The following features of M1 are consistent with a northeast dipping interface in agreement with the direction of the subducting Cocos Plate: (1) The arrival time of the Ps signal at different sites increasing towards the northeast, (2) A polarity reversal at 200-240º in the tangential

component of all stations, suggesting that the direction of maximum dip is ~N40ºE, (3) A clear positive arrival in the tangential component in the backazimuth range from 300º to 340º, and (4) A negative arrival in the tangential component in the backazimuth range from 150º to 180º at most stations. All these features were reproduced by creating synthetic receiver functions using simple models of a shallow northeast-dipping interface over a half-space (Figure 9). However, the comparison of observed and synthetic receiver functions does not resolve the finer features and is mostly confined to the first 10 s where complications of dipping structures are minimized.

Our depth estimates (Table 1) are in agreement with the location of M1, about 7 km deeper than the top of the slab estimated from refraction seismology [*Christeson et al.*, 1999] and WBZ seismicity [*DeShon et al.*, 2006]. To explore the possibility that the Ps corresponds to the top of the slab, we calculated the *Vp/Vs* required for the Ps to be migrated to that depth. We performed this analysis assuming a constant crustal Vp for each station (Table 1) and using only receiver functions along the strike of the subducting Cocos Plate, because complications in the stacking are minimized in the strike direction (Section 5.1, Figures 4 and 8). Sensitivity tests revealed that the bias in calculating the *Vp/Vs* using the Ps time of along-strike receiver functions is only ~0.01, for an interface at ~20-km depth dipping 13°, as expected for M1 beneath the coastline. We found that the *Vp/Vs* required for the Ps conversion to be migrated to the top of the slab is unrealistically high (~ 2.25). On the other hand, a *Vp/Vs* of 1.80-1.85, which is in agreement with our corrected *Vp/Vs* solutions from the *H*-κ algorithm, places the

interface depth at 21-25 km, which is the expected M1 depth. Hence, we interpret the observed Ps as produced at M1 and not at the top of the oceanic crust.

There are some receiver function features that may correlate to the top of the oceanic crust but are not consistent at all stations and backazimuths. For example, receiver functions at stations INDI and JUDI, in central Nicoya, show an additional positive arrival about one second earlier than M1 at some backazimuths (Figures 7). If this signal corresponds to the top of the slab, it would require an increase in wave speed across the top of the oceanic crust. For stations BANE and PNCB there is a negative arrival about one second before the M1 Ps over a broad backazimuth range, especially at PNCB (Figures 7). A negative arrival is also present at some backazimuths at stations MARB and GRAN (Figure 7). In all these cases, the negative polarity arrival characterizes higher to lower wavespeeds with increasing depth, indicating a low-velocity zone.

A strong negative polarity reflection from the top of the subducting Cocos Plate has been interpreted as caused by free water coming from dehydration reactions of subducted clays [*Ranero et al.* 2008]. Low-velocity anomalies parallel to the top of the subducting plate and detected using receiver functions have also been correlated with a hydrated subducting oceanic crust in southern Alaska [e.g., *Rossi et al.*, 2006], northeast Japan [e.g., *Kawakatsu and Watada,* 2007], and Cascadia [*Nikulin et al*., 2009] subduction zones. As the observed negative arrival is not consistent at all stations and backazimuths, we are not able to discriminate whether this feature indicates a hydrated subducting oceanic crust or a hydrated base of the overriding plate.

6.2. Hydration State Variability in the Subducting Cocos Plate

The Ps amplitude observed at stations located in the Nicoya Peninsula reveals a very interesting pattern. The M1 amplitude from stations located in the southernmost part of the peninsula (i.e., BANE and PNCB-MOSD) is considerably larger compared to that observed at stations located in the central and northern parts (Figure 8). Because the amplitude of receiver functions scales with the velocity contrast at the interface, a larger impedance contrast at the base of the oceanic crust (M1) is likely for stations located in the southernmost part of the Nicoya Peninsula.

Oceanic crust generated at both the EPR and CNS1 subducts beneath the northern and southern half of the Nicoya Peninsula, respectively (Figure 1). While both types of lithosphere are of similar age at the MAT (21-24 Ma), there is a distinct thermal change across the EPR-CNS1 suture. Heat flow measurements in the 24-Ma EPR crust average 14 mW/m^2 [*Langseth and Silver*, 1996], which is exceptionally low when compared to the heat flow of ~100 mW/m^2 expected for a 20-25 Ma oceanic crust [*Stein and Stein*, 1992]. In contrast, heat flow measurements in the similarly dated (21-23 Ma) CNS1 crust have values of 105-115 mW/m^2 which are higher than the heat flow values expected from global models [*Fisher et al.*, 2003].

The effective hydrothermal cooling of the EPR-generated seafloor has been attributed to an unusually high permeability facilitated by the presence of outer-rise normal faulting [*Grevemeyer et al.*, 2005]. Seismic reflection images acquired in the EPR-generated seafloor, offshore Nicaragua, show a pervasive set of trenchward-dipping features that cross the crust and extend into the upper mantle to depths of ~20 km

[*Ranero et al.*, 2003; *Grevemeyer et al.*, 2007]. In this region, tomographic images revealed anomalously low Vp in the uppermost mantle, suggesting 12-17 % serpentinization [*Ivandic et al.*, 2008]. This observation supports the idea that pervasive bending-related normal faulting in the subducting slab is creating pathways for seawater to hydrate upper mantle rocks [*Grevemeyer et al.*, 2007; *Ivandic et al.*, 2008] and it is also consistent with the hypothesis that the stronger slab signal in the volcanic arc geochemistry inland of the EPR segment is reflecting greater amounts of fluid released from dehydration of a more extensively serpentinized EPR-mantle [*Rüpke et al.*, 2002]. In contrast, the CNS1-generated seafloor displays only a few small-offset faults in the outer rise [*Ranero et al.*, 2003].

Figure 8 shows the location of the EPR-CNS1 suture zone, at present time and 1 and 2 Ma, based on *Barckhausen et al.* [2001]. Assuming that the current plate velocity vectors have remained constant during the last 2 Ma, we expect that the oceanic lithosphere visible beneath the southernmost part of the Nicoya Peninsula has CNS1-origin. In contrast, the oceanic lithosphere beneath stations in central and northern Nicoya corresponds to EPR-origin, with the exception of station INDI, which likely originated near the EPR-CNS1 suture region.

We created synthetic receiver functions for simple models involving hydrated and dry oceanic crust and upper mantle, to recreate the subduction of EPR and CNS1 lithospheres (Figure 9). As expected, the Ps amplitude is considerably larger in the presence of a hydrated oceanic crust over a dry upper mantle (Figure 9c) and smaller if the oceanic mantle is serpentinized (Figure 9a). Differences in the hydration state of the

subducting oceanic crust may account for the amplitudes observed at some backazimuths at INDI and JUDI (Figure 9b). In order to reproduce the Ps amplitude observed in our receiver functions, a Vs contrast of 0.3-0.5 km/s is required at M1 for stations located above the EPR segment and a much larger Vs contrast of 1.7 km/s is required for the CNS1 segment.

The observed Ps conversions in the Nicoya region are then consistent with a hydrated oceanic crust and a drier oceanic mantle being subducted beneath the southernmost part the Nicoya Peninsula, as compared to a variably hydrated oceanic crust and serpentinized EPR oceanic mantle subducting beneath central and northern Nicoya. Pervasive bending-related normal faulting in the EPR segment may extend through the entire oceanic crust and facilitates the hydration of both the oceanic crust and upper mantle, as opposed to the CNS1 segment, where hydration may occur only within the oceanic crust, resulting in a low-velocity layer beneath the southernmost part of the peninsula. Hence, our receiver function observations are in agreement with previous studies which suggest a serpentinized EPR oceanic mantle and a drier CNS1 oceanic mantle; based on outer rise fault patterns [*Ranero et al.*, 2005] and the thermal state [*Fisher et al.*, 2003] of both Cocos Plate segments, as well as volcanic arc geochemistry [*Rüpke et al.*, 2002].

6.3. The Upper Plate Moho (M2) and *H*-κ Estimates

We identified M2 for individual stations beneath the fore-arc (JTS, PAPA-COND, and SARO), volcanic arc (HDC), and back-arc (JOC-TIR) regions (Figures 10 and 11a). The M2 Ps amplitude is consistent with Vs contrasts of 0.5-1.0 km/s. Combining our

results with those presented by [*MacKenzie et al.,* 2008, Figure 12a], we see that the deepest M2 is observed in the volcanic arc region (~40-42 km) and the shallowest M2 in parts of the fore arc (29-33 km, Papagayo Gulf region) and back arc (27-33 km, Nicaragua border region).

In the fore-arc region, beneath station JTS, we identified the M2 Ps at 4 s from northwest (backazimuth 235-330°) and northeast (40-135°) directions and at 5 s from southern (135-235°) directions (Figure 10a). Moveout analysis for each backazimuth subsets revealed that the signal observed is a Ps and not a multiple. We calculated synthetic receiver functions based on simple models and concluded that the complex azimuthal behavior of the M2 Ps in the region sampled beneath JTS (Figure 11b) is difficult to reproduce and may reflect a complex Moho topography or a combination of factors including dip, a significant azimuthal variation in the crustal *Vp/Vs* on a local scale, and/or seismic anisotropy. If exposures of oceanic assemblages at Tortugal (Figure 11b), for which high *Vp/Vs* are expected, continue at depth in the region south of JTS, they may account for the Ps time delay from the southern direction. Our more robust *H* and κ estimates for JTS come from the northwest subset, for which we calculated a Moho depth of 36.7±2.4 km and crustal *Vp/Vs* of 1.69±0.05 (Figure 11a), similar to previous estimates of 41±7.3 km and 1.78±0.06 using 24 receiver functions [*MacKenzie et al.*, 2008] and 36±4km determined by best-fitting synthetic and observed receiver functions [*DeShon and Schwartz*, 2004].

In the central segment of the volcanic arc region, beneath station HDC, M2 is observed as a clear positive Ps at ~6 s, and is particularly clear in the backazimuth range

from 290° to 360° (Figure 10a). We observed a well-developed M1 PpPs multiple as well as a negative conversion at 3 s, which represents a low-velocity layer in the midcrust (Figure 10b). Our more robust *H*-κ estimates come from a northwest subset (290-360°, Figure 11a) for which we obtained 41.7±2.3 km and 1.92±0.05 (Table 1). *MacKenzie et al.* [2008] obtained 37.0±2.3 km and 1.87±0.08 for a station (HDC5) located at HDC by using 20 receiver functions that spanned the duration of the TUCAN deployment.

In the back arc, beneath stations of the Pocosol network (JOC-TIR), we observed a coherent M2 Ps at ~4 s (Figure 10a) and a well-developed PpPs multiple (Figure 10b). Our more robust solution comes again from a northwest subset (260-360°) for which we obtained 28.7±1.4 km and 1.85±0.06 (Table 1).

6.4. Crustal Terranes in Northern Costa Rica

6.4.1. The Mesquito Terrane

We link the crustal *Vp/Vs* ratios observed in the Costa Rica-Nicaragua border region (1.82-1.88), Papagayo Gulf region (1.62-1.67), and Nicoya Gulf and northern volcanic arc segment (1.68-1.80) to the Mesquito Terrane (Figures 12 and 13). The Mequito Terrane is composed of a collage of Pacific oceanic terranes that includes both enriched-OIB and depleted-arc rocks [*Baumgartner et al*., 2008] and may represent the Late Cretaceous basement upon which fragments of the CLIP were accreted during Late Cretaceous-Miocene, as interpreted for the Santa Elena-Tortugal area (Figure 13a) by *Denyer and Gazel* [2009].

The high *Vp/Vs* (1.82-1.88) in the Costa Rica-Nicaragua border region is consistent with mafic lithologies and/or partially serpentinized peridotites [e.g., see *Rudnick and Fountain*, 1995; *Horen et al.*, 1996; *Carlson and Miller*, 1997; *Christensen*, 2004]. Serpentinized peridotites (Figure 13a) are found in the Santa Elena Peninsula (i.e., Santa Elena Nappe), El Castillo, and in the Tonjibe borehole as a ~200-m-thick layer at ~2 km depth [*Astorga*, 1992; *Pizarro*, 1993]. In the Santa Elena Peninsula, these rocks have an island arc affinity and have been interpreted as an uplifted mantle wedge of the Chortis subduction zone [*Hauff et al.*, 2000]. Other lithologies that may be correlated to the Mesquito Terrane are the alkaline basalts of the Tortugal Suite, located east of the Nicoya Gulf (Figure 13a), as well as those exposed in the Santa Elena Peninsula (i.e., Santa Rosa Accretionary Complex). These basalts have OIB affinity without Galapagos signature [*Hauff et al.*, 2000]. If partially serpentinized peridotites together with mafic lithologies are widespread in the midcrust and/or lower crust, these rocks could account for the high *Vp/Vs* ratios observed in the Costa Rica-Nicaragua border region.

Within the Mequito Terrane, there is a progressive decrease in the crustal *Vp/Vs* from higher (1.82-1.88) in the back arc near Lake Nicaragua to lower (1.74-1.79) in the volcanic arc to even lower (1.68-1.74) near the Nicoya Gulf [Figure 12b, *MacKenzie et al.*, 2008]. As silicic rocks have low *Vp/Vs* [*Christensen*, 1996], this pattern may imply a transition from a mafic/ultramafic crust in the back arc to a more quartz-rich felsic crust in the inner fore arc. The global *Vp/Vs* averages for the continental and oceanic crusts are 1.78 and 1.87, respectively [*Zandt and Ammon*, 1995; *Christensen*, 1996]. Then, the *Vp/Vs* in the Papagayo and Nicoya Gulf regions, as well as in the northern volcanic arc

segment, are more compatible with lithologies constituting continental crust rather than mafic oceanic crust. These *Vp/Vs* values are somewhat surprising, given that most studies agree that the modern volcanic arc in Costa Rica is built either on the Chorotega or the Mesquito terranes [*Baumgartner et al*., 2008, and references therein].

Interestingly, extensive silicic magmatism, dominated by rhyolitic ignimbrites, has occurred in the Guanacaste region (Figures 2a and 13a) since the Miocene, suggesting the formation of new continental crust [*Vogel et al.*, 2004]. Additional evidence for continental crust formation is given by *Sallarès et al.* [2001], who obtained velocity-density relationships for the lower crust and upper mantle comparable to continental island arcs. Moreover, the crustal thickness in Costa Rica is nearly double the average for the CLIP [*MacKenzie et al.*, 2008]. We suggest that the low to moderate *Vp/Vs* in the fore-arc and volcanic arc regions of northern Costa Rica, together with the record of voluminous silicic magmatism, seismic velocities, and crustal thickness support the idea of new continental crust formation. Perhaps the addition of silicic magma to the crust, together with the removal of the mafic/ultramafic residues and cumulates from the base of the crust, as has been proposed for other regions [e.g., *Zandt et al.*, 2004], have lead to the modification of this crust over time into a more continental-type crust.

6.4.2. The Chorotega Block

The high *Vp/Vs* ratios (1.85-1.93, Figure 12b) in the central Costa Rica volcanic arc segment are consistent with mafic lithologies constituting the CLIP. The very high *Vp/Vs* found at station HDC could be also explained by the presence of partial melts in the midcrust and/or beneath this part of the volcanic arc, as we observed a negative

conversion at 3 s, which represents a low-velocity layer in the midcrust (Figure 10b). In the Nicoya Peninsula (Nicoya Terrane), the *Vp/Vs* varies from 1.80 to 1.87 (Figure 12b, Table 1), which is similar to the average *Vp/Vs* for ophiolite exposures in the world; for example, the Samail (Oman) and the Newfoundland (Canada) ophiolites have average *Vp/Vs* of 1.88 and 1.89, respectively [*Christensen*, 1996]. This suggests that the entire crustal wedge beneath the Nicoya Peninsula may be composed of mafic lithologies, as has been previously suggested for the margin wedge [*Ye et al.*, 1996; *Christeson et al.*, 1999].

6.4.3. Terrane Boundaries

In northern Costa Rica, within the region correlated to the Mesquito Terrane, *Vp/Vs* is highly variable (see Figure 12) and thus it is difficult to correlate *Vp/Vs* changes with terrane boundaries. An additional complication is that the Mesquito Terrane may be partly thrust-faulted over the Chorotega Block, as demonstrated by the large-scale nappe emplacement in the Santa Elena Peninsula [*Geldmacher et al.*, 2008]. At Tortugal (Figure 13a) there are exposures of both the Nicoya Complex and alkaline basalts with no Galapagos signature similar to those in the Santa Elena Peninsula [*Hauff et al.*, 2000]. The structural relationship between these exposures is not well known and may indicate that the basement is composed of both the CLIP and the Mesquito Terrane as proposed by *Baumgartner et al.* [2008]. In addition, magmatic processes may be modifying the crustal *Vp/Vs,* making it more difficult to identify terrane boundaries at surface.

The traditionally accepted Chortis-Chorotega boundary interpreted along an east-west suture zone joining the Santa Elena and El Castillo peridotites with the Hess

Escarpment [e.g., *Dengo*, 1985; Figures 1 and 13a] is not visible from crustal *Vp/Vs* estimates. In addition, serpentinized peridotites at the Tonjibe borehole [*Astorga*, 1992], in central Nicaragua [*Baumgartner et al.*, 2008], and off the coast of El Salvador [*Geldmacher et al.*, 2008] suggest that peridotites may be regionally widespread within the basement, as opposed to restricted to this narrow suture zone. Another possible Chortis-Chorotega boundary was inferred by *MacKenzie et al.* [2008] in southern Nicaragua (Figure 1) based on the transition in the crustal *Vp/Vs* between two stations in the back-arc region. However, this boundary would place the Mesquito Terrane exposures of El Castillo and Tonjibe as part of the Chorotega Terrane. We suggest that this *Vp/Vs* transition may reflect a compositional change within the Mesquito Terrane.

We favor the Chortis (Mesquito)-Chorotega boundary as the southwestward projection of the Hess Escarpment into central Costa Rica, as proposed by *Baumgartner et al.* [2008] (Figure 13a). This boundary does not conflict with geology and *Vp/Vs* estimates. In general, *Vp/Vs* is higher on the Chorotega side, although more *Vp/Vs* data will be needed to determine if its location is visible from *Vp/Vs* changes. We suggest that this boundary continues on the western margin of the Nicoya Gulf, separating the Mesquito and Nicoya Terranes (Figures 12 and 13) and following the boundary suggested by *Hauff et al*. [2000] who consider the Nicoya Peninsula as part of the Chorotega Block and both the Tortugal and Santa Elena areas as part of the Chortis Block (i.e., Mesquito Terrane).

7. Conclusions

We identify the upper plate Moho (M2) as a relatively strong Vs contrast (0.5-1.0 km/s) beneath the fore-arc, volcanic arc, and back-arc regions. In the Nicoya Peninsula, M2 was not recognized but instead we observe a signal that is consistent with a dipping interface, which we interpret as the dipping oceanic Moho (M1) of the subducting Cocos Plate. The deepest M2 is observed in the volcanic arc region (~42 km) and the shallowest M2 in parts of the fore arc (27-33 km, Papagayo Gulf region) and back arc (29 km, Costa Rica-Nicaragua border region). The strong azimuthal variation of the M2 Ps at JTS may reflect a complex M2 topography in the fore-arc region.

Our receiver function observations are consistent with variability in the hydration state of the incoming Cocos Plate as was proposed in previous studies based on outer rise fault patterns, thermal state, and volcanic arc geochemistry [*Rüpke et al.*, 2002; *Fisher et al.*, 2003; *Ranero et al.*, 2005]. We conclude that the observed Ps amplitude is consistent with a drier CNS1 oceanic mantle being subducted beneath the southernmost part of the Nicoya Peninsula, as compared to a serpentinized EPR oceanic mantle subducting beneath central and northern Nicoya. Our observations may imply that pervasive bending-related normal faulting in the EPR segment extends throughout the entire oceanic crust and facilitates the hydration of both the oceanic crust and upper mantle, as opposed to the CNS1, where hydration may occur more extensively only within the oceanic crust, resulting in a low-velocity layer that is visible beneath the southernmost part of the peninsula.

By integrating our new receiver function estimates with published geological data and the receiver function estimates from *MacKenzie et al.* [2008], we describe crustal *Vp/Vs* estimates in terms of three different crustal terranes: Mesquito, Nicoya, and Chorotega. The Mesquito Terrane shows variable *Vp/Vs*, suggesting mafic and ultramafic lithologies beneath the Costa Rica-Nicaragua border region, where *Vp/Vs* estimates are high (1.82-1.88), and more silicic content in the Papagayo Gulf region and northern volcanic arc segment, where *Vp/Vs* are moderate to low (1.62-1.80) and resemble those of the continental crust. We conclude that the low to moderate *Vp/Vs* in the fore arc and volcanic arc regions, together with the record of voluminous silicic magmatism, seismic velocities, and crustal thickness, may indicate that the midcrust and upper crust have been profoundly modified by emplacement of silicic melts. The Chorotega Block is characterized by high crustal *Vp/Vs* (1.85-1.92) consistent with mafic lithologies constituting the CLIP. The Nicoya Peninsula is also a region of high crustal *Vp/Vs* (1.80-1.87), which is consistent with mafic rocks, including the Nicoya Complex exposed at surface.

Through a sensitivity study, we found that when dealing with a dipping interface, the *H* and κ calculations are biased towards shallower depths and higher *Vp/Vs* estimates than true model parameters. Our synthetic tests indicate that the *H*-κ stacking algorithm should be used with caution when the dip angle is known to be greater than 12º, as the bias in *Vp/Vs* could be geologically significant, especially if the interface depth is greater than 35 km. In addition, we found that the *H*-κ stacking algorithm is not particularly sensitive to the assumed Vp. We found that the Ps phase of receiver functions in the

region along the strike of a dipping interface is very similar to a flat-interface case, and may be used when available to facilitate the interpretation of structures in regions with known dipping layers.

8. Acknowledgments

A special thanks to S. Husen and V. Maurer for making data of the CORISUBMOD Experiment available and W. Taylor for assembling the Pocosol data set. Thanks to J. Calkins, A. Frassetto, I. Arroyo, and C. Gans for comments and helping with receiver function codes, and two anonymous reviewers who significantly improved the manuscript. We used software written by C. Ammon and T. Owens and Matlab scripts initially created by H. Gilbert. Data from stations JTS, HDC, and CRSEIZE (in part) were obtained from the Data Management Center via the Incorporated Research Institutions for Seismology. Figures were in part created with the Generic Mapping Tool [Wessel and Smith, 1998]. Partial funding for this study was provided by NSF grants EAR0510966 (S. Beck and G. Zandt) and EAR0506463 (S. Schwartz).

9. References

Arroyo, I. G., S. Husen, E. R. Flueh, J. Gossler, E. Kissling, and G. E. Alvarado (2009), Three-dimensional *P* wave velocity structure on the shallow part of the Central Costa Rican Pacific margin from local earthquake tomography using off- and onshore networks, *Geophys. J. Int.,* 179(2), 827-849, doi: 10.1111/j.1365-246X.2009.04342.x.

Astorga, A. (1992), Descubrimiento de corteza oceánica mesozoica en el Norte de Costa Rica y el Sur de Nicaragua, *Rev. Geol. Am. Cent., 14*, 109-112.

Barckhausen, U., C. R. Ranero, R. von Huene, S. C. Cande, and H. A. Roeser (2001), Revised tectonic boundaries in the Cocos Plate off Costa Rica: Implications for the segmentation of the convergent margin and for plate tectonic models, *J. Geophys. Res.*, *106*(B9), 19,207–19,220.

Baumgartner, P. O., K. Flores, A. N. Bandini, F. Girault, and D. Cruz (2008), Upper Triassic to Cretaceous radiolaria from Nicaragua and northern Costa Rica - The Mesquito Composite Oceanic Terrane, *Ofioliti, 33*, 1-19.

Bullock, A. D., W. S. Holbrook, D. Lizarralde, H. van Avendonk, M. M. Mora, S. Harder, and G. Alvarado (2007), Results From the TICO-CAVA Land Seismic Refraction Survey, *Eos Trans. AGU, 88*(52), Fall Meet. Suppl., T43C-08.

Carlson, R. L., and D. J. Miller (1997), A new assessment of the abundance of serpentinite in the oceanic crust, *Geophys. Res. Lett.*, 24(4), 457–460.

Cassidy, J. F. (1992), Numerical experiments in broadband receiver function analysis, *Bull. Seismol. Soc. Am.*, *82*,1453-1474.

Christensen, N. I. (1996), Poisson's ratio and crustal seismology, *J. Geophys. Res.*, *101*(B2), 3139–3156.

Christensen, N. I. (2004), Serpentinites, Peridotites, and Seismology, *Int. Geol. Rev., 46*, 795–816.

Christeson, G. L., K. D. McIntosh, T. H. Shipley, E. R. Flueh, and H. Goedde (1999), Structure of the Costa Rica convergent margin, offshore Nicoya Peninsula, *J. Geophys. Res.*, *104*(B11), 25,443–25,468.

DeMets, C., R. G. Gordon, D. F. Argus, and S. Stein (1994), Effect of recent revisions to the geomagnetic reversal time scale on estimates of current plate motions, *Geophys. Res. Lett.*, *21*(20), 2191–2194.

Dengo, G. (1985), Mid America: Tectonic setting for the Pacific margin from southern Mexico to northwestern Columbia, in *The ocean basins and margins*, edited by A. E. Nairn, and F. G. Stechli, pp. 123–180, Plenum Press, New York.

Denyer P., and E. Gazel (2009), The Costa Rican Jurassic to Miocene oceanic complexes: Origin, tectonics and relations, *J. S. Am. Earth Sci.,* doi:10.1016/j.jsames.2009.04.010, in press.

Denyer, P., W. Montero, and G. Alvarado (2003), *Atlas tectónico de Costa Rica*, 81 pp., Editorial UCR, San José, Costa Rica.

DeShon, H. R., and S. Y. Schwartz (2004), Evidence for serpentinization of the forearc mantle wedge along the Nicoya Peninsula, Costa Rica, *Geophys. Res. Lett.*, *31*, L21611, doi: 10.1029/2004GL021179.

DeShon, H., S. Y. Schwartz, A. V. Newman, V. González, M. Protti, L. M. Dorman, T. H. Dixon, D. E. Sampsom, and E. R. Flueh (2006), Seismogenic zone structure beneath the Nicoya Peninsula, Costa Rica, from three-dimensional local earthquake P- and S-wave tomography, *Geophys. J. Int.*, *164*, 109-124, doi:10.1111/j.1365-246X.2005.02809.x.

Di Marco, G., P. O. Baumgartner, and J. E. T. Channell (1995), Late Cretaceous-early Tertiary paleomagnetic data and a revised tectonostratigrapic subdivision of Costa Rica and western Panama, *Geol. Soc. Am. Spec. Pap., 295*, 1-27.

Drummond, M. S., M. Bordelon, J. Z. de Boer, M. J. Defant, H. Bellon, and M. D. Feigenson (1995), Igneous petrogenesis and tectonic setting of plutonic and volcanic rocks of the Cordillera de Talamanca, Costa Rica-Panama, Central American arc, *Am. J. Sci., 295*, 875-919.

Fisher, A. T., C. A. Stein, R. N. Harris, K. Wang, E. A. Silver, M. Pfender, M. Hutnak, A. Cherkaoui, R. Bodzin, and H. Villinger (2003), Abrupt thermal transition reveals hydrothermal boundary and role of seamounts within the Cocos Plate, *Geophys. Res. Lett., 30,* doi:10.1029/2002GL016766.

Geldmacher, J., K. Hoernle, P. Van Den Bogaard, F. Hauff, and A. Klügel (2008), Age and Geochemistry of the Central American Forearc Basement (DSDP Leg 67 and 84): Insights into Mesozoic Arc Volcanism and Seamount Accretion on the Fringe of the Caribbean LIP, *J. Petrol., 49*(10), 1781-1815, doi:10.1093/petrology/egn046.

Grevemeyer, I., N. Kaul, J. L. Diaz-Naveas, H. W. Villinger, C. R. Ranero, and C. Reichert (2005), Heat flow and bending-related faulting at subduction trenches: Case studies offshore of Nicaragua and Central Chile, *Earth Planet. Sci. Lett., 236*: 238-248, doi:10.1016/j.epsl.2005.04.048.

Grevemeyer, I., C. R. Ranero, E. R., Flueh, D. Kläschen, and J. Bialas (2007), Passive and active seismological study of bending-related faulting and mantle

serpentinization at the middle America Trench, *Earth Planet. Sci. Lett., 258*: 528-542, doi:10.1016/j.epsl.2007.04.013.

Hauff, F., K. Hoernle, P. van den Bogaard, G. Alvarado, and D. Garbe-Schönberg (2000), Age and geochemistry of basaltic complexes in western Costa Rica: Contributions to the geotectonic evolution of Central America, *Geochem. Geophys. Geosyst., 1*(1), 1009, doi:10.1029/1999GC000020.

Hayes G., and K. P. Furlong (2007), Abrupt changes in crustal structure beneath the Coast Ranges of northern California – developing new techniques in receiver function analysis, *Geophys. J. Int.*, *170*, 313–336, 10.1111/j.1365-246X.2007.03401.x.

Hoernle, K., P. van den Bogaard, R. Werner, B. Lissinna, F. Hauff, G. Alvarado, and D. Garbe-Schönberg (2002), Missing history (16–71 Ma) of the Galápagos hotspot: Implications for the tectonic and biological evolution of the Americas, *Geology*; 30(9), 795-798; doi: 10.1130/0091-7613(2002)030<0795:MHMOTG>2.0.CO;2.

Horen, H., M. Zamora, and G. Dubuisson (1996), Seismic waves velocities and anisotropy in serpentinized peridotites from xigaze ophiolite: Abundance of serpentine in slow spreading ridge, *Geophys. Res. Lett.*, 23(1), 9–12.

Husen, S., R. Quintero, E. Kissling, and B. Hacker (2003), Subduction-zone structure and magmatic processes beneath Costa Rica constrained by local earthquake tomography and petrological modeling, *Geophys. J. Int.*, *155*, 11-32, 10.1046/j.1365-246X.2003.01984.x.

Ivandic, M., I. Grevemeyer, A. Berhorst, E. R. Flueh, and K. McIntosh (2008), Impact of bending related faulting on the seismic properties of the incoming oceanic plate offshore of Nicaragua, *J. Geophys. Res.*, *113*, B05410, doi:10.1029/2007JB005291.

Kawakatsu, H., and S. Watada (2007), Seismic Evidence for Deep-Water Transportation in the Mantle, *Science*, *316*(5830), 1468-1471, doi:10.1126/science.1140855.

Langseth, M. G., and E. A. Silver (1996), The Nicoya Convergent Margin—A region of exceptionally low heat flow, *Geophys. Res. Lett.*, *23*(8), 891–894.

Langston, C. A. (1977), The effect of planar dipping structure on source and receiver responses for constant ray parameter, *Bulletin of Seismological Society of America*, *67*(4), 1029-1050.

Langston, C. A. (1979), Structure Under Mount Rainier, Washington, Inferred From Teleseismic Body Waves, *J. Geophys. Res.*, *84*(B9), 4749–4762.

Ligoría, J. P., and C. J. Ammon (1999), Iterative Deconvolution and receiver funciton estimation, *Bull. Seismol. Soc. Am.*, *89*, 1395-1400.

Lombardi, D., J. Braunmiller, E. Kissling, and D. Giardini (2008), Moho depth and Poisson's ratio in the Western-Central Alps from receiver functions, *Geophys. J. Int., 173*(10), 249-264, doi: 10.1111/j.1365-246X.2007.03706.x.

MacKenzie, L., G. A. Abers, K. M. Fischer, E. M. Syracuse, J. M. Protti, V. Gonzalez, and W. Strauch (2008), Crustal structure along the southern Central American volcanic front, *Geochem. Geophys. Geosyst.*, *9*, Q08S09, doi:10.1029/2008GC001991.

Matumoto, T., M. Ohtake, and J. Umana (1977), Crustal Structure in southern Central America, *Bull. Seismol. Soc. Am.*, *67*, 121-134.

Newman, A. V., S. Y. Schwartz, V. Gonzalez, H. R. DeShon, J. M. Protti, and L. M. Dorman (2002), Along-strike variability in the seismogenic zone below Nicoya Peninsula, Costa Rica, *Geophys. Res. Lett.*, *29*(20), 1977, doi:10.1029/2002GL015409.

Nikulin, A., V. Levin, and J. Park (2009), Receiver function study of the Cascadia megathrust: Evidence for localized serpentinization, *Geochem. Geophys. Geosyst., 10*, Q07004, doi:10.1029/2009GC002376.

Owens, T. J. (1984), Determination of crustal and upper mantle structure from analysis of broadband teleseismic P-waveforms, Ph.D. thesis, 146 pp., Univ. of Utah, Salt Lake City.

Pizarro, D. (1993), Los pozos perforados en Costa Rica: aspectos litológicos y bioestratigráficos, *Rev. Geol. Am. Cent., 14*, 81-85.

Protti, M., F. Güendel, and K. McNally (1994), The geometry of the Wadatti-Benioff zone under southern Central America and its tectonic significance: results from a high resolution local seismograph network, *Phys. Earth Planet. Inter.*, *84*, 271-287, doi:10.1016/0031-9201(94)90046-9.

Quintero R., and K. Kulhánek (1998), Pn-wave observations in Costa Rica, *Geofis. Int.*, *37*: 171-182.

Ranero, C. R., Morgan, J. P., McIntosh, K., and Reichert, C. (2003), Bending-related faulting and mantle serpentinization at the Middle America trench. *Nature*, *425*: 367-373, doi:10.1038/nature01961.

Ranero, C. R., I. Grevemeyer, H. Sahling, U. Barckhausen, C. Hensen, K. Wallmann, W. Weinrebe, P. Vannucchi, R. von Huene, and K. McIntosh (2008), Hydrogeological system of erosional convergent margins and its influence on tectonics and interplate seismogenesis, *Geochem. Geophys. Geosyst.*, 9, Q03S04, doi:10.1029/2007GC001679.

Ranero, C. R., A. Villaseñor, J. Phipps Morgan, and W. Weinrebe (2005), Relationship between bend-faulting at trenches and intermediate-depth seismicity, *Geochem. Geophys. Geosyst.*, *6*, Q12002, doi:10.1029/2005GC000997.

Rogers, R. D., P. Mann, and P.A. Emmet (2007), Tectonic terranes of the Chortis block based on integration of regional aeromagnetic and geologic data, *Geol. Soc. Am. Spec. Pap., 428*, 65-88, doi: 10.1130/2007.2428(04).

Rossi, G., G. A. Abers, S. Rondenay, and D. H. Christensen (2006), Unusual mantle Poisson's ratio, subduction, and crustal structure in central Alaska, *J. Geophys. Res.*, *111*, B09311, doi:10.1029/2005JB003956.

Rudnick, R. L., and D. M. Fountain (1995), Nature and Composition of the Continental Crust: A Lower Crustal Perspective, *Rev. Geophys., 33*(3), 267–309.

Rüpke, L. H., Morgan, J. P. Hort, M., and Connolly, J. A. D. (2002), Are the regional variations in Central American arc lavas due to differing basaltic versus

peridotitic slab sources of fluids?, *Geology*, *30* (11), 1035-1038, doi: 10.1130/0091-7613(2002)030.

Sallarès, V., J. J. Dañobeitia, and E. Flueh (2000), Seismic tomography with local earthquakes in Costa Rica, *Tectonophysics, 329*, 61-78, doi:10.1016/S0040-1951(00)00188-8.

Sallarès, V., J. J. Dañobeitia, and E. R. Flueh (2001), Lithospheric structure of the Costa Rican Isthmus: Effects of subduction zone magmatism on an oceanic plateau, *J. Geophys. Res.*, *106*(B1), 621–643.

Sallarès, V., J. J. Dañobeitia, E. Flueh, and G. Leandro (1999), Seismic velocity structure across the Middle America land bridge in northern Costa Rica, *J. Geodyn., 27*, 327-344, doi:10.1016/S0264-3707(98)00007-6.

Sinton, C. W., R.A. Duncan, M. Storey, J. Lewis, and J. J. Estrada (1998), An oceanic flood basalt province within the Caribbean Plate, *Earth Planet. Sci. Lett.*, *155*, 221-235, doi:10.1016/S0012-821X(97)00214-8.

Stein, C. A., and S. Stein (1992), A model for the global variation in oceanic depth and heat flow with lithospheric age, *Nature, 359*, 123, doi:10.1038/359123a0.

Syracuse, E. M., G. A. Abers, K. Fischer, L. MacKenzie, C. Rychert, M. Protti, V. González, and W. Strauch (2008), Seismic tomography and earthquake locations in the Nicaraguan and Costa Rican upper mantle, *Geochem. Geophys. Geosyst.*, *9*, Q07S08, doi:10.1029/2008GC001963.

Vogel, T. A., L. C. Patino, G. E. Alvarado**,** and P. B. Gans (2004), Silicic ignimbrites within the Costa Rican volcanic front: evidence for the formation of continental crust, *Earth Planet. Sci. Lett., 226*, 149-159, doi:10.1016/j.epsl.2004.07.013.

Vogel, T. A., L. C., Patino, J. K. Eaton, J. W. Valley, W. I. Rose, G. E. Alvarado, and E. L. Viray (2006), Origin of silicic magmas along the Central American volcanic front: Genetic relationship to mafic melts, *J. Volcanol. Geotherm. Res.*, *156*, 217-228. doi:10.1016/j.jvolgeores.2006.03.002.

von Huene, R., C. R. Ranero, W. Weinrebe, and K. Hinz (2000), Quaternary convergent margin tectonics of Costa Rica, segmentation of the Cocos Plate, and Central American volcanism, *Tectonics*, *19*(2), 314–334.

Wessel, P., and W. H. F. Smith (1998), New improved version of the generic mapping tools released, *Eos Trans. AGU, 79*, 579.

Ye, S., J. Bialas, E. R. Flueh, A. Stavenhagen, R. von Huene, G. Leandro, and K. Hinz (1996), Crustal structure of the Middle American Trench off Costa Rica from wide-angle seismic data, *Tectonics*, *15*(5), 1006–1021.

Zandt, G., and Ammon, C. J. (1995), Continental crust composition constrained by measurements of crustal Poisson's ratio, *Nature, 374*, 152-154, doi:10.1038/374152a0.

Zandt, G., H. Gilbert, T. J. Owens, M. Ducea, J. Saleeby, and C. H. Jones (2004), Active foundering of a continental arc root beneath the southern Sierra Nevada in California, *Nature, 431*, 41-46, doi:10.1038/nature02847.

Zhu, L., and H. Kanamori (2000), Moho depth variation in southern California from teleseismic receiver functions, *J. Geophys. Res.*, *105*(B2), 2969–2980.

Table 1. Results by individual station

Station	Lat	Lon	Vp[a]	N[b]	Depth to M1[c]	Depth to M2[c]	*Vp/Vs* to M1[c]	*Vp/Vs* to M2[c]
GRAN	10.340	-85.846	6.0	14	26.8±1.9[d]	---	1.84±0.06[d]	---
HDC	10.002	-84.112	6.3	85	---	41.7±2.3	---	1.92±0.05
INDI	9.865	-85.502	6.0	10	21.8±1.7[d]	---	1.87±0.05[d]	---
JOC	10.925	-83.370	6.3	46	---	28.7±1.4	---	1.85±0.06
TIR	10.948	-83.343						
JTS	10.291	-84.952	6.5	111	---	36.7±2.4	---	1.69±0.05
MARB	10.063	-85.754	6.0	27	23.8±1.3[d]	---	1.80±0.05[d]	---
MOSD	9.647	-85.083	6.0	26	24.8±2.3[d]	---	1.83±0.06[d]	---
PNCB	9.589	-85.092						
PAPA	10.590	-85.677	6.0	30	---	27.1±2.0	---	1.62±0.09
COND	10.580	-85.674	6.0					
SARO	10.839	-85.609	6.3	9	---	32.9±1.1	---	1.65±0.03

[a] Based on previous studies (see references in Section 4.2).

[b] Number of receiver functions with variance reduction > 80%

[c] Depth in km. M1, Continental Moho, M2 Oceanic Moho. The uncertainty range is estimated as presented by *Zhu and Kanamori* [2000].

[d] A post stack correction was applied as described in Section 5.2.

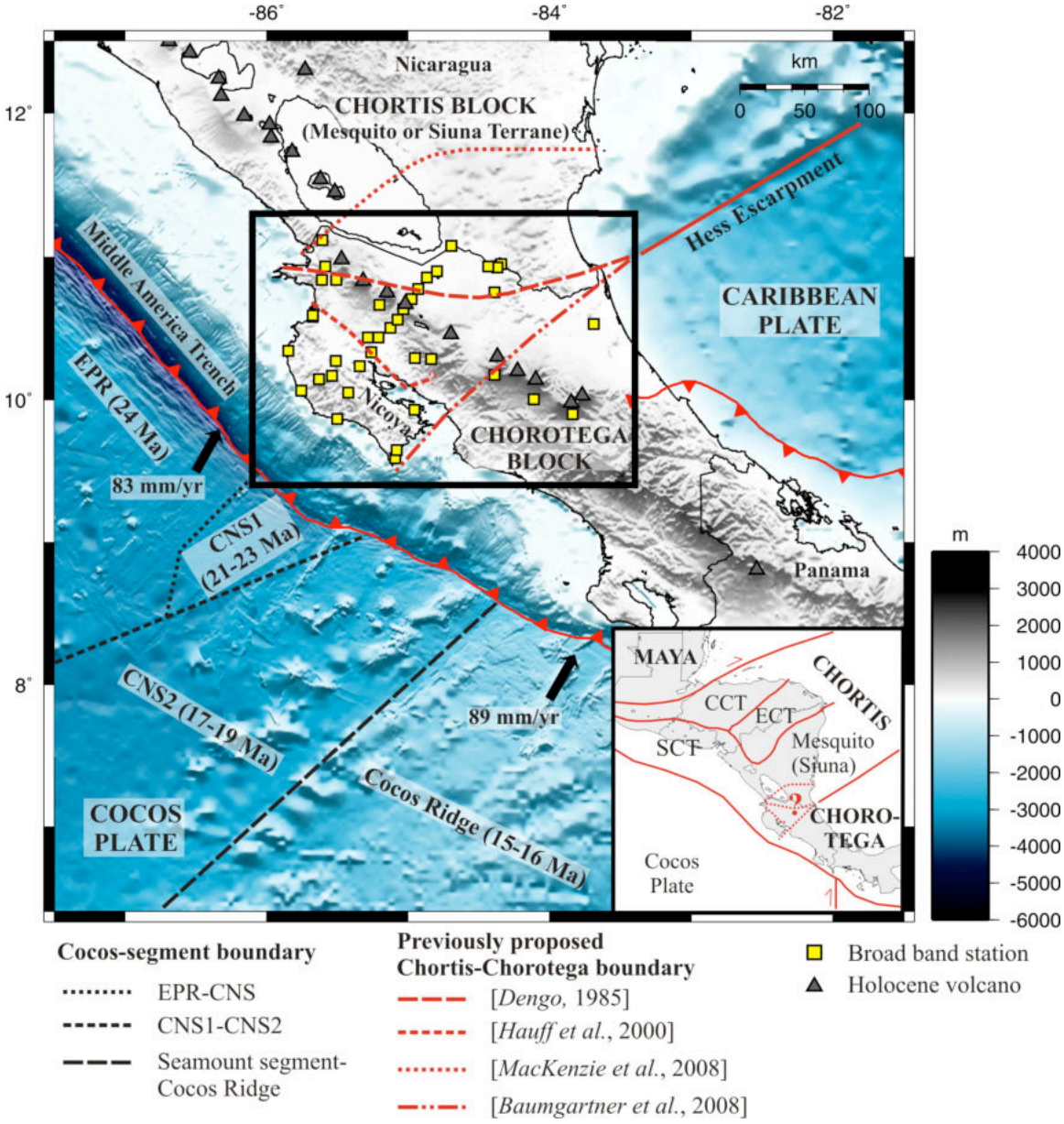

Figure 1. Major tectonic features of southern Central America. The age of the Cocos Plate shown in parentheses corresponds to the age at the trench axis [*Barckhausen et al.*, 2001]. Velocity plate vectors come from *DeMets et al.,* [1994] and bathymetry from *Ranero et al.* [2005] available through the Marine Geoscience Data System. Rectangle denotes close-up region shown in Figure 2. Inset map of Central America shows regional terrane boundaries based on *Rogers et al.* [2007] and *Baumgartner et al.* [2008]. CCT, Central Chortis Terrane; CNS, Cocos Nazca Spreading Center; ECT, Eastern Chortis Terrane, EPR, East Pacific Rise; SCT, Southern Chortis Terrane.

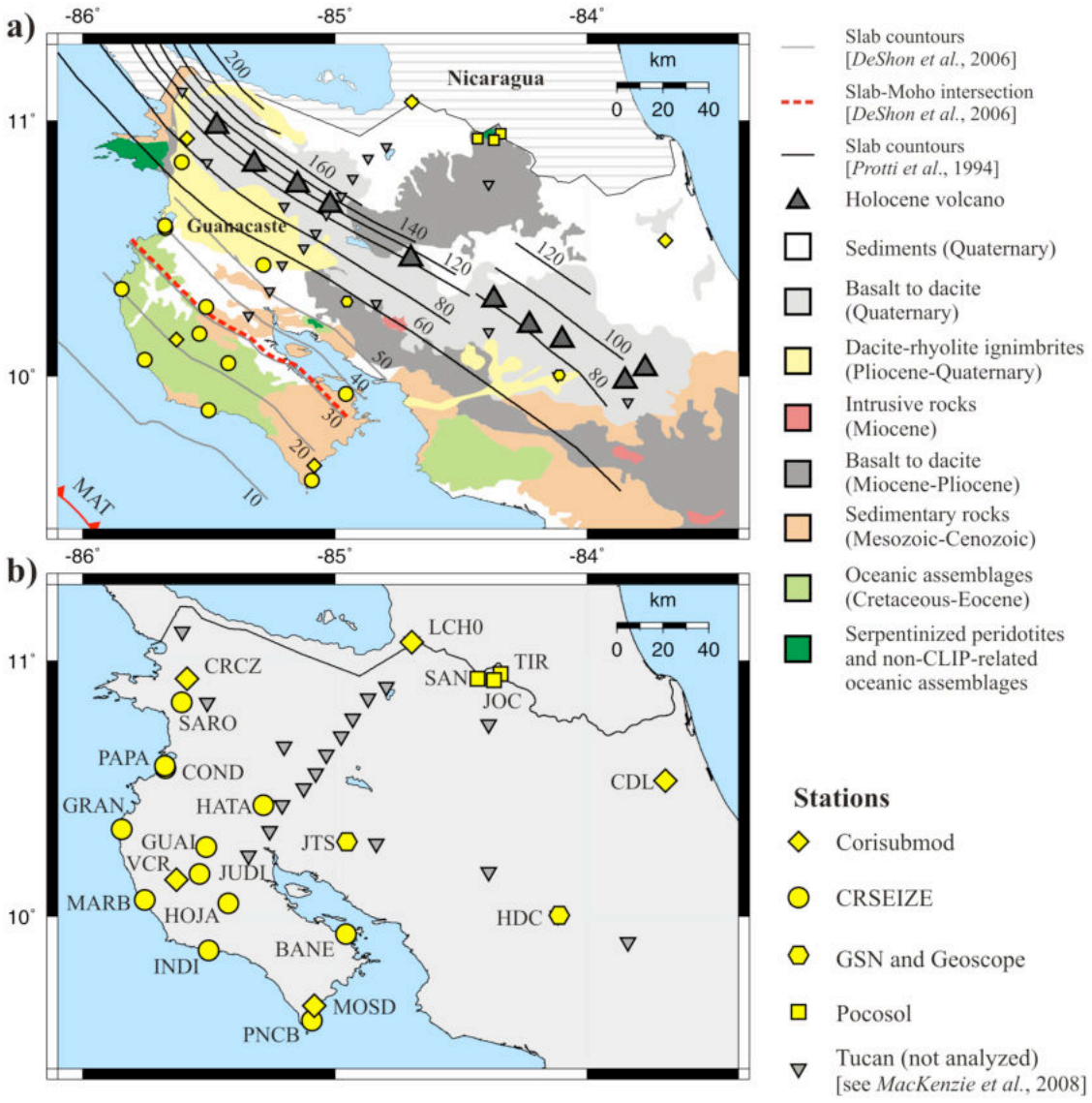

Figure 2. (a) Simplified geologic map of northern Costa Rica [*Denyer et al.*, 2003; *Vogel et al.*, 2004] and contours of the top of the slab (in km). MAT, Middle America Trench. (b) Location of recent broadband deployments in northern Costa Rica. Yellow symbols represent stations analyzed in this study.

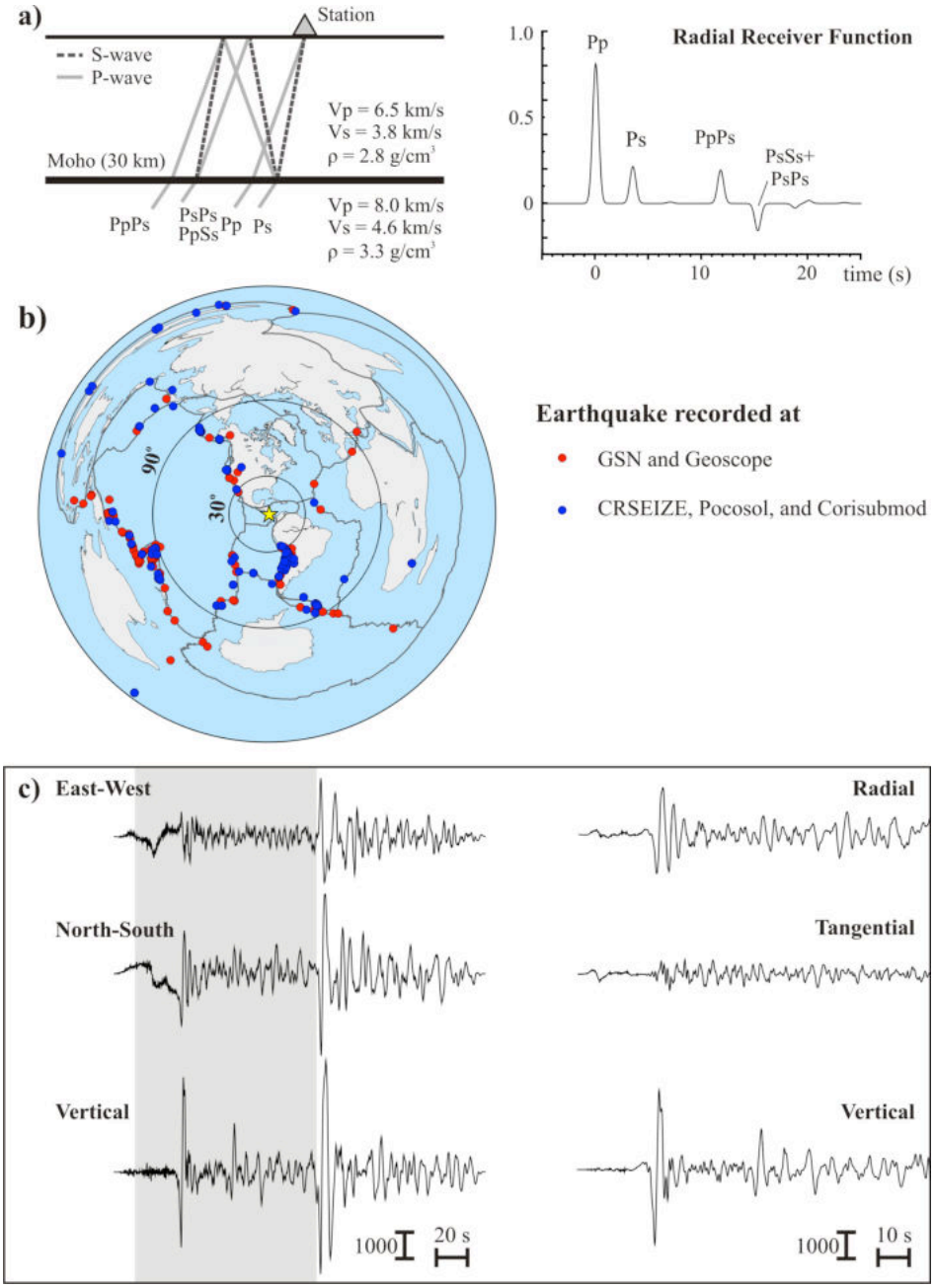

Figure 3. (a) Ray path geometry and nomenclature of *P*-to-*S* converted waves recorded in receiver functions for a model of a layer over a half-space with a flat Moho (left) and synthetic radial receiver function response (right). (b) Epicenter distribution of teleseismic earthquakes used. Yellow star denotes the location of Costa Rica. (c) Example of a three-component seismogram recorded at station JOC (left). The window used for the receiver function calculation is shaded in gray and shown as the band-pass-filtered signal (0.1-3Hz) after the horizontal components were rotated (right).

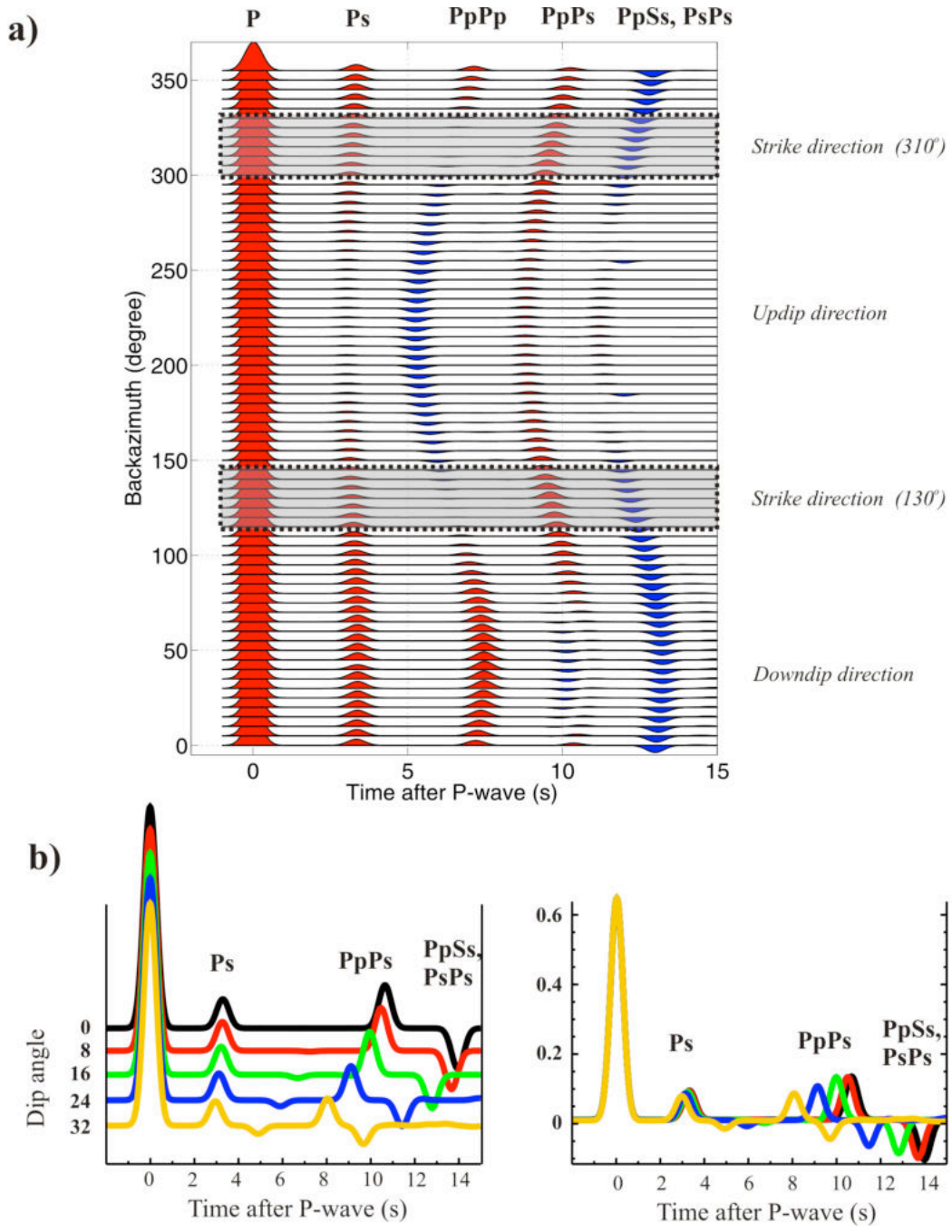

Figure 4. (a) Azimuthal variation of the radial component of synthetic receiver functions for a model of a dipping layer over a half-space. The model has an interface at 25 km depth, dipping 20º towards N40ºE. We used Vp = 6.3 km/s, *Vp/Vs* of 1.80, and a constant ray parameter of 0.06. Note the absence of the Pop phase (shaded region) along the strike of the dipping interface. (b) Along-strike receiver functions for the same velocity model in (a) but varying dip angle. Note that the Ps amplitude is not very sensitive to the dip angle.

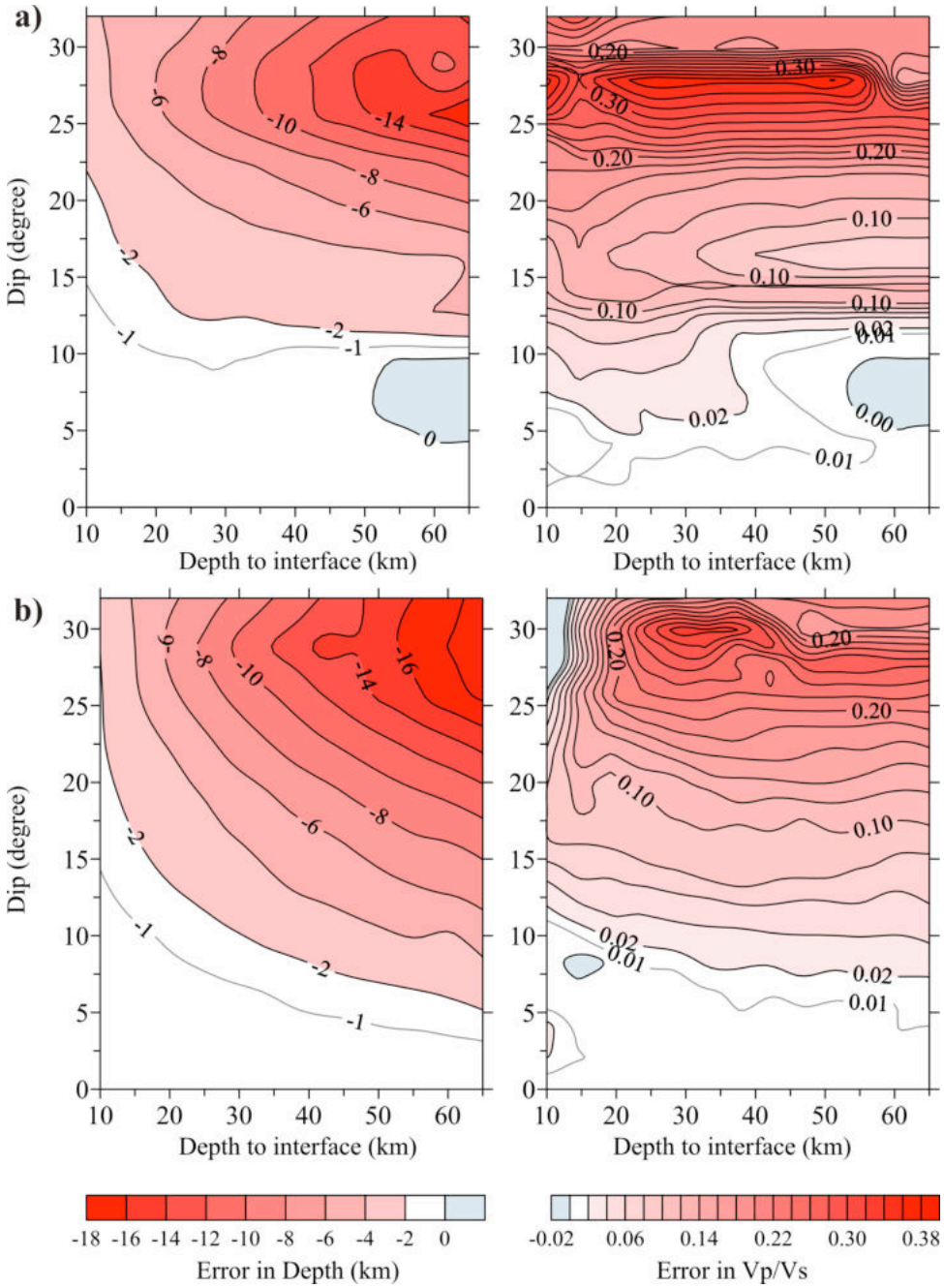

Figure 5. (a) Bias in interface depth (left) and *Vp/Vs* (right) estimate from *H*–κ analysis for models with varying interface depth and dip angle. The contour map is based on synthetic receiver functions created using a model that intends to represent the subducting Cocos Plate dipping towards the northeast, beneath a mafic crustal wedge with Vp = 6.3 km/s and *Vp/Vs* of 1.80. The map of the bias for models with *Vp/Vs* from 1.70 to 1.90 is not significantly different (not shown). (b) Same as (a) but using synthetics computed with the azimuthal coverage and ray parameters of our data set. Contours were constructed using a method of triangulation with linear interpolation.

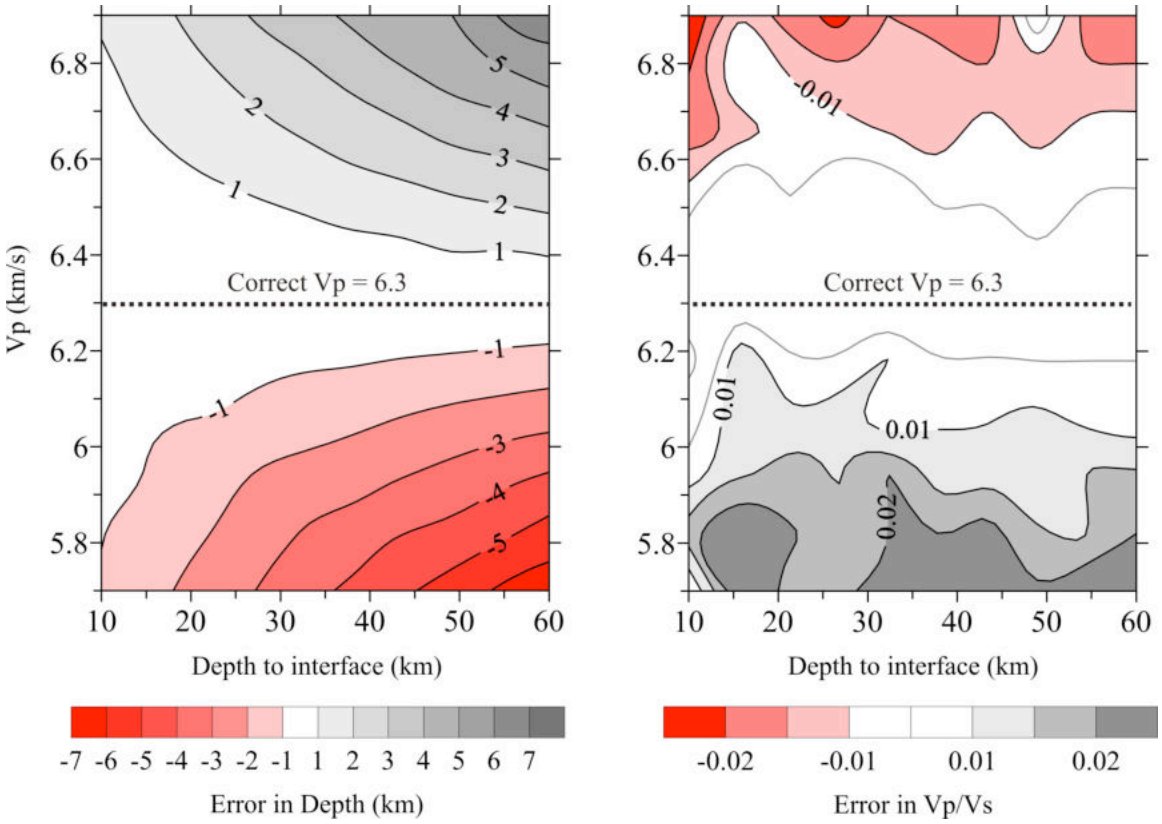

Figure 6. Bias in interface depth (left) and *Vp/Vs* (right) estimated from *H*–κ analysis for models with varying interface depth and Vp (Vp = 6.3 km/s is the correct model value). The map of the bias is based on synthetic receiver functions with a symmetric azimuthal coverage every five degrees and a constant ray parameter of 0.06. We used *Vp/Vs* of 1.80 for a model of a flat layer over a half-space. Contours were constructed using a method of triangulation with linear interpolation.

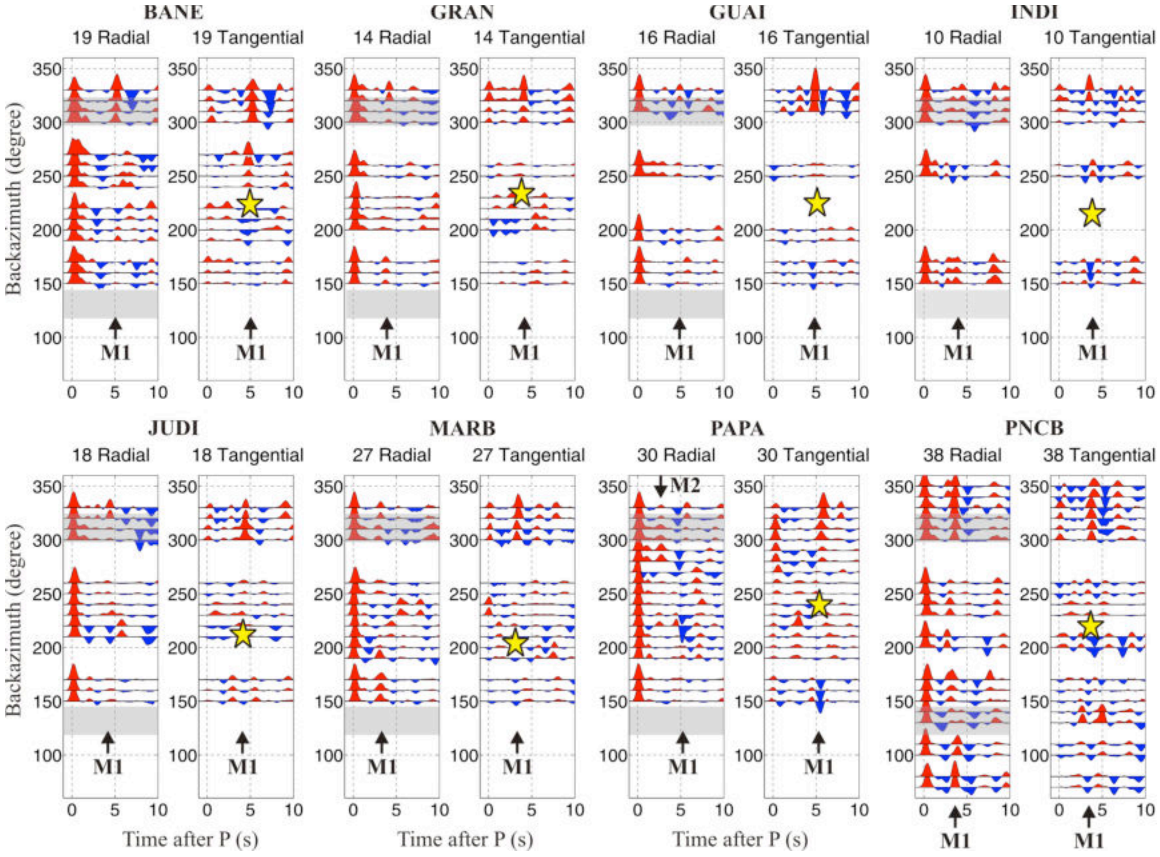

Figure 7. Receiver functions binned over 10º for stations in the Nicoya Peninsula region. Receiver functions are normalized to the maximum amplitude. Station name and number of receiver functions are given above each plot. Positive and negative amplitudes are shaded red and blue, respectively. Black arrows mark the location of the signal correlated to the oceanic Moho (M1) and yellow stars denote the location of the polarity reversal common to all stations. Gray areas mark the radial receiver functions stacked along the strike of the dipping Cocos Plate shown in Figure 8.

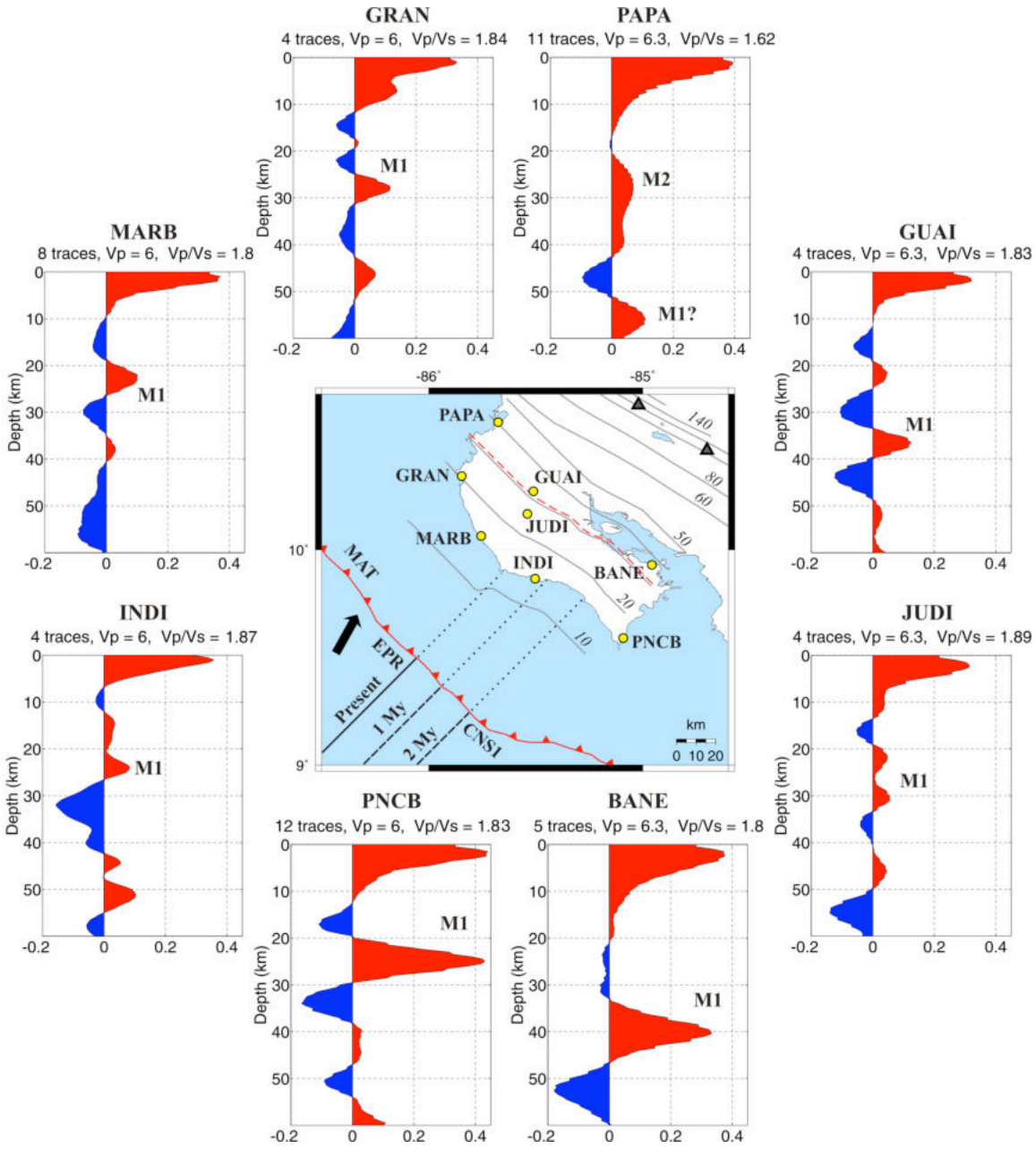

Figure 8. Absolute-amplitude receiver functions for CRSEIZE stations stacked along the strike of the subducting Cocos Plate. Station name, number of receiver functions, and Vp and *Vp/Vs* ratio used for migrating time to depth are given above each plot. M1 and M2 denote oceanic and upper plate Moho, respectively. The inset map shows slab contours (in km) to the top of the subducting Cocos Plate according to *DeShon et al.* [2006] and *Protti et al.* [1995] and the location of the EPR-CNS1 suture at specified geologic times, based on *Barckhausen et al.* [2001]. Other symbols and acronyms as in Figure 1.

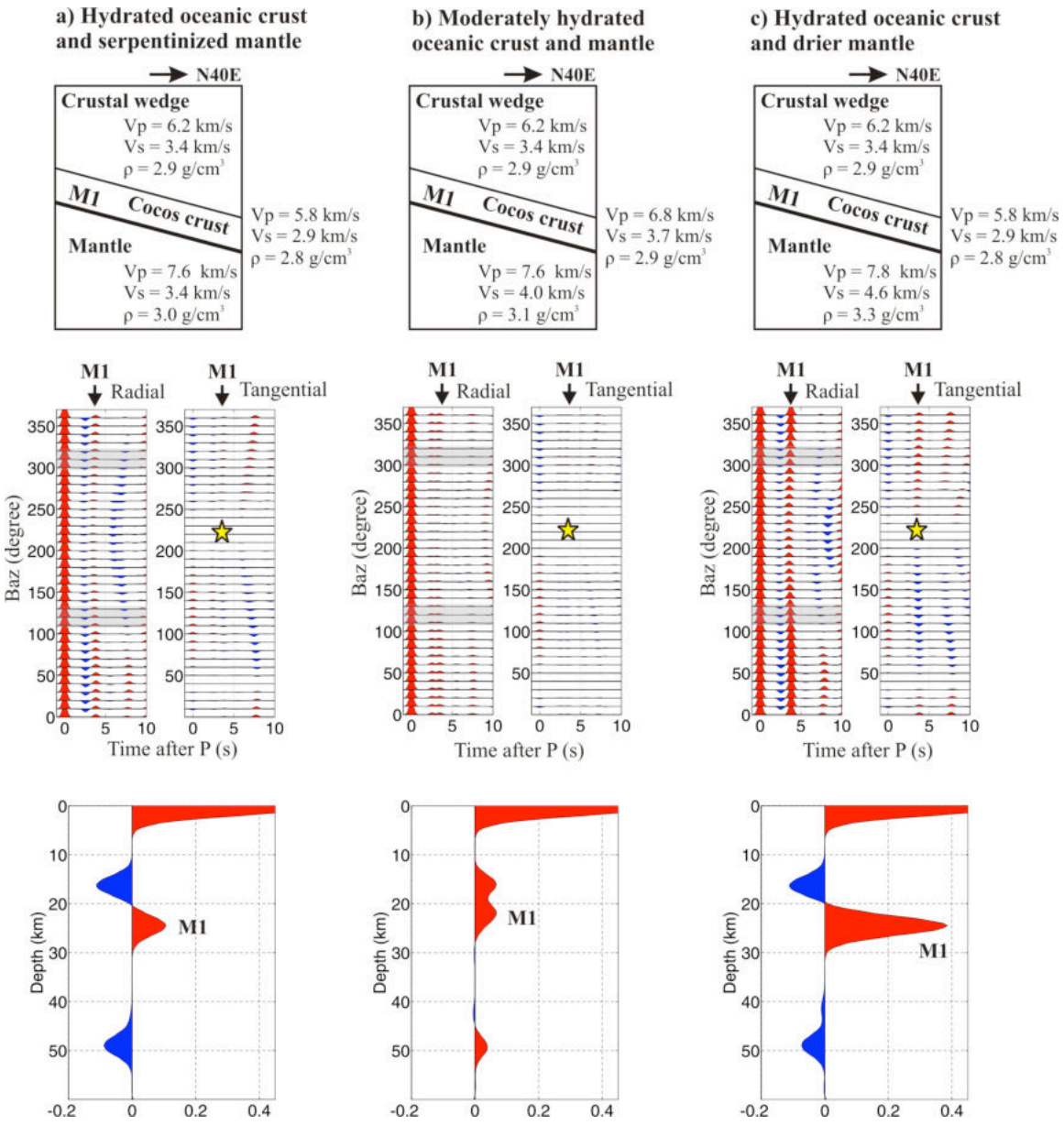

Figure 9. Synthetic receiver functions for simple models recreating the subducting Cocos Plate beneath a mafic crustal wedge over a hydrated (a and b) and dry (c) oceanic mantle. In the schematic velocity structures (top) the subducting Cocos crust is 7 km thick, dipping 15º towards N40ºE, and the oceanic Moho (M1) is at 25 km depth. Synthetic receiver functions were calculated every five degrees in backazimuth and with a constant ray parameter of 0.068 (middle). Black arrows at the top of the plots mark the location of the signal correlated to M1 and yellow stars denote the location of polarity reversals. Gray areas mark the radial receiver functions stacked along the strike of the dipping interface shown as an absolute-amplitude stack (bottom).

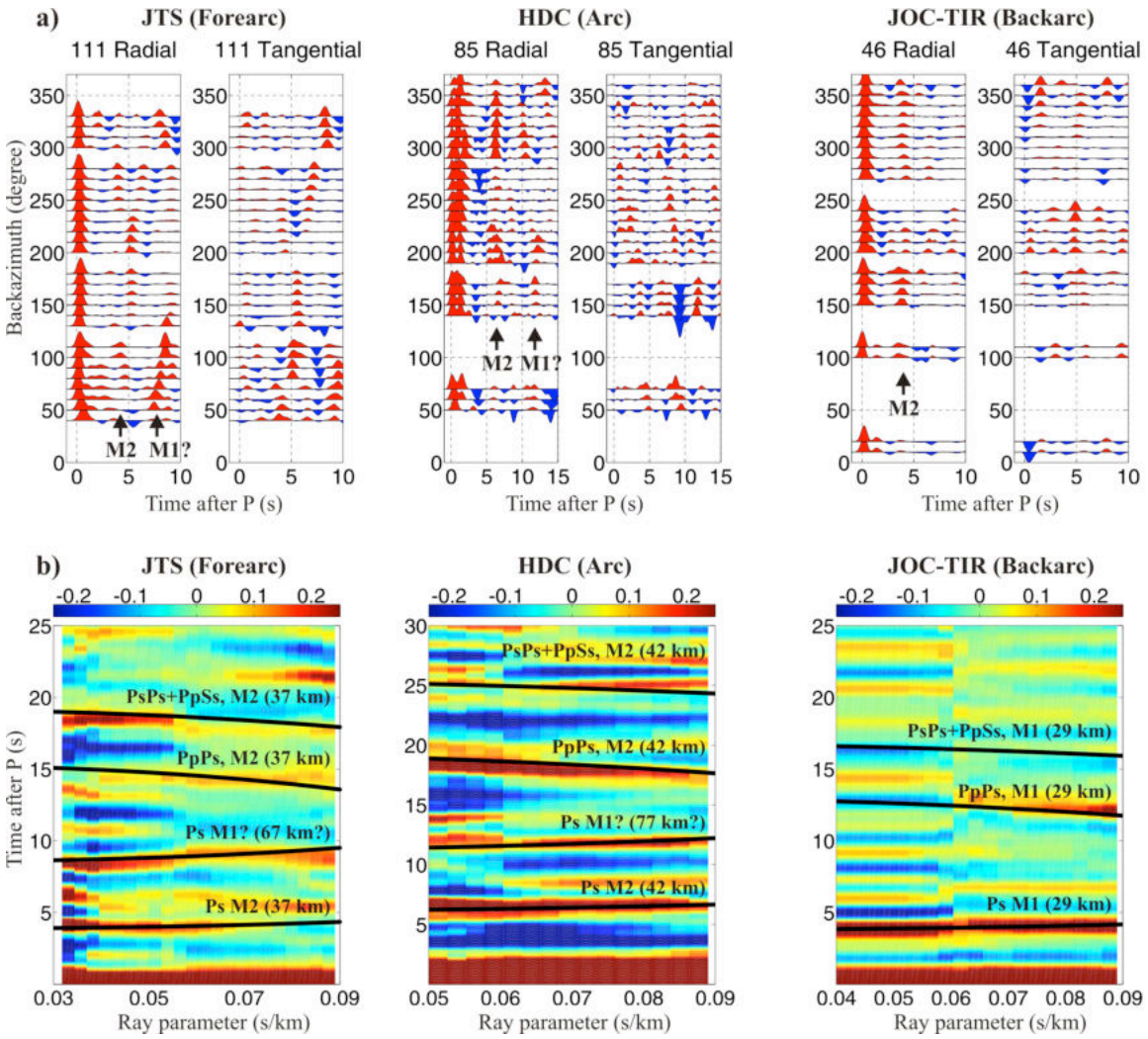

Figure 10. (a) Receiver functions binned over 10° for the specified stations at the top of each plot. (b) Amplitude plots of the radial component of receiver function as a function of ray parameter for the specified stations. Color bars at the top of each plot denote the scale of normalized amplitude receiver function. Black lines show the predicted moveout of Ps conversions and multiples for the slab (M1?) and upper plate Moho (M2) using the specified depths (shown in parenthesis) and *Vp/Vs* obtained from the *H*-κ algorithm (Figure 11A).

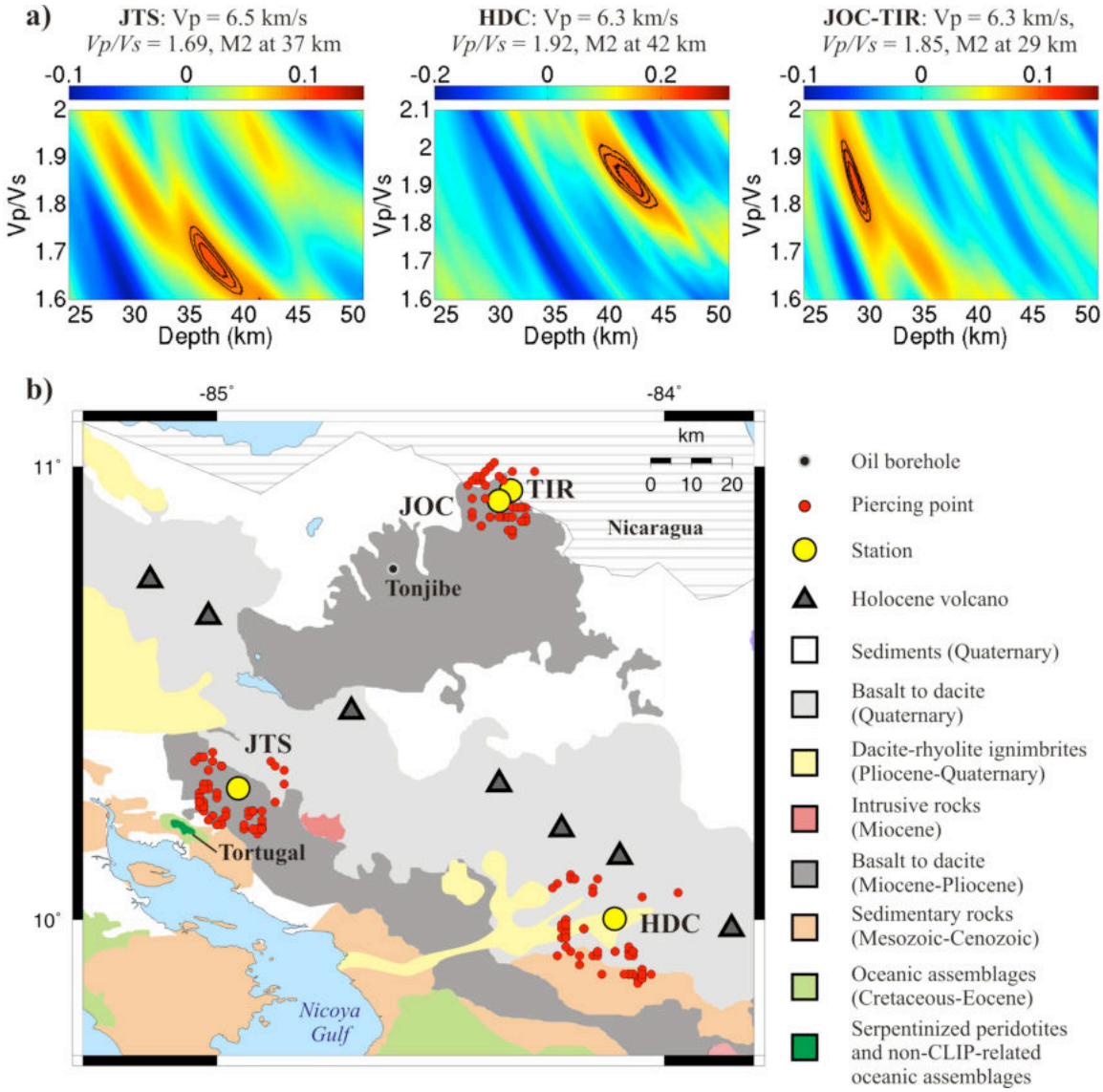

Figure 11. (a) Amplitude *H*–κ stacks for specified stations. Depth to M2 and crustal *Vp/Vs* ratio for each maximum are given above each plot. Black contours delineate regions with 85, 90, and 95% of the maximum amplitude. Color bars at the top of each plot denote the amplitude scale for the stacked receiver functions. (b) Map of the predicted location of points piercing M2 for the specified stations and depths in (a).

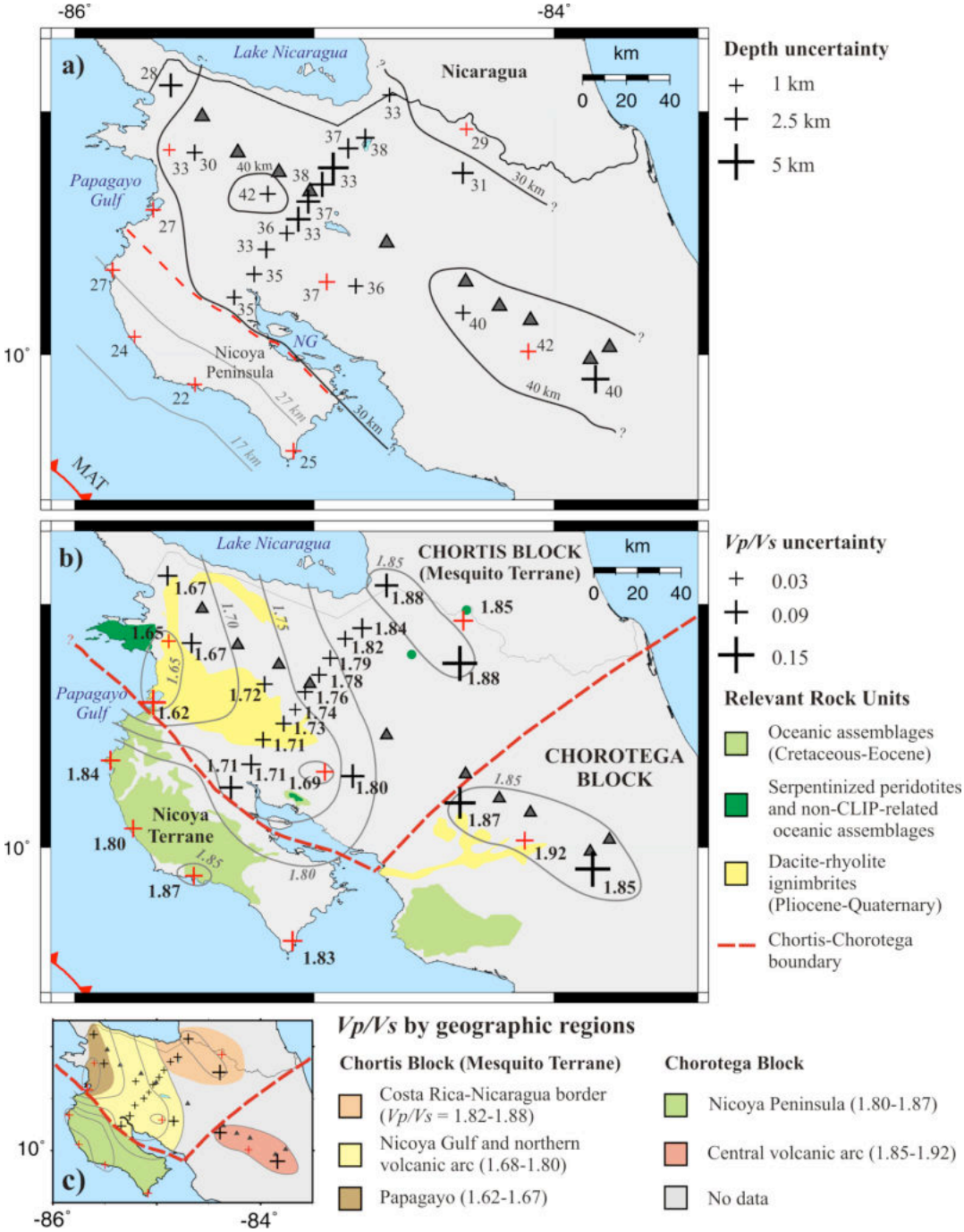

Figure 12. (a) Map of Moho depth (in km). Gray lines represent contours to M1 and red dashed line the slab-M2 intersection based on *DeShon et al.* [2006]. (b) Map of the crustal *Vp/Vs*. Estimates for red crosses were calculated in this study. The remaining estimates come from *MacKenzie et al.* [2008]. Note that symbol size scales to uncertainties, as defined on the right side of each map. (c) *Vp/Vs* by geographic regions as described in the text. See Figure 2 for station names and explanation of symbols. NG, Nicoya Gulf.

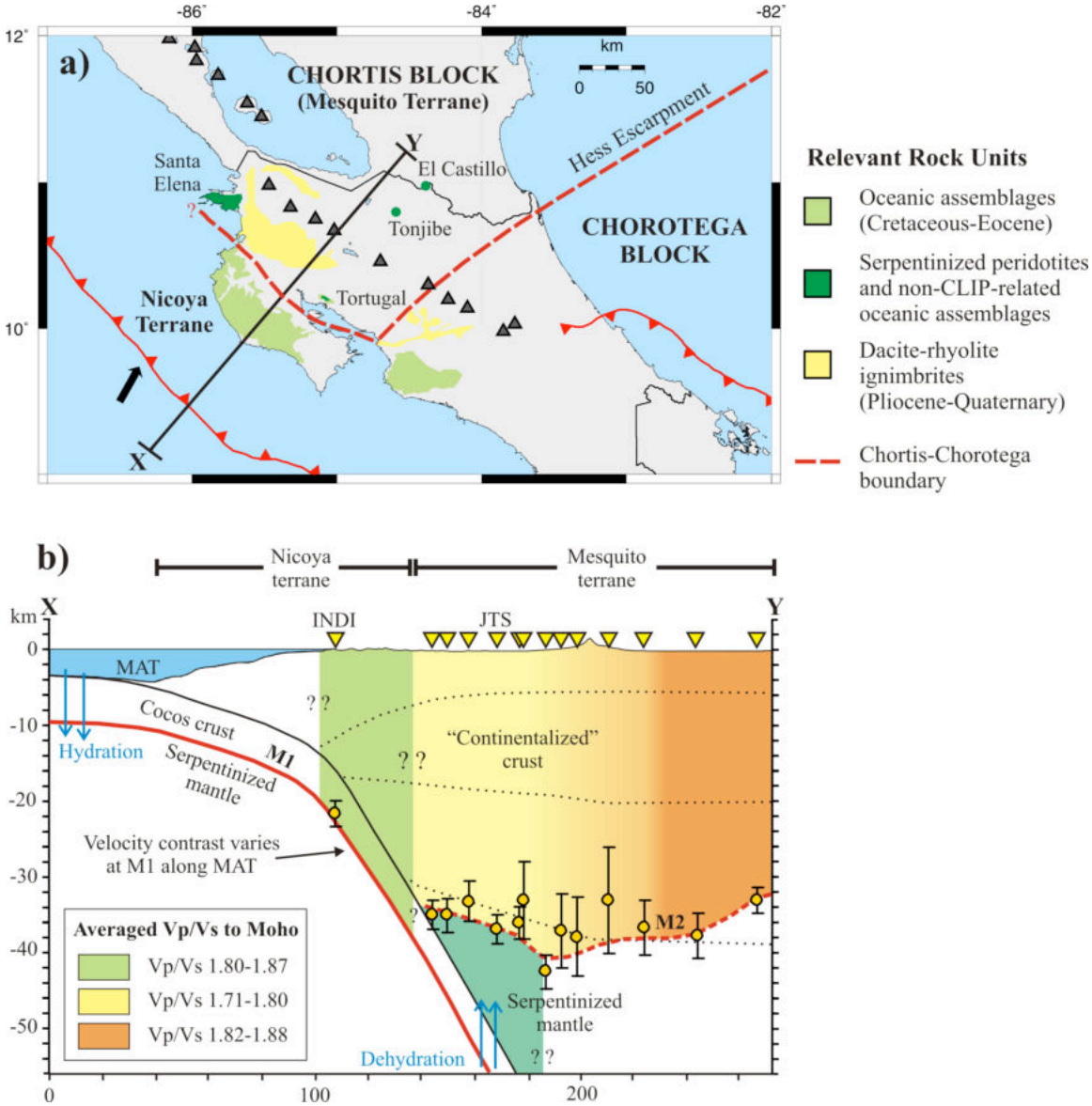

Figure 13. (a) Generalized interpretation of terrane boundaries integrating results from this study, *Hauff et al.* [2000], and *Baumgartner et al.* [2008]. (b) Generalized interpretation along the X-Y cross-section shown in (a) integrating results from this study, *MacKenzie et al.* [2008], *Sallarès et al.* [2001], and *DeShon and Schwartz* [2004]. Depth estimates are shown as yellow circles with error bars. Depth and *Vp/Vs* for station INDI correspond to the oceanic Moho (M1) while the remaining estimates correspond to the upper plate Moho (M2). A possible M2 interpretation is sketched as a dashed red line. Inverted triangles represent broadband stations located < 13 km from cross section. Station JTS, located 30 km from the profile, was also projected onto the cross section. Note vertical scale is three times the horizontal scale. Terranes, as interpreted at surface, are shown at the top of the plot. The orientation of terrane boundaries at depth is unknown. Colors represent crustal regions with distinct vertically averaged *Vp/Vs*.

APPENDIX B: LITHOSPHERIC STRUCTURE OF THE PAMPEAN FLAT SLAB REGION FROM DOUBLE-DIFFERENCE TOMOGRAPHY

Lepolt Linkimer[1], Susan Beck[1], George Zandt[1], Patricia Alvarado[2], Megan Anderson[3], Hersh Gilbert[4], Haijiang Zhang[5]

[1]*Department of Geosciences, University of Arizona*

[2]*Departamento de Geofísica y Astronomía, Universidad Nacional de San Juan-CONICET, Argentina*

[3]*Department of Geology, Colorado College*

[4]*Department of Earth and Atmospheric Sciences, Purdue University*

[5]*Department of Earth, Atmospheric and Planetary Sciences, Massachusetts Institute of Technology*

Abstract

We obtain earthquake locations and a detailed three-dimensional model of the subduction zone velocity structure in west-central Argentina (lat. 30-32°S and lon. 64-70°W) by applying a regional-scale double-difference tomography algorithm to earthquake data recorded by the SIEMBRA (2007-2009) and ESP (2008-2010) broadband seismic networks. In this region, the flat subduction of the Nazca Plate including the Juan Fernandez Ridge is spatially correlated in the overriding South

America Plate with a gap in the arc volcanism and the thick-skinned, basement-cored uplifts of the Sierras Pampeanas. In addition, we present results from a series of careful tests to investigate the sensitivity of our results to many parameters, such as the inter-event distances for calculating the differential times, the starting velocity model, the starting earthquake locations, model parameterization, and the influence of random error in the data. Our model shows the subducting Nazca Plate as a mostly continuous band of increased (2-6%) P- and S- wave velocities (Vp and Vs). The lithospheric mantle of the South America Plate appears to be heterogeneous but mostly characterized by Vp of 8.0-8.2 km/s, Vs of 4.5-4.7 km/s and Vp/Vs ratio of 1.75-1.78, which is consistent with either a depleted lherzolite or a chlorite harzburgite. We observe a region of higher Vp/Vs ratio (1.78-1.80) that we correlated with up to 10% hydration of mantle peridotite above the flat slab. In addition, we observe localized regions of lower Vp/Vs ratio (1.71-1.73) in the mantle above the westernmost part of the flat slab, suggesting orthopyroxene enrichment. Our results from both the 1D and 3D inversion are consistent with a thicker South America crust in the Western Sierras Pampeanas than in the Eastern Sierras Pampeanas. Our model shows the middle-to-upper crust in the Precordillera as a lower Vp and Vs compared to that of the Cuyania and Pampia terranes. In addition, the Vp/Vs is generally higher in the Cuyania Terrane compared to the Pampia Terrane. These observations are consistent with the presence of Paleozoic carbonate rocks in the Precordillera and the differences in composition for the Sierras Pampeanas basement: a more mafic composition for Cuyania Terrane in the west and a more felsic composition for the Pampia Terrane in the east. The more variability in the Vp/Vs ratio in the Cuyania

Terrane is also in agreement with a more complex structure for this region. The relocated slab earthquakes illuminate the slab geometry and suggest that the flat slab region is broader than the width of Juan Fernandez Ridge offshore.

Keywords: Lithosphere Structure, Subduction Zone, Double-difference Tomography, Upper Mantle Hydration.

1. Introduction

Earthquakes in subducted slabs are often associated with dehydration processes, which provide a source of water in subduction zones [e.g., Thompson, 1992; Kirby, et al., 1996; Hacker et al., 2003b; Ranero et al., 2005]. In the outer rise, earthquakes often occur along faults that are believed to act as conduits for hydrating the downgoing lithosphere, thus providing a mechanism to recycle water into the mantle [e.g., Rüpke et al., 2004; Ranero et al., 2005]. One example is the M_w 6.7, 2001 earthquake that occurred off the coast of Chile close to the intersection between the incoming Juan Fernandez Ridge and the trench. This tensional event and aftershock distribution indicate a conjugate normal fault system extending at depths of 30 km into the oceanic lithospheric mantle [Fromm et al., 2006]. Additional evidence of hydrated slabs is the abundant intermediate-depth seismicity, which is often associated with dehydration processes [e.g., Kirby, et al., 1996; Peacock, 2001, Hacker et al., 2003b]. In a normal subduction zone, the water released as the downgoing slab dehydrates will migrate into the hot overlying mantle wedge and

could ultimately induce melting in this region [Thompson, 1992; Peacock et al., 1993; Hacker et al., 2003b]. However, in a flat slab subduction case, the released water would penetrate into and presumably hydrate the cold upper plate lithospheric mantle, which is too cool to trigger melting [Kay et al., 1988].

In the south-central Andes (30-33ºS), flat subduction of the Nazca Plate including the Juan Fernandez Ridge is spatially correlated with the cessation of arc volcanism and the basement-cored uplifts of the Sierras Pampeanas [e.g., Pilger, 1981; Ramos et al., 2002; Fig. 1], which makes this region an ideal place to investigate the role of water in the subduction zone processes as well as the effects of flat slab subduction in the upper plate deformation. This region is relevant for understanding the geologic history of western United States as it is considered a modern analogue of the Laramide deformation [Jordan and Allmendinger, 1986] when a proposed aseismic ridge on the Farallon Plate was subducted beneath the North America Plate [Henderson et al., 1984].

Volcanic activity in the main Andean Cordillera above the flat slab region terminated about 9 Ma as the flattening slab presumably squeezed out the mantle asthenosphere wedge [Kay and Mpodozis, 2002; Ramos et al., 2002]. At depths of ~100 km, dehydration of the subducting Nazca Plate is expected where intra-slab earthquakes are particularly abundant [e.g., Anderson et al., 2007]. If substantial amounts of water are present in the upper plate above where it was released by the slab, seismic tomography should be able to detect it as regions with a high ratio between P-wave (Vp) and S-wave (Vs) velocities (Vp/Vs ratio). Hydrated mantle mineralogies, such as serpentine, are characterized by decreases in P- and S-wave velocities and an increase in the Vp/Vs ratio

[e.g., Carlson and Miller, 2003; Hyndman and Peacock, 2003; Christensen, 2004]. However, previous studies using a regional seismic network (CHARGE, December 2000-May 2002, Fig. 1) showed that the mantle above this flat slab displays an unusual low Vp/Vs ratio that is inconsistent with a hydrated mantle [Wagner et al., 2005, 2006, 2008]. The lack of seismic evidence of hydration above the region of high seismicity in the flat slab is one of the puzzling aspects of the subduction zone water cycle that motivated this study.

Despite the fact that results from the broad-scale CHARGE deployment outlined first-order larger-scale structure, a denser seismic array was required to refine previous results and obtain higher-resolution images of the lithosphere above the flat slab. For these reasons, two local broadband seismic networks were deployed in the region: SIEMBRA (December 2007-November 2009) and ESP (August 2008-August 2010). In this study we apply the double-difference (DD) tomography method to the SIEMBRA and ESP data set to obtain a more detailed model of the three-dimensional P- and S-wave velocity structure of the subduction zone. As a starting point for the 3D modeling we derived a Minimum 1D Model following Kissling et al. [1994]. In addition, we performed a series of tests to investigate the sensitivity of the results to the starting model, starting earthquake locations, and model parameterization. Our final velocity model shows the subducting Nazca Plate and a heterogeneous lithospheric mantle of the South America Plate. We also image the Precordillera, Cuyania and Pampia terranes as regions of distinct seismic velocities.

2. Tectonic Setting

The western edge of the South America Plate along the Andean Cordillera displays significant along- and across-strike variations in mountain elevation, crustal thickness, crustal shortening, Wadati-Benioff Zone seismicity, and magmatism [e.g., Barazangi and Isacks 1976; Allmendinger et a., 1990; Cahill and Isacks, 1992; Kay and Abruzzi, 1996]. In the south-central Andes, the continental margin can be divided into three along-strike segments. North of 28°S and south of 33°S the subducting Nazca Plate dips ~30°E in the upper mantle and the upper plate displays an active volcanic arc. In contrast, between 28°S and 33°S, the subducting Nazca Plate has a nearly horizontal section at depths of ~100 km and the upper-plate volcanism is absent [e.g., Smalley and Isacks, 1987; Jordan et al., 1983; Cahill and Isacks, 1992; Ramos et al., 1996]. This segment is spatially correlated with the subduction of the Juan Fernandez Ridge; a ~100 km wide chain of 11 seamount groups that extend for 900 km from the present hotspot within the Nazca Plate to the Chilean trench [von Huene et al., 1997, Yáñez et al., 2001, 2002]. A westward shift of 50-100 km in the highest peaks of the Andes and the thick-skinned, basement-cored uplifts of the Sierras Pampeanas are also spatially correlated with the subduction of the Juan Fernandez Ridge [e.g., Pilger, 1981; Pardo et al., 2002a; Ramos et al., 2002]. In this study, we refer to this region as the Pampean flat slab.

Across-strike variations are present through different morphotectonic units and terranes. From west to east, our study area includes the following units: Principal and Frontal Cordillera, Precordillera, and Sierras Pampeanas (Figure 1b). These units represent the margin response to subduction during the Late Cenozoic [e.g., Ramos et al.,

2002]. The Principal and Frontal Cordillera, which correspond to the main part of the Andes, are mostly composed of Mesozoic sedimentary rocks and Paleozoic-Triassic magmatic rocks [Ramos et al., 1996]. The Precordillera corresponds to a thin-skinned, fold-and-thrust belt developed on Paleozoic carbonate and younger rocks [Baldis et al., 1984]. The Sierras Pampeanas unit corresponds to thick-skinned, basement-cored uplifts mostly composed of crystalline Precambrian–Early Paleozoic rocks and separated by relatively undeformed broad basins [e.g., Jordan and Allmendinger, 1986; Ramos et al., 2002]. The western and eastern Sierras Pampeanas have different rock compositions [Caminos, 1973]. In the western Sierras Pampeanas (e.g., Pie de Palo) metamorphic rocks predominate over granites [e.g., Caminos, 1973; Vujovich et al., 1994]. In contrast, the Eastern Sierras Pampeanas (e.g. Sierra de Chepes, San Luis, Cordoba, del Norte) are dominated by granitic rocks [e.g., Baldo et al., 1996; von Gosen, 1998; Leal et al., 2003; Dahlquist and Galindo, 2004]. These differences in composition have been detected in the average seismic velocities [e.g., Alvarado et al., 2005; 2007]. Significant variation across strike is also observed in crustal thickness: the Moho depth is at ~70 km beneath the Principal and Frontal Cordillera, at ~50 km in the western Sierras Pampeanas, and at ~35 km in the eastern Sierras Pampeanas [Gans et. al., 2011]. In addition more complexity in crustal structure is observed beneath Cuyania and Chilenia terranes compared to Pampia Terrane [e.g., Gilbert et al., 2006; Gans et al., 2011].

The South America Plate can be described as a mosaic of accreted terranes, with generally north-south trending boundaries added to the much older Rio de la Plata craton [e.g., Ramos et al., 1986; Astini et al., 1995]. From east to west, our study area includes

the Pampia, Cuyania, and Chilenia terranes and is bounded to the east by the Rio de la Plata craton (Figure 1b). Some studies interpret the Cuyania Terrane as a composite terrane formed by the amalgamation of the Precordillera and Pie de Palo terranes [Ramos, 2004] but the provenance and time of amalgamation is still debated [e.g., Finney et al., 2003; Mulcahy et al., 2007]. All these terranes are remnants of the tectonic evolution of the proto-Andean margin of Gondwana during the Paleozoic [e.g., Ramos et al., 1986; Rapela et al., 1998]. Some of the main tectonic events are: the Pampean orogeny and the collision between the Pampia and Rio de la Plata craton during the Cambrian [Rapela et al., 1998; 2007], the development of the Famatinean orogeny on the western margin of Pampia during Early to Mid-Ordovician [Dalla Salda et al., 1992; Rapela et al., 1998, Pankhurst et al., 1998], the collision between Cuyania and Gondwana in Middle Ordovician times [Ramos, 2004], and the collision between Chilenia and Cuyania at the end of the Devonian [Ramos et. al., 1986].

There are several proposed contributing factors for flat subduction, including the subduction of plume-generated over-thickened oceanic crust, subduction below a trenchward moving overthrusting continent, slab suction forces in the mantle wedge, the hydrous weakening of the mantle wedge region, the subduction of young slabs, and a delay in the basalt to eclogite transition due to cool thermal structure [e.g., Gutscher et al., 2000a, b; van Hunen et al., 2002, 2004]. The Pampean flat slab is generally related to the subduction of the Juan Fernandez Ridge [e.g., Pilger, 1981] that may have provided the extra compositional buoyancy to the slab to prohibit it from sinking into the mantle [Yáñez et al., 2001, 2002, Espurt et a., 2008]. This is supported by receiver function

analysis, which suggests a moderately overthickened subducted oceanic crust of 13-19 km in the Pampean flat slab region [Gans et al., 2011].

The geometry of the Juan Fernandez Ridge trend with respect to the direction of plate convergence has lead to the southward migration of the ridge-trench intersection over time, decreasing from a very rapid migration during the Miocene (~200 km/Ma) to only ~275 km during the last 12 Ma [Yáñez et al., 2001]. Based on the arrival of the Juan Fernandez Ridge to the current latitude and the cessation of arc volcanism, the age of slab flattening is likely to have occurred at ~8-11 Ma [Kay et al., 1988]. Arc magmatism migrated progressively eastward, shutting off completely in the Main Cordillera and Precordillera between 7 and 11 Ma [Kay et al., 1988]. Further east, in the Sierras Pampeanas, the most recent volcanism occurred in the Pocho volcanic field in the Sierra de Cordoba at ~7.9-4.5 Ma [Gordillo and Linares, 1982; Kay et al., 1988; Kay and Gordillo, 1994] and at ~9.5-1.9 Ma in the Sierra de San Luis [Urbina et al., 1997].

Besides the cessation of volcanism [e.g., McGeary et al., 1985] other significant effects attributed to the flattening of the slab are the cooling of both upper and subducting plates [Gutscher et al., 2000a], the increase in length of the subduction channel [Martinod et al., 2010], and a decrease of the convergence velocity [Espurt et a., 2008]. Some of these effects favor an increase in plate coupling, which enable deformation to be transferred far into the upper plate and an increase in seismic energy release [Scholz and Small 1997; Gutscher, et al., 2000b; Alvarado et al., 2007]. Large crustal earthquakes (e.g., 1861, 1894, 1944, and 1977) have occurred in the Precordillera and Sierras

Pampeanas region and have caused major human and economic losses in Argentina [e.g., Alvarado and Beck, 2006; Alvarado et al., 2009].

3. Data and Field Deployments

We used data from two temporary broadband seismic deployments: SIEMBRA and ESP (Fig. 1, Table 1). In total, these networks cover an area of 640 km by 450 km. The SIerras pampeanas Experiment using a Multicomponent BRoadband Array (SIEMBRA) consisted of 40 broadband seismometers deployed between December 2007 and November of 2009 (see supplemental materials, Fig. S1 and S2). The network seismometers included 32 STS-2, 4 Trillium, and 4 Guralp CMG-3T (Table 1). Data were collected using Quanterra Q330 dataloggers recording at 40 samples per second and stored on external Balers that were exchanged every 4-6 months. The Eastern Sierras Pampeanas (ESP) experiment was deployed between August 2008 and August 2010 (Fig. S2) and consisted of 12 Guralp CMG-3T seismometers with Reftek 130 dataloggers recording at 40 samples per second. For both networks, position and timing at each station were synchronized using GPS receivers. GPS problems were carefully checked by plotting for each station all GPS positions acquired during the extent of the experiments (Fig. S3a). Instrumentation for the SIEMBRA deployment was provided by the Program for Array Seismic Studies of the Continental Lithosphere (PASSCAL) of the Incorporated Research Institutions for Seismology (IRIS) and for the ESP deployment by Purdue University and Colorado College. These experiments are a follow-up to the CHile ARgentina Geophysical Experiment (CHARGE) that took place between December 2000

and May 2002 (Fig. 1) and two other temporary seismic networks in the region: PANDA (August 1987-May 1988, Chiu et al. [1991]) and CHARSME (November 2002-March 2003, Pardo et al. [2002b]).

We built a single database for both SIEMBRA and ESP experiments using Antelope software. By using a short-term-average versus long-term-average (STA/LTA) trigger algorithm, we captured ~80,000 events detected by more than 8 stations. In order to achieve good ray coverage distribution for the tomography, we selected events with the largest number of station detections using a variable trigger threshold value of > 30 where seismicity is high to only 10 in areas with sparse seismicity. We completed this subset by including all reported events from the catalogs of the Instituto Nacional de Prevención Sísmica (INPRES) and the Preliminary Determination Epicenter (PDE-NEIC) of the U.S. Geological Survey National Earthquake Information Center. The final subset is composed of 1,562 earthquakes (Fig. S4). We handpicked P- and S-wave phases that were weighted based on the uncertainty caused by noise (Fig. 2) and used these weights in the inversion procedure. The weighting scheme for phase reading ranges from quality 0, corresponding to a reading uncertainty of < 0.10 s to quality 4 which correspond to > 0.30 s. The average P- and S-wave reading uncertainties are ±0.06 s and ±0.10 s, respectively.

Phase readings and initial locations were accomplished using the programs MULPLT and HYP [Lienert and Havskov, 1995] included in the software package SEISAN [Havskov and Ottemöller, 1999; Ottemöller et al., 2011]. P waves were picked exclusively on the vertical component. Initial locations were first obtained only based on

the P-wave arrivals using the velocity model used by Smalley et al. [1993] so that earthquakes could be rotated to pick S waves exclusively on the transverse component. In addition, S-wave picks have been checked by plotting Wadati diagrams for each event to identify outliers laying far off the main trend (Fig. S5). Our final database of 1,562 earthquakes is composed of 54,414 P-wave and 30,576 S-wave observations (Fig. S6). Once initial locations were performed with both P- and S-wave arrivals, we plotted histograms of the residuals (observed travel time minus calculated travel time) for each station seeking for erroneous picks and possible GPS timing errors (Fig. S3b). As expected, all sites displayed a Gaussian distribution for P- and S- wave residuals.

For the velocity inversions, we selected 1,157 well-located earthquakes. These events have an azimuthal gap of observations (GAP) $\leq 180°$, have at least 10 P-wave and 6 S-wave observations, and include at least one observation within a distance of 1.5 times their focal depth. This dataset is mostly composed of earthquakes with depths from 0 to 40 km and from 100 to 200 km (Fig. 3).

4. Initial Velocity Model

We used the concept of the minimum 1D model introduced by Kissling [1988] and Kissling et al. [1994] to generate a simple starting velocity model that reflects a velocity gradient based on information obtained by other studies [e.g., Smalley et al., 1993; Alvarado et al., 2005; Gilbert et al., 2006; Anderson et al., 2007] and at the same time lead to a minimum average root mean square (RMS) of traveltime residuals for our earthquake dataset. The concept of the minimum 1D model incorporates the iterative

simultaneous inversion of velocity and hypocenter parameters, and is complemented by station corrections that account for lateral velocity heterogeneity. Besides serving as an initial velocity model, the minimum 1D model provides the high precision hypocenter locations required as input for the 3D earthquake tomography [Kissling, 1988; Kissling et al., 1995].

We used the program VELEST [Kissling et al., 1995] to find the Minimum 1D Model. A total of 39,112 P-wave observations were used to invert for the P-wave Minimum 1D Model. We first evaluated the selected dataset by performing inversions using the velocity models presented by Smalley et al. [1993] and Anderson et al. [2007]. We tested many layer geometries in a trial and error process and searched for a simple 1D model considering that our dataset covers a large region (640 x 450km) with a significant crustal thickness variation [e.g., Gans et al., 2011] and that there is a lack of seismicity in the depth range 50-100 km. We found that the model that produces the minimum RMS has layers at 0, 20, 40, 60, and 100 km with resulted velocities of 6.25, 6.46, 7.19, 8.10, and 8.32 km/s, respectively (Fig. 4a). The final average RMS and variance for the dataset after the inversion are 0.186 s and 0.038 s respectively, contrasting with the initial values of 0.430 s and 0.202 s, respectively.

Station corrections are calculated relative to a reference station CONE, which was chosen according to the following criteria: it lies toward the center of the SIEMBRA and ESP networks, it operated during the whole period of the experiments, has a high signal-to-noise ratio, and it is located on hard rock. P-wave station corrections show an

interesting pattern with positive and negative corrections on the western and eastern parts of the study area, respectively, which we discuss in section 7.3 (Fig 4b).

In order to study the dependence of the solution to the initial model, we conducted additional inversions both increasing and decreasing the initial velocities by 0.5 and 1.0 km/s for each layer. Our results show a strong convergence to the velocity model noted above which we considered the Minimum 1D model for this dataset (Fig. 4a). Following Husen et al. [1999] we conducted several tests with randomly shifted hypocenter locations to assess the stability of the final Minimum 1D model. For the first series of tests, hypocenters resulting from the inversion procedure were shifted randomly up to a maximum of 15 km in any direction and then used as starting locations for a new inversion. We obtained a very good retrieval of the original hypocenter locations, indicating that they are not systematically biased (Fig. S7).

We used a Vp/Vs ratio of 1.74 as a starting model for the tomography inversion. This value corresponds to the regional average Vp/Vs ratio calculated using the Wadati diagrams of 1,092 events with more than six observations of both P- and S-waves per station (Fig. S5).

5. Double-Difference Tomography

In this study we used a regional-scale DD tomography algorithm [tomoFDD; Zhang et al., 2004; Zhang and Thurber, 2006], which is based on the DD location method of Waldhauser and Ellsworth [2000]. This algorithm is designed to solve jointly for 3D velocity structure and earthquake locations using a combination of absolute arrival times

and differential times, leading to a substantially higher resolution in the source region compared to that obtained via conventional tomography [Zhang and Thurber, 2007].

The absolute arrival times correspond to the first arrival times directly picked on the seismograms. Our absolute arrival time catalogue is composed of 40,729 and 25,183 P-wave and S-wave observations, respectively, from 1,157 earthquakes recorded at 55 sites. The differential times were obtained by directly subtracting travel times from event pairs with inter-event distance of < 20 km at common stations located within 400 km from the earthquake cluster centroid. Following Zhang et al. [2004], we tested several inter-event distances for calculating the differential times and found that our results are relatively insensitive to the choice of a distance cut-off of 10 and 20 km (Fig. S9). In our differential time catalogue, any event is linked to a maximum of 10 neighboring events by at least eight pair-wise observations, which resulted in an average separation between strongly linked events of ~9 km. Our differential time catalogue is composed of 170,241 P wave and 92,325 S waves.

We produced a velocity model for Vp and Vs using our complete catalog of absolute and differential times. Given that computing Vp/Vs ratio directly from P- and S-wave tomography models is only meaningful if both models are equally well constrained [e.g., Eberhart-Phillips, 1990; Zhang et al., 2009; Husen et al., 2010], we repeated the set of inversions from P- and S- wave velocity models with an even distribution of P- and S-wave observations (i.e., we performed a joint inversion for both Vp and Vs by using a data set that contains the same number of P and S phases for exactly the same events). This subset is composed by 1092 events, which correspond to 24,555 P- and S-wave

picks and 90,132 P- and S-wave differential times. We present results for the inversions performed using the same number of P and S phases in Figures 6 to 10.

A hierarchical weighting scheme is applied with 20 times greater weight to the absolute data for the first few set of iterations in order to establish the large scale result and then 20 times greater weight to the differential data for the final set of iterations to refine the event locations and the velocity structure near the source regions. A priori weights are used based on the uncertainty of the first arrival reading (Fig. 2). In addition, to control the large residuals during the inversion the data is reweighted by multiplying the a priori quality weights with weights that depend on the misfit of the data from the previous iteration and the offset between events.

TomoFDD uses a finite-difference method for calculating travel times and ray paths, and maps the desired regional portion of the spherical Earth into a uniform Cartesian grid [Zhang and Thurber, 2006]. The coordinate origin of our inverted region is located at 30.8° S and 67.1° W. The inversion grid nodes are uniformly spaced at 20 km intervals in the horizontal directions and extend for 640 km in the E-W direction and 450 km in the N-S direction. In the vertical direction, the nodes are positioned every 10 km from 0 to 210 km. Travel times were calculated using a 3-km uniform Cartesian grid. We started the inversion from a one dimensional velocity model (Minimum 1D model, Fig. 4). In order to account for the known crustal thickness variations we followed the approach of Lin et al. [2010] for a regional tomography, and performed an inversion using a reference model that incorporates a rough 3D Moho interface based on the results of Gans et al. [2011].

To make the inversion more stable, the algorithm includes smoothing and damping parameters as regularization methods. Optimum values for these parameters were obtained via trade-off curves constructed by running a series of inversions with a large range of damping and smoothing values and plotting the data variance versus model variance (Fig. 5). An analysis of the "L-shape" curve is made to chose the values that reduce most of the data variance without causing large increase in the solution variance [e.g., Eberhart-Phillips, 1986; Zhang and Thurber et al., 2007; Thurber et al., 2009]. The choice for the damping factor strongly depends on the condition of the system to be solved. The condition of the system is expressed by the condition number, which is the ratio of the largest to smallest eigenvalue. We chose a smoothing weight of 100 and damping of 150 to 80 (varying with iterations), which lead to condition numbers of 100-150.

Since slowness models converge faster than earthquake locations [e.g., Thurber, 1992] we performed eight sets of iterations alternating the simultaneous inversion with event relocation. The RMS and variance of travel time residuals decreases from 0.526 to 0.138 s, and from 0.3057 s to 0.0019 s. After the 3-D inversion, travel time residuals are drastically reduced and sharply peaked symmetrically around zero (Fig. S8).

6. Resolution and Sensitivity Analysis

We used the Derivative Weighted Sum (DWS; e.g., Thurber and Eberhart-Phillips, 1999) to qualitatively characterize the model resolution. DWS is proportional to the number of rays passing through a grid; hence, areas of good resolution will have high

DWS values [Zhang and Thurber, 2007, Fig. S9]. In addition to analyzing DWS values, we performed a series of tests to investigate the sensitivity of our results to inter-event distances for calculating the differential times, the starting model, starting locations, parameterization, and influence of random error in the data (Figs. S9-S12). We performed these tests using the same number of P and S phases.

We explored the effects of several starting models (Fig. S10). As shown by Koulakov et al. [2006], inversion with different initial models clearly demonstrates the non-uniqueness of the inverse problem as quite different velocity models can equally fit the data, which gives special relevance to a priori information and the choice of an initial model. We performed inversions with initial models based on our Minimum 1D Model and using a Vp/Vs ratio of 1.74, as determined from Wadati diagrams, for both a flat Moho and a 3D Moho model based the results of Gans et al. [2011]. We repeated the inversions for the flat and 3D Moho but using a Vp/Vs ratio of 1.79 for the upper mantle as used in the initial model of Wagner et al. [2008]. We found that these initial models do not change the general patterns in velocity perturbations but impact the extent and amplitude of upper mantle anomalies if the initial upper mantle Vp/Vs ratio is higher (Fig. S10c). We present results from the inversion performed using an initial model based on our calculated Minimum 1D Model with a simple 3D Moho, but we always consider the amplitude and extent of anomalies from the results using other initial models for interpretation.

We also study the effects of different model parameterizations performing inversions using a coarse horizontal grid of 20 x 20 km and a horizontal grid of 10 x 10

km (Fig. S11). The location and amplitude of the main velocity anomalies are not significantly dependent on the aforementioned grid size nodes; however, the size of some anomalies is decreased when reducing the horizontal grid spacing to 10 x 10 km. In addition, resolution is reduced (i.e., DWS values are lower) when decreasing the horizontal grid size.

To explore the influence of random error in the data, we conducted a test in which an integer number was assigned to each earthquake sequentially and then the total number of earthquakes was arbitrarily subdivided into two equal groups of 546 earthquakes corresponding to the earthquakes with even and odd numbers (Fig S12). Differences in the final models reflect the role of the random factor in the data. A comparison with the model resulting from inverting the entire dataset shows how dividing the data affects the model resolution. We found that the resulting velocity models from even and odd events both contain the main anomalies and trends. In addition, both models have a high similarity to the results obtained from inverting the entire data set. This is an indicator of the high quality of the initial data and stability of the inversion.

We carried out three types of synthetic tests to examine the resolution of our study: checkerboard, restoration, and characteristic tests [e.g., Zhao et al., 1992; Haslinger 1999]. For the checkerboard test, we calculated synthetic travel times through a checkerboard model. We used the same source-receiver distribution as the actual data set but we added Gaussian random noise to the arrival times whose level is comparable to the picking uncertainty of the real data (0.06 s and 0.10 s, for P and S waves,

respectively). In addition, we also added a constant noise term to the arrivals at each station, whose value was based on the final RMS of travel time residuals (0.16 s and 0.13 for absolute and differential time data, respectively). This constant noise term simulates the case that the systematic errors (model errors and pick bias) associated with the arrival times are larger than the random ones [Zhang et al., 2003]. These calculated times were then inverted for Vp and Vs by applying the same procedure as for the real data to see how much of the original checkerboard pattern could be recovered.

Each checkerboard model consists of alternating high- and low-velocity anomalies with one grid node left open in between to test for horizontal smearing; at the same time, every other layer is free of anomalies to test for vertical smearing. We repeated the exercise shifting the checkerboard pattern to the initially free layers, so that we were able to explore the smearing in all layers. We designed three sets of checkerboard tests. The first one consists of high- and low-velocity anomalies (±10 per cent) in both Vp and Vs so that the resulted Vp/Vs model is constant (Fig. S13). The second set consists of high- and low-velocity anomalies (±10 per cent) in Vs only and the Vp is kept without anomalies so that the Vp/Vs model has high and low anomalies (±10 per cent) as well (Fig. S14). The third set consists of high- and low-velocity anomalies (± 5 per cent) of opposite sign for Vp and Vs, so that the resulted Vp/Vs model has high and low anomalies (±10 per cent) (Fig. S15).

Our checkerboard pattern is best recovered for both Vp and Vs in areas with DWS above 2,500 which in general correspond to the region between latitude 32 and 30ºS and longitude 67 and 69.5 ºW at depths from 20 to 100 km. Within this region, the overall

checkerboard pattern is clearly observable in both the Vp and Vs models, as well as in the resulted Vp/Vs model. Very importantly, for the first and second set of checkerboard tests, anomalies do not "bleed over" into the Vp/Vs and Vp models, respectively, which do not contain checkerboard anomalies. We observed that when repeating these tests using a larger number of P-wave data compared to S-wave data, checkerboard anomalies "migrate" between models, giving special relevance to the use of exactly the same amount of P- and S- wave data for deriving the Vp/Vs model. Amplitude recovery is especially good for the upper mantle at depths of 70-100 km and somewhat underestimated in the crust between 20 and 50 km. Vertical and horizontal smearing is low at all depths, but it is stronger at the edges of the well resolved area, when DWS < 2,500 (Fig S16).

For the restoration test [e.g., Zhao et al., 1992], we took the velocity model obtained by inverting the real dataset and used it as initial model to calculate synthetic arrival times. We added the same random and constant noise described above for the checkerboard tests. By following the same inversion strategies as those for the real data we obtained the restoring image of the real result. We found that the main anomalies and trends from the true model are restored over well-resolved areas (Fig S15).

7. Results

Tomography results are presented on vertical cross-sections and depth maps (Figs. 6-10). A more complete set of depth slices and vertical cross sections are presented in the supplemental materials (Figs. S18-S22). We present results for the inversion

performed using an even distribution of P- and S-wave observations (i.e., a data set that contains the same number of P and S phases for exactly the same events). We only display results from well-resolved areas with DWS above 100 and interpret anomalies within regions of DWS above 2,500, where we have the best recovery from synthetic tests (Figs. S13-S16). We focused our results on the description of two velocity anomalies in the South America upper mantle, and the general trends observed within the South America crust and the subducting Nazca Plate (Fig. 6).

7.1. Subducting Nazca Plate

The subducted Nazca Plate is clearly marked by the slab seismicity (Wadati-Benioff Zone, WBZ, Figs. 6-8). The region in and above the WBZ is imaged as a mostly continuous flat band of increased (2-6%) Vp between longitude 70ºW and 68.5ºW (Fig. 6b) and especially along E-W cross sections at 31.4ºS, 31.6ºS, and 31.8ºS (Fig. S20). There is an indication of the descending part of the subducting Nazca Plate east of longitude 68.5ºW, especially in the Vp model, where an inclined band of 2-6% increased velocity is observed above the slab seismicity (Fig. 6b). Unfortunately, east of longitude 68.5ºW our resolution is not optimum as indicated by lower DWS values (< 2,500). The Vs velocities are more variable than Vp and are characterized by mostly increased (2-4%) velocities and fewer portions of reduced (2-4%) velocities. The resulting absolute velocities tend to be in a range from 8.2 to 8.5 km/s for Vp and from 4.7 to 4.9 km/s for Vs.

We associated the region of increased velocities with the subducting Nazca Plate and it may correspond to the oceanic upper mantle and/or Moho region. Given that most

of the earthquakes probably occur within the oceanic mantle part of the slab [Gans et al., 2011], we do not have sufficient resolution to image the oceanic crust. Even though the oceanic crust in the Pampean flat slab is described as moderately over-thickened, ranging from 13 to 19 km [Gans et al., 2011], we are not able to image this layer because there is insufficient criss-crossing of seismic rays to resolve it.

7.2. South America Upper mantle

In general, we image the upper mantle of the South America Plate as a region characterized by Vp of 8.0-8.2 km/s, Vs of 4.5-4.7 km/s and Vp/Vs ratio of 1.75-1.775. We refer to this mantle as the "most common" mantle in the region, which is mostly visible from 70 to 100 km above the flat slab, with the greatest extent at depths of 70 and 90 km (Figs. 10, S19). Above the western part of the flat slab, we observe two distinct regions that deviate from these values, which we refer as anomalies A and B (Fig. 6).

Anomaly A is characterized by Vp of 7.7-8.0 km/s, Vs of 4.5-4.65 km/s, and Vp/Vs ratio of 1.71-1.73. Along the path of the Juan Fernandez Ridge (Fig. 6), the region of reduced Vp and Vs extends at depths from 60 to 80 km between 70.5°W and 69°W. This anomaly is also visible in the E-W profile along latitude 31.8°S (Fig. S20) and in the N-S profile along longitude 69°W (Fig. S21).

Previously, a very low Vp/Vs ratio (1.65–1.72) characterized by Vp of 7.8–8.2 km/s and Vs of 4.7–4.8 km/s was imaged above the flat slab, just north of the Juan Fernandez Ridge [Wagner et al., 2005, 2006, 2008]. In this previous tomography, the low Vp/Vs anomaly was large, extending ~300 km in E-W, 120 km in N-S, and appeared to be 20-40 km thick above the flat slab [Wagner et al., 2005]. This regional tomography

study used a coarser grid spacing of 40x40x20 km in latitude, longitude, and depth, respectively [Wagner et al., 2005], used a starting mantle model of IASPEI-91 [Kennett, 1991] and fixed the crustal Vp and Vp/Vs ratio to 6.0 km/s and 1.73, respectively [Wagner et al., 2005]. Both the spatial extent and the amplitude of the low Vp/Vs anomaly were well recovered from synthetic tests in the region between 70.5 and 68.5°W [Wagner et al., 2008]. Wagner et al. [2005, 2006, and 2008] explored the possible explanations for an anomaly with this seismic signature. They concluded that this anomaly cannot be modeled using hydrated peridotite but instead required orthopyroxene enrichment in the continental lithosphere to explain it.

Anomaly B corresponds to Vp of 8.0-8.1 km/s, Vs of 4.4-4.5 km/s, and Vp/Vs ratio of 1.78-1.81. This anomaly occurs at depths from 60 to 80 km, is approximately 80 km long and appears to be inclined towards the east when seen in a profile along the projected path of Juan Fernandez Ridge (Fig. 6). In map view, the largest extent of the anomaly occurs at depths of 70 km where it covers an area of 80 x 20 km (Fig. 10).

The closest high Vp/Vs anomaly found in previous studies [Wagner et al., 2005 and 2006] was found above the region where the plate starts descending normally, immediately to the south of the flat slab portion. That anomaly is characterized by Vs of 4.65 km/s and Vp/Vs of 1.775 and was interpreted as cooled asthenosphere that was displaced in advance of the eastward progression of the flattening slab between 10 and 2 Ma, and eventually trapped by the increased shallowing of the slab in the transition zone [Wagner et al., 2006].

7.3. South America Crust

Our results from both the 1D and 3D inversions are consistent with a thicker South America crust in the Western Sierras Pampeanas than in the Eastern Sierras Pampeanas. According to the receiver function study by Gans et al. [2011] the crustal thickness varies from ~70 km in the Main Cordillera, to ~50 km in the Western Sierras Pampeanas, to ~35 km in the Eastern Sierras Pampeanas. This crustal thickness variation has been widely observed in other studies using receiver functions [Calkins et al., 2006; Gilbert et al., 2006; Heit et al., 2008], Pn phase velocity [Fromm et al., 2004], and S-to-P converted phases [Regnier et al., 1994].

The P-wave station corrections obtained from our 1D inversion show a clear pattern of positive values in the east and negative values in the west (Fig. 4b). This pattern indicates that arrivals on the west side of the network are delayed with respect to those on the east which may be reflecting a large scale velocity variation due to changes in crustal thickness or to a lower average velocity to the west as interpreted by Smalley et al. [1993]. A similar pattern with a profound variation of station corrections with Moho depth was also found by Pujol et al. [1991] and Anderson et al. [2007].

Our 3D inversion also shows evidence of the crustal thickness variation. Velocity contours in the 7.0-7.9 km/s range for Vp tend to get deeper in the Precordillera region, west of longitude 68.4ºW (Fig. 6b). For example, the 7.8 km/s contour appears at depths of 60 km beneath the Precordillera and shallows progressively to the east to depths of only 40 km. We observe a similar trend when performing an inversion using an initial model with a flat Moho.

Our model shows that the middle-to-upper crust in the Precordillera has lower Vp and Vs compared to that of the Cuyania and Pampia terranes (Fig. 6A, 6C). Similarly, a portion of the Pampia Terrane exhibit lower Vp compared the Cuyania Terrane, which is visible as a region with increased velocities (Fig. 6B, 6D). The Vp/Vs ratio is more variable at middle-to-upper crust beneath the Precordillera and Cuyania, compared to the Pampia Terrane. In general, the Vp/Vs is higher in the Cuyania Terrane compared to the Pampia Terrane, which has the lowest Vp/Vs anomaly we imaged at crustal levels. Our results are consistent with the differences in composition for the Sierras Pampeanas basement: a more mafic-ultramafic composition dominates the Cuyania Terrane (e.g. Ramos 2004) versus a more felsic quartz-rich composition of the Pampia Terrane (e.g. Rapela et al. 1998). The more variability in the Vp/Vs ratio in the Cuyania Terrane is also in agreement with a more complex structure for this region [Gilbert et al., 2006; Gans et al., 2011].

7.4. Earthquake locations

Seismicity in the San Juan region has a bimodal distribution in depth (Fig. 3) with earthquakes concentrated in the crust at depths of less than 40 km and in the subducting Nazca Plate at depths grater than 100 km. The recorded crustal seismicity is especially abundant in the Cuyania Terrane beneath the Pie de Palo mountain range and in the thin-skinned Precordillera (Figs. 6E, 7E).

Along E-W cross sections, the WBZ is flat at a depth of ~100 km between longitude 70.5 and 68.5ºW (Fig. 6). East of longitude 68.5ºW the WBZ dips to the east, and earthquakes range from depths of 100 to 200 km (Fig 6, 7). Along N-S cross

sections, the WBZ is flat at a depth of ~100 km from latitude 30 to 32.5ºS beneath the Precordillera (Fig. 8a). N-S cross sections beneath the Cuyania Terrane also show a flat WBZ at ~100 km but mostly from latitude 30ºS to 31ºS, and south of 31ºS the WBZ is inclined towards the south (Fig. 8b, 8c, 8d). Our earthquake locations imply that the flat slab region is as wide as 240 km, which is broader than the width of Juan Fernandez Ridge offshore, which is only ~100 km [von Huene et al., 1997, Yáñez et al., 2001]. The recorded slab seismicity is particularly abundant in the flat segment defining a continuous band from 70.5 and 68.5ºW. In contrast, in the inclined part east of 68.5ºW the seismicity is less abundant and discontinuous (Figs. 6, 7).

Initial single locations (Fig. 3) show that, within the flat slab region (longitude from 70°W to 68°W), there is a progressive shallowing of the seismicity towards the NE opposite to the direction of subduction. When earthquakes are relocated in the tomography using a 3D velocity model, earthquakes flatten out, aligning more closely at ~100 km depth but still retain a small westward dip, especially to the north of the projected path of Juan Fernandez Ridge along E-W cross sections at latitude 30.8, 31.0, and 31.2ºS (Figs. S18, S20).

Analysis of these earthquake locations together with receiver function migration results using the same velocity model [Gans et al., 2011] suggest that the slab earthquakes appear to be occurring in the oceanic mantle of the slab. If slab earthquakes illuminate the slab geometry the slight westward dip still retained within our tomography locations likely reflects true variations in earthquake depth resolved by our study

suggesting some “topography” in the subducted Nazca Plate. A detailed description of the earthquake locations will be presented in a separate paper.

8. Discussion

The occurrence of the outer-rise seismicity in the oceanic mantle suggests the existence of lithospheric scale faults acting as conduits to hydrate the incoming plate before subduction [e.g., Ranero et al., 2005; Kopp et al., 2004; Fromm et al., 2006]. Offshore the Chilean coast, to the west of our study area, plate bending-faulting is pervasive [e.g., Kopp et al., 2004; Ranero et al., 2005]. Near the intersection of the subducting Juan Fernandez Ridge and the Chilean trench, outer-rise aftershock seismicity shows evidence of conjugate normal faults extending to of 30 km into the oceanic lithospheric mantle [Fromm et al., 2006]. Uppermost mantle hydration in the outer rise region limited to the flexed and faulted lithosphere of the Juan Fernandez Ridge has been suggested by imaging of reduced uppermost mantle velocities in tomographic inversions [Kopp et al., 2004].

Once the hydrated slab subducts, it is thought to dehydrate through embrittlement reactions that have been proposed as a mechanism for producing intra-slab earthquakes [e.g., Abers, 1992; Kirby, et al., 1996]. Thermal modeling shows that seismicity within the subducting slab is distributed in a narrow belt of pressure-temperature conditions, which coincides with the breakdown of high-pressure hydrous phases [e.g., Abers et al., 2006]. It is generally understood that significant quantities of aqueous fluids are expelled from the down going slab as they encounter increasing pressure and temperature [e.g.,

Peacock, 1993; Rondenay et al., 2008]. The conceptual model of Ranero et al. [2005] for intermediate-depth seismicity proposes that it starts between 60-80 km, when dehydration of oceanic crust reactivates the upper segment of bend-faults, which causes concentration of earthquakes on the upper part of slab. Deeper than ~100 km, eclogitization is completed; here or slightly deeper dehydration of slab mantle occurs reactivating bend-faults and generating seismicity within the upper slab mantle [Ranero et al., 2005].

Petrologic models [e.g., Thompson, 1992; Kirby et al., 1996; Hacker et al., 2003a,b] predict a causal connection between intra-slab earthquakes and a hydrated mantle above the subducting slab. In the Pampean flat slab, the seismicity is abundant along the projected path of the Juan Fernandez Ridge; therefore mantle hydration above the slab is expected. Hydration of peridotite, the dominant rock type in the mantle, will stabilize a variety of hydrous minerals, in particular, serpentine. Antigorite is the main serpentine mineral in ultramafic rocks metamorphosed under moderate temperatures and is stable to temperatures of 620-720°C at depths between 30 and 150 km [Ulmer and Trommsdorff, 1995].

Beneath the forearc region of subduction zones, moderate temperatures allow serpentinization of antigorite. Hacker et al. [2003a] support the idea that seismic velocities and Vp/Vs ratios indicate that mantle wedges beneath forearc regions locally reach 60-80% hydration. Very high serpentinization values (> 50%) have been found in other subduction zones forearcs such as central Japan [Kamiya and Kobayashi, 2000] and the Cascades [Bostock et al., 2002]. Our study region is located in the backarc, which is usually hotter than the forearc in a normal dipping subduction zone. However, the flat

subduction should alter the thermal structure of the region and temperatures at depths of 100 km are cooler than a normal dipping subduction zone although they may still be warmer than most forearc settings. However, the serpentinization of antigorite may still be stable. The Vp/Vs ratio for serpentinization of antigorite varies between 1.74 (0%) to 1.85 (100%) [Christensen, 2004]. Thus, high Vp/Vs ratios directly above the area of most active seismicity in the cold flat slab are expected.

Following Wagner et al. [2006; 2008] we investigate the seismic properties of common upper mantle end-member compositions using the method of Hacker et al. [2003b]. Figure 11 shows the Vs and Vp/Vs ratio for common mantle mineralogies. Lherzolite and harzburgite are the common enriched and depleted rock types of the upper mantle; depleted lherzolite is intermediate. Harzburgite (olivine + orthopyroxene) is the dominant rock type in mantle wedges and the uppermost oceanic mantle [Hacker et al., 2003b]. Forsterite is the magnesium rich end-member of olivine and enstatite **is** the magnesium end-member of the orthopyroxene.

The most common Vs and Vp/Vs ratio we found above the flat slab correspond to 4.5-4.7 km/s and 1.75-178, respectively. According to the petrologic models from Hacker et al. [2003b] at 3GPa, these values are consistent with either a depleted lherzolite (chlorite lherzolite) or a chlorite harzburgite (Fig. 11). Both rocks are stable at 3 GPa at temperatures from ~650ºC to 800ºC. Similar velocities are obtained for a garnet lherzolite and garnet harzburgite, but both rocks are stable at higher temperatures above 800ºC, which is unlikely above the cold flat slab, where temperatures are expected in the range

from 600ºC to 900ºC [Gutscher et al., 2000b]. For temperatures lower than 650ºC, it is difficult to find mantle compositions that exhibit the observed seismic velocities.

We found two velocity anomalies that deviate from the aforementioned values. Anomaly A is characterized by Vs of 4.5-4.65 km/s and Vp/Vs ratio of 1.71-1.73. These values suggest enstatite, the Mg end-member of orthopyroxene as previously suggested by Wagner [2005, 2006, and 2008] who concluded that orthopyroxene enrichment in the continental lithosphere can explain it and suggested that the metasomatization of olivine to orthopyroxene occurred on a massive scale above the flat slab implying the transit time of the fluid through the lower portion of the overlying mantle must be short, and that this fluxing by siliceous fluids was a transient phenomena. Our tighter constraints on the velocities values and the smaller volume of the low Vp/Vs anomaly we found make the interpretation from Wagner et al. [2008] stronger.

Anomaly B, characterized by Vs of 4.4-4.5 km/s, and Vp/Vs ratio of 1.78-1.80 is consistent with up to 10% hydration of mantle peridotite above the flat slab (Fig. 11). Given the cold temperatures (< 700ºC) predicted for the flat slab region [e.g., Gutscher et al., 2000b; Gutscher, 2002; van Hunen et al., 2002] we rule out the possibility that the seismic signature found corresponds to melts. This higher Vp/Vs anomaly may represent the evidence of upper mantle hydration expected from the high seismicity in the flat slab.

Booker et al. [2004] estimated that the entire plate from 400 km depth up to the trench has never been below active volcanism, so none of the water released by this plate segment has triggered upper plate volcanism and therefore the lithosphere may still retain significant quantities of fluids. These authors based this estimate on the convergence of

the Nazca Plate with respect to stable South America [Norabuena et al., 1999] and the age of the cessation of volcanism across the Pampean flat slab region about at ~9 Ma [Kay and Mpodozis, 2002; Ramos et al., 2002]. Our finding of moderately hydrated regions are also consistent with previous work on paleo-flat slabs in the western U.S. and beneath the Bolivian Altiplano which have suggested that flat slabs serve to hydrate the lithosphere above them [Humphreys et al., 2003; James and Sacks, 1999]. However, the amount of hydration we found seems to be low for the abundant seismicity above the flat slab. In addition, anomaly B is not present above the entire area of abundant seismicity, which suggests there may be pathways for fluids to circulate and concentrate in certain regions in the mantle.

9. Conclusions

We obtain a detailed three-dimensional model of the subduction zone velocity structure in west-central Argentina. The subducting Nazca Plate is imaged as a mostly continuous band of increased (2-6%) Vp and Vs, probably corresponding to the oceanic upper mantle and/or Moho region.

The lithospheric mantle of the South America Plate appears to be heterogeneous. It is mostly characterized by Vp of 8.0-8.2 km/s, Vs of 4.5-4.7 km/s and Vp/Vs ratio of 1.75-1.78, which is consistent with either a depleted lherzolite (chlorite lherzolite) or a chlorite harzburgite. We found two velocity anomalies that deviate from the aforementioned values (referred to anomalies A and B). Anomaly A is characterized by Vs of 4.5-4.65 km/s and Vp/Vs ratio of 1.71-1.73, consistent with enrichment of enstatite,

the Mg end-member of orthopyroxene as previously suggested by Wagner [2005, 2006, and 2008]. Anomaly B, characterized by Vs of 4.4-4.5 km/s, and Vp/Vs ratio of 1.78-1.80 is consistent with up to 10% hydration of mantle peridotite above the flat slab.

Our results from both the 1D and 3D inversion are consistent with a thicker South America crust in the Western Sierras Pampeanas than in the Eastern Sierras Pampeanas. This is supported by a clear pattern in the P-wave station corrections obtained from our 1D inversion that shows positive values in the east and negative values in the west. In the 3D inversion, a thicker crust beneath the Western Sierras Pampeanas is supported by the tendency of Vp contours in the 7.0-7.9 km/s range to get deeper in the Precordillera region.

We imaged the middle-to-upper crust in the Precordillera as a lower Vp and Vs compared to that of the Cuyania and Pampia terranes. In addition, the Vp/Vs is higher in the Cuyania Terrane compared to the Pampia Terrane. These observations are consistent with a Paleozoic carbonate rocks in the Precordillera and the differences in composition for the Sierras Pampeanas basement: a more mafic composition for Cuyania Terrane in the west and a more felsic composition for the Pampia Terrane in the east. The greater variability in the Vp/Vs ratio in the Cuyania Terrane is also in agreement with a more complex structure for this region.

The relocated slab earthquakes illuminate the slab geometry and suggest that the flat slab region is as wide as 240 km, which is broader than the width of Juan Fernandez Ridge offshore (~100 km). Analysis of these earthquake locations together with receiver

function results [Gans et al., 2011] suggest that the slab earthquakes appear to be occurring in the oceanic mantle of the slab.

10. Acknowledgments.

We are grateful to IRIS and personnel at the PASSCAL Instrument Center for their help and support throughout the SIEMBRA deployment. The seismic instruments were provided by the Incorporated Research Institutions for Seismology (IRIS) through the PASSCAL Instrument Center (NSF Cooperative Agreement EAR-0552316). We also sincerely thank the Instituto Nacional de Prevención Sísmica, Argentina, for their help in logistics, as well as Noel Barstow (PASSCAL) for her invaluable assistance in the field. This research was supported by the National Science Foundation (EAR-0510966, EAR-0738935 and EAR-0739001). Special thanks to C. Berk Biryol and Ivonne Arroyo for helping with codes and discussions. Thanks to Ryan Porter, Christine Gans, and the GSAT group of the University of Arizona. Maps were created using the Generic Mapping Tools (GMT) software [Wessel and Smith, 1998].

11. References

Abers, G.A., 1992. Relationship between shallow- and intermediate-depth seismicity in the Eastern Aleutian Subduction Zone, *Geophys. Res. Lett.,* **19,** 2019-2022, doi:10.1029/92gl02060.

Abers, G.A., van Keken, P.E., Kneller, E.A., Ferris, A. & Stachnik, J.C., 2006. The thermal structure of subduction zones constrained by seismic imaging: Implications for slab

dehydration and wedge flow, *Earth Planet. Sci. Lett.,* **241,** 387-397, doi:doi: 10.1016/j.epsl.2005.11.055.

Allmendinger, R.W., Figueroa, D., Snyder, D., Beer, J., Mpodozis, C. & Isacks, B.L., 1990. Foreland shortening and crustal balancing in the Andes at 30°S latitude, *Tectonics,* **9,** 789-809, doi:10.1029/TC009i004p00789.

Alvarado, P. & Beck, S., 2006. Source characterization of the San Juan (Argentina) crustal earthquakes of 15 January 1944 (Mw 7.0) and 11 June 1952 (Mw 6.8), *Earth Planet. Sci. Lett.*, doi:10.1016/j.epsl.2006.01.015.

Alvarado, P., Beck, S. & Zandt, G., 2007. Crustal structure of the south-central Andes Cordillera and backarc region from regional waveform modelling, *Geophys. J. Int.,* **170,** 858-875, doi:10.1111/j.1365-246X.2007.03452.x.

Alvarado, P., Beck, S., Zandt, G., Araujo, M. & Triep, E., 2005. Crustal deformation in the south-central Andes backarc terranes as viewed from regional broad-band seismic waveform modelling, *Geophys. J. Int.,* **163,** 580-598, doi:10.1111/j.1365-246X.2005.02759.x.

Alvarado, P., Pardo, M., Gilbert, H., Miranda, S., Anderson, M., Saez, M. & Beck, S., 2009. Flat-slab subduction and crustal models for the seismically active Sierras Pampeanas region of Argentina, *Mem. - Geol. Soc. Am.,* **204,** 261-278, doi:10.1130/2009.1204(12).

Astini, R.A., Benedetto, J.L. & Vaccari, N.E., 1995. The early Paleozoic evolution of the Argentine Precordillera as a Laurentian rifted, drifted, and collided terrane: A geodynamic model, *Geol. Soc. Am. Bull.,* **107,** 253-273, doi:10.1130/0016-7606(1996)108<0372:TEPEOT>2.3.CO;2.

Baldis, B.A., Beresi, M., Bordonaro, O. & Vaca, A., 1984. The Argentine Precordillera as a key to Andean structure, *Episodes,* **7,** 14-19.

Baldo, E.G.A., Demange, M. & Martino, R.D., 1996. Evolution of the Sierras de Cordoba, Argentina, *Tectonophysics,* **267,** 1-4, doi:10.1016/S00401951(96)000923.

Barazangi, M. & Isacks, B., 1976. Spatial distribution of earthquakes and subduction of the Nazca Plate beneath South America, *Geology,* **4,** 686-692, doi:10.1130/0091-7613(1976)4<686:SDOEAS>2.0.CO;2.

Booker, J.R., Favetto, A. & Pomposiello, M.C., 2004. Low electrical resistivity associated with plunging of the Nazca flat slab beneath Argentina, *Nature,* **429,** 399-403, doi:10.1038/nature02565.

Bostock, M.G., Hyndman, R.D., Rondenay, S. & Peacock, S.M., 2002. An inverted continental Moho and serpentinization of the forearc mantle, *Nature,* **417,** 536-538, doi:10.1038/417536a.

Cahill, T. & Isacks, B.L., 1992. Seismicity and shape of the subducted Nazca Plate, *J. Geophys. Res.,* **97,** 17503-17529, doi:10.1029/92JB00493.

Calkins, J.A., Zandt, G., Gilbert, H.J. & Beck, S.L., 2006. Crustal images from San Juan, Argentina, obtained using high frequency local event receiver functions, *Geophys. Res. Lett.,* **33,** 1-4, doi:10.1029/2005GL025516.

Caminos, R., 1973. Some granites, gneisses and metamorphites of Argentina, *in Symposium on Granites, Gneisses and Related Rocks*, pp. 333-338, ed. Lister, L. A., Special Publication - Geological Society of South Africa, Salisbury.

Carlson, R.L. & Miller, D.J., 1997. A new assessment of the abundance of serpentinite in the

oceanic crust, *Geophys. Res. Lett.,* **24,** 457-460, doi:10.1029/97GL00144.

Carlson, R.L. & Miller, D.J., 2003. Mantle wedge water contents estimated from seismic velocities in partially serpentinized peridotites, *Geophys. Res. Lett.,* **30,** 1250, doi:10.1029/2002GL016600.

Chiu, J.M., Steiner, G., Smalley, R., Jr. & Johnston, A.C., 1991. PANDA: A simple, portable seismic array for local- to regional-scale seismic experiments, *Bull. Seismol. Soc. Am.,* **81,** 1000-1014.

Christensen, N.I., 2004. Serpentinites, Peridotites, and Seismology, *Int. Geol. Rev.,* **46,** 795-816, doi:10.2747/0020-6814.46.9.795.

Cloos, M., 1993. Lithospheric buoyancy and collisional orogenesis: Subduction of the oceanic plateaus, continental margins, island arcs, spreading ridges, and seamounts, *Geol. Soc. Am. Bull.,* **105,** 715-737, doi:10.1130/0016-7606(1993)105<0715:LBACOS>2.3.CO;2.

Dahlquist, J.A. & Galindo, C., 2004. Geoquímica isotópica de los granitoides de la sierra de Chepes: un modelo geotectónico y termal, implicancias para el orógeno famatiniano, *Rev. Asoc. Geol. Argent.,* **59,** 57-69.

Dalla Salda, L., Cingolani, C. & Varela, R., 1992. Early Paleozoic orogenic belt of the Andes in southwestern South America: Result of Laurentia-Gondwana collision?, *Geology,* **20,** 617-620, doi:10.1130/00917613(1992)020<0617:EPOBOT>2.3.CO;2.

Eberhart-Phillips, D., 1986. Three-dimensional velocity structure in Northern California Coast Ranges from inversion of local earthquake arrival times, *Bull. Seismol. Soc. Am.,* **76,** 1025-1052.

Eberhart-Phillips, D., 1990. Three-dimensional P and S velocity structure in the Coalinga

region, California, *J. Geophys. Res.,* **95,** 15343-15363.

Espurt, N., Funiciello, F., Martinod, J., Guillaume, B., Regard, V., Faccenna, C. & Brusset, S., 2008. Flat subduction dynamics and deformation of the South American Plate: insights from analog modeling, *Tectonics,* **27**, doi:10.1029/2007TC002175.

Finney, S., Gleason, J., Gehrels, G., Peralta, S. & Aceñolaza, G., 2003. Early Gondwanan connection for the Argentine Precordillera terrane, *Earth Planet. Sci. Lett.,* **205,** 349-359, doi:10.1016/S0012-821X(02)01063-4.

Fromm, R., Alvarado, P., Beck, S. & Zandt, G., 2006. The April 9, 2001 Juan Fernandez Ridge (Mw 6.7) Tensional Outer-Rise Earthquake and its Aftershock Sequence, *J. Seismol.,* **10,** 163-170, doi:10.1007/s10950-006-9013-3.

Fromm, R., Zandt, G. & Beck, S.L., 2004. Crustal thickness beneath the Andes and Sierras Pampeanas at 30°S inferred from Pn apparent phase velocities, *Geophys. Res. Lett.,* **31,** L06625, doi:10.1029/2003gl019231.

Gans, C.R., Beck, S.L., Zandt, G., Gilbert, H., Alvarado, P., Anderson, M. & Linkimer, L., 2011. Continental and oceanic crustal structure of the Pampean flat slab region, western Argentina, using receiver function analysis: new high-resolution results, *Geophys. J. Int.,* **186,** 45-58, doi:10.1111/j.1365-246X.2011.05023.x.

Gilbert, H., Beck, S. & Zandt, G., 2006. Lithospheric and upper mantle structure of central Chile and Argentina, *Geophys. J. Int.,* **165,** 383-398, doi:10.1111/j.1365-246X.2006.02867.x.

Gordillo, C.E. & Linares, A., 1981. Geocronología y petrografía de las vulcanitas terciarias del Departamento de Pocho. Provincia de Córdoba, *Rev. Asoc. Geol. Argent.,* **36,** 380-

388.

Gutscher, M.-A., 2002. Andean subduction styles and their effect on thermal structure and interplate coupling, *J. South Am. Earth Sci.,* **15,** 3-10, doi:10.1016/S0895-9811(02)00002-0.

Gutscher, M.-A., Maury, R., Eissen, J.-P. & Bourdon, E., 2000a. Can slab melting be caused by flat subduction?, *Geology,* **28,** 535-538, doi:10.1130/0091-7613(2000)28<535:CSMBCB>2.0.CO;2.

Gutscher, M.-A., Spakman, W., Bijwaard, H. & Engdahl, E.R., 2000b. Geodynamics of flat subduction: Seismicity and tomographic constraints from the Andean margin, *Tectonics,* **19,** 814-833, doi:10.1029/1999tc001152.

Hacker, B.R., Abers, G.A. & Peacock, S.M., 2003a. Subduction factory 1. Theoretical mineralogy, densities, seismic wave speeds, and H2O contents, *J. Geophys. Res.,* **108,** 2029, doi:10.1029/2001jb001127.

Hacker, B.R., Peacock, S.M., Abers, G.A. & Holloway, S.D., 2003b. Subduction factory 2. Are intermediate-depth earthquakes in subducting slabs linked to metamorphic dehydration reactions?, *J. Geophys. Res.,* **108,** 2030, doi:10.1029/2001jb001129.

Haslinger, F., 1998. *Velocity structure, seismicity and seismotectonics of Northwestern Greece between the Gulf of Arta and Zakynthos*, PhD thesis, ETH Zurich.

Havskov, J. & Ottemoller, L., 1999. SeisAn Earthquake Analysis Software, *Seis. Res. Lett.,* **70,** 532-534, doi:10.1785/gssrl.70.5.532.

Heit, B., Yuan, X., Bianchi, M., Sodoudi, F. & Kind, R., 2008. Crustal thickness estimation beneath the southern central Andes at 30°S and 36°S from S wave receiver function

analysis, *Geophys. J. Int.,* **174,** 249-254, doi:10.1111/j.1365-246X.2008.03780.x.

Henderson, L.J., Gordon, R.G. & Engebretson, D.C., 1984. Mesozoic aseismic ridges on the Farallon Plate and southward migration of shallow subduction during the Laramide Orogeny, *Tectonics,* **3,** 121-132, doi:10.1029/TC003i002p00121.

Husen, S., Kissling, E., Flueh, E. & Asch, G., 1999. Accurate hypocentre determination in the seismogenic zone of the subducting Nazca Plate in northern Chile using a combined on-/offshore network, *Geophys. J. Int.,* **138,** 687-701, doi:10.1046/j.1365-246x.1999.00893.x.

Husen, S., van Stiphout, T. & Kissling, E., 2010. Coupling between P- and S-wave velocities in earthquake location and seismic tomography, *in EGU General Assembly 2010*, pp. EGU2010-11896, Vienna.

Hyndman, R.D. & Peacock, S.M., 2003. Serpentinization of the forearc mantle, *Earth Planet. Sci. Lett.,* **212,** 417-432, doi:10.1016/S0012-821X(03)00263-2.

Jordan, T.E. & Allmendinger, R.W., 1986. The Sierras Pampeanas of Argentina; a modern analogue of Rocky Mountain foreland deformation, *Am. J. Sci.,* **286,** 737-764, doi:10.2475/ajs.286.10.737.

Jordan, T.E., Isacks, B., Ramos, V.A. & Allmendinger, R.W., 1983. Mountain building in the central Andes, *Episodes,* **6,** 20-26.

Kamiya, S.i. & Kobayashi, Y., 2000. Seismological evidence for the existence of serpentinized wedge mantle, *Geophys. Res. Lett.,* **27,** 819-822.

Kay, S.M. & Abbruzzi, J.M., 1996. Magmatic evidence for Neogene lithospheric evolution of the central Andean "flat-slab" between 30°S and 32°S, *Tectonophysics,* **259,** 15-28,

doi:10.1016/0040-1951(96)00032-7.

Kay, S.M. & Gordillo, C.E., 1994. Pocho volcanic rocks and the melting of depleted continental lithosphere above a shallowly dipping subduction zone in the central Andes, *Contrib. Mineral. Petrol.,* **117,** 25-44, doi:10.1007/bf00307727.

Kay, S.M., Maksaev, V., Moscoso, R., Mpodozis, C., Nasi, C. & Gordillo, C.E., 1988. Tertiary andean magmatism in Chile and Argentina between 28°S and 33°S: Correlation of magmatic chemistry with a changing Benioff zone, *J. South Am. Earth Sci.,* **1,** 21-38, doi:10.1016/0895-9811(88)90013-2|.

Kendrick, E., Bevis, M., Smalley, R., Jr., Brooks, B., Vargas, R.B., Lauría, E. & Fortes, L.P.S., 2003. The Nazca-South America Euler vector and its rate of change, *J. South Am. Earth Sci.,* **16,** 125-131, doi:10.1016/S0895-9811(03)00028-2.

Kirby, S., Engdahl, E.R. & Denlinger, R., 1996. Intermediate-depth intraslab earthquakes and arc volcanism as physical expressions of crustal and uppermost mantle metamorphism in subducting slabs (Overview), *in Subduction from Top to Bottom*, pp. 195-215, eds. Bebout, G. E., Scholl, D. W., Kirby, S. H. & Platt, J. P., American Geophysical Union Geophysical Monograph.

Kissling, E., 1988. Geotomography with local earthquake data, *Rev. Geophys.,* **26,** 659-698.

Kissling, E., Ellsworth, W.L., Eberhart-Phillips, D. & Kradolfer, U., 1994. Initial reference models in local earthquake tomography, *J. Geophys. Res.,* **99,** 19635-19646, doi:10.1029/93jb03138.

Kissling, E., Kradolfer, U. & Maurer, H., 1995.*VELEST User's Guide-short Introduction*, Institute of Geophysics & Swiss Seismological Service ETH Zurich.

Kopp, H., Flueh, E.R., Papenberg, C. & Klaeschen, D., 2004. Seismic investigations of the O'Higgins Seamount Group and Juan Fernandez Ridge: Aseismic ridge emplacement and lithosphere hydration, *Tectonics,* **23,** TC2009, doi:10.1029/2003tc001590.

Koulakov, I., Sobolev, S.V. & Asch, G., 2006. *P*- and *S*-velocity images of the lithosphere–asthenosphere system in the Central Andes from local-source tomographic inversion, *Geophys. J. Int.,* **167,** 106-126, doi:10.1111/j.1365-246X.2006.02949.x.

Leal, P.R., Hartmann, L.A., Santos, J.O.S., Miró, R.C. & Ramos, V.A., 2003. Volcanismo postorogénico en el extremo norte de las Sierras Pampeanas Orientales: Nuevos datos geocronológicos y sus implicancias tectónicas, *Rev. Asoc. Geol. Argent.,* **58,** 593-607.

Lienert, B.R. & Havskov, J., 1995. A Computer Program for Locating Earthquakes Both Locally and Globally, *Seis. Res. Lett.,* **66,** 26-36, doi:10.1785/gssrl.66.5.26.

Lin, G., Thurber, C.H., Zhang, H., Hauksson, E., Shearer, P.M., Waldhauser, F., Brocher, T.M. & Hardebeck, J., 2010. A California Statewide Three-Dimensional Seismic Velocity Model from Both Absolute and Differential Times, *Bull. Seismol. Soc. Am.,* **100,** 225-240, doi:10.1785/0120090028.

Martinod, J., Husson, L., Roperch, P., Guillaume, B. & Espurt, N., 2010. Horizontal subduction zones, convergence velocity and the building of the Andes, *Earth Planet. Sci. Lett.,* **299,** 299-309, doi:10.1016/j.epsl.2010.09.010.

McGeary, S., Nur, A. & Ben-Avraham, Z., 1985. Spatial gaps in arc volcanism: The effect of collision or subduction of oceanic plateaus, *Tectonophysics,* **119,** 195-221, doi:10.1016/0040-1951(85)90039-3.

Mulcahy, S.R., Roeske, S.M., McClelland, W.C., Nomade, S.b. & Renne, P.R., 2007.

Cambrian initiation of the Las Pirquitas thrust of the western Sierras Pampeanas, Argentina: Implications for the tectonic evolution of the proto-Andean margin of South America, *Geology,* **35,** 443-446, doi:10.1130/G23436A.1.

Norabuena, E.O., Dixon, T.H., Stein, S. & Harrison, C.G.A., 1999. Decelerating Nazca-South America and Nazca-Pacific Plate motions, *Geophys. Res. Lett.,* **26,** 3405-3408, doi:10.1029/1999gl005394.

Ottemöller, L., Voss, P. & Havskov, J., 2011.*SEISAN: the Earthquake Analysis Software for Windows, Solaris, LINUX, and MACOSX, version 9.0.1*, University of Bergen, pp. 361.

Pankhurst, R.J., Rapela, C.W., Saavedra, J., Baldo, E., Dahlquist, J., Pascua, I. & Fanning, C.M., 1998. The Famatinian magmatic arc in the central Sierras Pampeanas; an Early to Mid-Ordovician continental arc on the Gondwana margin (in The proto-Andean margin of Gondwana), *Geol. Soc. Spec. Publ.,* **142,** 343-367.

Pardo, M., Comte, D. & Monfret, T., 2002a. Seismotectonic and stress distribution in the central Chile subduction zone, *J. South Am. Earth Sci.,* **15,** 11-22, doi:doi: 10.1016/S0895-9811(02)00003-2.

Pardo, M., Monfret, T., Vera, E., Eisenberg, A., Gaffet, S., Lorca, E. & Perez, A., 2002b. Seismotectonic and Body-wave Tomography of Central Chile-NW Argentina Flat-slab Subduction Zone Using Local Earthquakes, *in EGS XXVII General Assembly*, Nice.

Peacock, S.M., 1993. Large-scale hydration of the lithosphere above subducting slabs, *Chem. Geol.,* **108,** 49-59.

Peacock, S.M., 2001. Are the lower planes of double seismic zones caused by serpentine dehydration in subducting oceanic mantle?, *Geology,* **29,** 299-a-302, doi:10.1130/0091-

7613(2001)029<0299:ATLPOD>2.0.CO;2.

Pilger, R.H.J., 1981. Plate reconstructions, aseismic ridges, and low-angle subduction beneath the Andes, *Geol. Soc. Am. Bull.,* **92,** 448-456, doi:10.1130/0016-7606(1981)92<448:PRARAL>2.0.CO;2.

Pujol, J., Chiu, J.M., Smalley, R., Jr., Regnier, M., Isacks, B., Chatelain, J.L., Vlasity, J., Vlasity, D., Castano, J. & Puebla, N., 1991. Lateral velocity variations in the Andean foreland in Argentina determined with the JHD method, *Bull. Seismol. Soc. Am.,* **81,** 2441-2457.

Ramos, V.A., 2004. Cuyania, an Exotic Block to Gondwana: Review of a Historical Success and the Present Problems, *Gondwana Res.,* **7,** 1009-1026, doi:10.1016/S1342-937X(05)71081-9.

Ramos, V.A., Cegarra, M. & Cristallini, E.O., 1996. Cenozoic tectonics of the High Andes ofwest-central Argentina (30–36◦S latitude), *Tectonophysics,* **259,** 185-200.

Ramos, V.A., Cristallini, E.O. & Pérez, D.J., 2002. The Pampean flat-slab of the Central Andes, *J. South Am. Earth Sci.,* **15,** 59-78, doi:10.1016/S0895-9811(02)00006-8.

Ramos, V.A., Jordan, T.E., Allmendinger, R.W., Mpodozis, C., Kay, S.M., Cortés, J.M. & Palma, M., 1986. Paleozoic terranes of the central Argentine-Chilean Andes, *Tectonics,* **5,** 855-880, doi:10.1029/TC005i006p00855.

Ranero, C.R., Villaseñor, A., Phipps Morgan, J. & Weinrebe, W., 2005. Relationship between bend-faulting at trenches and intermediate-depth seismicity, *Geochem., Geophys., Geosyst.,* **6,** Q12002, doi:10.1029/2005gc000997.

Rapela, C.W., Pankhurst, R.J., Casquet, C., Baldo, E., Saavedra, J. & Galindo, C., 1998. Early

evolution of the Proto-Andean margin of South America, *Geology,* **26,** 707-710, doi:10.1130/0091-7613(1998)026<0707:EEOTPA>2.3.CO;2.

Rapela, C.W., Pankhurst, R.J., Casquet, C., Fanning, C.M., Baldo, E.G., González-Casado, J.M., Galindo, C. & Dahlquist, J., 2007. The Río de la Plata craton and the assembly of SW Gondwana, *Earth-Sci. Rev.,* **83,** 49-82, doi:10.1016/j.earscirev.2007.03.004.

Regnier, M., Chiu, J.-M., Smalley, R., Jr., Isacks, B.L. & Araujo, M., 1994. Crustal thickness variation in the Andean foreland, Argentina, from converted waves, *Bull. Seismol. Soc. Am.,* **84,** 1097-1111.

Rondenay, S.p., Abers, G.A. & van Keken, P.E., 2008. Seismic imaging of subduction zone metamorphism, *Geology,* **36,** 275-278, doi:10.1130/G24112A.1.

Schmeling, H., 1985. Numerical models on the influence of partial melt on elastic, anelastic and electric properties of rocks. Part I: elasticity and anelasticity, *Phys. Earth Planet. Inter.,* **41,** 34-57, doi:10.1016/0031-9201(85)90100-1.

Scholz, C.H. & Small, C., 1997. The effect of seamount subduction on seismic coupling, *Geology,* **25,** 487-490, doi:10.1130/0091-7613(1997)025<0487:TEOSSO>2.3.CO;2.

Smalley, R., Jr. & Isacks, B.L., 1987. A High-Resolution Local Network Study of the Nazca Plate Wadati-Benioff Zone Under Western Argentina, *J. Geophys. Res.,* **92,** 13903-13912.

Smalley, R., Jr., Pujol, J., Regnier, M., Chiu, J.-M., Chatelain, J.-L., Isacks, B.L., Araujo, M. & Puebla, N., 1993. Basement seismicity beneath the Andean precordillera thin-skinned thrust belt and implications for crustal and lithospheric behavior, *Tectonics,* **12,** 63-76, doi:10.1029/92tc01108.

Thompson, A.B., 1992. Water in the Earth's upper mantle, *Nature,* **358,** 295-302, doi:10.1038/358295a0.

Thurber, C. & Eberhart-Phillips, D., 1999. Local earthquake tomography with flexible gridding, *Computers & Geosciences,* **25,** 809-818, doi:10.1016/S0098-3004(99)00007-2.

Thurber, C., Zhang, H., Brocher, T. & Langenheim, V., 2009. Regional three-dimensional seismic velocity model of the crust and uppermost mantle of northern California, *J. Geophys. Res.,* **114,** B01304, doi:10.1029/2008jb005766.

Thurber, C.H., 1992. Hypocenter-velocity structure coupling in local earthquake tomography, *Phys. Earth Planet. Inter.,* **75,** 55-62, doi:10.1016/0031-9201(92)90117-E.

Ulmer, P. & Trommsdorff, V., 1995. Serpentine Stability to Mantle Depths and Subduction-Related Magmatism, *Science,* **268,** 858-861, doi:10.1126/science.268.5212.858.

Urbina, N.P., Sruoga, P. & Malvicini, L., 1997. Late Tertiary Gold-Bearing Volcanic Belt in the Sierras Pampeanas of San Luis, Argentina, *Int. Geol. Rev.,* **39,** 287-306, doi:10.1080/00206819709465272.

van Hunen, J., van den Berg, A.P. & Vlaar, N.J., 2002. On the role of subducting oceanic plateaus in the development of shallow flat subduction, *Tectonophysics,* **352,** 317-333, doi:10.1016/S0040-1951(02)00263-9.

van Hunen, J., van den Berg, A.P. & Vlaar, N.J., 2004. Various mechanisms to induce present-day shallow flat subduction and implications for the younger Earth: a numerical parameter study, *Phys. Earth Planet. Inter.,* **146,** 179-194, doi:10.1016/j.pepi.2003.07.027.

von Gosen, W., 1998. Transpressive deformation in the southwestern part of the Sierra de San Luis (Sierras Pampeanas, Argentina), *J. South Am. Earth Sci.,* **11,** 233-264, doi:10.1016/S0895-9811(98)00013-3.

von Huene, R., Corvalán, J., Flueh, E.R., Hinz, K., Korstgard, J., Ranero, C.R., Weinrebe, W. & Condor Scientists, 1997. Tectonic control of the subducting Juan Fernandez Ridge on the Andean margin near Valparaiso, Chile, *Tectonics,* **16,** 474-488, doi:10.1029/96tc03703.

Vujovich, G., Miller, H. & Ramos, V.A., 1994. Proterozoic metavolcanics from western Sierras Pampeanas terrane, Argentina, *J. South Am. Earth Sci.,* **7,** 309-323, doi:10.1016/0895-9811(94)90017-5.

Wagner, L.S., Anderson, M.L., Jackson, J.M., Beck, S.L. & Zandt, G., 2008. Seismic evidence for orthopyroxene enrichment in the continental lithosphere, *Geology,* **36,** 935-938, doi:10.1130/G25108A.1.

Wagner, L.S., Beck, S. & Zandt, G., 2005. Upper mantle structure in the south central Chilean subduction zone (30° to 36°S), *J. Geophys. Res.,* **110,** B01308, doi:10.1029/2004jb003238.

Wagner, L.S., Beck, S., Zandt, G. & Ducea, M.N., 2006. Depleted lithosphere, cold, trapped asthenosphere, and frozen melt puddles above the flat slab in central Chile and Argentina, *Earth Planet. Sci. Lett.,* **245,** 289-301, doi:10.1016/j.epsl.2006.02.014.

Waldhauser, F. & Ellsworth, W.L., 2000. A Double-Difference Earthquake Location Algorithm: Method and Application to the Northern Hayward Fault, California, *Bull. Seismol. Soc. Am.,* **90,** 1353-1368, doi:10.1785/0120000006.

Wessel, P. & Smith, W.H.F., 1998. New, improved version of generic mapping tools released, *Eos Trans. Am. Geophys. Union,* **79,** 579.

Yáñez, G., Cembrano, J., Pardo, M., Ranero, C. & Selles, D., 2002. The Challenger-Juan Fernandez-Maipo major tectonic transition of the Nazca-Andean subduction system at 33-34°S: geodynamic evidence and implications, *J. South Am. Earth Sci.,* **15,** 23-38, doi:10.1016/S0895-9811(02)00004-4.

Yáñez, G.A., Ranero, C.R., von Huene, R. & Díaz, J., 2001. Magnetic anomaly interpretation across the southern central Andes (32°-34°S): The role of the Juan Fernandez Ridge in the late Tertiary evolution of the margin, *J. Geophys. Res.,* **106,** 6325-6345, doi:10.1029/2000jb900337.

Zhang, H. & Thurber, C., 2006. Development and Applications of Double-difference Seismic Tomography, *Pure Appl. Geophys.,* **163,** 373-403-403, doi:10.1007/s00024-005-0021-y.

Zhang, H. & Thurber, C.H., 2007. Estimating the model resolution matrix for large seismic tomography problems based on Lanczos bidiagonalization with partial reorthogonalization, *Geophys. J. Int.,* **170,** 337-345, doi:10.1111/j.1365-246X.2007.03418.x.

Zhang, H., Thurber, C. & Bedrosian, P., 2009. Joint inversion for Vp, Vs, and Vp/Vs at SAFOD, Parkfield, California, *Geochem., Geophys., Geosyst.,* **10,** Q11002, doi:10.1029/2009gc002709.

Zhang, H., Thurber, C.H., Shelly, D., Ide, S., Beroza, G.C. & Hasegawa, A., 2004. High-resolution subducting-slab structure beneath northern Honshu, Japan, revealed by double-difference tomography, *Geology,* **32,** 361-364, doi:10.1130/G20261.2.

Zhao, D., Hasegawa, A. & Horiuchi, S., 1992. Tomographic Imaging of P and S Wave Velocity Structure Beneath Northeastern Japan, *J. Geophys. Res.,* **97,** 19909-19928, doi:10.1029/92jb00603.

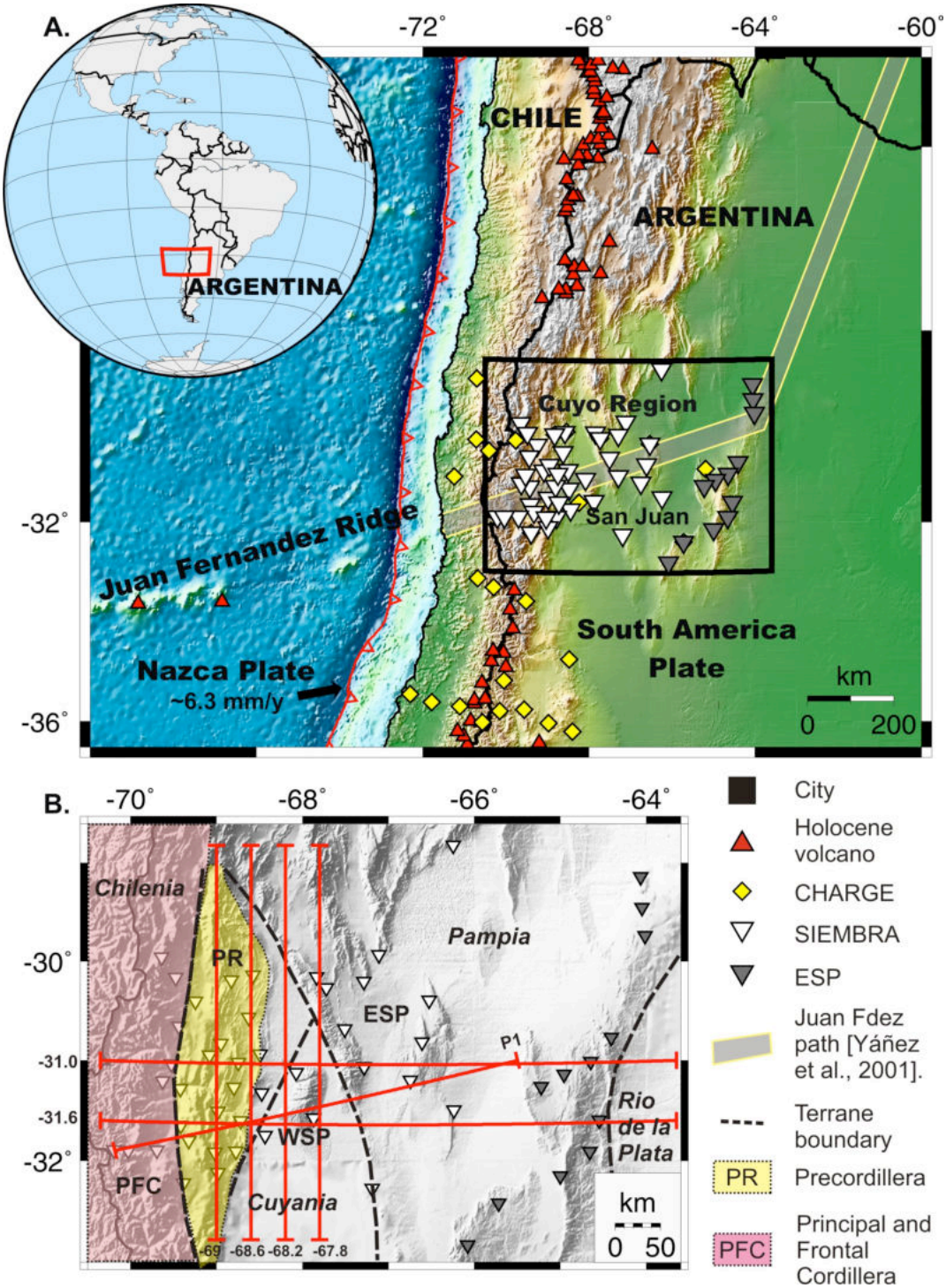

Figure 1. A. Location Map. Plate convergence velocity from Kendrick et al. [2003]. **B.** Morphotectonic units and terrane boundaries [Ramos et al., 2002; Rapela et al., 2007] and location of profiles shown in Figures 6, 7, and 8. ESP, Eastern Sierras Pampeanas; WSP, Western Sierras Pampeanas. P1, Profile 1.

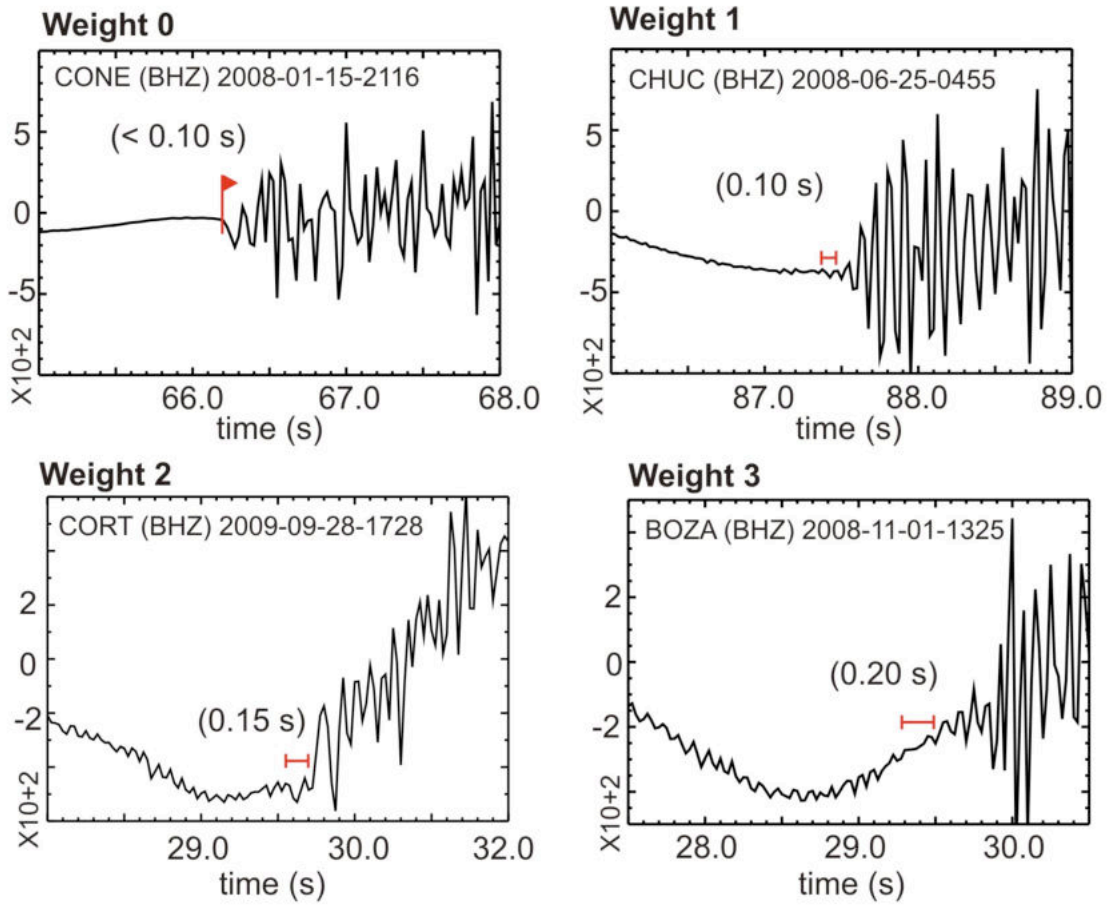

Figure 2. Example of unfiltered P-wave arrivals showing the weighing scheme used to describe the reading uncertainty.

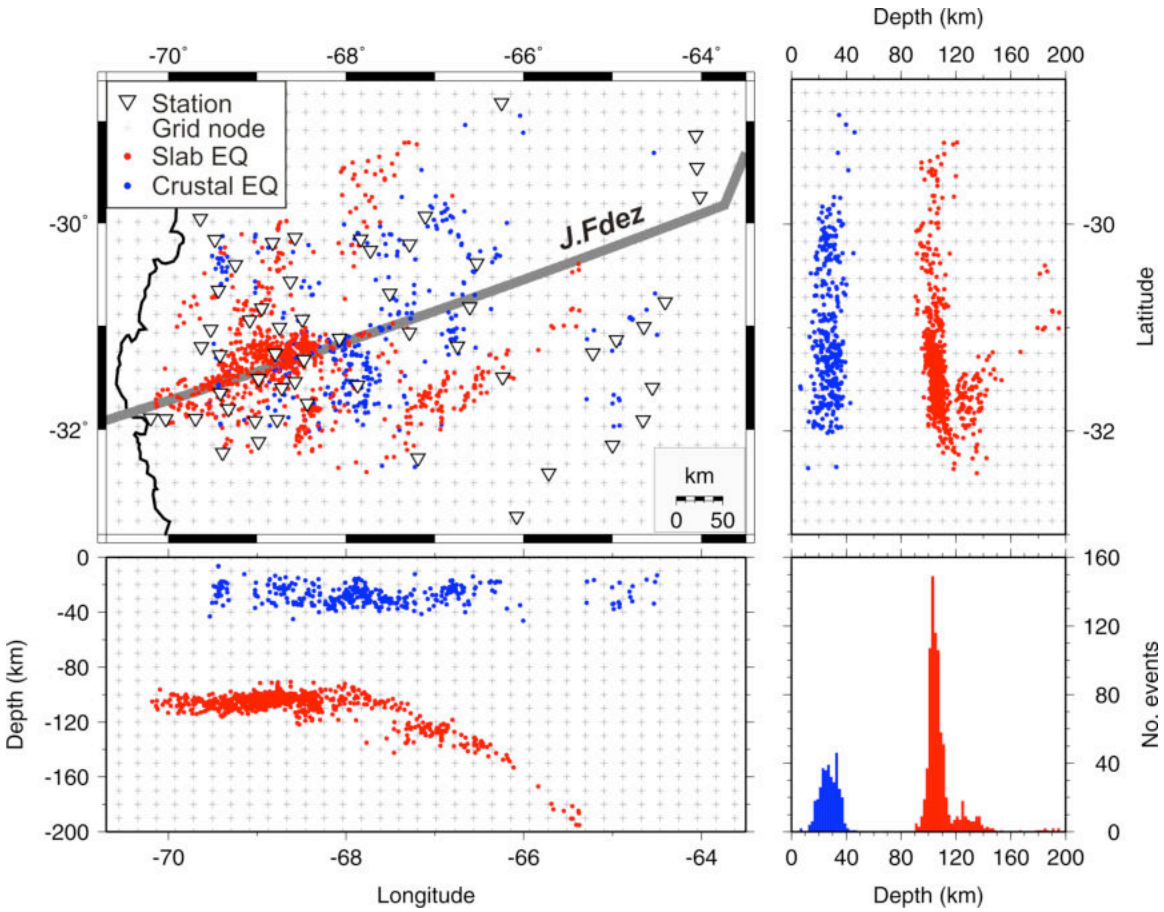

Figure 3. Distribution of the 1,157 earthquakes selected for the 1D and 3D inversions in map view and cross sections in E-W and N-S directions. Small gray crosses denote the grid nodes.

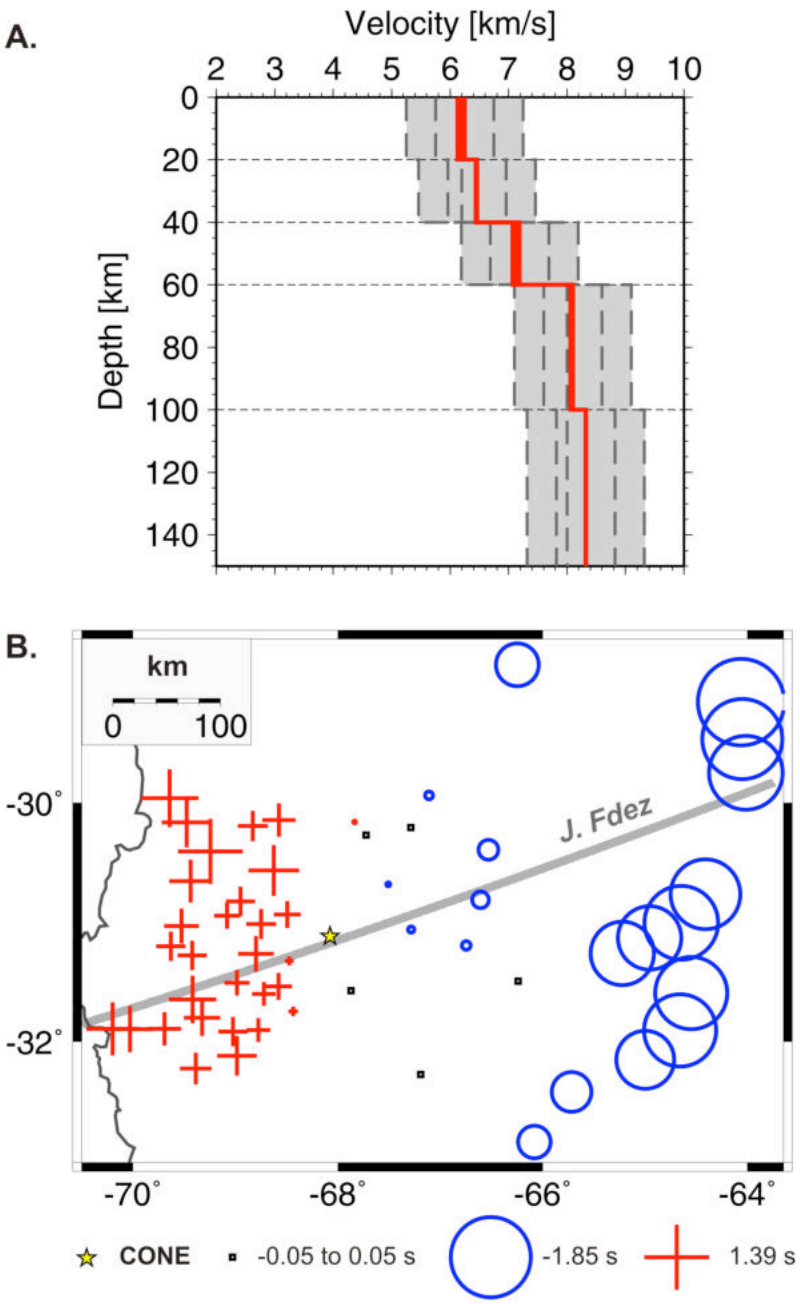

Figure 4. A. Initial (gray dashed) and final (red solid) Minimum P-wave 1D Model. Gray area shows the velocity space explored from initial velocities. All initial models converge into a Minimum 1D model (red). **B.** P-wave station corrections for the minimum 1 D model. The reference station CONE is marked by a yellow star and zero station corrections are indicated by squares. Crosses and circles denote positive and negative corrections, respectively and are scaled by the magnitude of the correction (Table 1). Maximum and minimum corrections are indicated below the map.

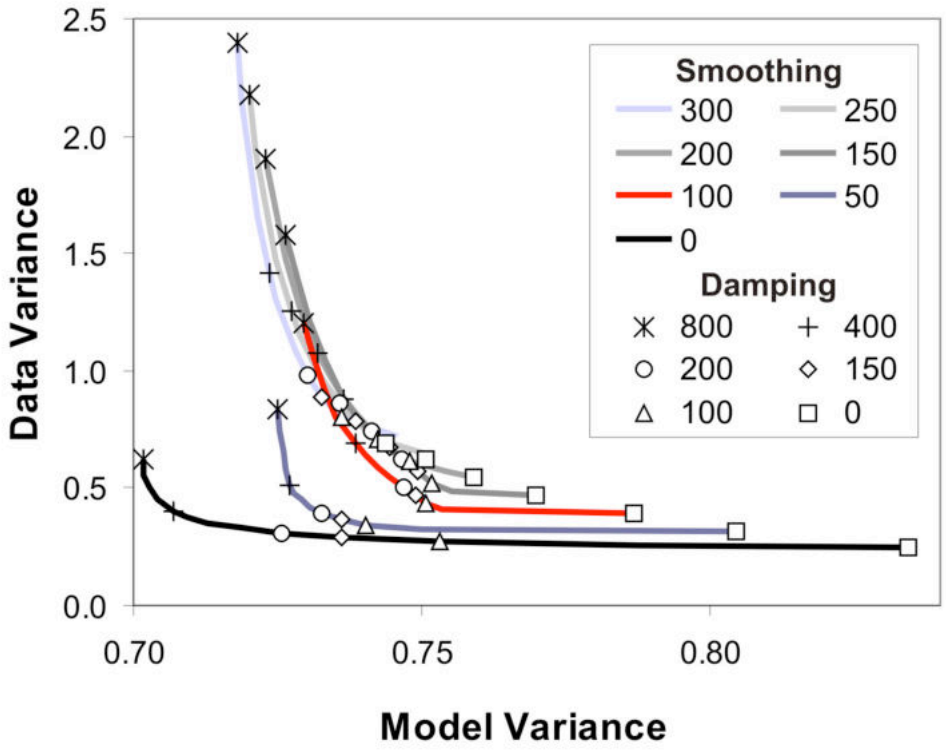

Figure 5. Trade-off curves between model variance and data variance for selecting damping and smoothing weight parameters. Each trade-off curve is indicated in a different color for a particular smoothing weight. Selected damping values are indicated by symbols. Our preferred smoothing value is 100 (red curve).

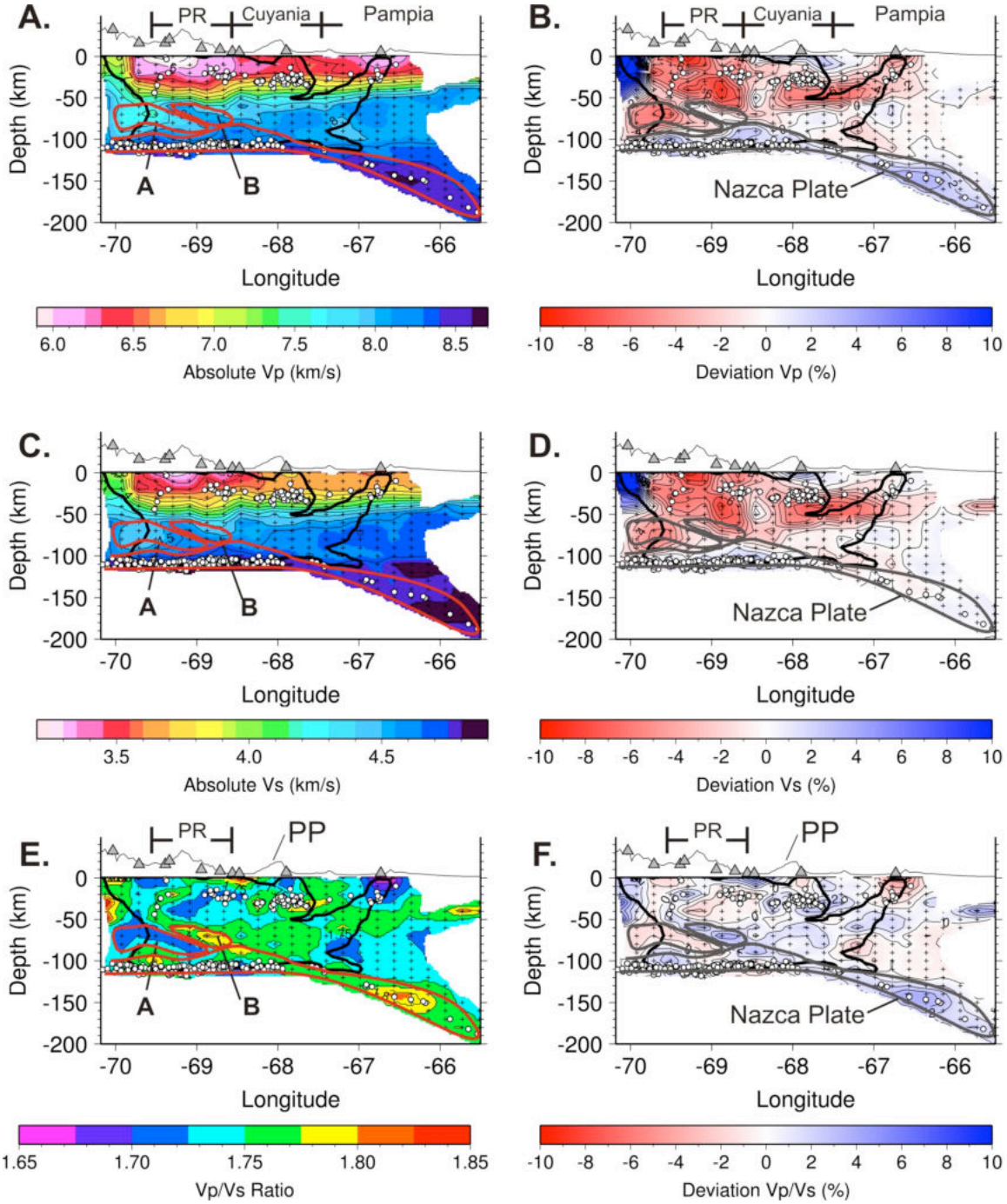

Figure 6. Vertical depth cross-section along Profile 1 (Fig 1b). **A.** Absolute P-wave velocity. **B.** P-wave velocity structure as a percentage change with respect to the P-wave initial model. **C.** Absolute S-wave velocity. **D.** S-wave velocity structure as a percentage change with respect to the initial S-wave model. **E.** Vp/Vs Ratio. **F.** Vp/Vs ratio structure as a percentage change with respect to the initial Vp/Vs model. We only show results for areas with DWS > 100. Back lines encompass regions with DWS > 2500 where we

recover checkerboard patterns in synthetic tests. Earthquakes (white circles) and stations (triangles) within 0.2 degree of the profile are plotted. Small crosses denote the grid nodes. Topography is exaggerated by a factor of 8. Marked anomalies are discussed in the test. PR, Precordillera, PP, Pie de Palo.

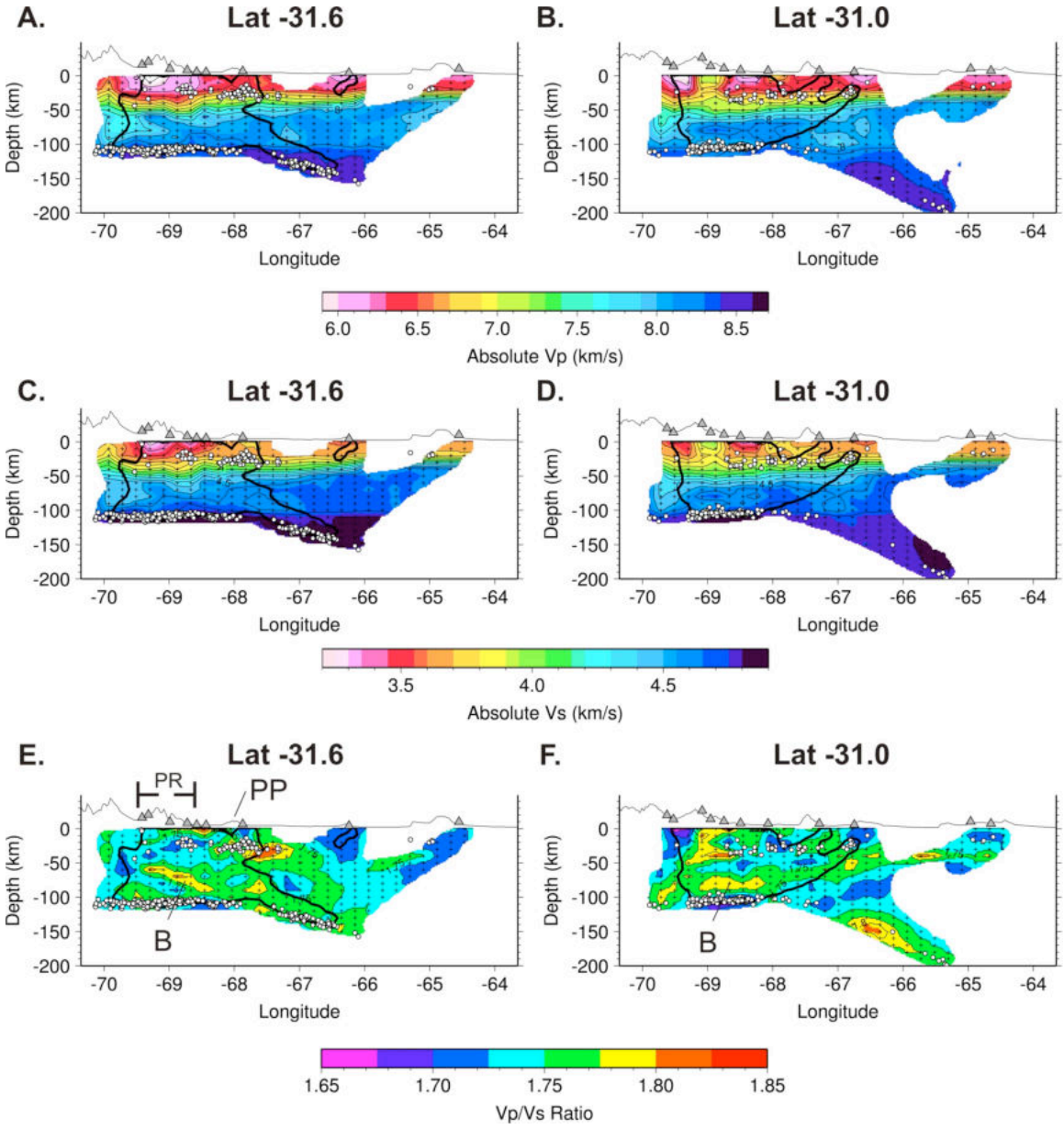

Figure 7. East-West cross sections through the absolute Vp, Vs, and Vp/Vs models. Latitude of each section is indicated. Location of profiles is indicated in Figure 1b. Other symbols as in Figure 6. PP, Pie de Palo.

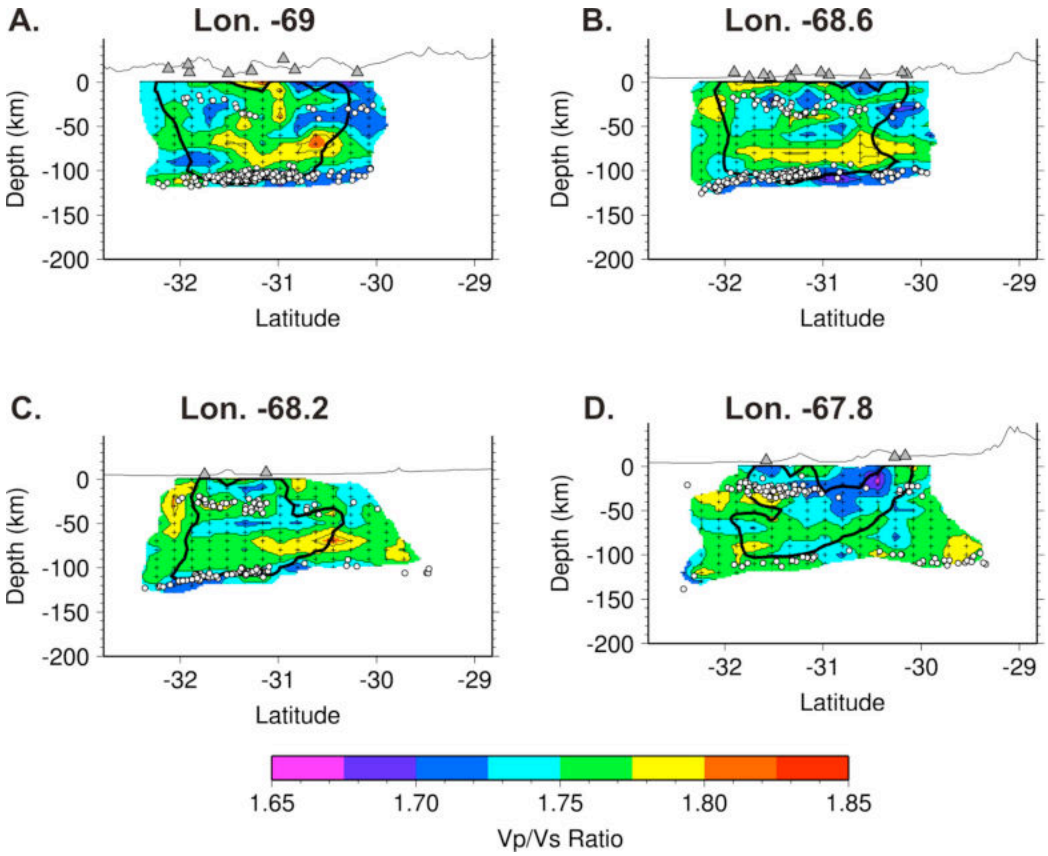

Figure 8. North-South cross sections through the Vp/Vs model. Longitude of each section is indicated above each plot and location of profiles is indicated in Figure 1b. Other symbols as in Figure 6.

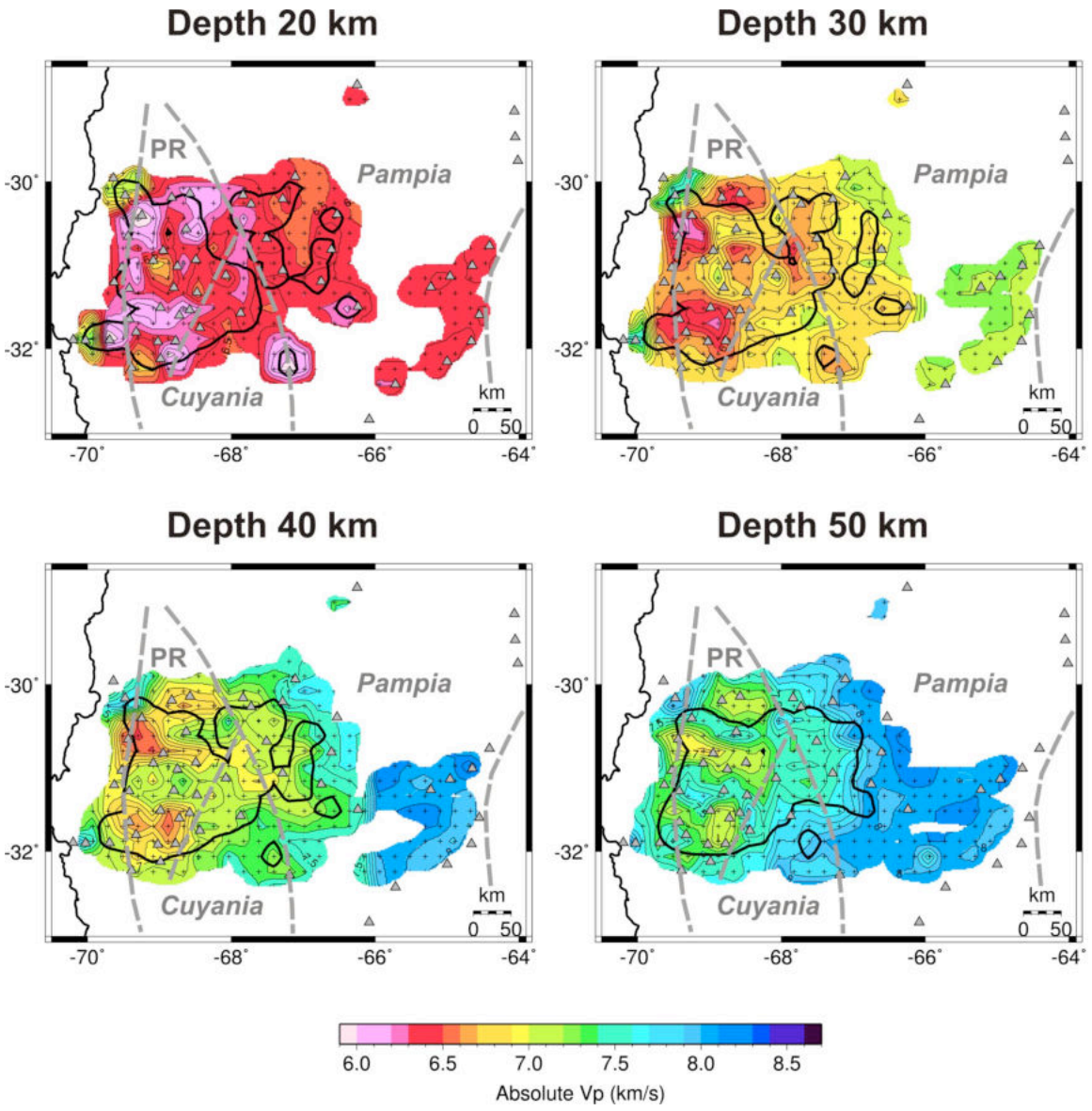

Figure 9. Slices at constant depth through the Vp model for the crust. Depth is indicated above each plot. Other symbols as in Figure 6. Terrane boundaries as in Figure 1.

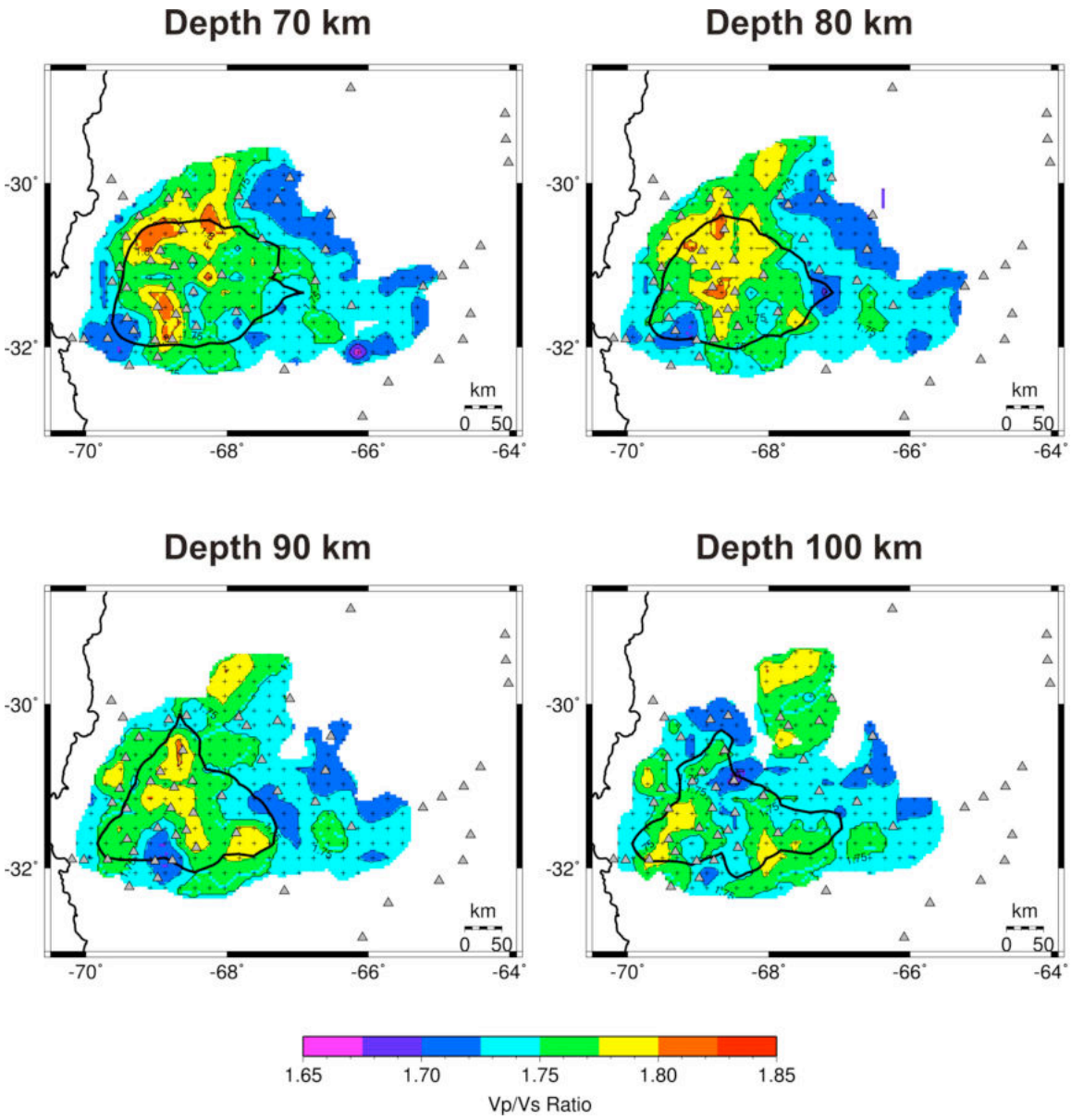

Figure 10. Slices at constant depth through the Vp/Vs model for the mantle. Depth is indicated above each plot. Other symbols as in Figure 6.

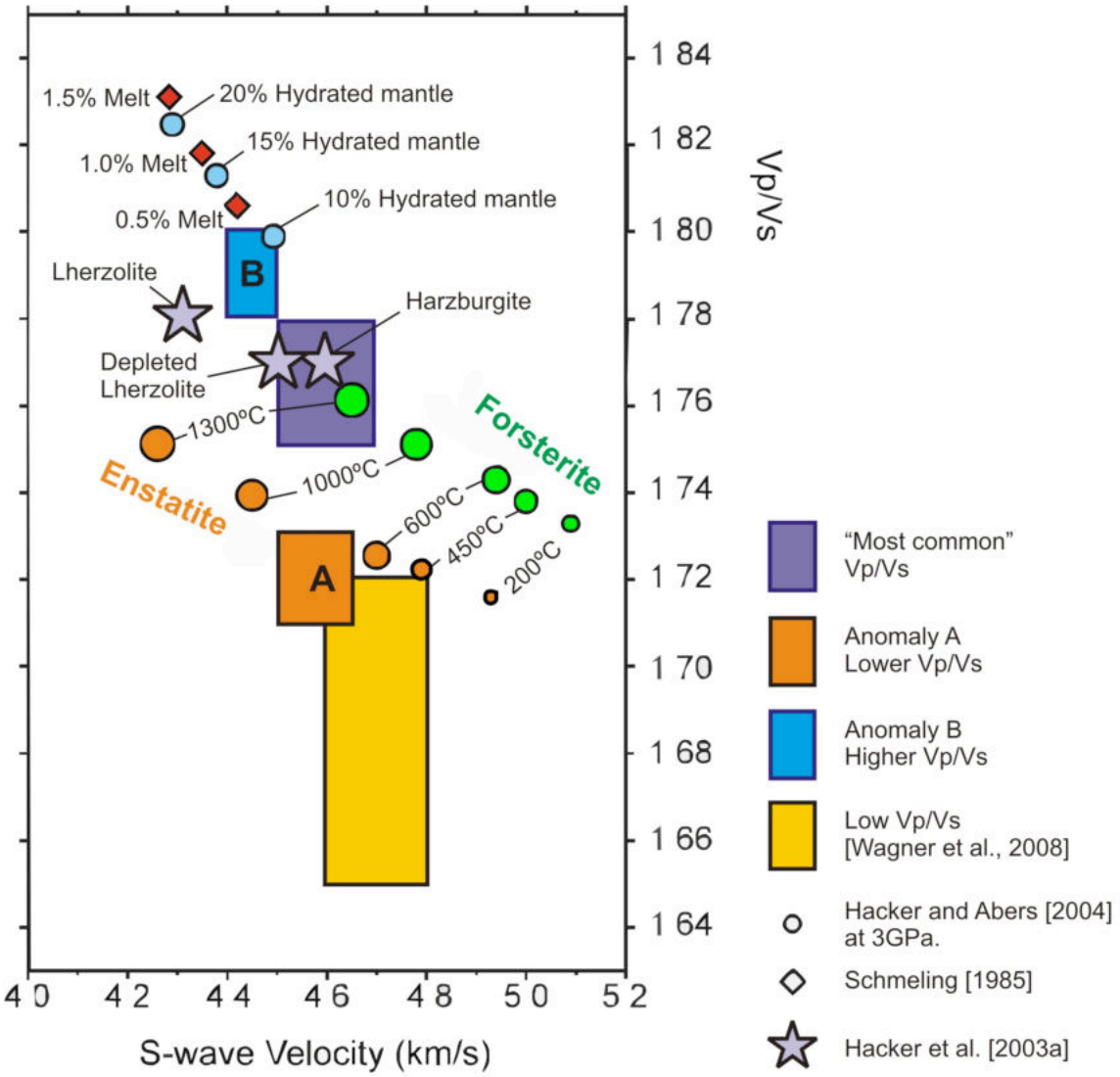

Figure 11. Predicted velocities for a range of possible mantle mineralogies and percent melts [modified from Wagner et al., 2006] and location of the low and high Vp/Vs anomalies observed in this study and the low Vp/Vs anomaly obtained by Wagner et al. [2008].

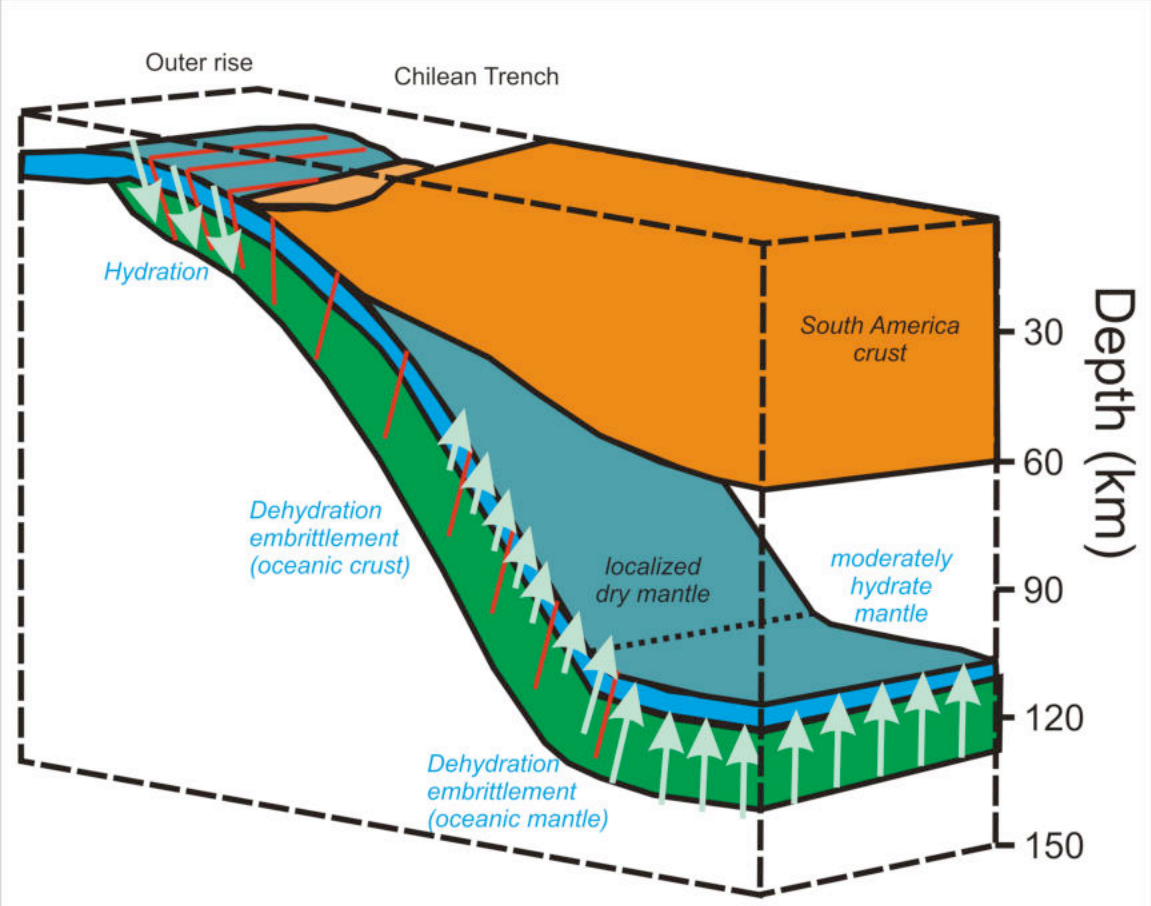

Figure 12. Conceptual model showing the interpretation of Vp/Vs anomalies in the upper mantle above the flat slab.

Table 1. Station Information

Station	Lat (S)	Lon (W)	Elev (m)	P correction (s)	Seismometer
ABRA	31.50	66.24	530	-0.56	STS-2
ARRO	30.41	69.25	1970	1.39	STS-2
BARR	31.65	69.42	1962	1.02	STS-2
BOZA	31.75	68.44	638	0.21	STS-2
CALI	31.28	69.42	1383	0.63	STS-2
CASP	31.21	69.63	2369	0.62	STS-2
CATA	32.27	67.19	647	0.01	Guralp CMG-3T
CHIL	31.91	68.78	1332	0.51	STS-2
CHUC	31.07	67.28	921	-0.13	STS-2
CHUM	28.82	66.25	642	-0.92	STS-2
CIGA	30.14	68.57	1095	0.71	STS-2
CLAR	32.12	68.98	1818	0.85	STS-2
COLO	29.94	67.11	685	-0.17	STS-2
CONE	31.12	68.07	913	0	STS-2
CORT	29.96	69.64	5051	1.23	STS-2
DOCA	30.95	69.08	3181	0.56	STS-2
GUAL	30.83	68.95	1672	0.62	STS-2
GUAR	31.89	70.20	4105	1.13	STS-2
LAJA	31.33	68.48	746	0.19	Guralp CMG-3T
LEON	31.80	69.32	2472	0.78	STS-2
LLAN	30.39	66.53	752	-0.43	Guralp CMG-3T
LUNA	30.16	67.84	1441	0.14	STS-2
MAJA	30.69	67.51	989	-0.08	STS-2
MALA	30.82	66.61	961	-0.36	STS-2
MONA	30.94	68.49	990	0.57	STS-2
NIKI	31.58	67.87	833	-0.05	STS-2
NOQE	31.20	66.75	695	-0.18	Trillium
NUEV	31.04	69.53	1658	0.74	Trillium
PACH	30.19	68.83	1324	0.64	STS-2
PAGA	30.21	67.29	944	0.03	STS-2
PATO	31.90	69.69	1970	0.71	STS-2
REGU	31.90	70.03	3886	0.99	STS-2
RINC	30.27	67.72	1286	-0.02	Trillium
SASO	31.51	68.98	1231	0.55	STS-2
SECA	31.27	68.80	1527	0.76	STS-2

SOMB	31.92	69.02	2397	0.63	STS-2
TALA	31.02	68.75	1317	0.65	STS-2
TOCO	30.66	69.44	2630	0.91	STS-2
TUCU	30.57	68.63	952	1.09	Trillium
USPA	32.22	69.39	2490	0.67	Guralp CMG-3T
VELA	30.17	69.48	2893	1.07	STS-2
ZOND	31.60	68.72	997	0.51	STS-2
UNSJ	31.54	68.58	676	0.57	STS-2
ESP01	29.14	64.06	215	-1.85	Guralp CMG-3T
ESP02	29.46	64.05	346	-1.71	Guralp CMG-3T
ESP03	29.74	64.01	648	-1.58	Guralp CMG-3T
ESP04	30.77	64.41	1192	-1.49	Guralp CMG-3T
ESP05	31.01	64.65	893	-1.57	Guralp CMG-3T
ESP06	31.14	64.96	1236	-1.36	Guralp CMG-3T
ESP07	31.27	65.22	1026	-1.35	Guralp CMG-3T
ESP08	31.60	64.55	1191	-1.54	Guralp CMG-3T
ESP09	31.91	64.66	1055	-1.54	Guralp CMG-3T
ESP10	32.15	65.00	1104	-1.24	Guralp CMG-3T
ESP11	32.42	65.72	1067	-0.84	Guralp CMG-3T
ESP12	32.83	66.08	1686	-0.69	Guralp CMG-3T

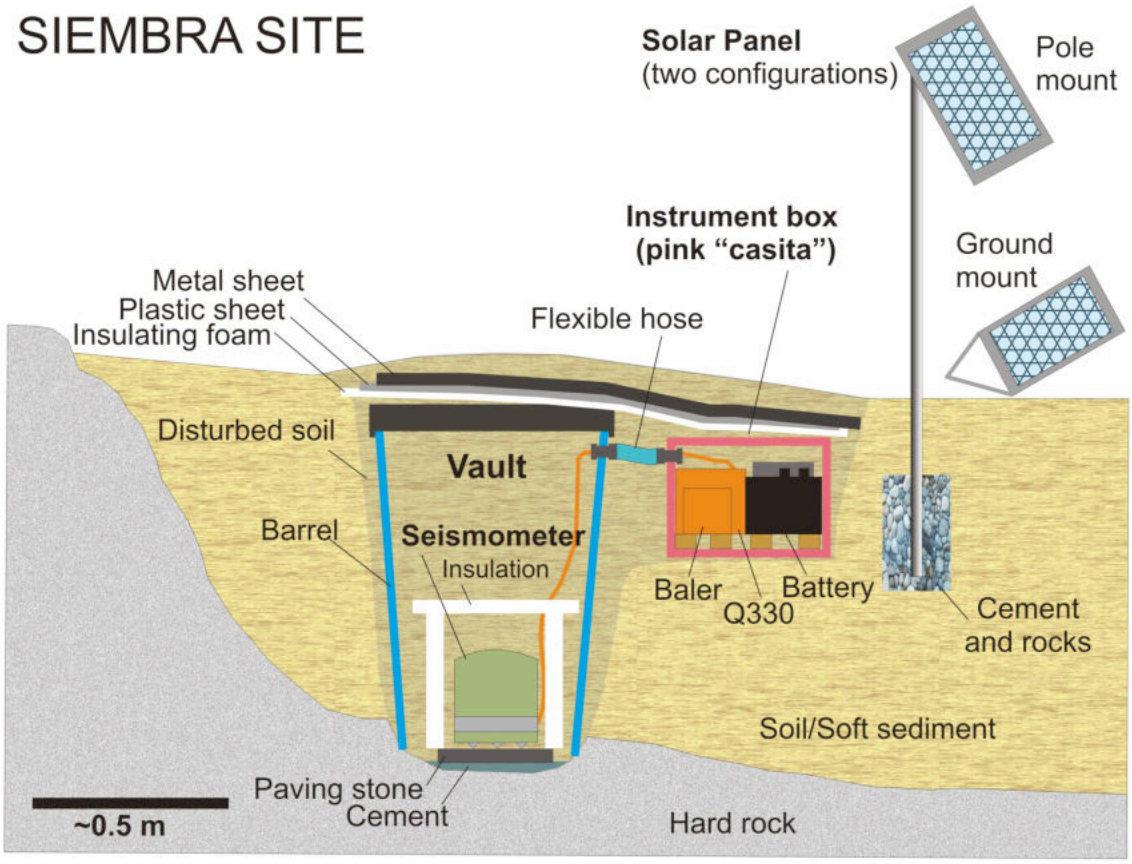

Figure S1. Vault design for SIEMBRA stations. We were careful to install our stations on hard rock whenever possible and avoided placing them in sedimentary basins. Hard rock sites were chosen to prevent basin reverberations caused by loose sediment. Two holes were dug, each large enough in diameter to hold the blue sensor barrel and the pink "casita" instrument box. The pink "casita" houses the digitizer, hard drive, power box, and battery. Each site was covered with a large plastic tarp and buried after installation to insulate from temperature variations.

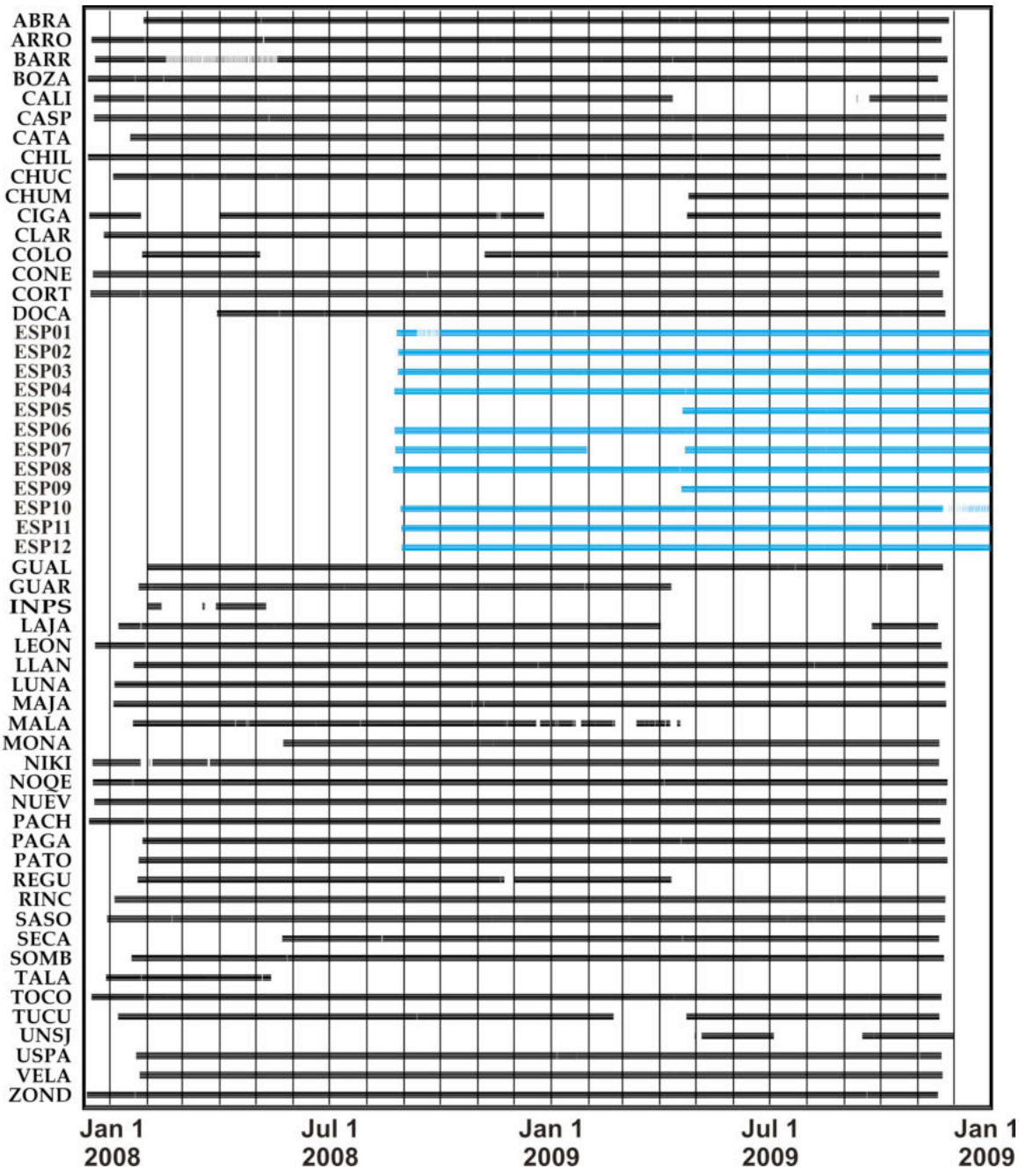

Figure S2. The effective recording periods for SIEMBRA and ESP stations. Black bars denote days of effective recording for the SIEMBRA stations while blue bars mark periods for ESP stations. The ESP network operated until August 2010 but in this study we used data from August 2008 to December 2009.

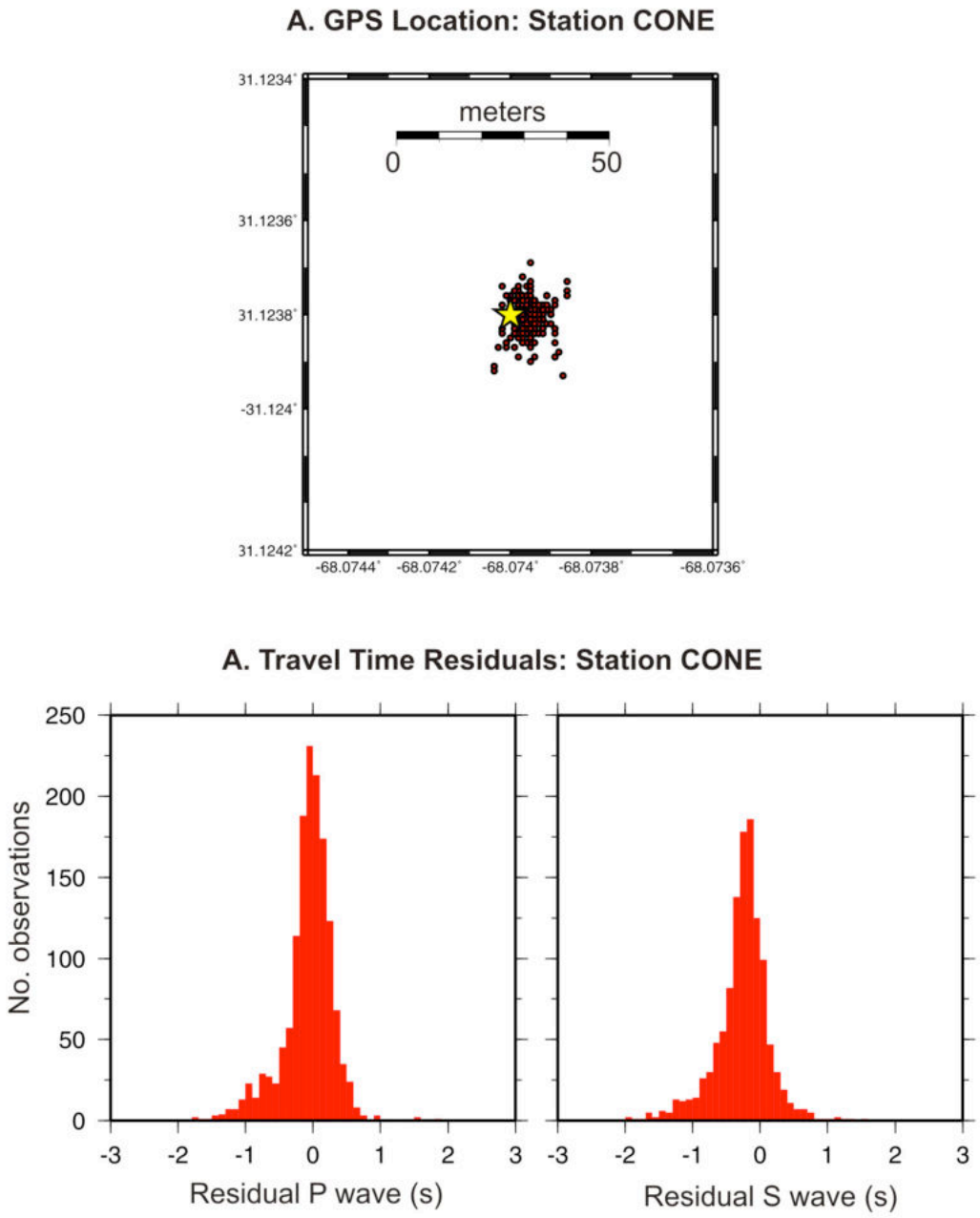

Figure S3. Example of exercises carried out to check the station performance. **A.** Example of plotting all GPS positions from LOG files for the reference station CONE. The star denotes de average location. **B.** Example of travel time residuals calculated for P and S waves using preliminary velocity model based on Smalley et al. [1993. As expected all stations display a Gaussian distribution.

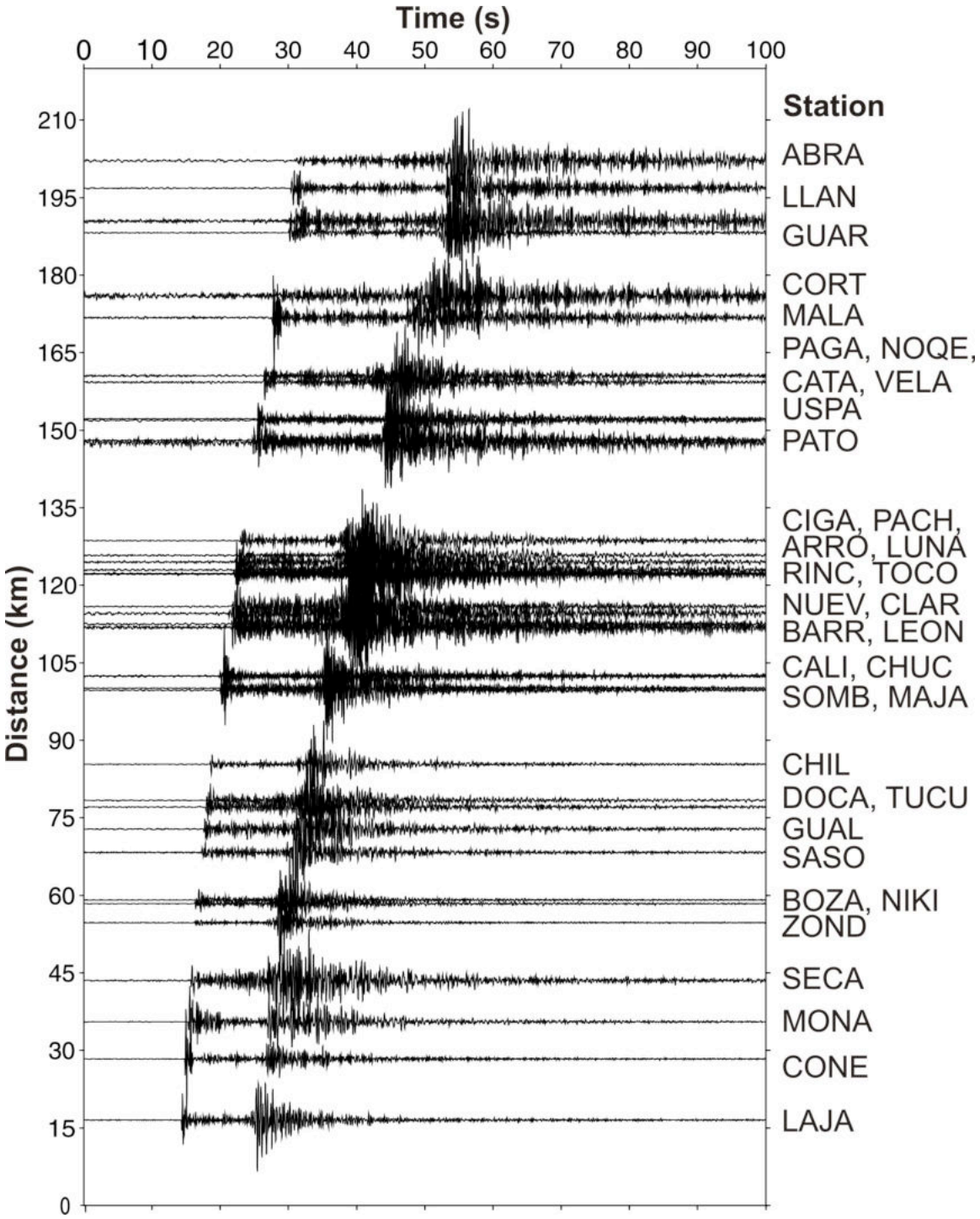

Figure S4. Example of a small earthquake (ML 2.3, May 26, 2008) recorded throughout the SIEMBRA network.

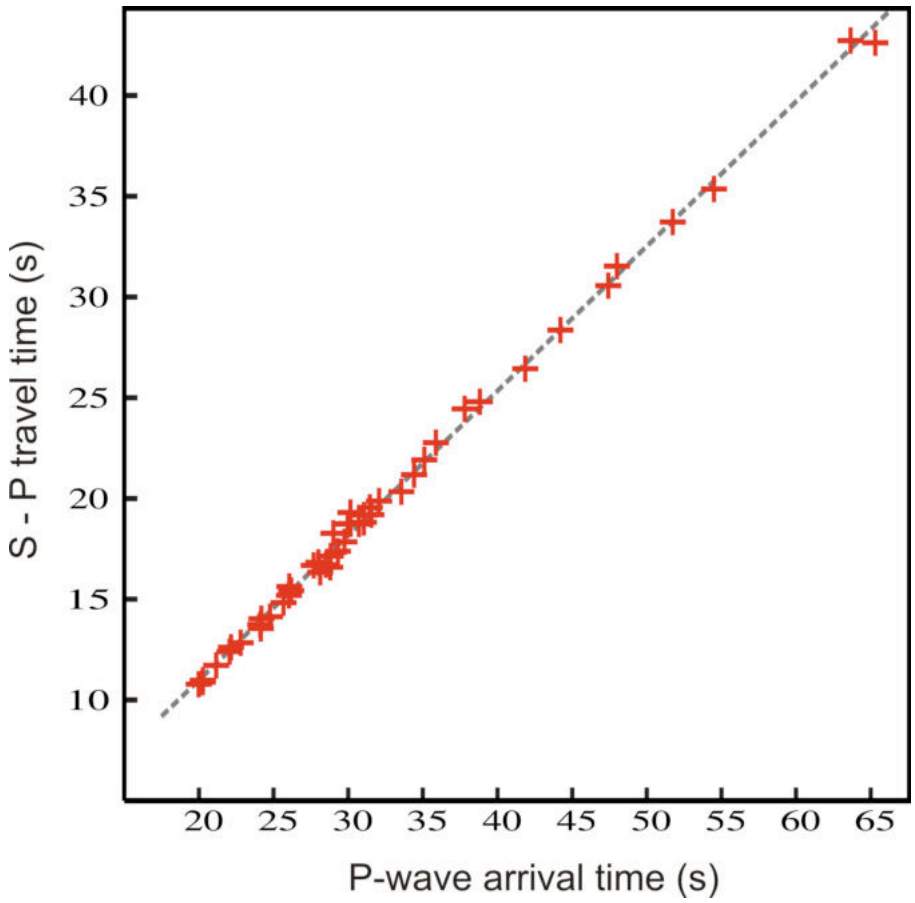

Figure S5. Example of a Wadati Diagram for a small slab earthquake (ML 2.3, August 31, 2008) with 43 P- and S- wave observations. Wadati diagrams were plotted for each event to identify pick outliers lying far off the main trend. A Wadati diagram is the simplest method to determine an average Vp/Vs ratio, which in this example is 1.72. In addition, Wadati diagrams were used to calculate a regional average Vp/Vs ratio, used as a starting Vp/Vs ratio in the tomography (1.74).

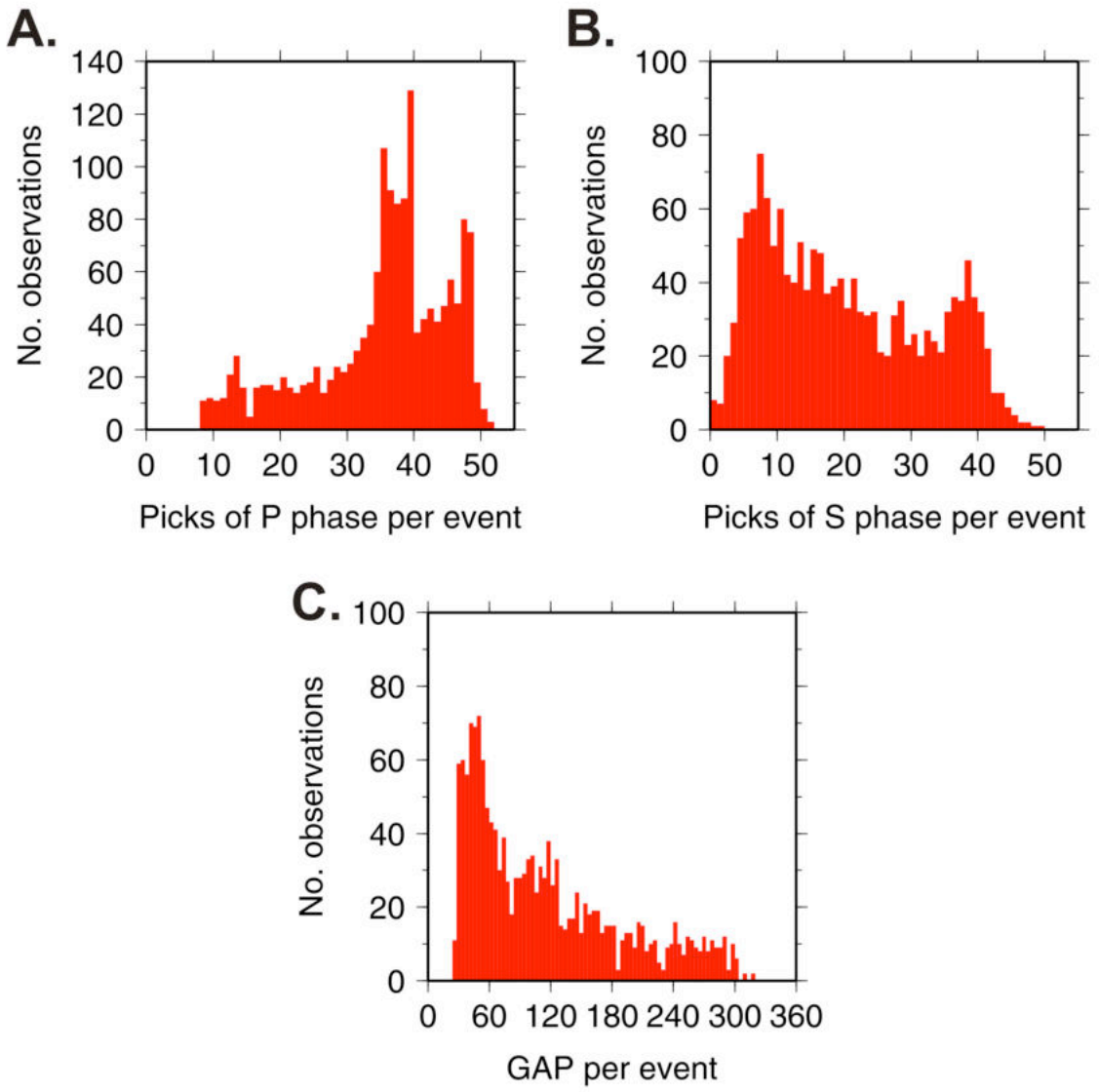

Figure S6. Phase observation and GAP distribution for 1,562 earthquakes recorded by the SIEMBRA and ESP networks **A.** Number of P-observations per event **B.** S-observations per **C.** GAP distribution per event.

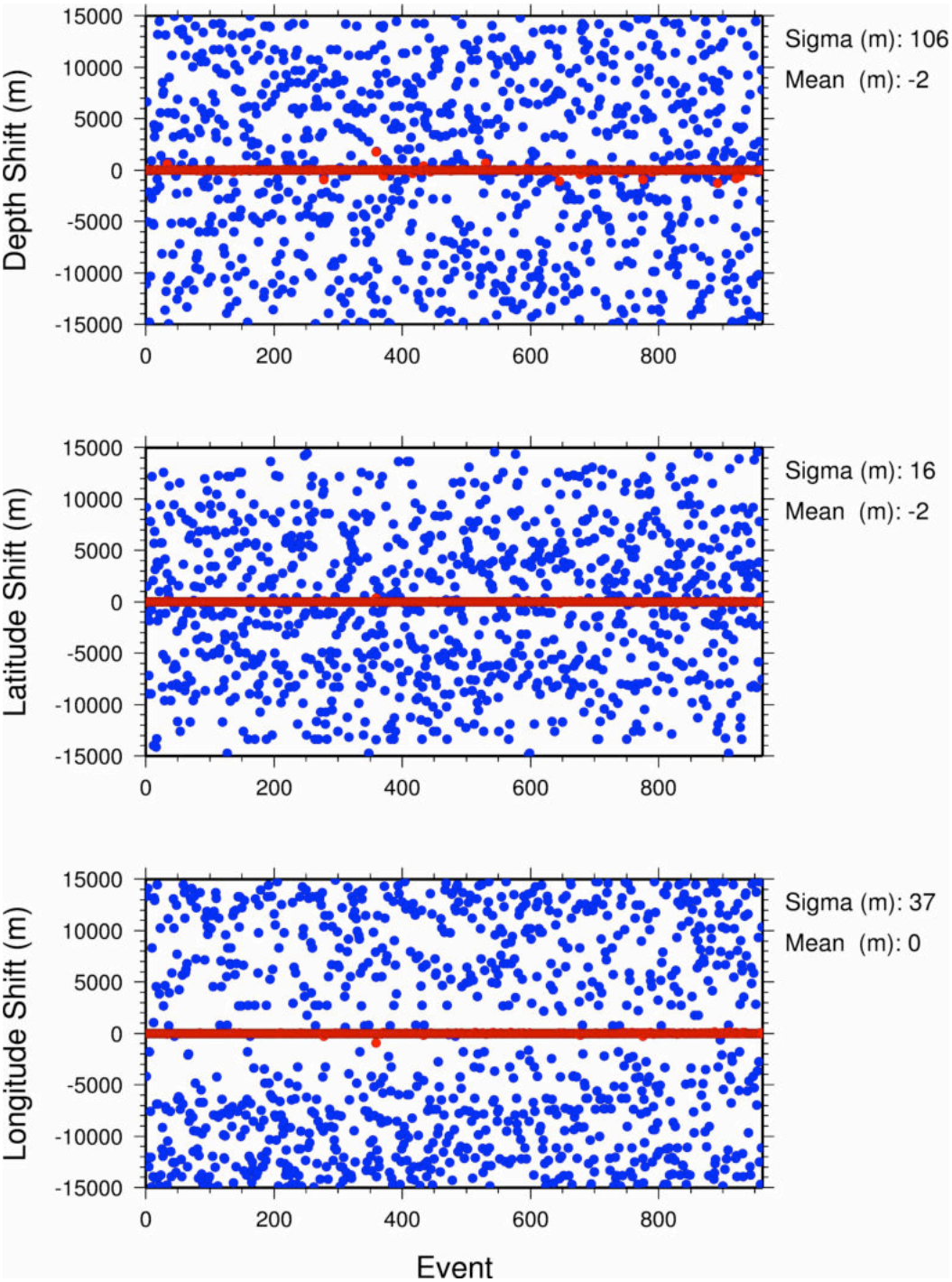

Figure S7. Stability test for the Minimum 1D model showing the difference in focal depth, latitude, and longitude between the original hypocenters and the hypocenters that are randomly shifted by 15 km before (blue) and after (red) the 1D inversion. All hypocenters are relocated to their original position demonstrating that no bias is present.

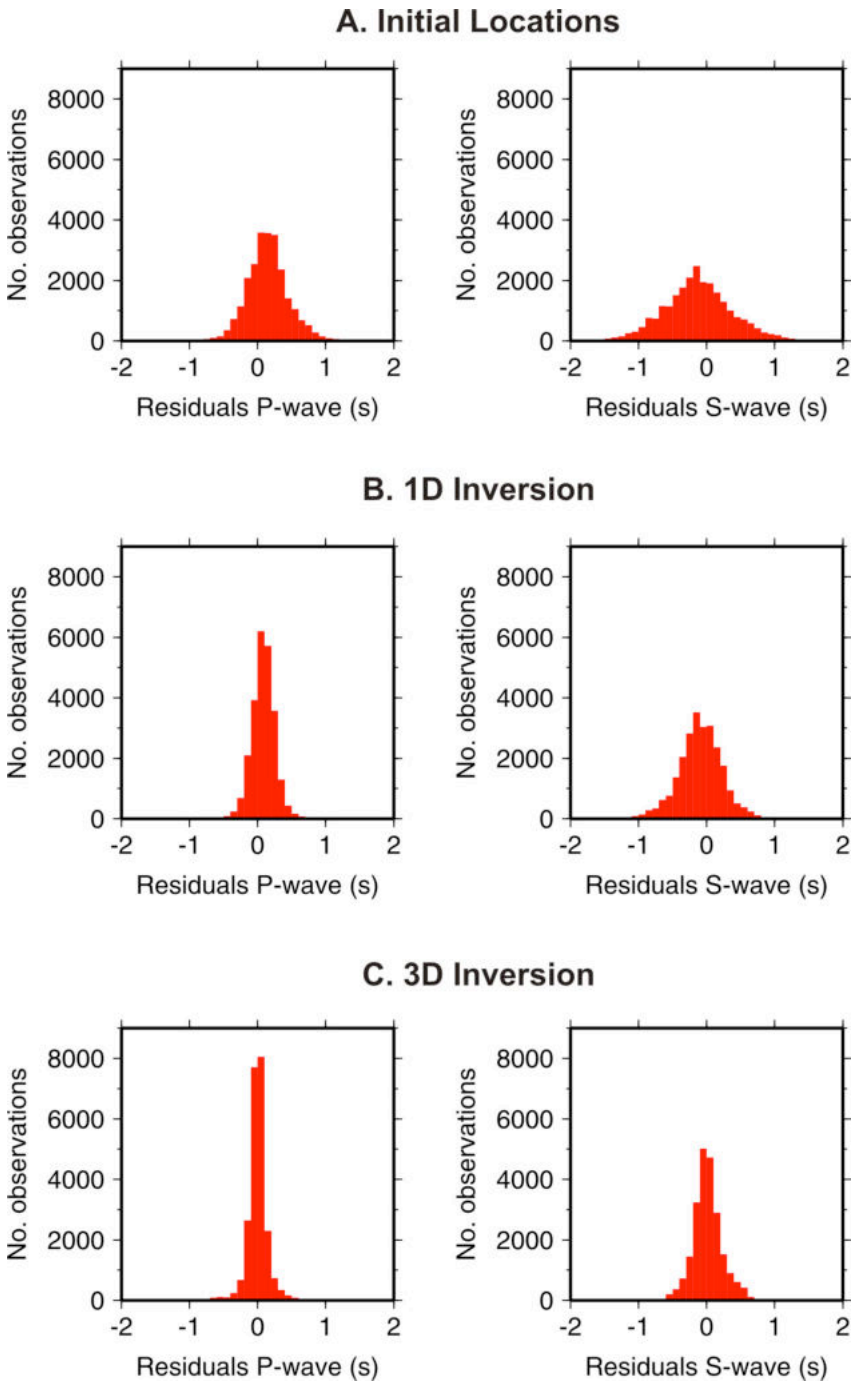

Figure S8. Residual misfit improvement for the 1,092 earthquakes used in the tomography inversion. **A.** Initial locations. **B.** After 1D inversion. **C.** After 3D inversion.

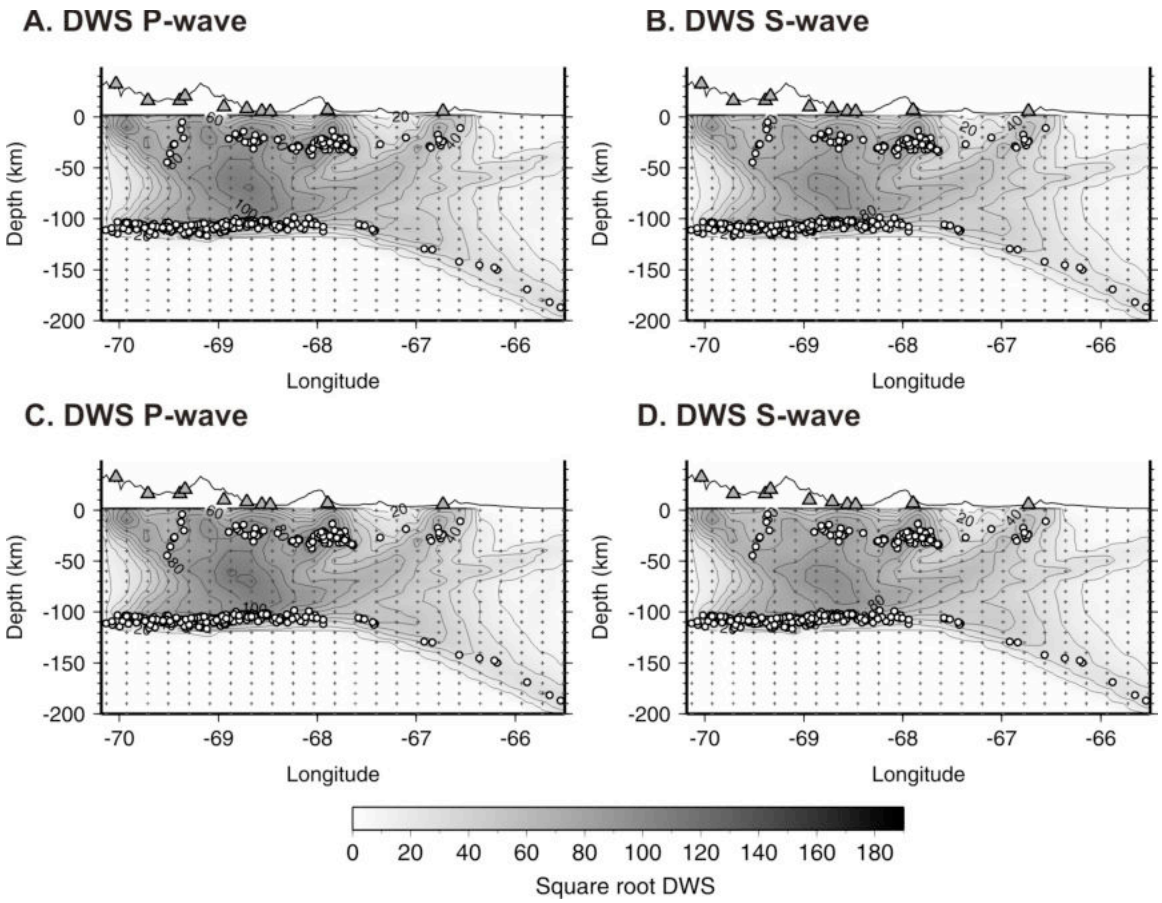

Figure S9. The square root of the DWS along Profile 1 (Fig 1b). **A.** DWS for P waves when differential times are constructed by using the event pairs with the inter-event distance < 10 km. **B.** Same as **A** but for S-waves. **C.** DWS for P waves when inter-event distance < 20 km. **D.** Same as **C** but for S waves. The DWS contours are very similar for both cases indicating that the inversion using either distance cutoff will give similar results.

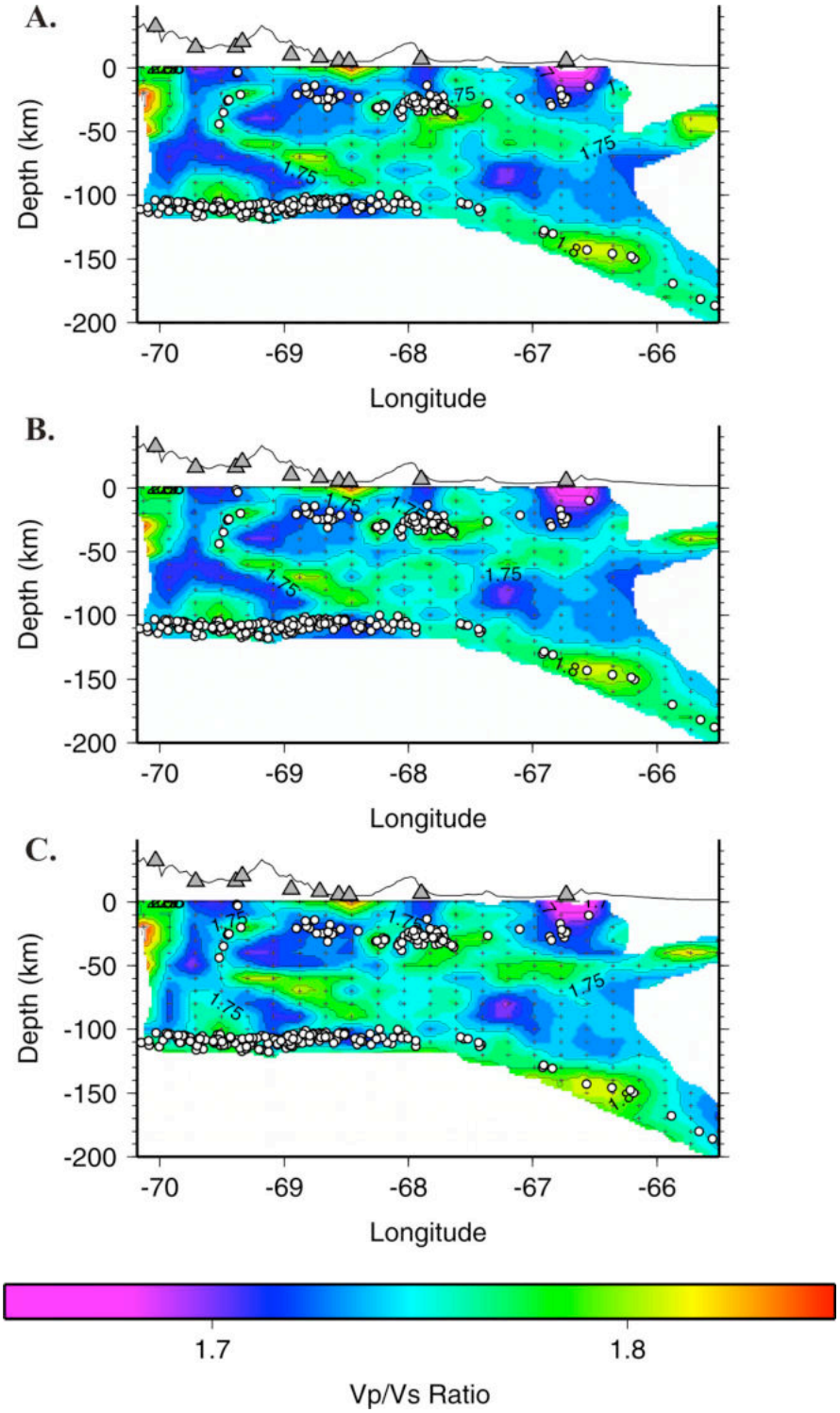

Figure S10. Sensitivity to the starting model along profile 1. **A.** Flat Moho. **B.** Simple 3D Moho. **C.** Same as **B.**, but using a Vp/Vs ratio of 1.79 for the upper mantle.

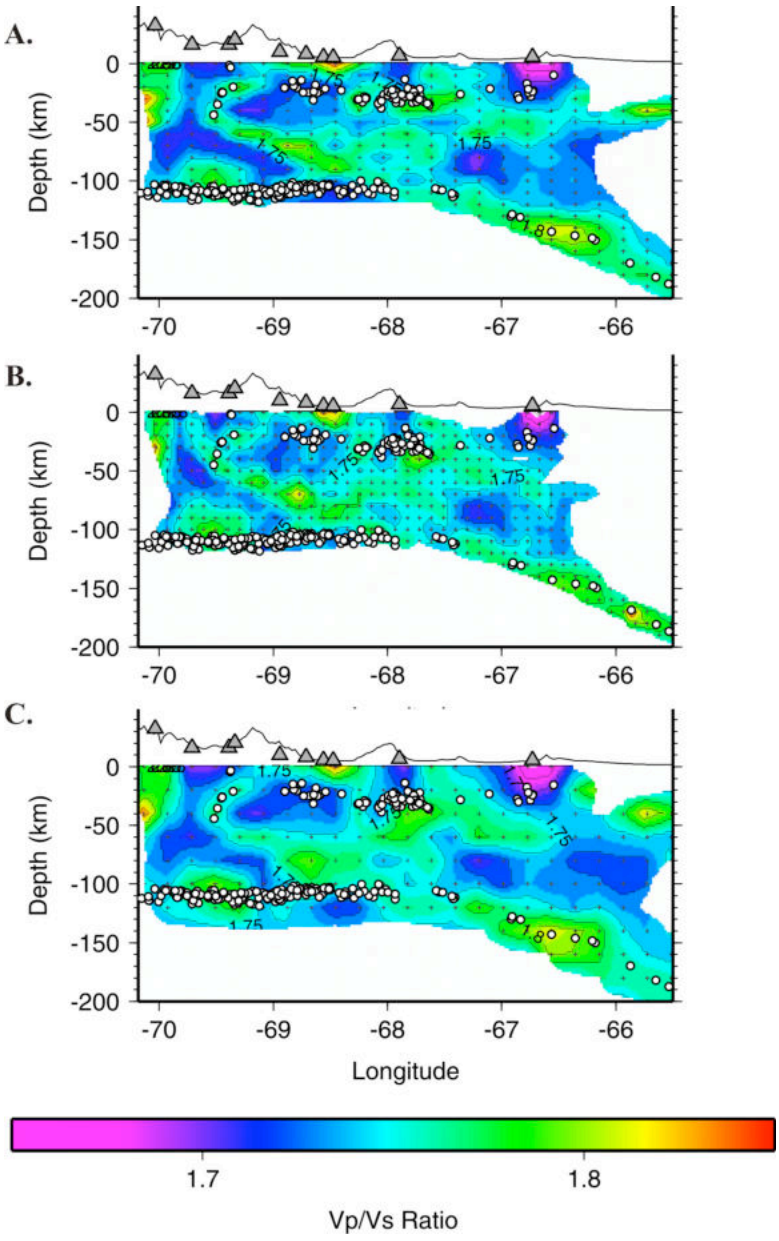

Figure S11. Effects of different model parameterizations on the tomographic images along profile 1. **A.** Grid 20x20x10 km. **B.** Grid 10X10x10 km. **C.** Grid 20X20X20 km. Small crosses denote the grid nodes.

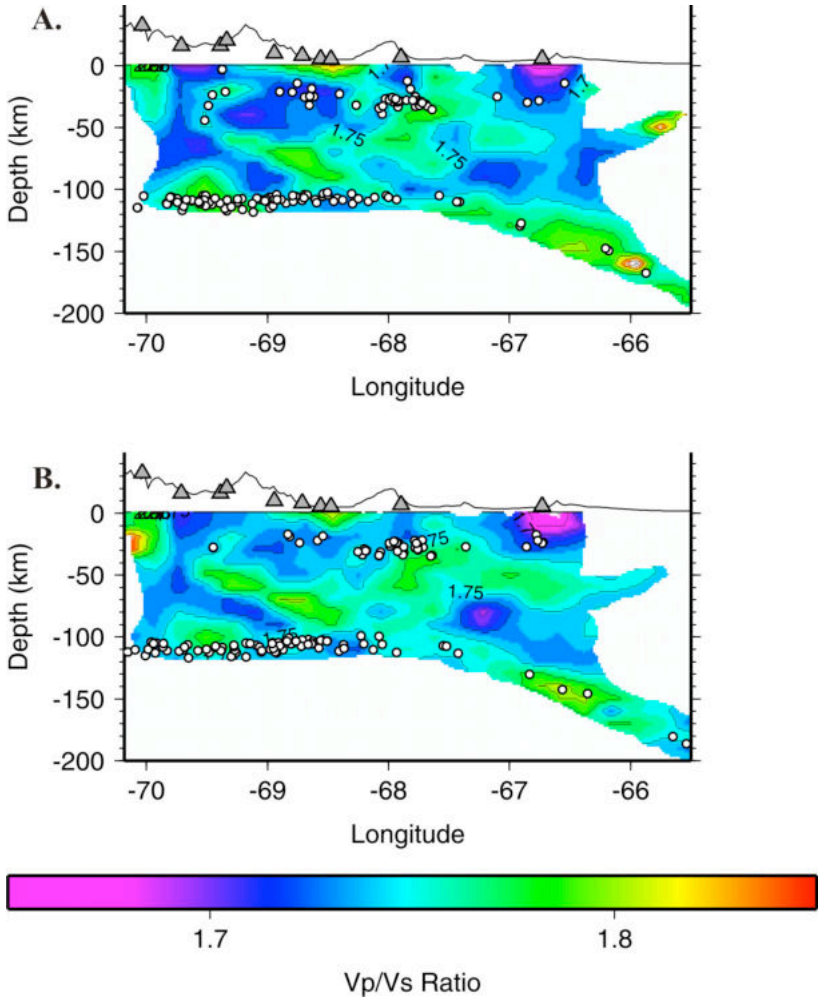

Figure S12. Inversion for two separate data subsets. **A.** Even earthquake number **B.** Odd earthquakes number.

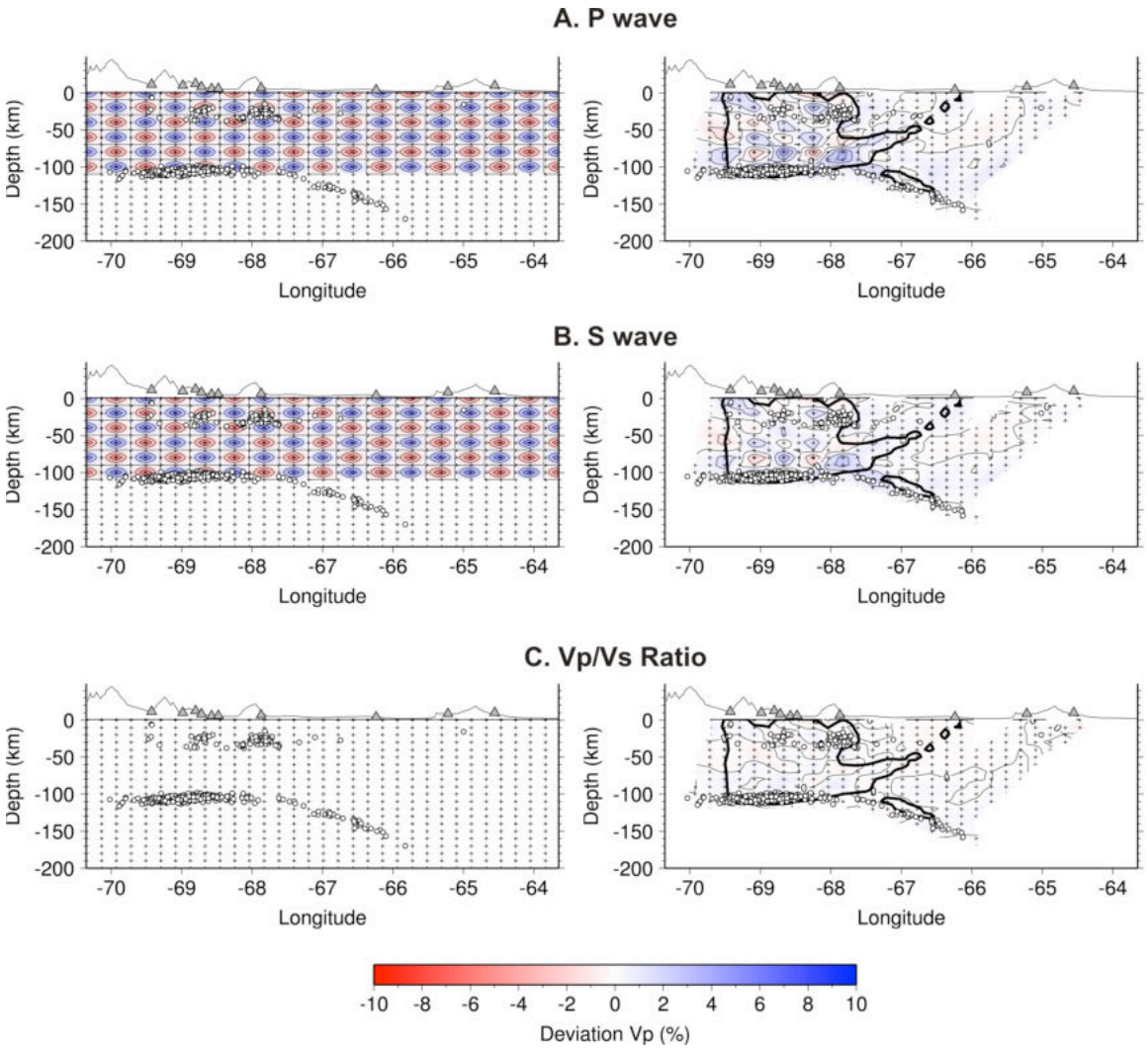

Figure S13. Solution quality assessment using synthetic checkerboard models along profile at Latitude 31.4°S. The input model is on the left and recovered model is on the right. **A.** P-wave. **B.** S-wave. **C.** Vp/Vs ratio.

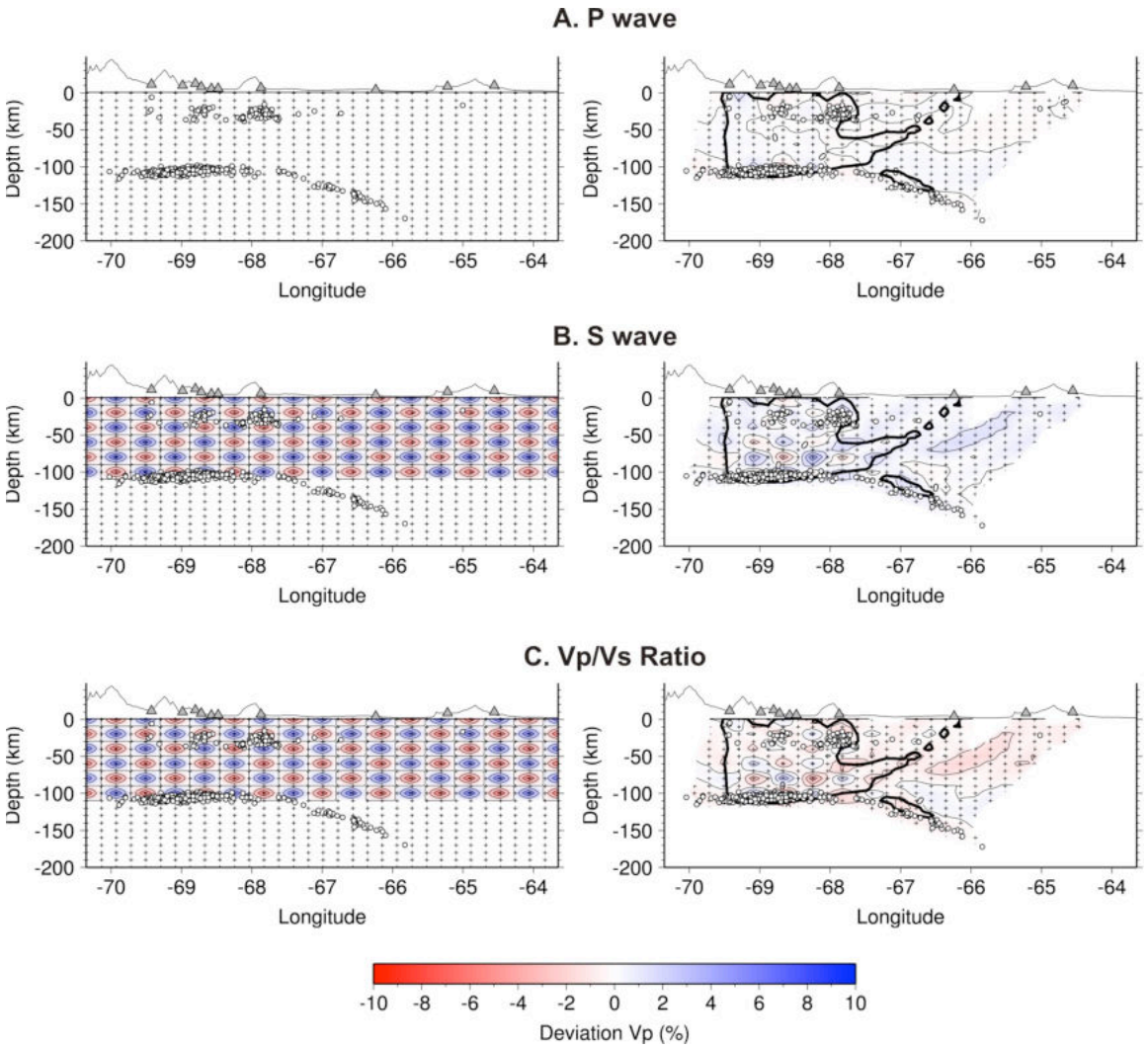

Figure S14. Solution quality assessment using synthetic checkerboard models along profile at Latitude 31.4°S. The input model is on the left and recovered model is on the right. **A.** P-wave. **B.** S-wave. **C.** Vp/Vs ratio.

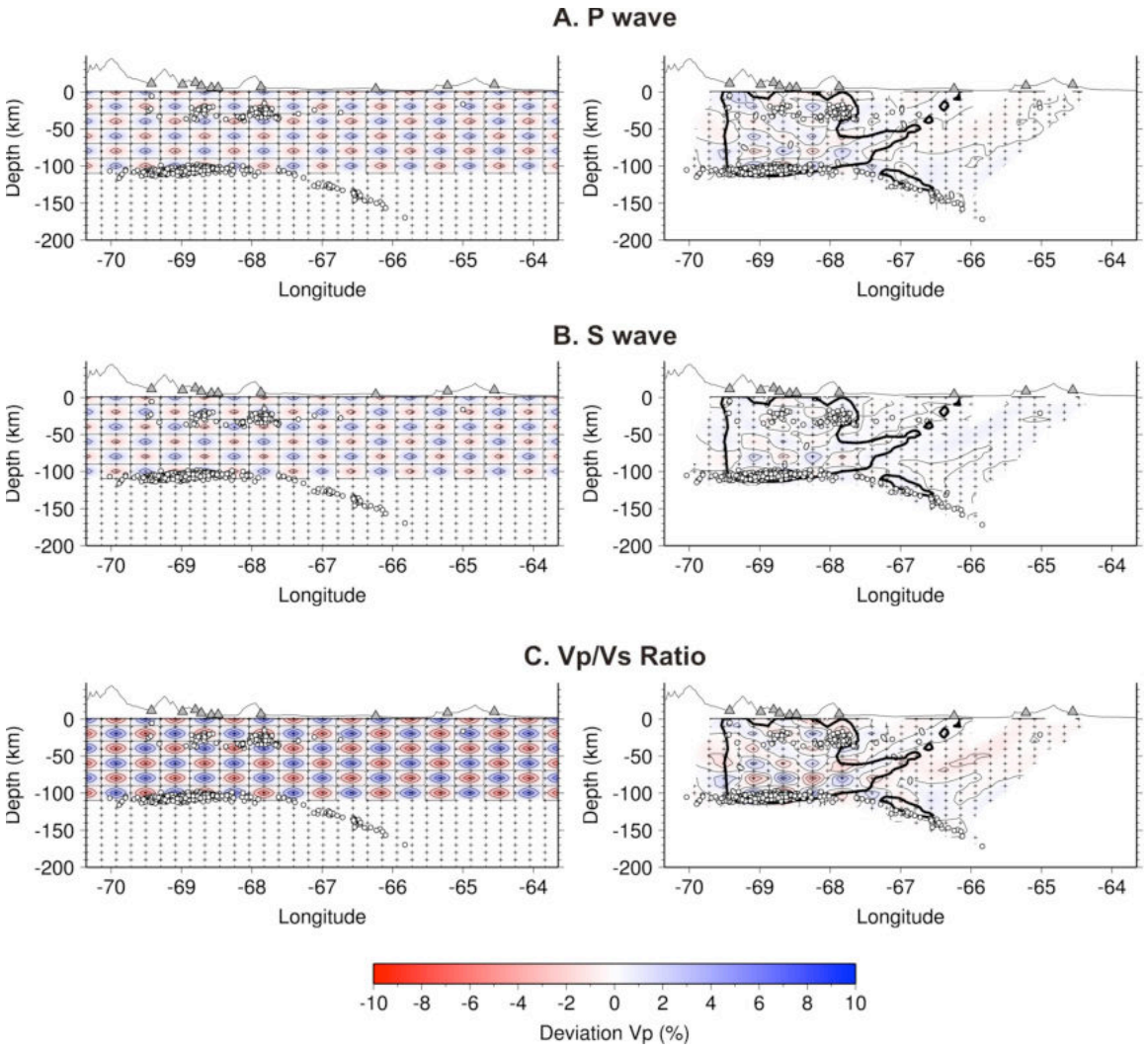

Figure S15. Solution quality assessment using synthetic checkerboard models along profile at Latitude 31.4°S. The input model is on the left and recovered model is on the right. **A.** P-wave. **B.** S-wave. **C.** Vp/Vs ratio.

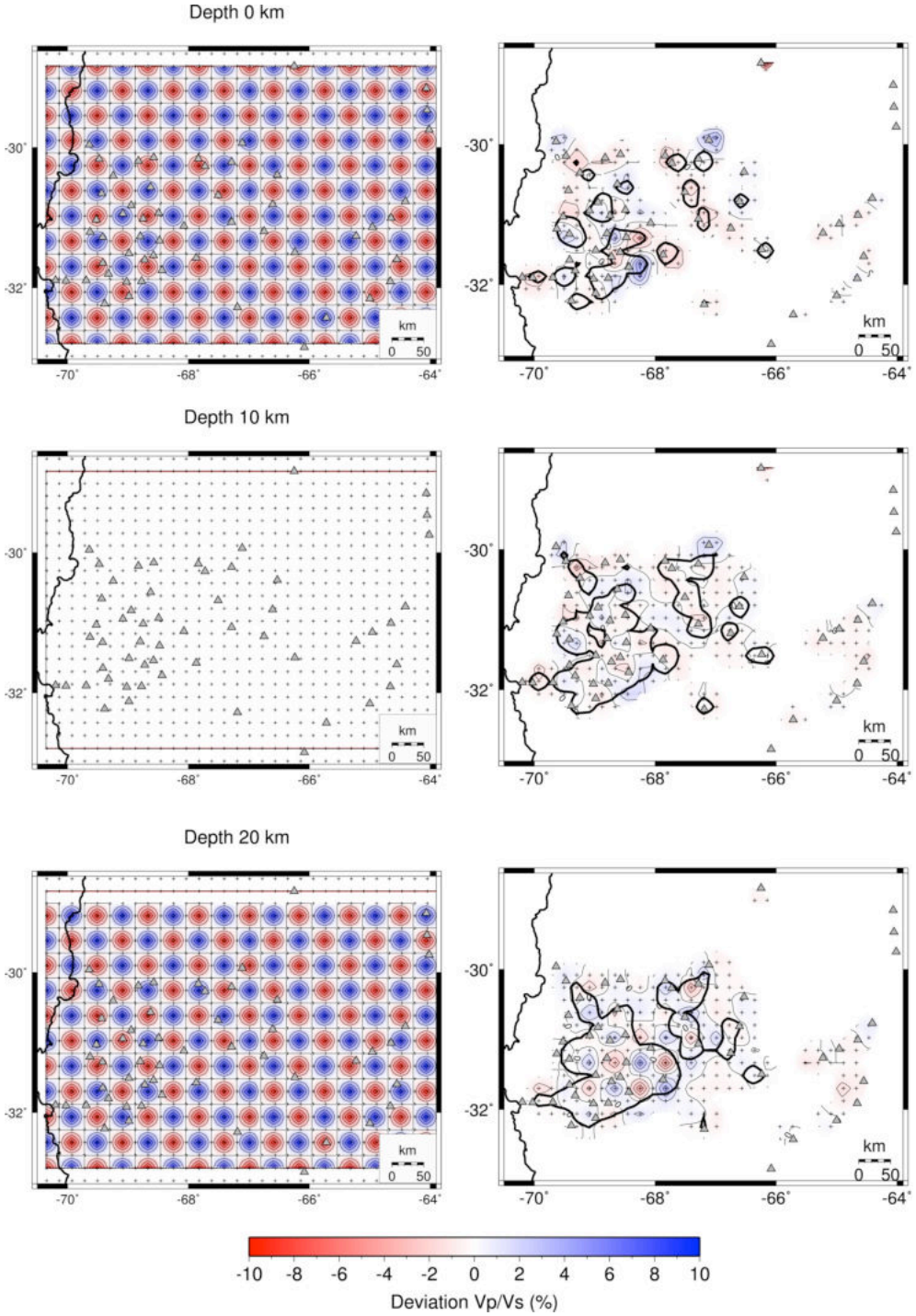

Figure S16. Solution quality assessment using synthetic checkerboard models for the case of high- and low-velocity anomalies (± 5 per cent) of opposite sing for Vp and Vs, so that the resulted Vp/Vs model has high and low anomalies of ±10 per cent. Depth is indicated above plots on the left. One layer is left free of anomalies to study vertical smearing.

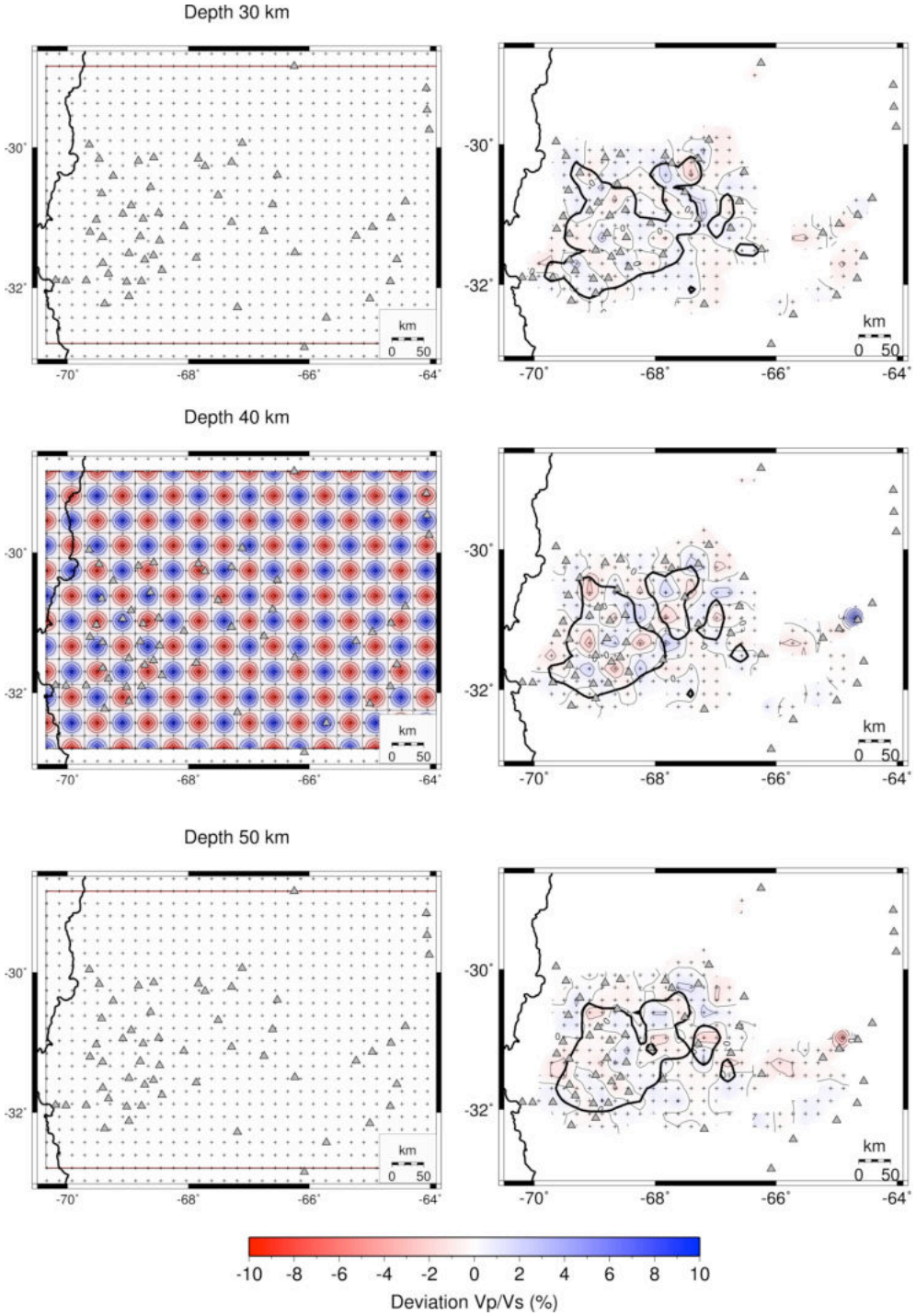

Figure S16. Solution quality assessment using synthetic checkerboard models for the case of high- and low-velocity anomalies (± 5 per cent) of opposite sing for Vp and Vs, so that the resulted Vp/Vs model has high and low anomalies of ±10 per cent. Depth is indicated above plots on the left. One layer is left free of anomalies to study vertical smearing.

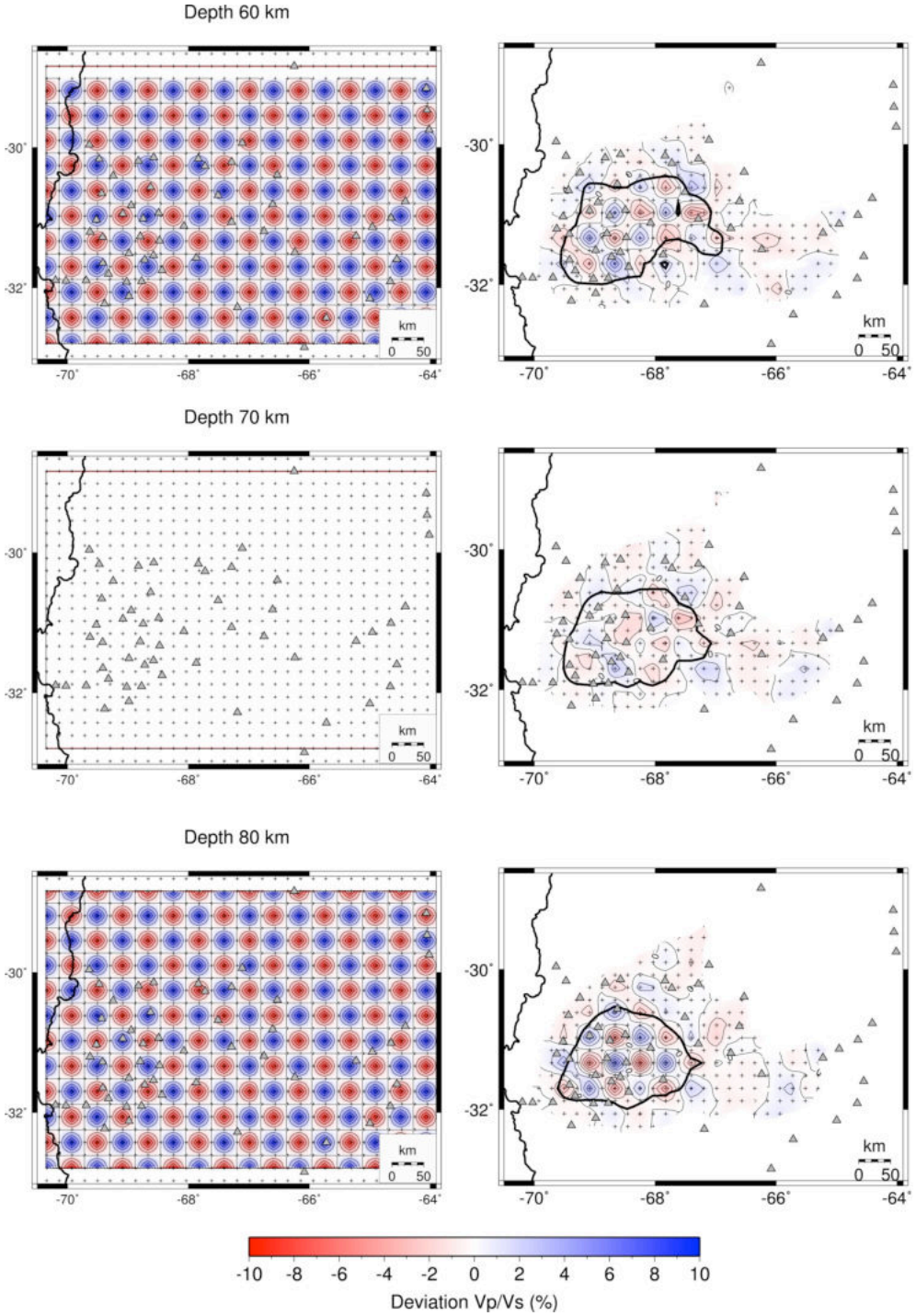

Figure S16. Solution quality assessment using synthetic checkerboard models for the case of high- and low-velocity anomalies (± 5 per cent) of opposite sing for Vp and Vs, so that the resulted Vp/Vs model has high and low anomalies of ±10 per cent. Depth is indicated above plots on the left. One layer is left free of anomalies to study vertical smearing.

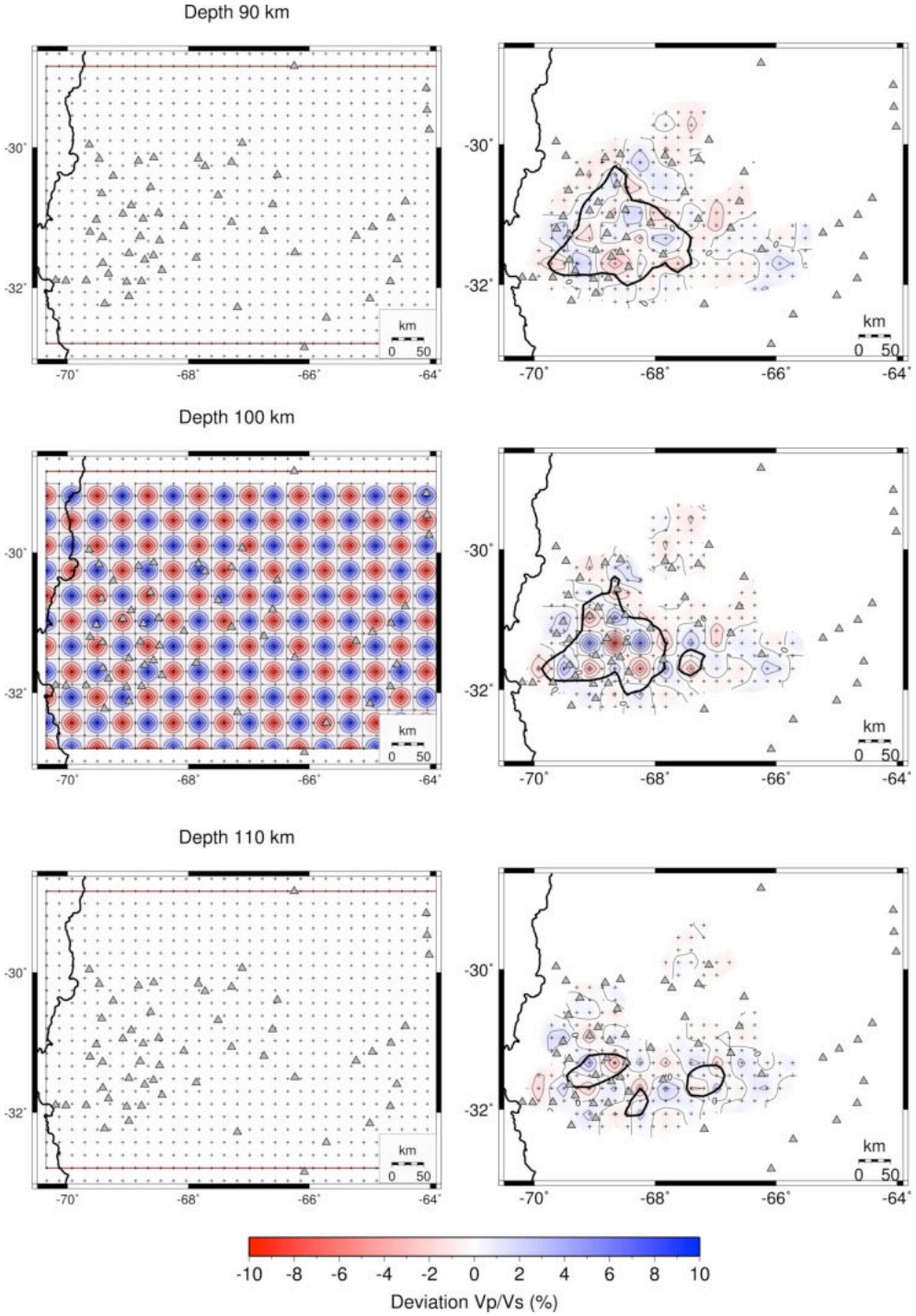

Figure S16. Solution quality assessment using synthetic checkerboard models for the case of high- and low-velocity anomalies (± 5 per cent) of opposite sing for Vp and Vs, so that the resulted Vp/Vs model has high and low anomalies of ±10 per cent. Depth is indicated above plots on the left. One layer is left free of anomalies to study vertical smearing.

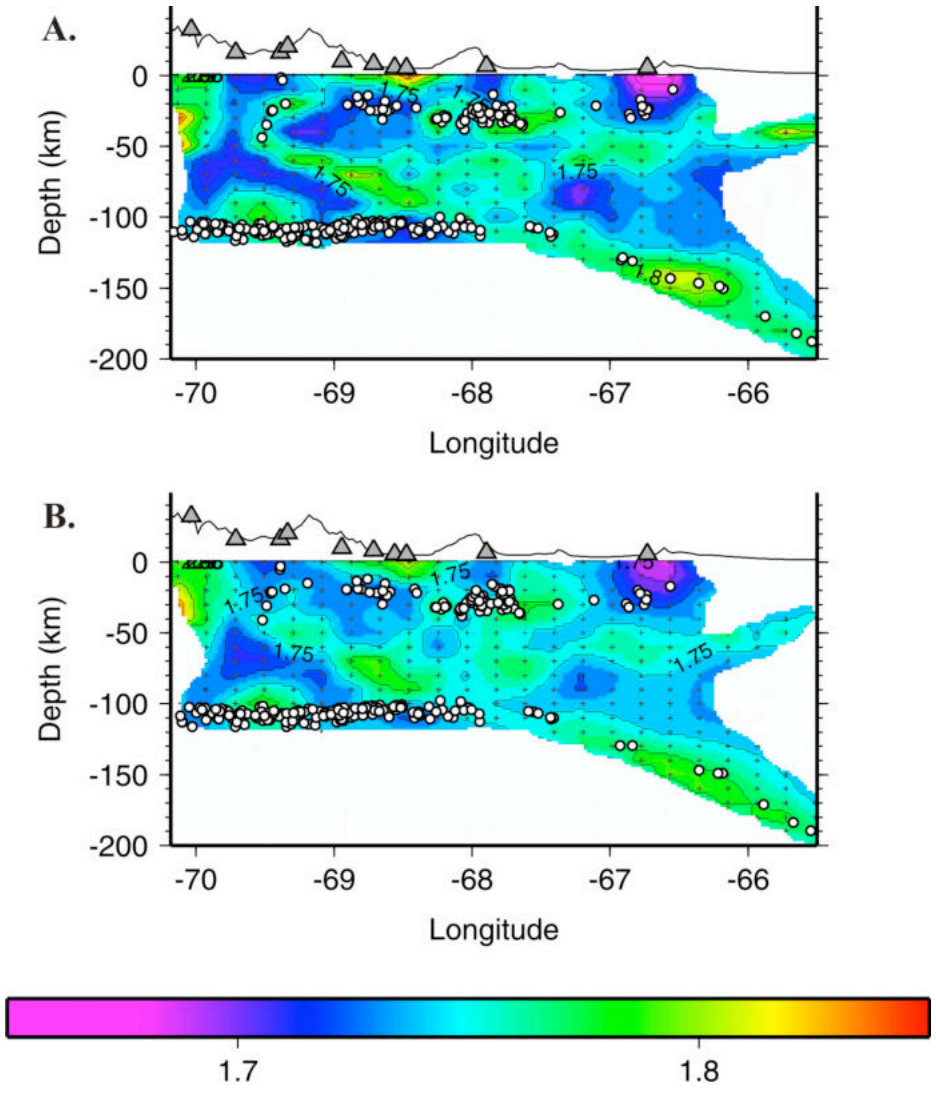

Figure S17. Solution quality assessment using a restoration test along profile 1. **A.** Initial Model. **B.** Recovered Model.

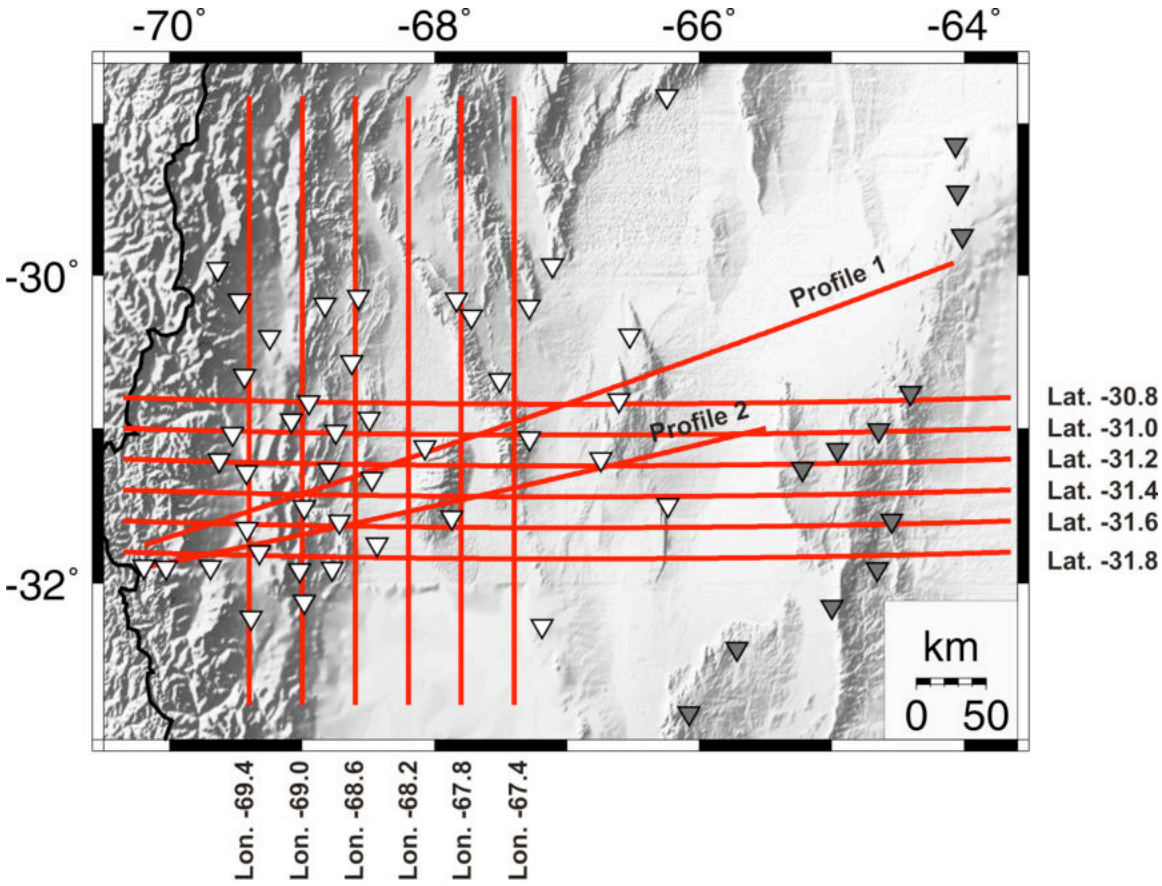

Figure S18. Location of profiles shown in figures S19-S22.

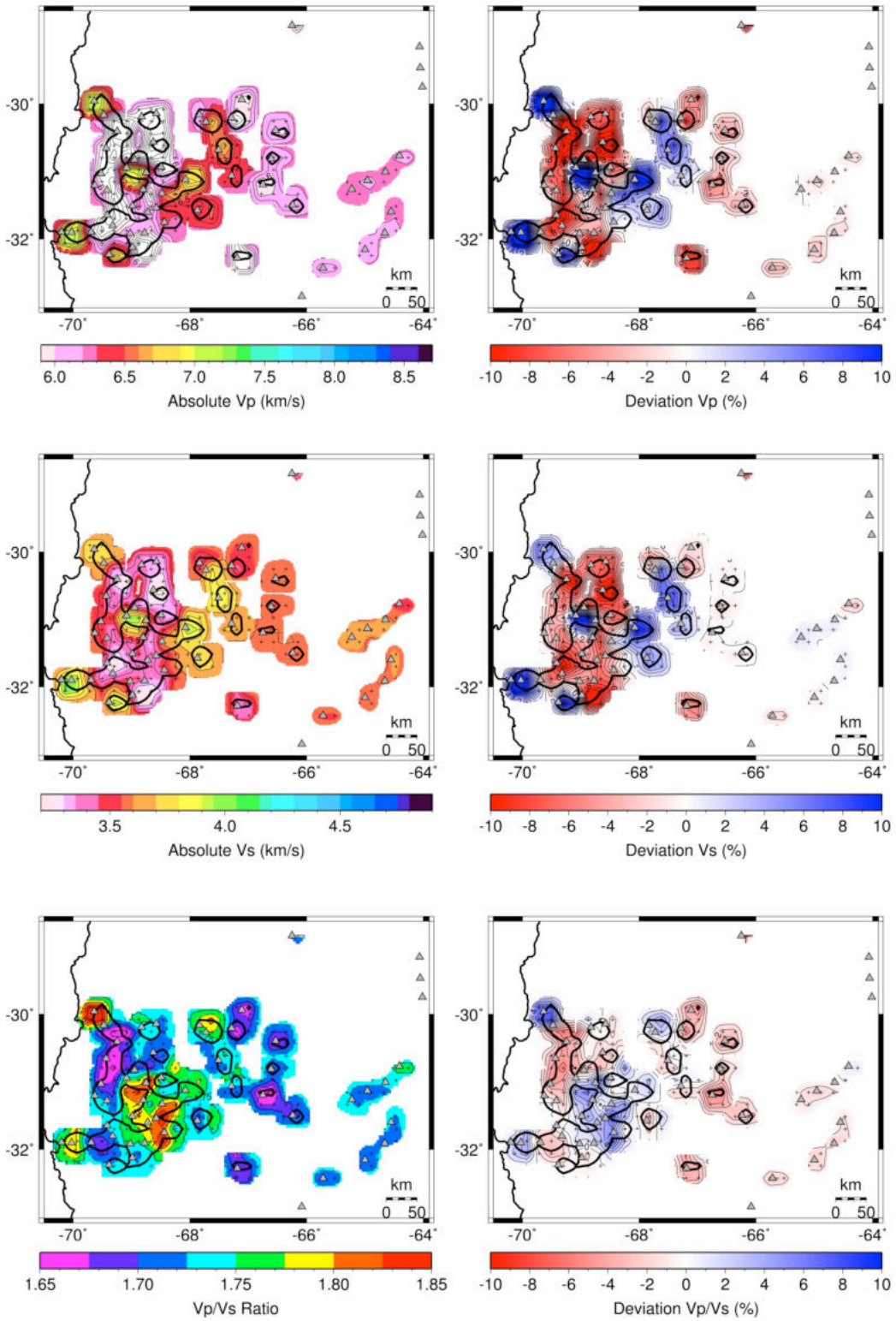

Figure S19. Slices at constant depth at 0 km through the Vp, Vs, and Vp/Vs models. Color scale is indicated below each plot. Other symbols as in Figure 6.

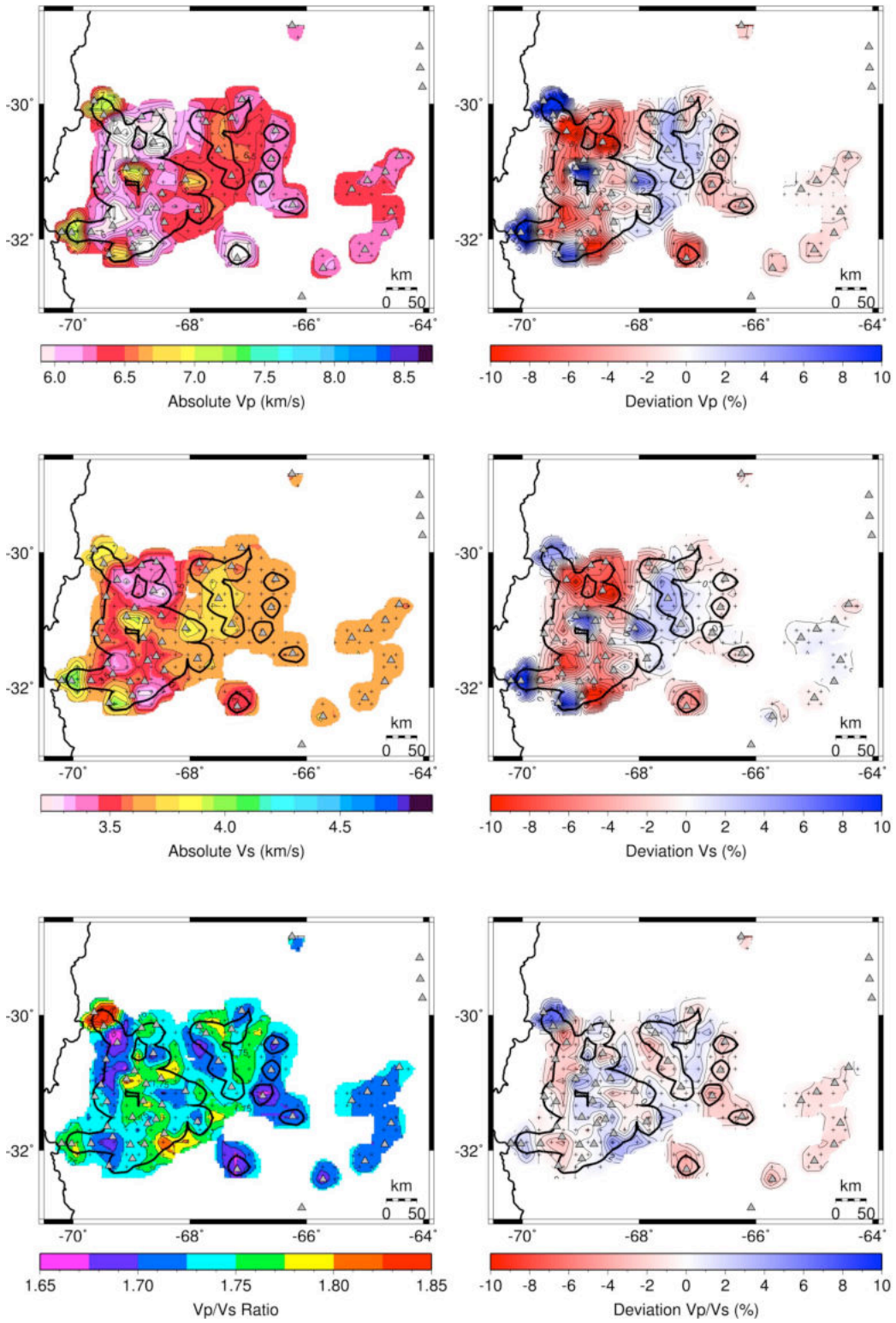

Figure S19. Slices at constant depth at 10 km through the Vp, Vs, and Vp/Vs models. Color scale is indicated below each plot. Other symbols as in Figure 6.

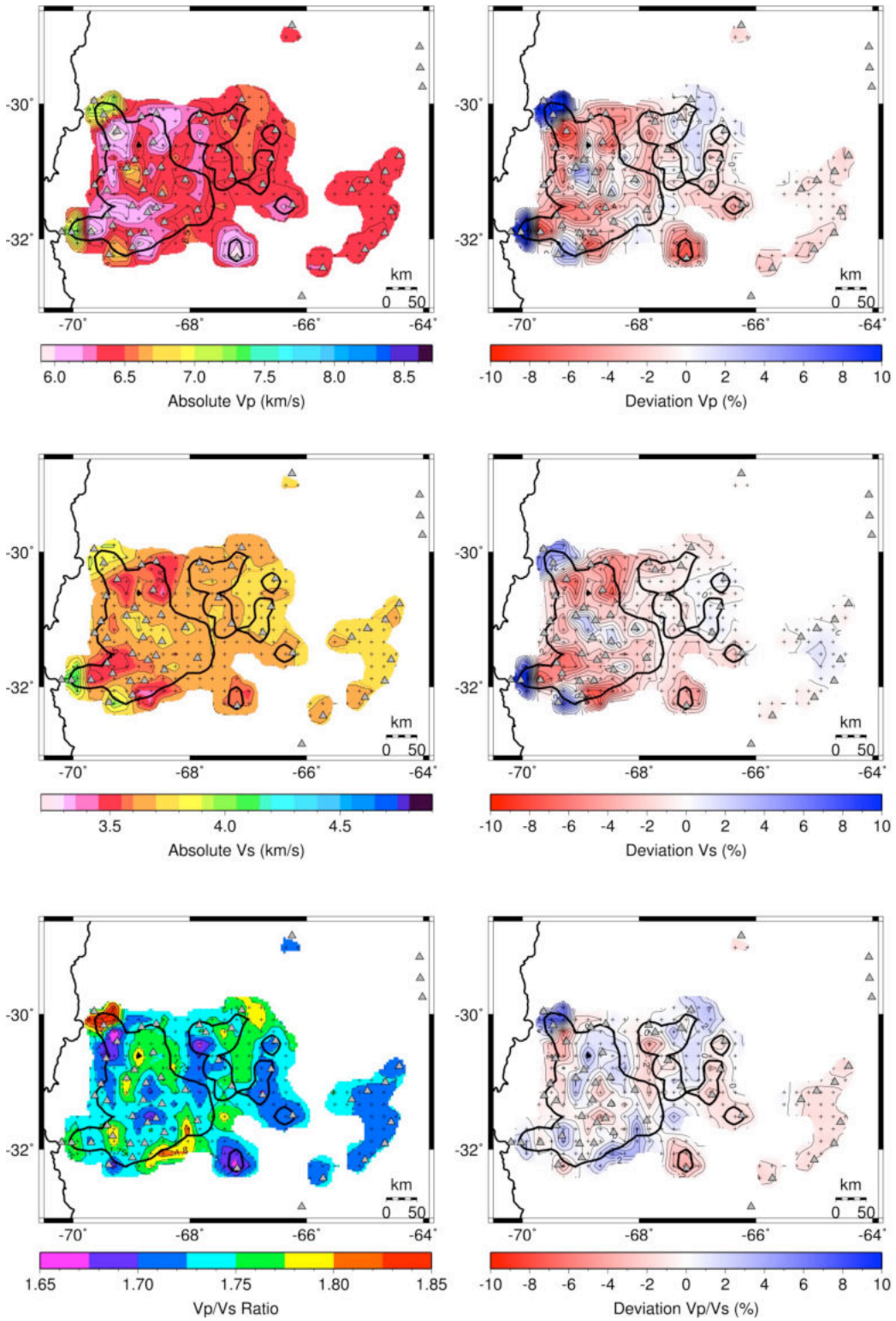

Figure S19. Slices at constant depth at 20 km through the Vp, Vs, and Vp/Vs models. Color scale is indicated below each plot. Other symbols as in Figure 6.

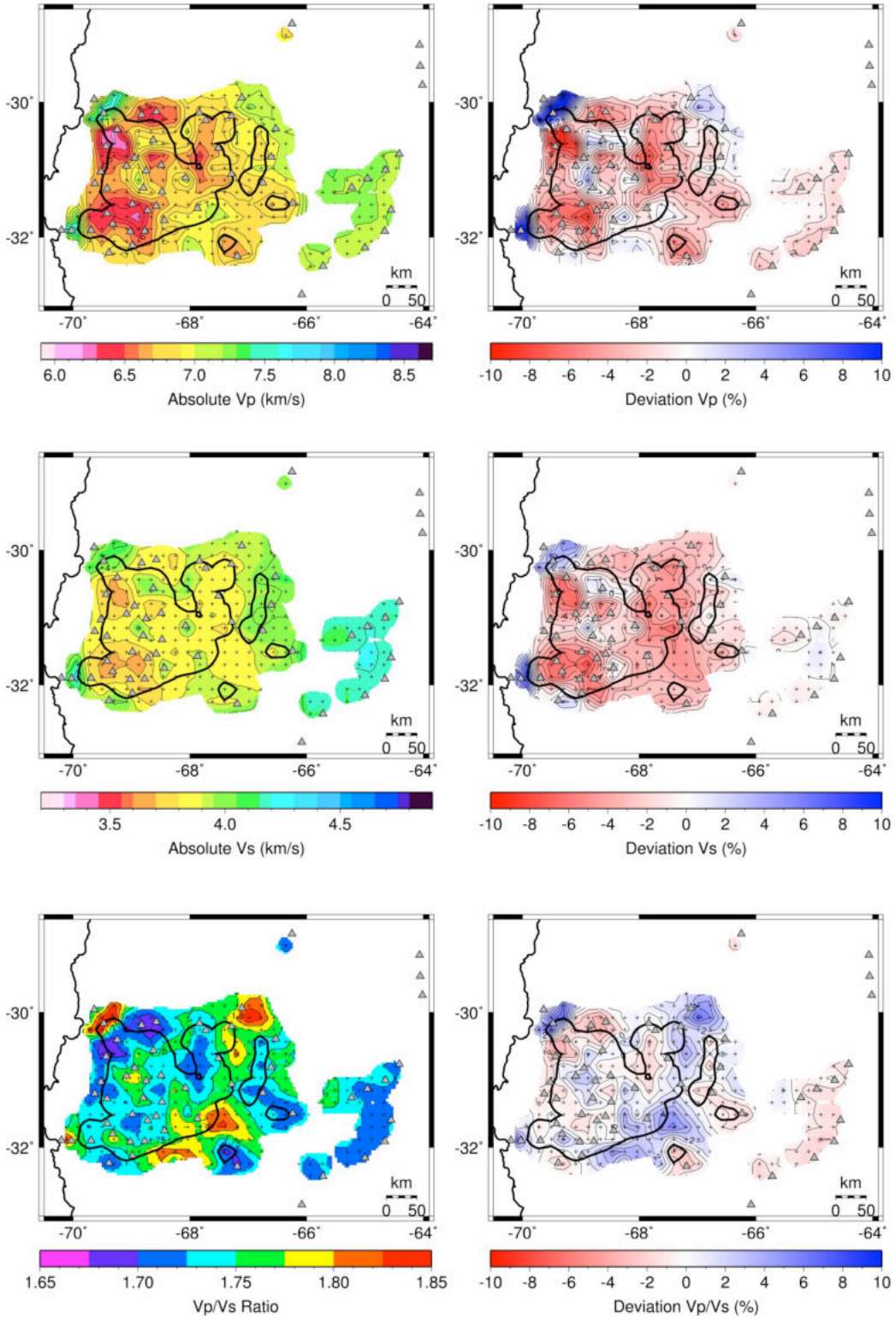

Figure S19. Slices at constant depth at 30 km through the Vp, Vs, and Vp/Vs models. Color scale is indicated below each plot. Other symbols as in Figure 6.

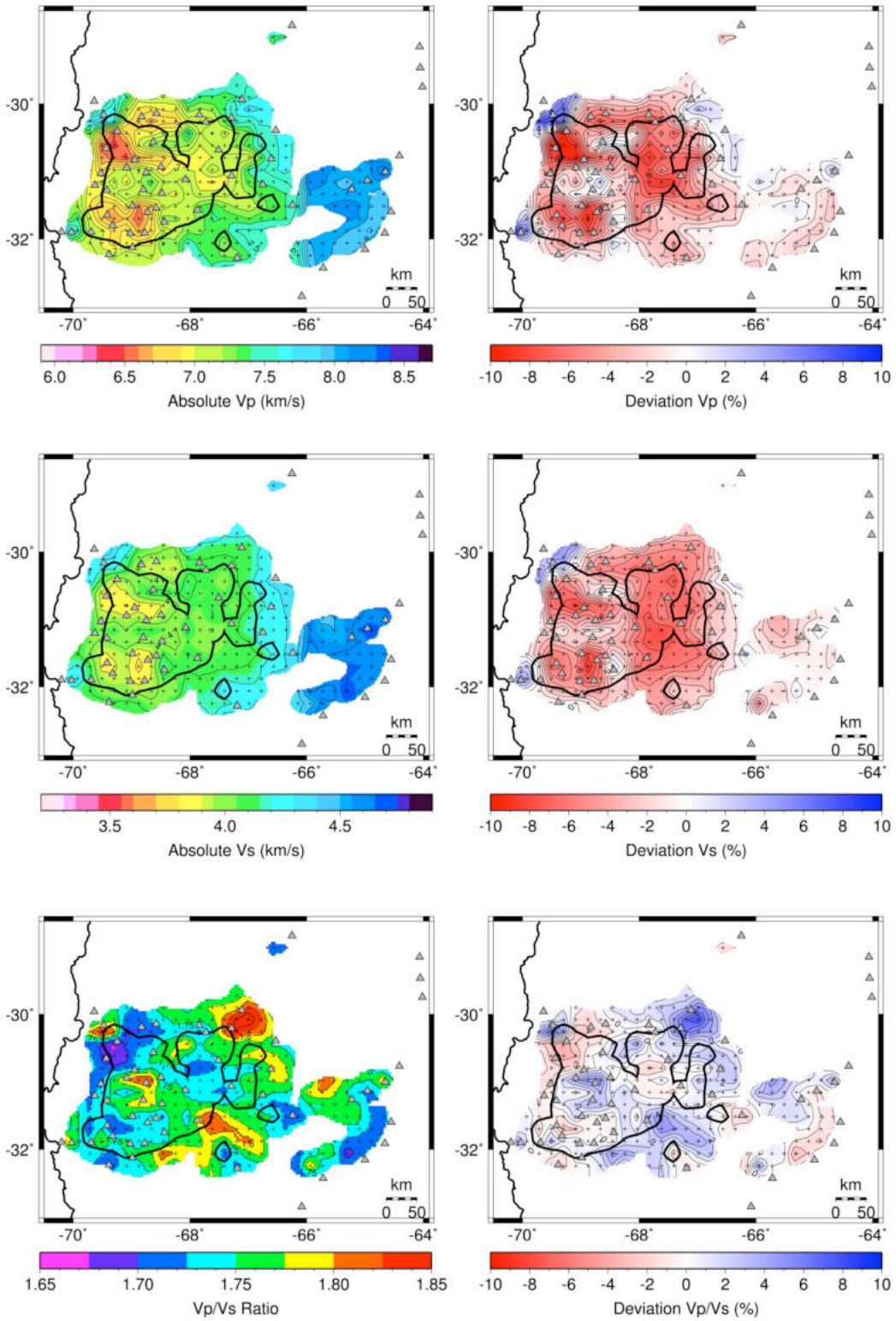

Figure S19. Slices at constant depth at 40 km through the Vp, Vs, and Vp/Vs models. Color scale is indicated below each plot. Other symbols as in Figure 6.

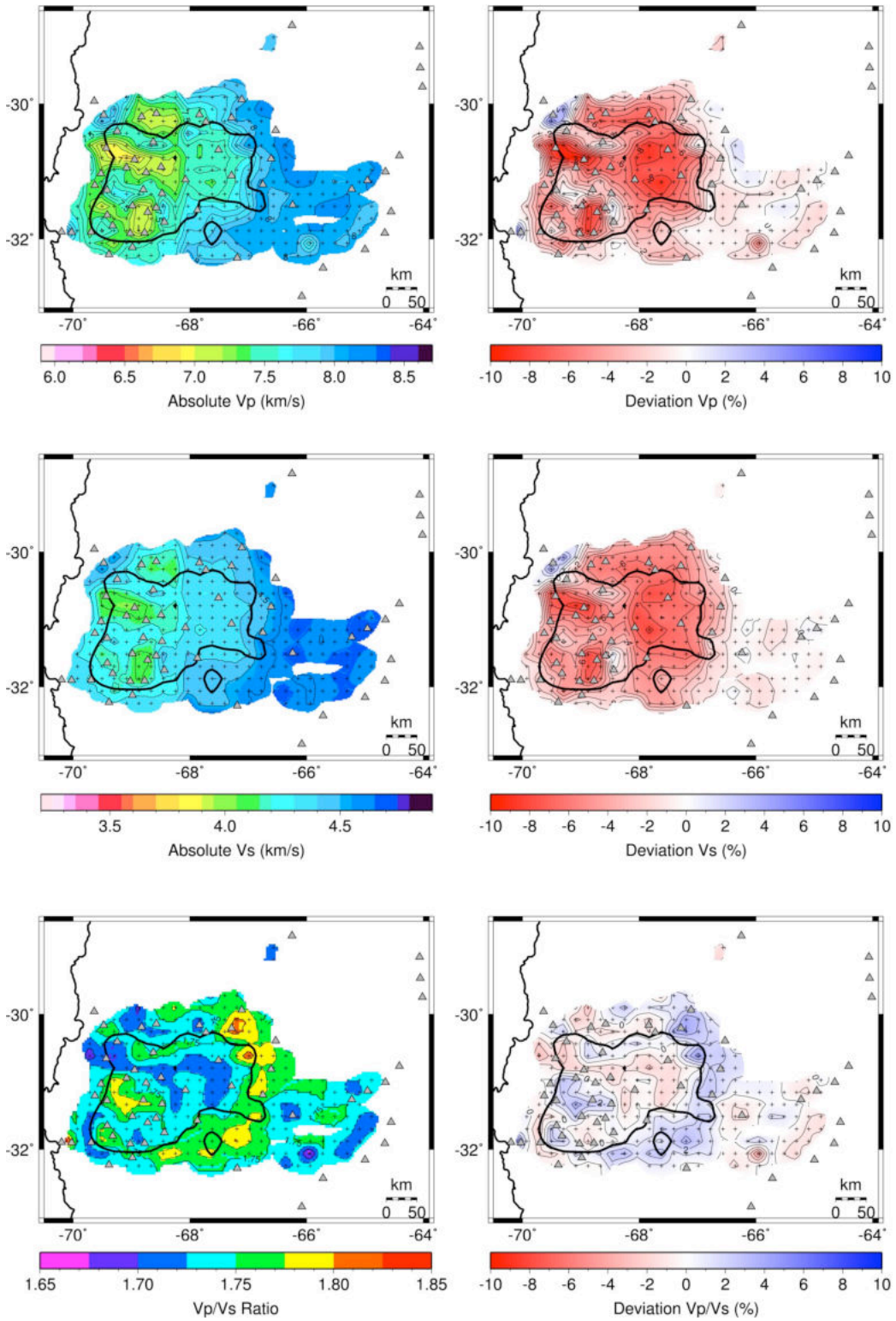

Figure S19. Slices at constant depth at 50 km through the Vp, Vs, and Vp/Vs models. Color scale is indicated below each plot. Other symbols as in Figure 6.

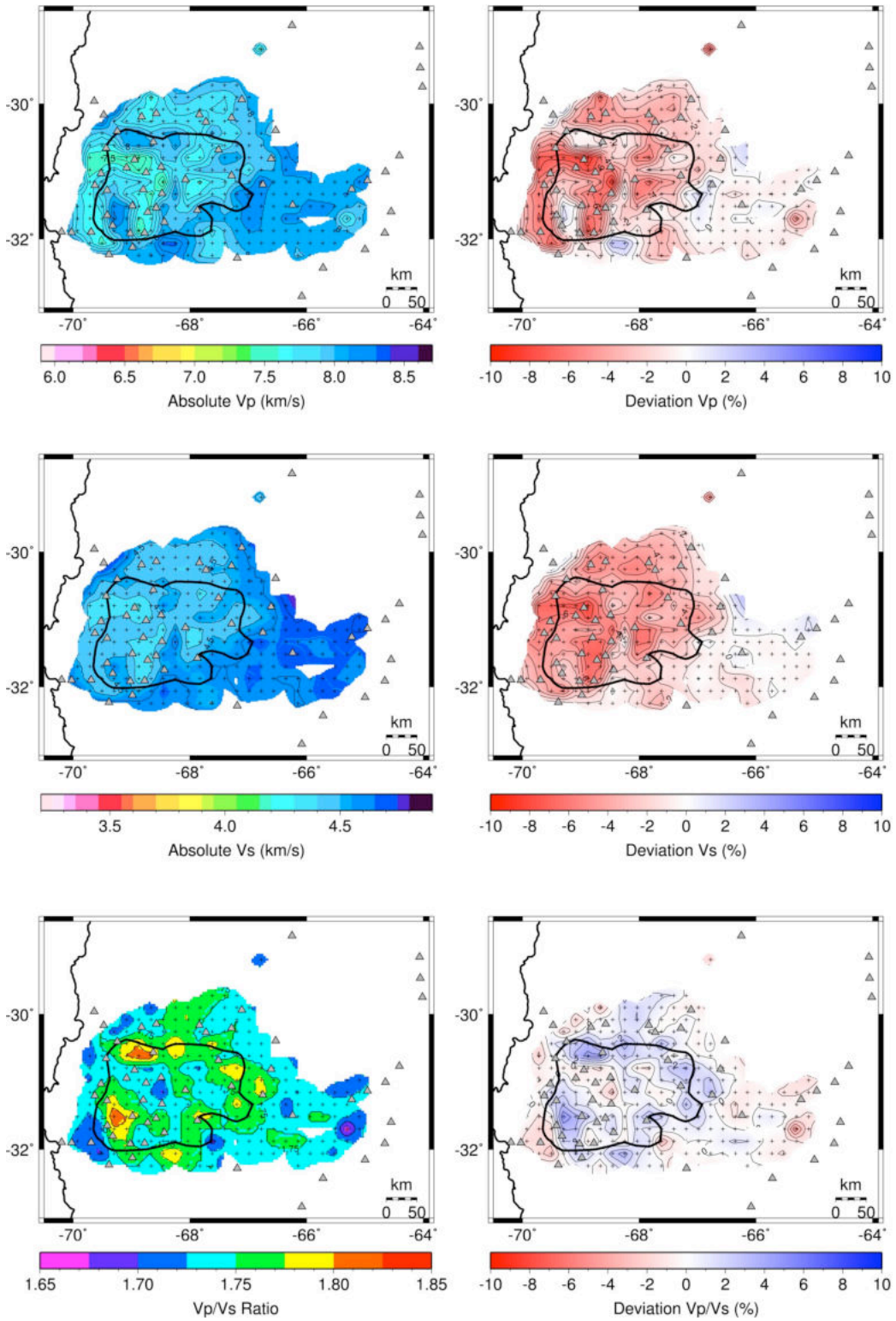

Figure S19. Slices at constant depth at 60 km through the Vp, Vs, and Vp/Vs models. Color scale is indicated below each plot. Other symbols as in Figure 6.

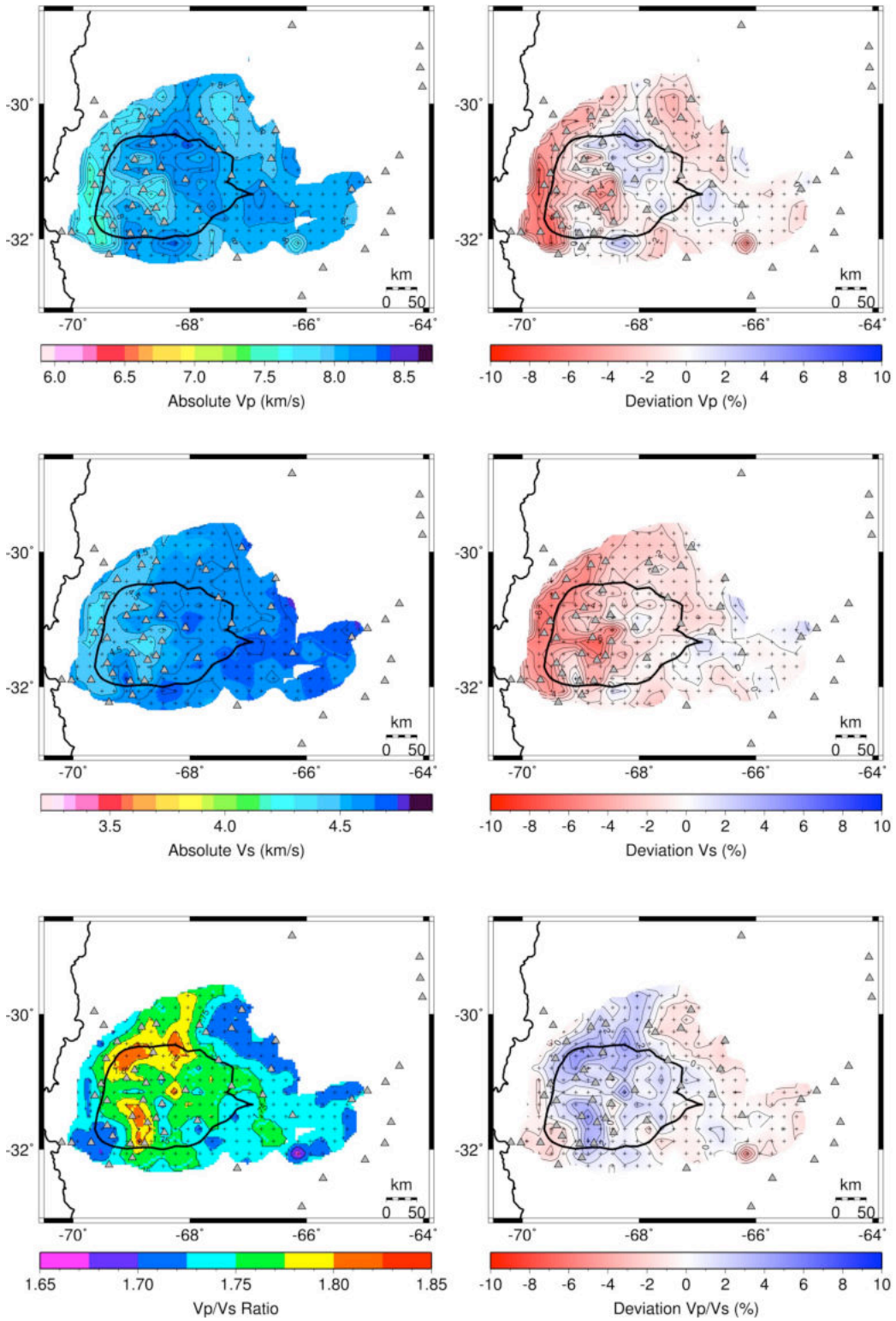

Figure S19. Slices at constant depth at 70 km through the Vp, Vs, and Vp/Vs models. Color scale is indicated below each plot. Other symbols as in Figure 6.

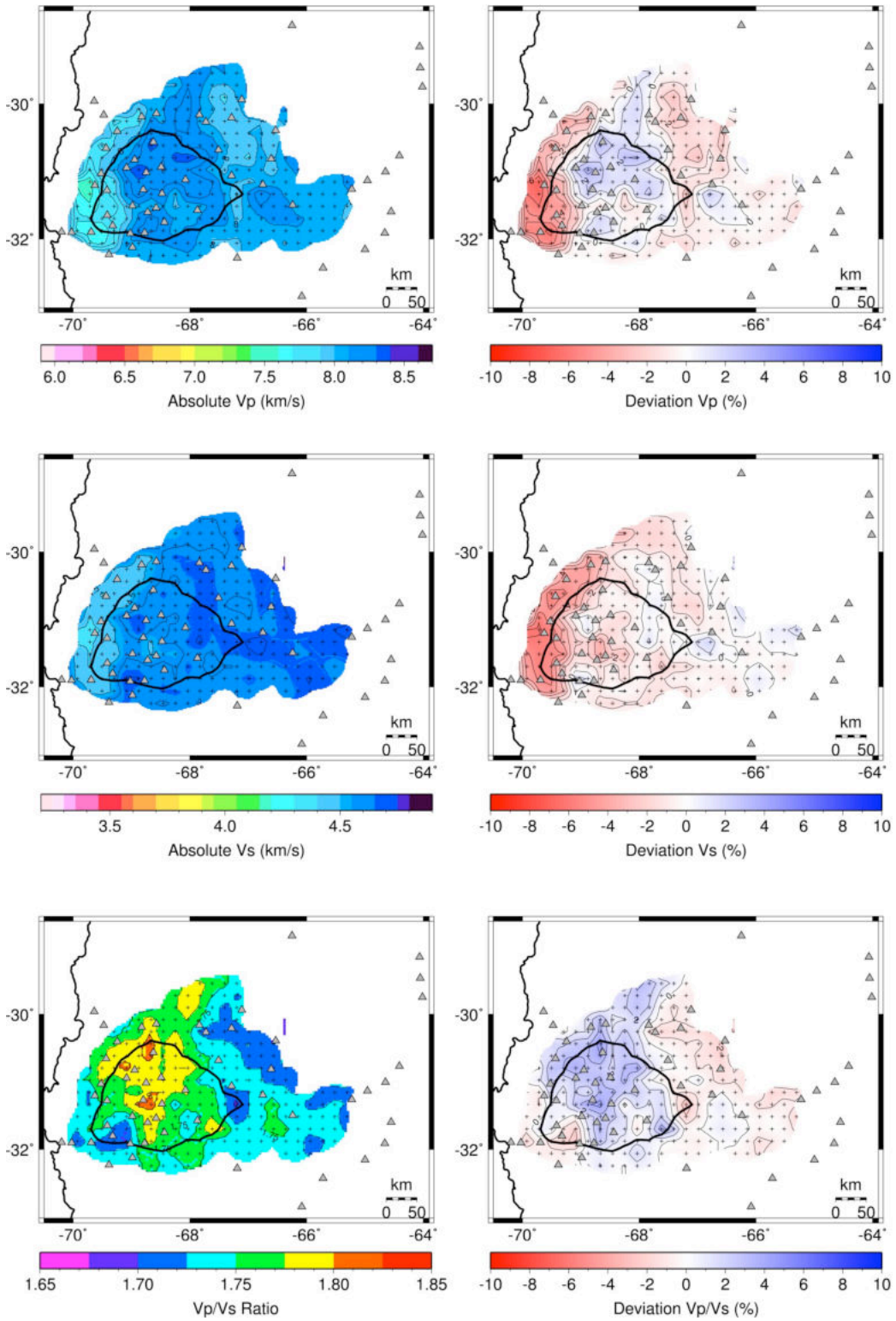

Figure S19. Slices at constant depth at 80 km through the Vp, Vs, and Vp/Vs models. Color scale is indicated below each plot. Other symbols as in Figure 6.

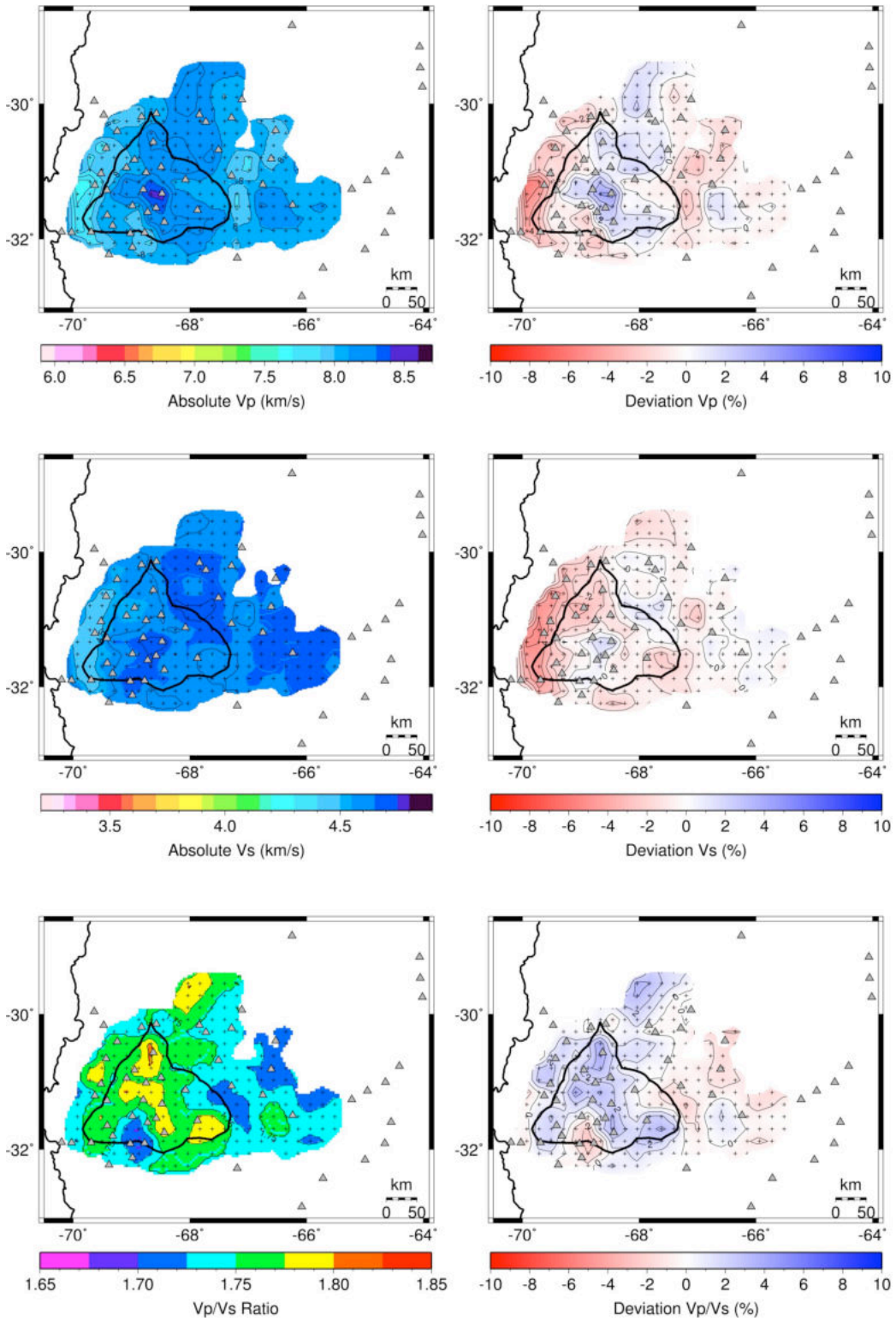

Figure S19. Slices at constant depth at 90 km through the Vp, Vs, and Vp/Vs models. Color scale is indicated below each plot. Other symbols as in Figure 6.

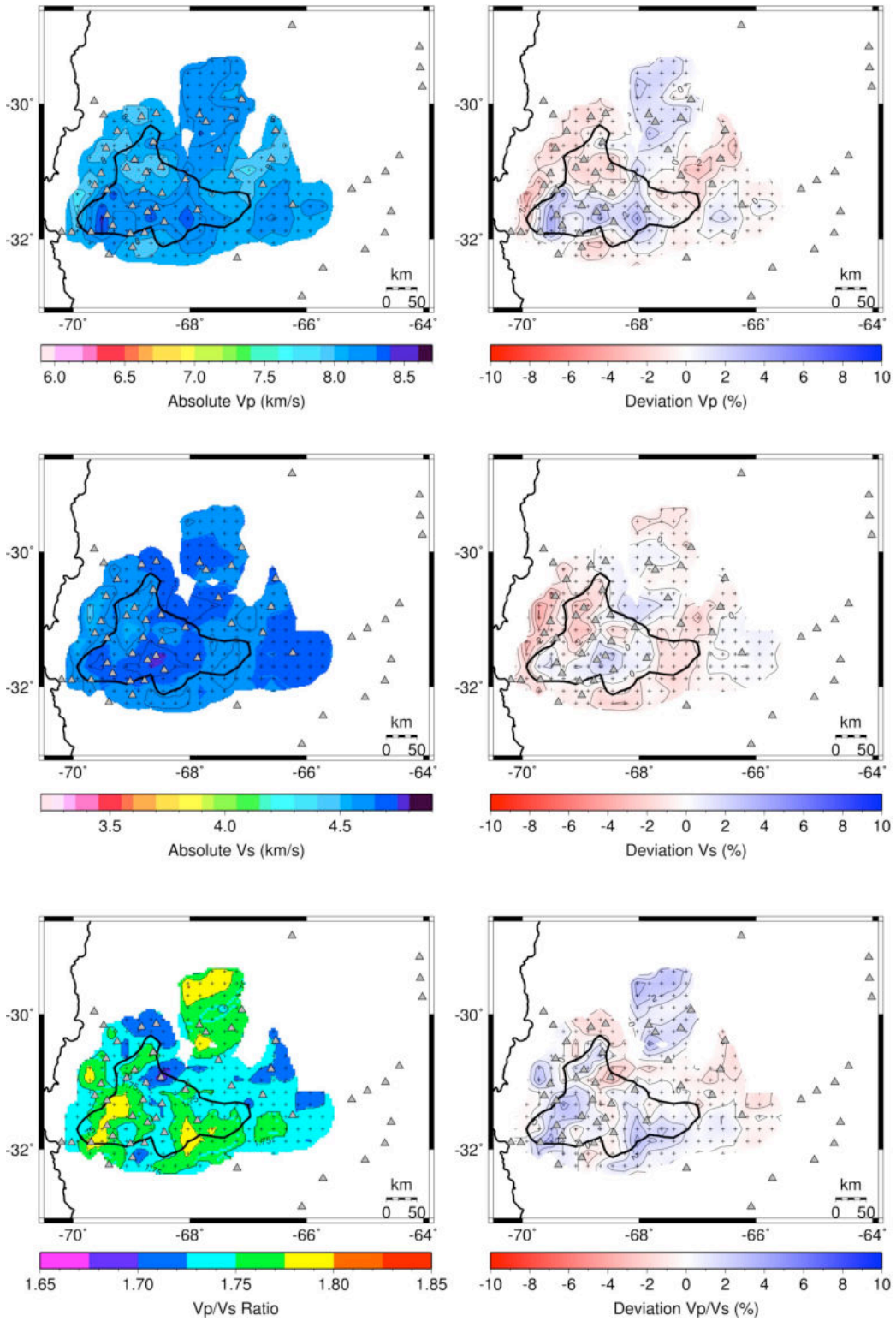

Figure S19. Slices at constant depth at 100 km through the Vp, Vs, and Vp/Vs models. Color scale is indicated below each plot. Other symbols as in Figure 6.

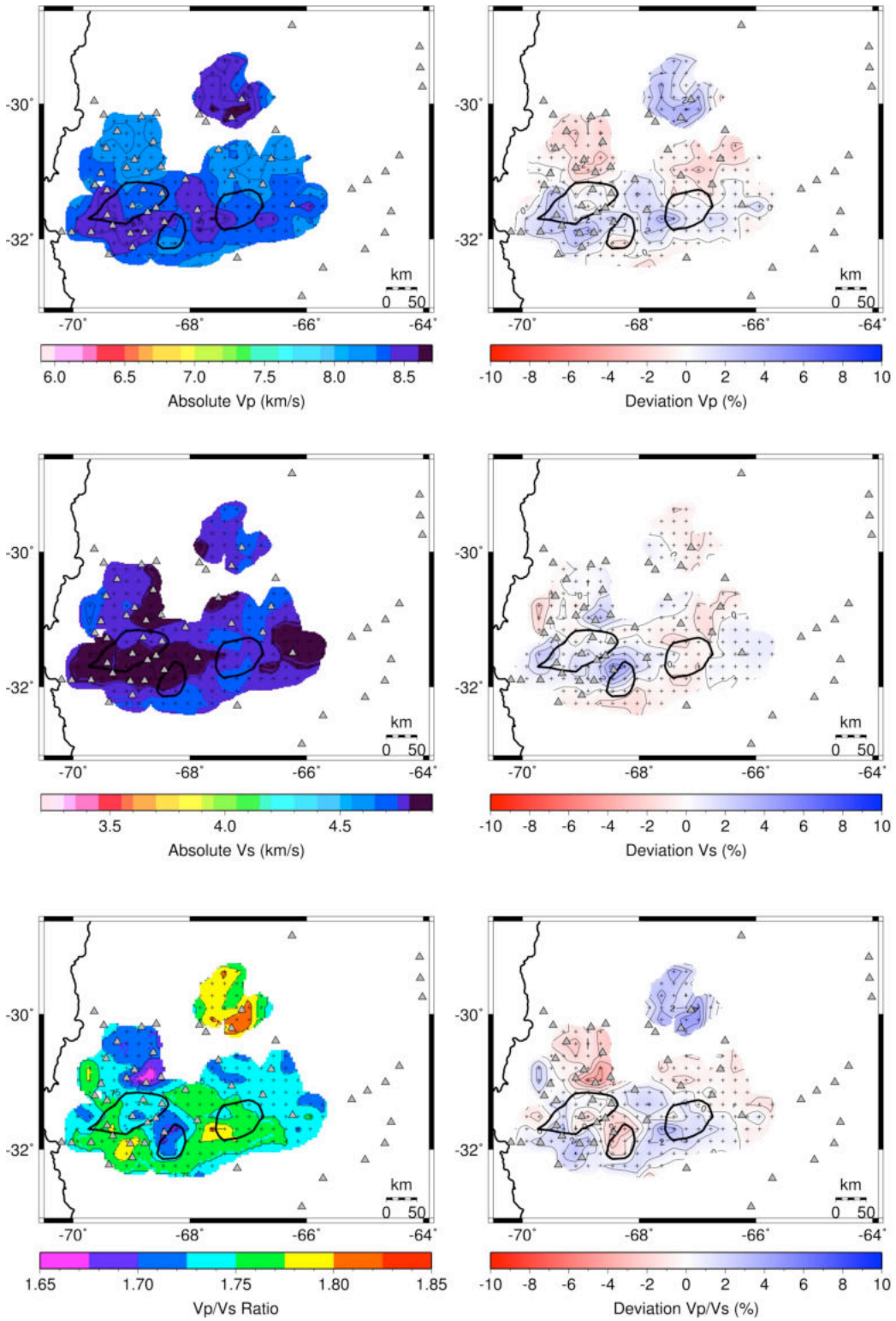

Figure S19. Slices at constant depth at 110 km through the Vp, Vs, and Vp/Vs models. Color scale is indicated below each plot. Other symbols as in Figure 6.

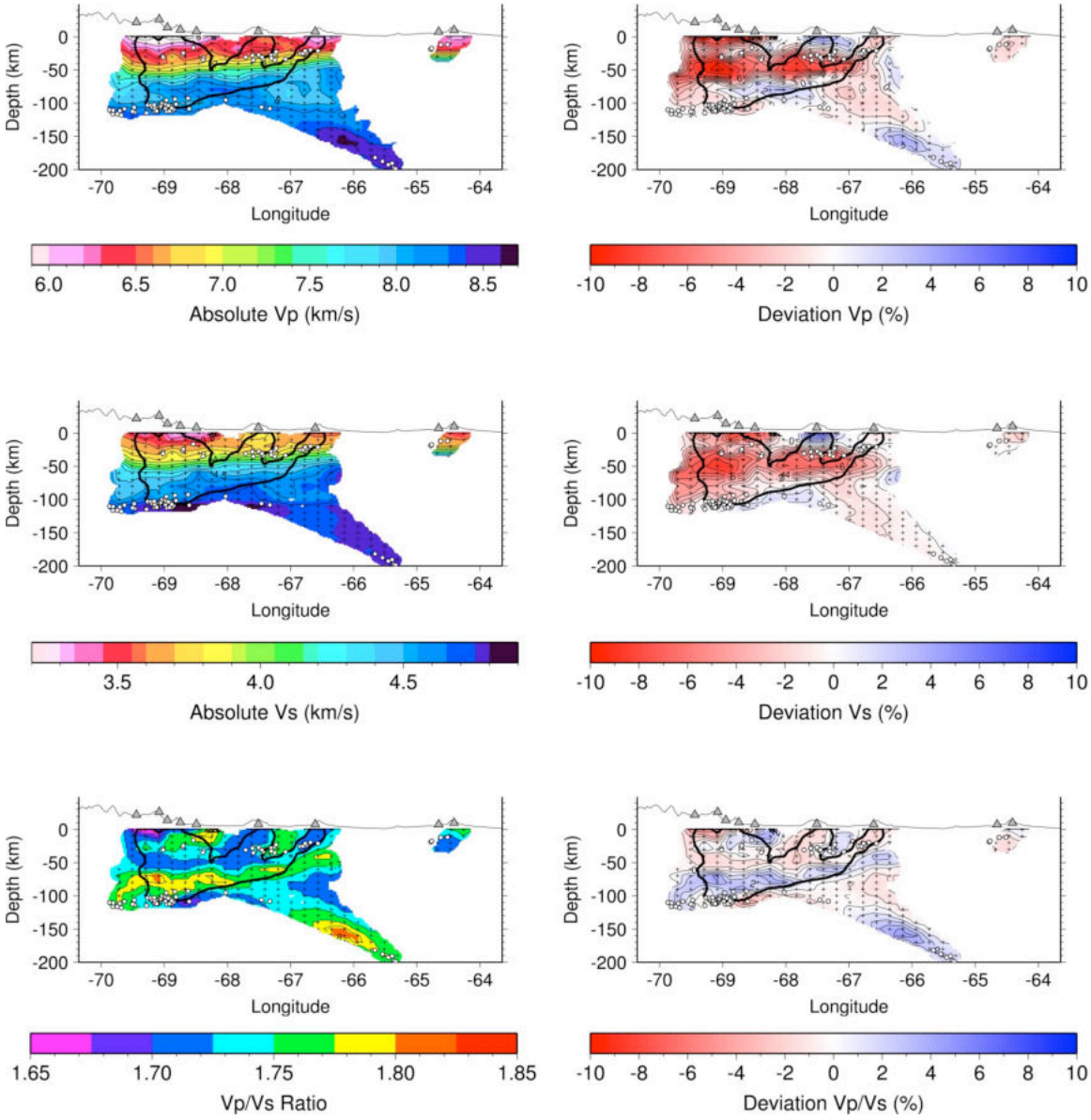

Figure 20. East-West cross sections through the absolute Vp, Vs, and Vp/Vs models at Latitude 30.8°S. Color scale is indicated below each plot. Location of profiles is indicated in Figure S18. Other symbols as in Figure 6.

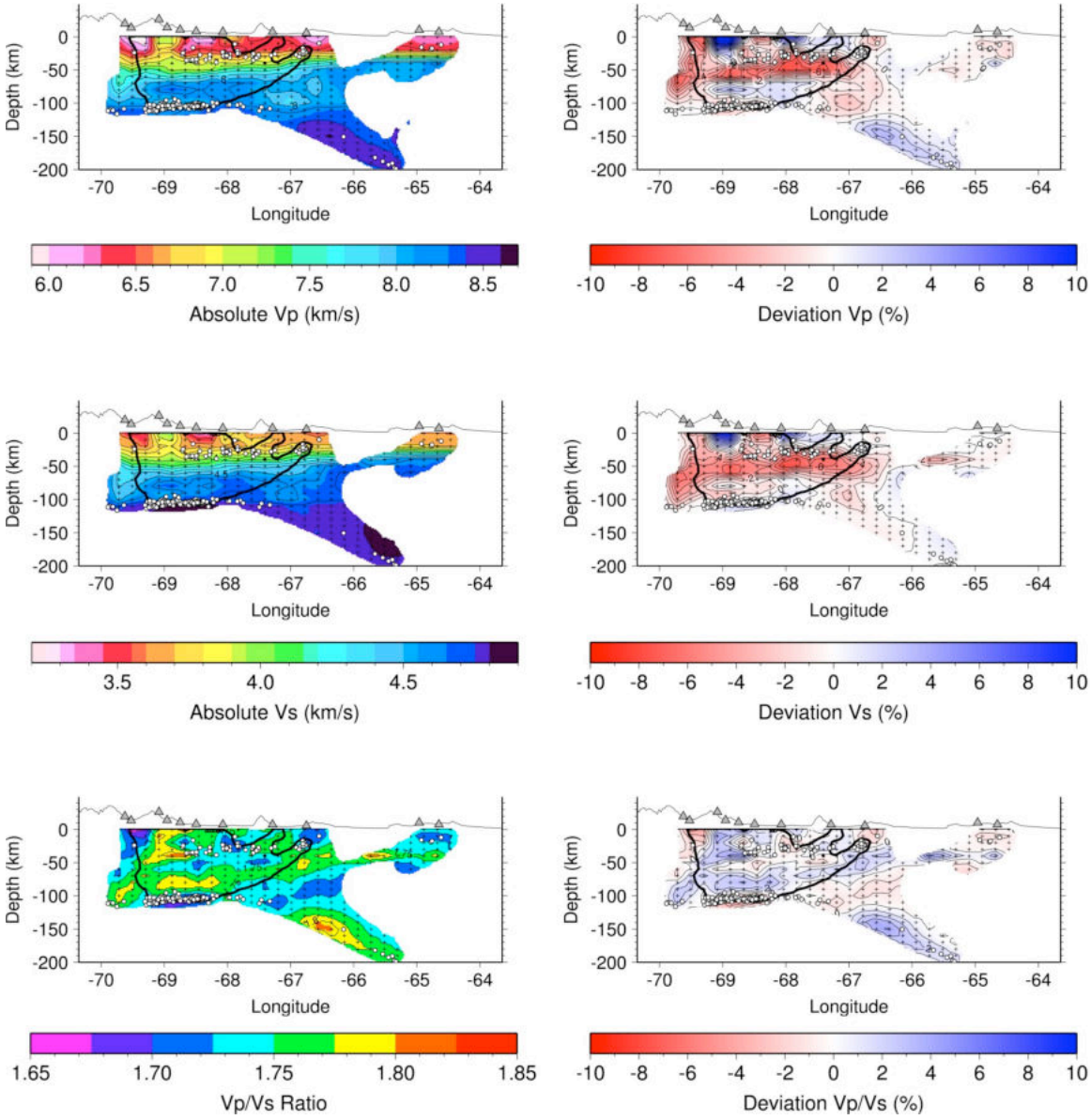

Figure 20. East-West cross sections through the absolute Vp, Vs, and Vp/Vs models at Latitude 31.0°S. Color scale is indicated below each plot. Location of profiles is indicated in Figure S18. Other symbols as in Figure 6.

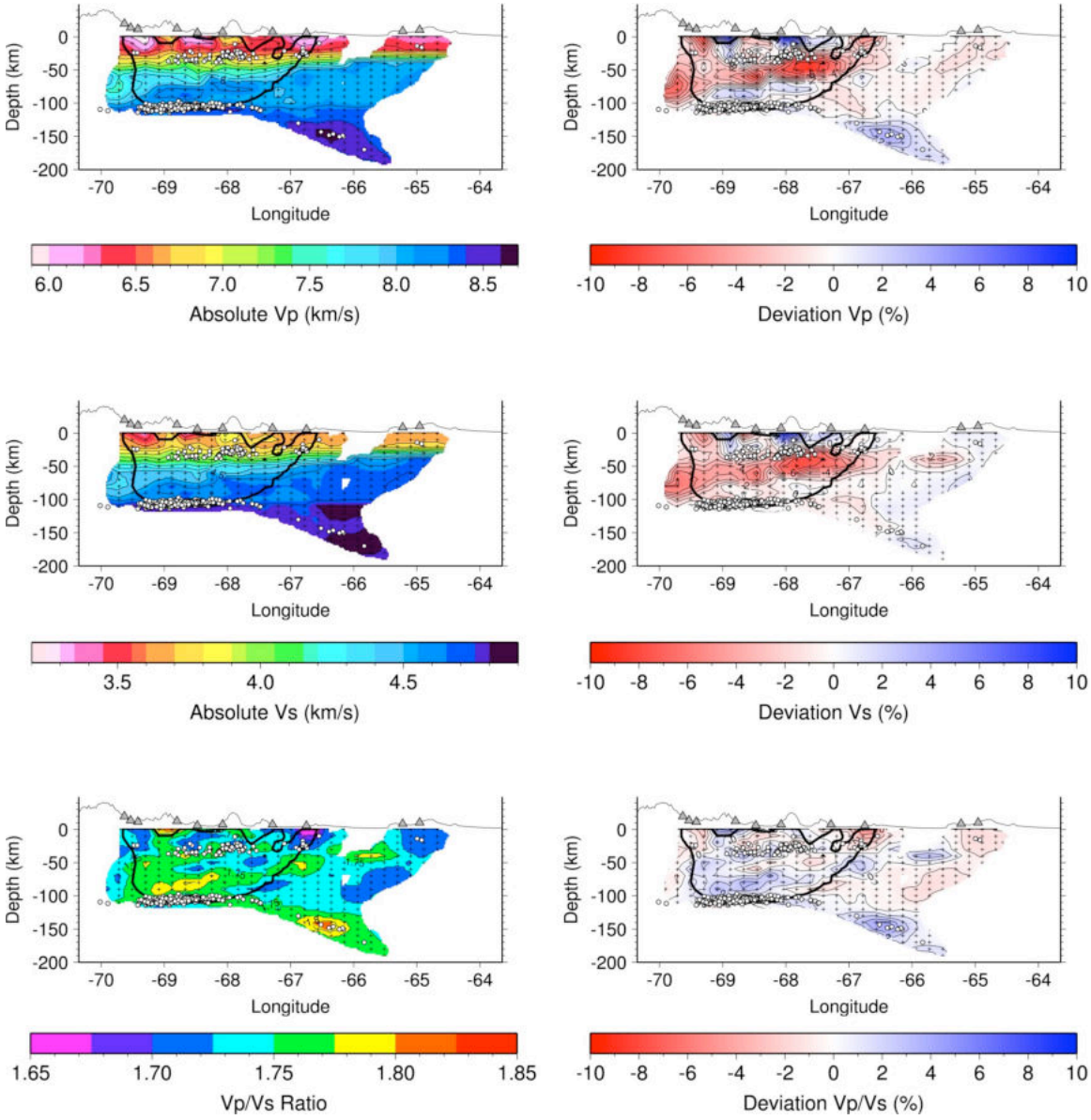

Figure 20. East-West cross sections through the absolute Vp, Vs, and Vp/Vs models at Latitude 31.2°S. Color scale is indicated below each plot. Location of profiles is indicated in Figure S18. Other symbols as in Figure 6.

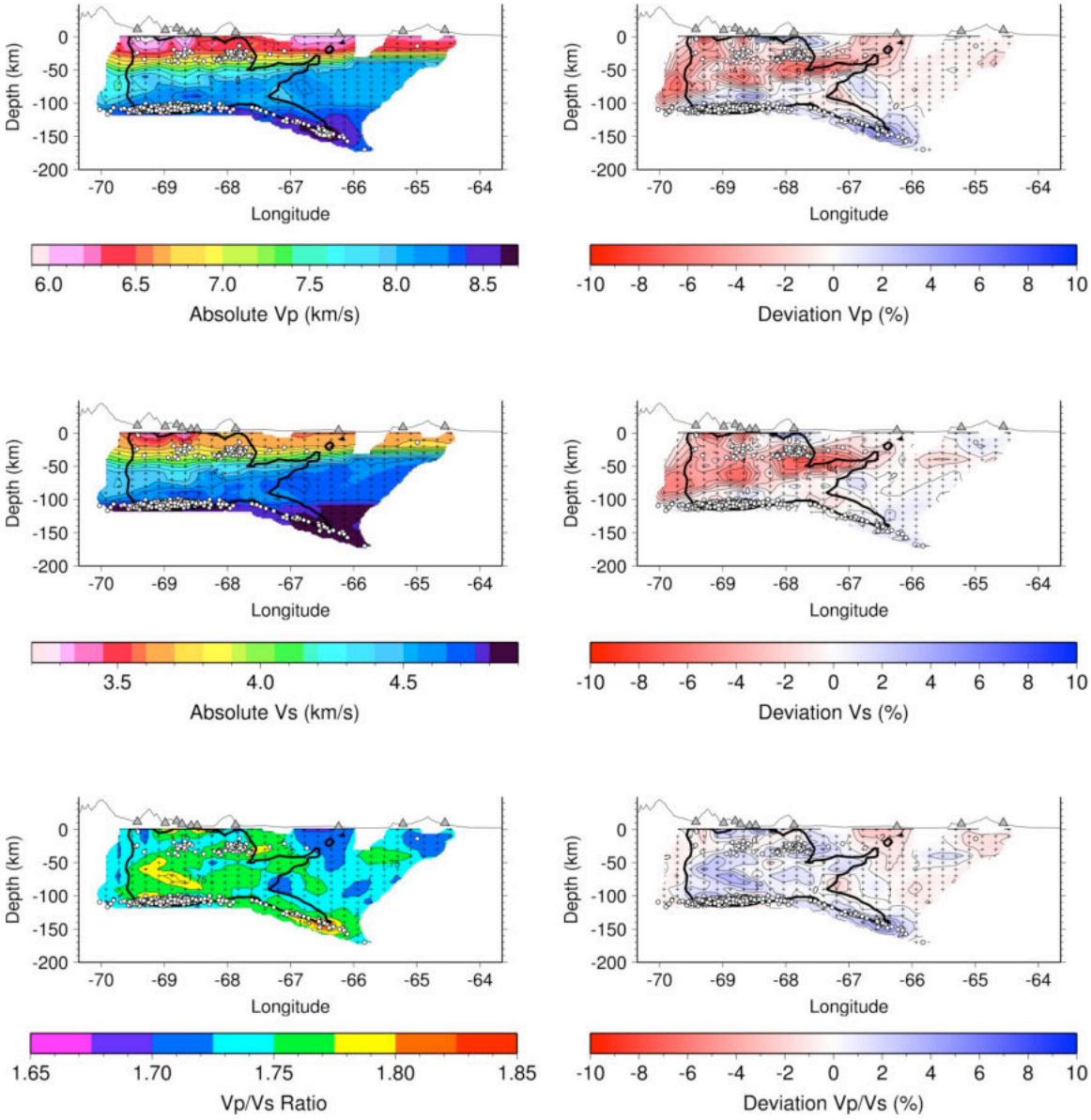

Figure 20. East-West cross sections through the absolute Vp, Vs, and Vp/Vs models at Latitude 31.4°S. Color scale is indicated below each plot. Location of profiles is indicated in Figure S18. Other symbols as in Figure 6.

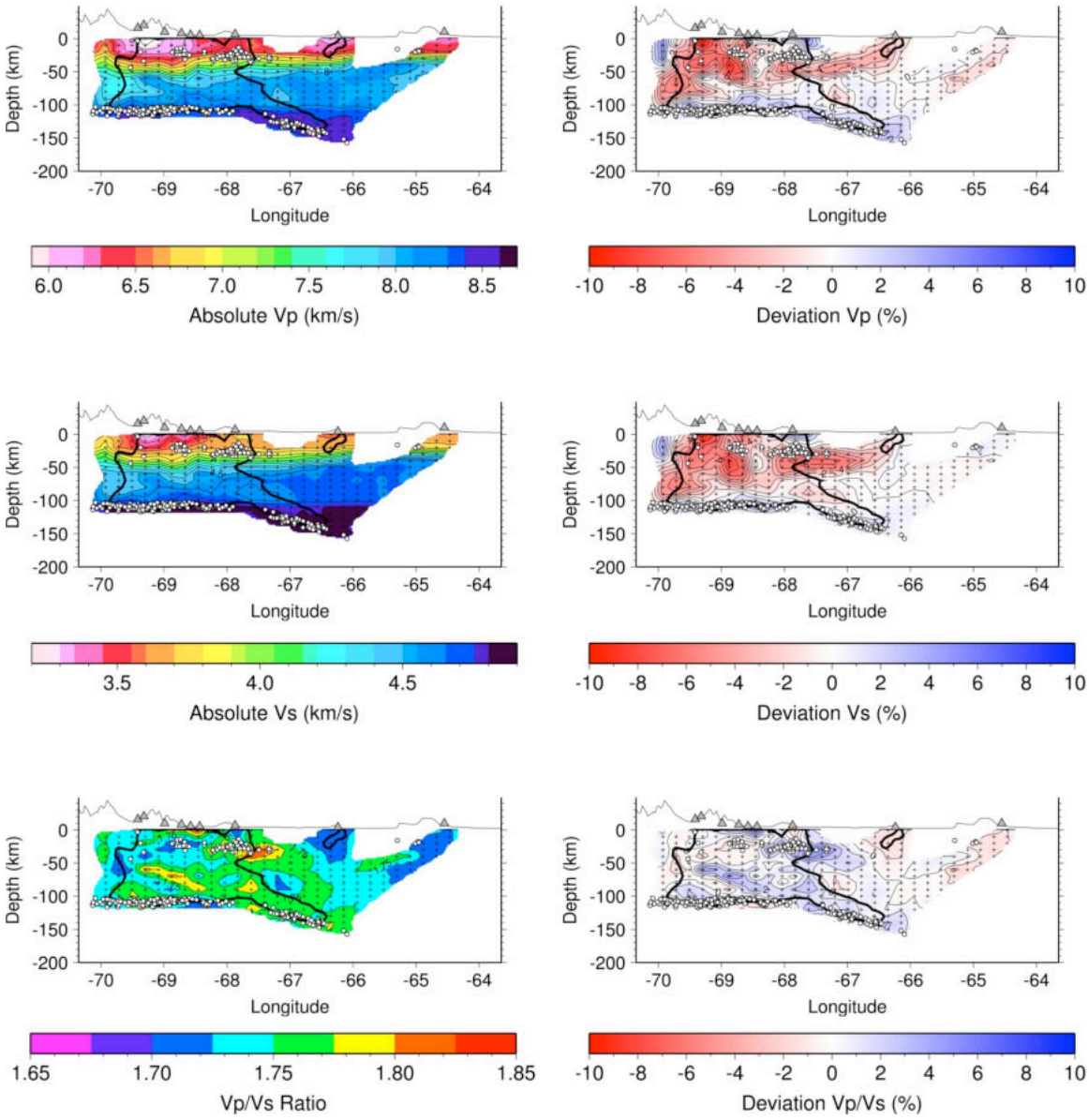

Figure 20. East-West cross sections through the absolute Vp, Vs, and Vp/Vs models at Latitude 31.6°S. Color scale is indicated below each plot. Location of profiles is indicated in Figure S18. Other symbols as in Figure 6.

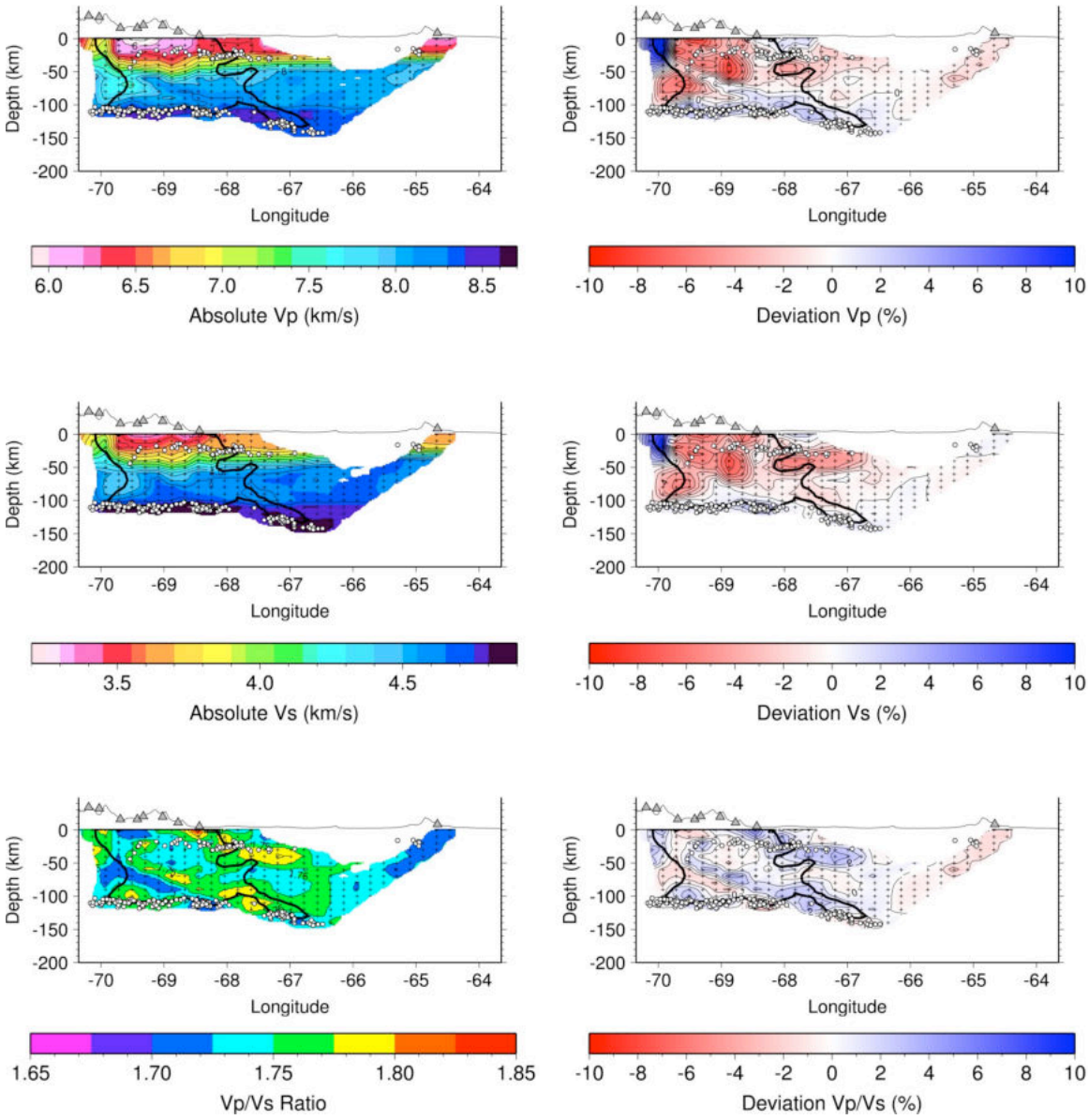

Figure 20. East-West cross sections through the absolute Vp, Vs, and Vp/Vs models at Latitude 31.8°S. Color scale is indicated below each plot. Location of profiles is indicated in Figure S18. Other symbols as in Figure 6.

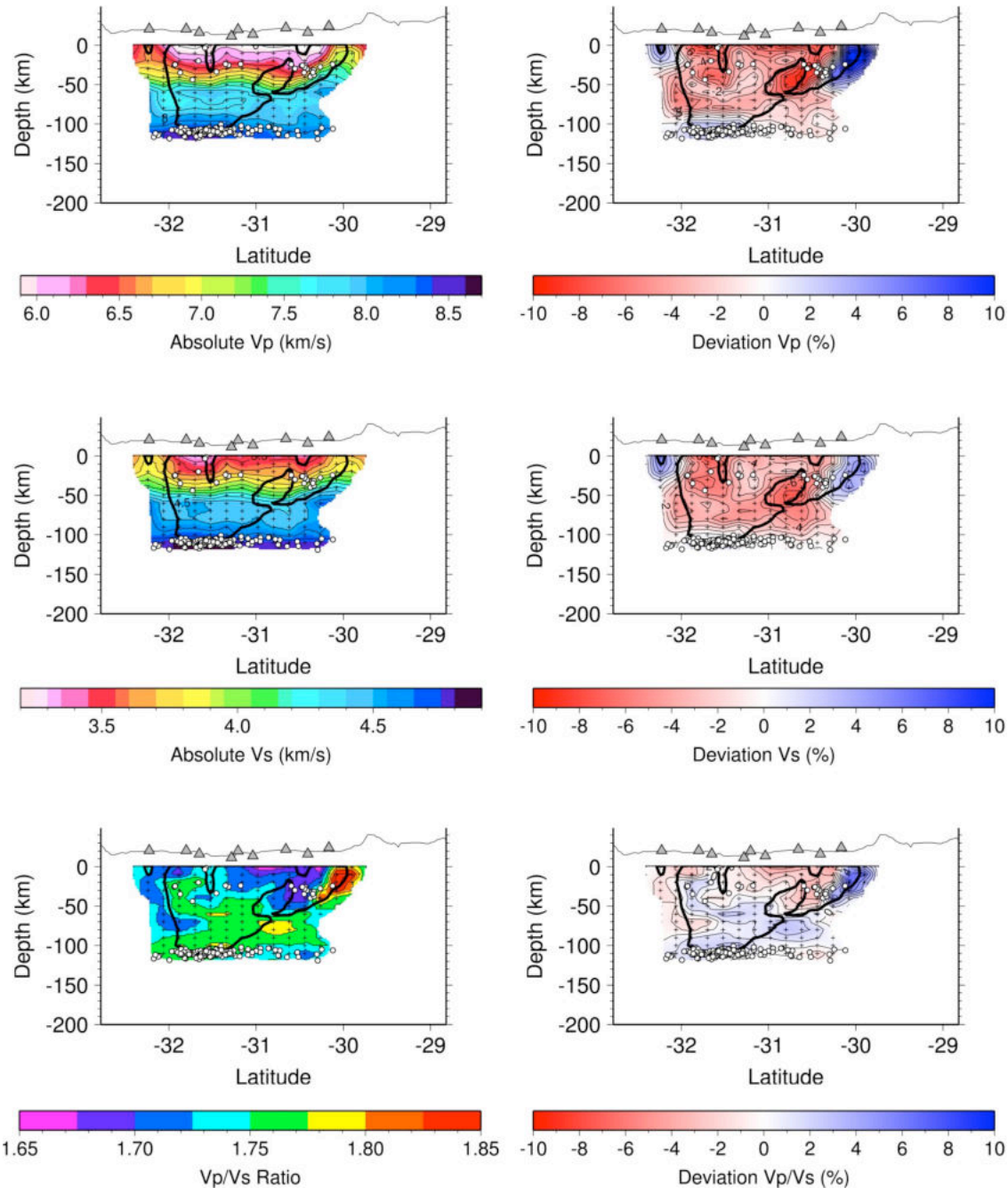

Figure S21. North-South cross sections through the Vp, Vs, and Vp/Vs models at Longitude 69.4°W. Color scale is indicated below each plot. Location of profiles is indicated in Figure S18. Other symbols as in Figure 6.

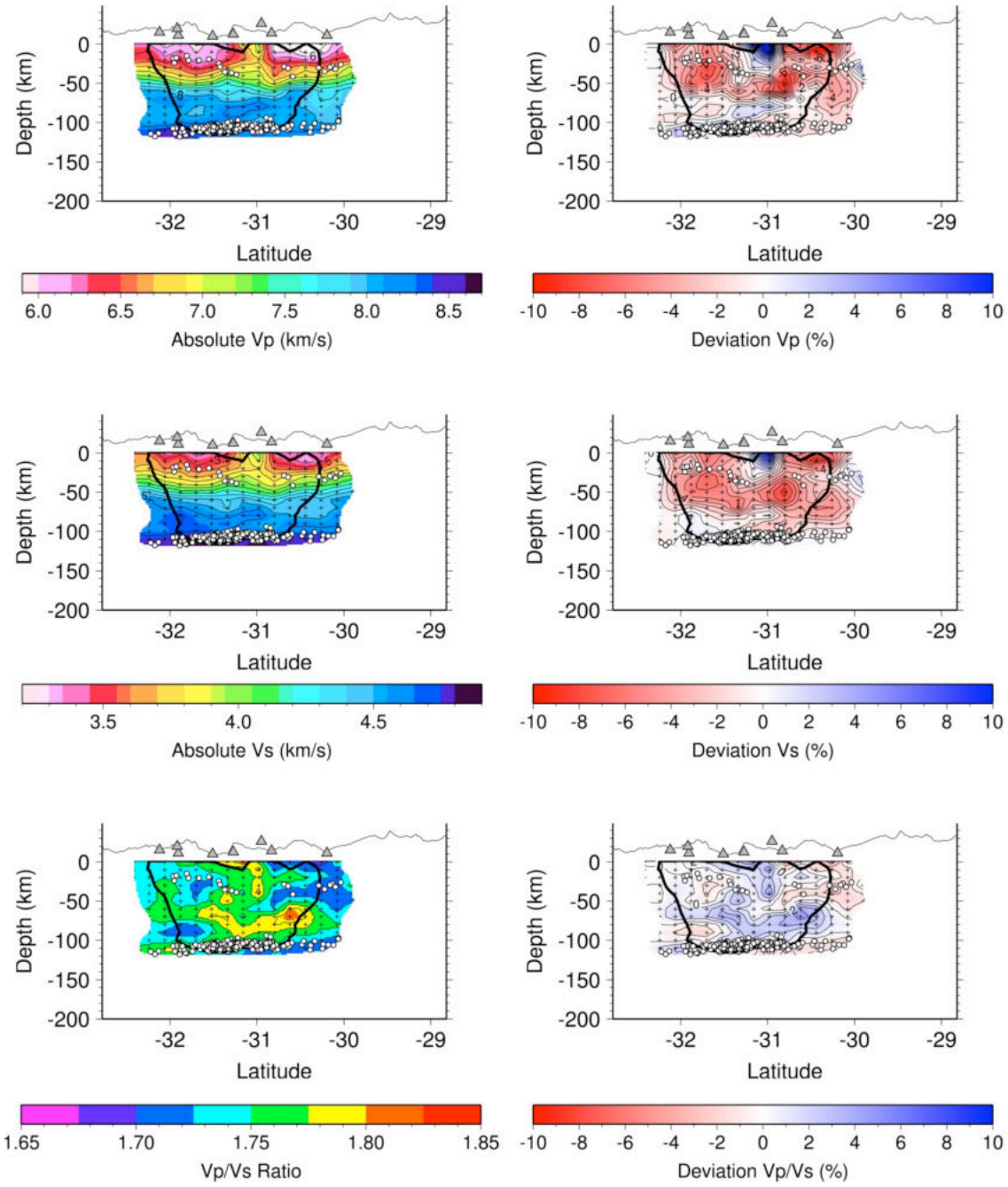

Figure S21. North-South cross sections through the Vp, Vs, and Vp/Vs models at Longitude 69.0°W. Color scale is indicated below each plot. Location of profiles is indicated in Figure S18. Other symbols as in Figure 6.

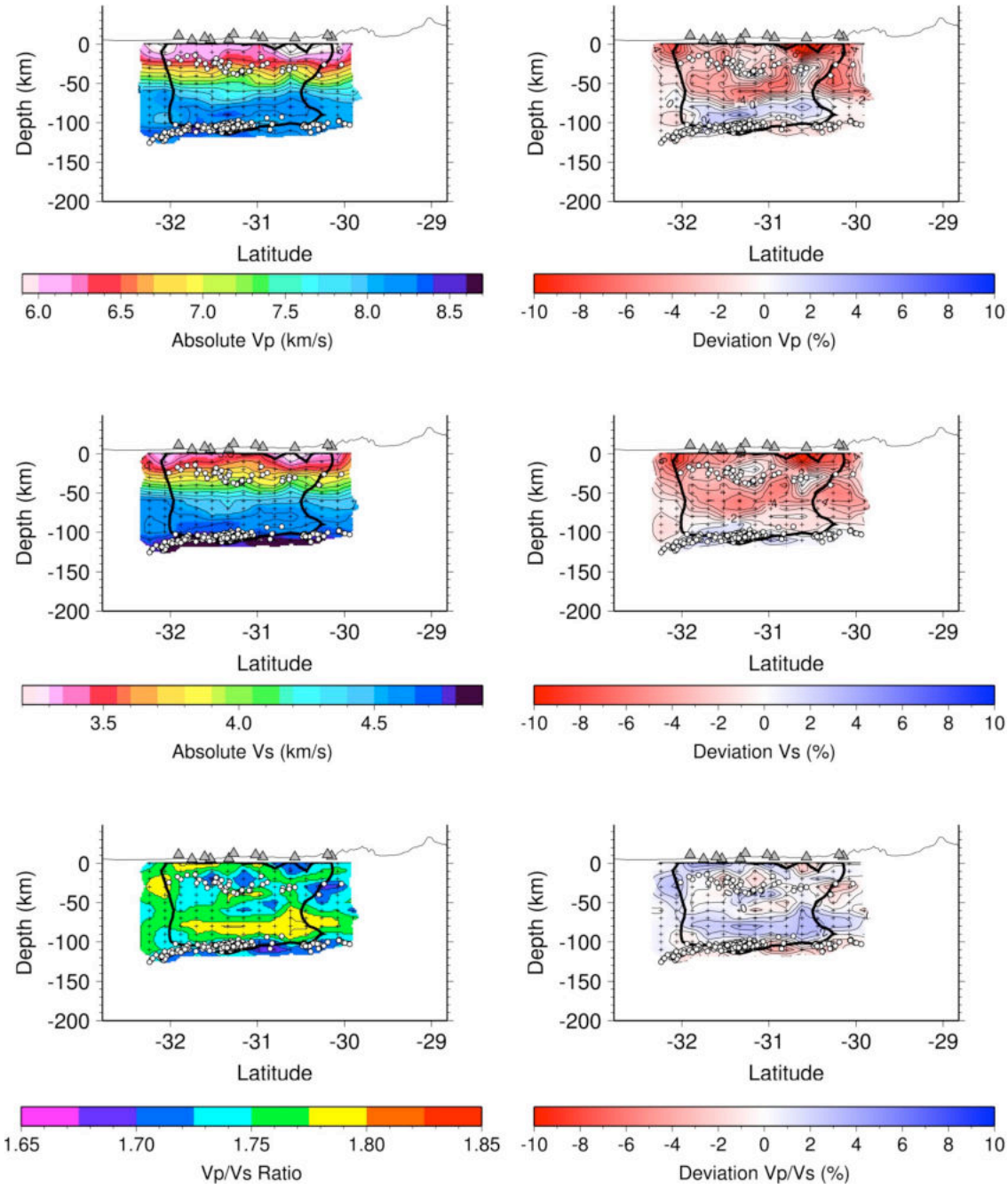

Figure S21. North-South cross sections through the Vp, Vs, and Vp/Vs models at Longitude 68.6°W. Color scale is indicated below each plot. Location of profiles is indicated in Figure S18. Other symbols as in Figure 6.

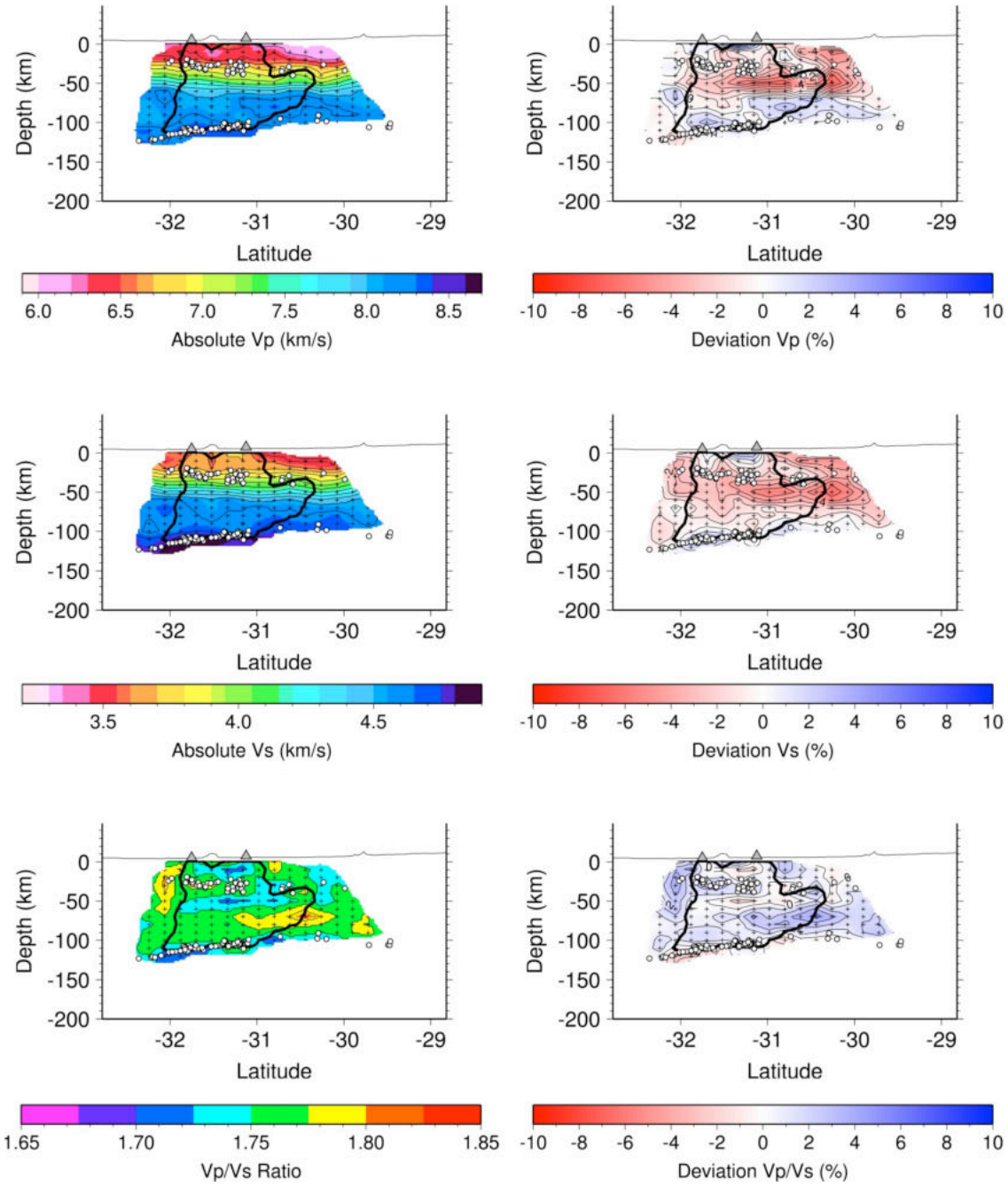

Figure S21. North-South cross sections through the Vp, Vs, and Vp/Vs models at Longitude 68.2°W. Color scale is indicated below each plot. Location of profiles is indicated in Figure S18. Other symbols as in Figure 6.

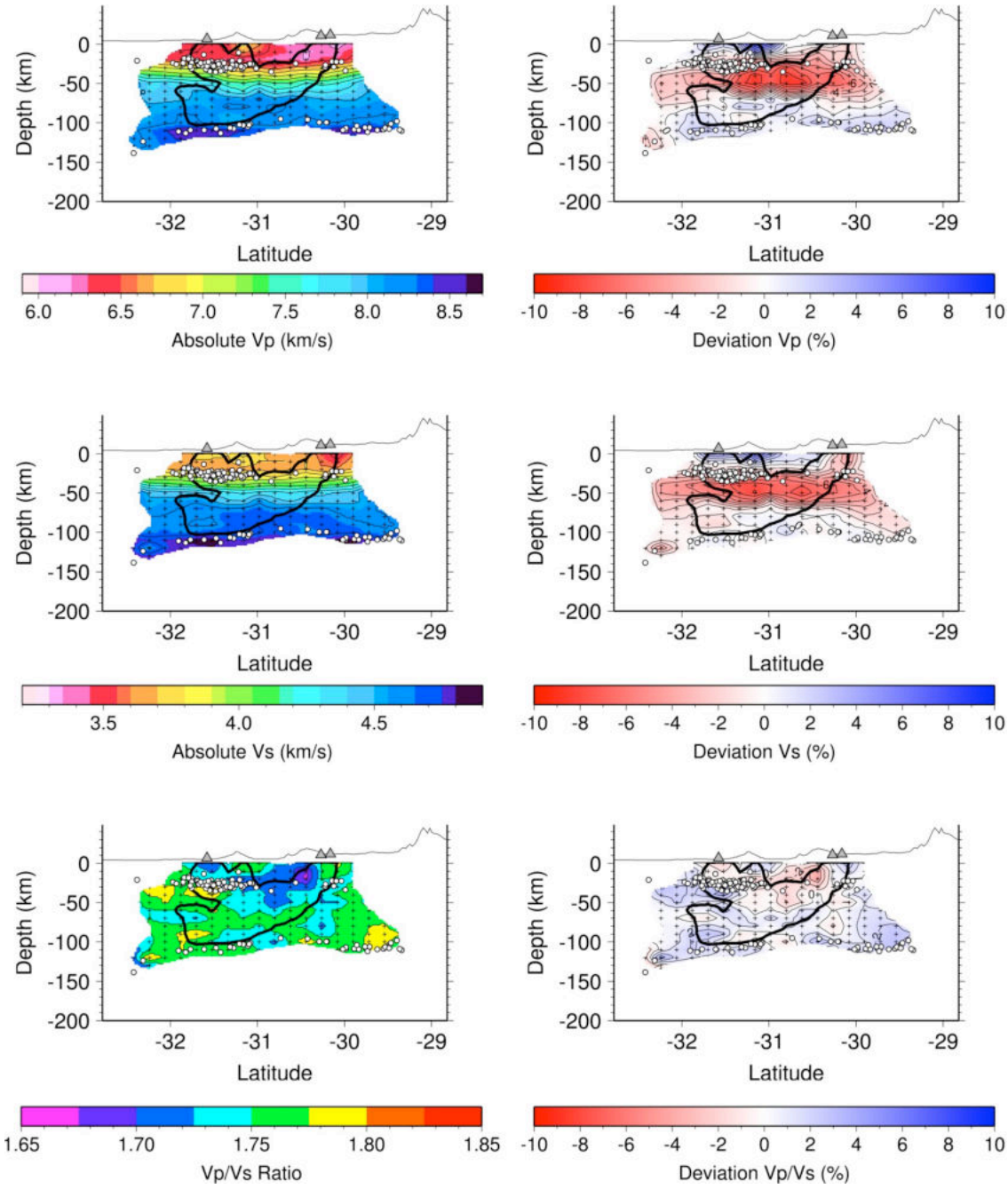

Figure S21. North-South cross sections through the Vp, Vs, and Vp/Vs models at Longitude 67.8°W. Color scale is indicated below each plot. Location of profiles is indicated in Figure S18. Other symbols as in Figure 6.

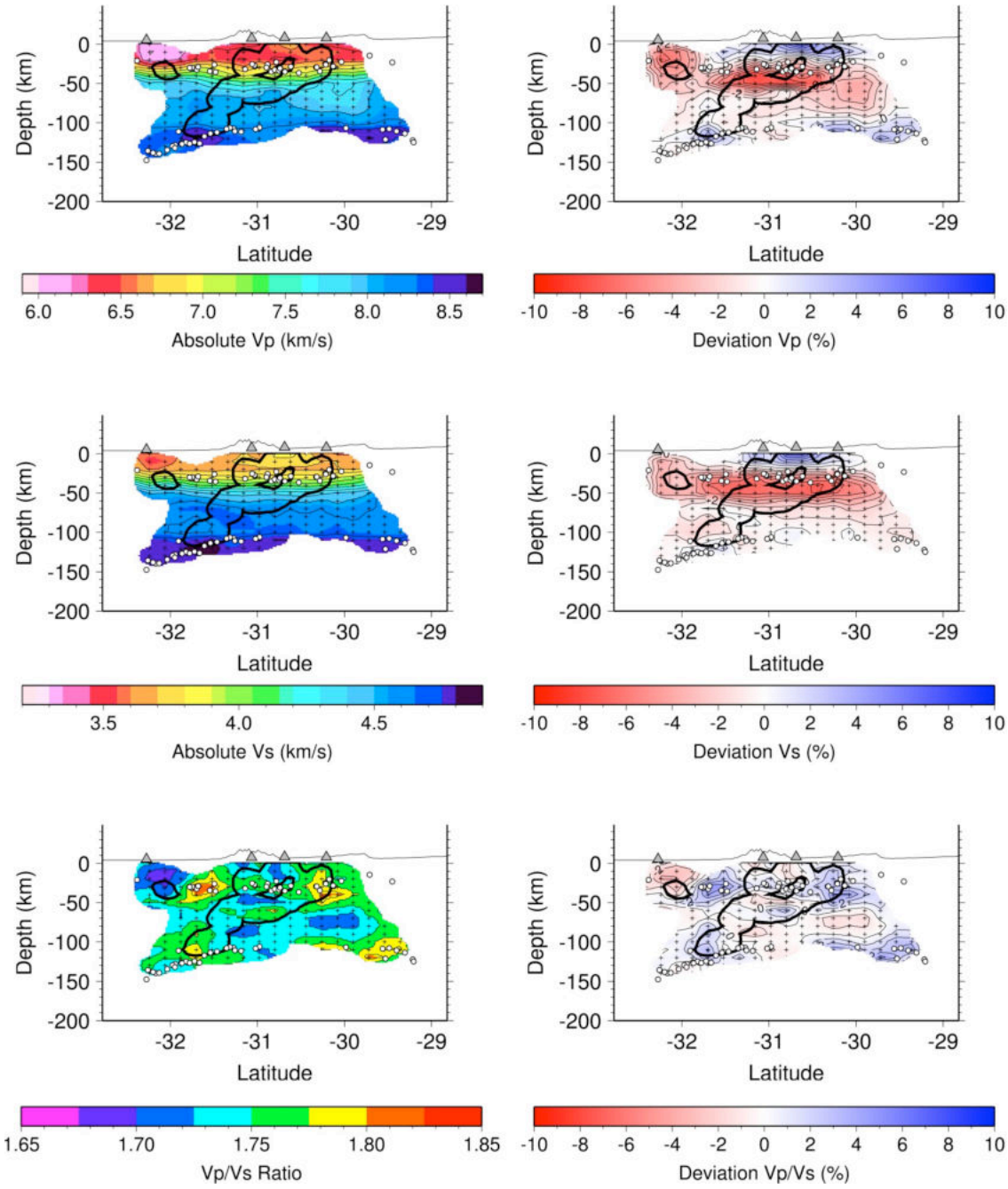

Figure S21. North-South cross sections through the Vp, Vs, and Vp/Vs models at Longitude 67.4°W. Color scale is indicated below each plot. Location of profiles is indicated in Figure S18. Other symbols as in Figure 6.

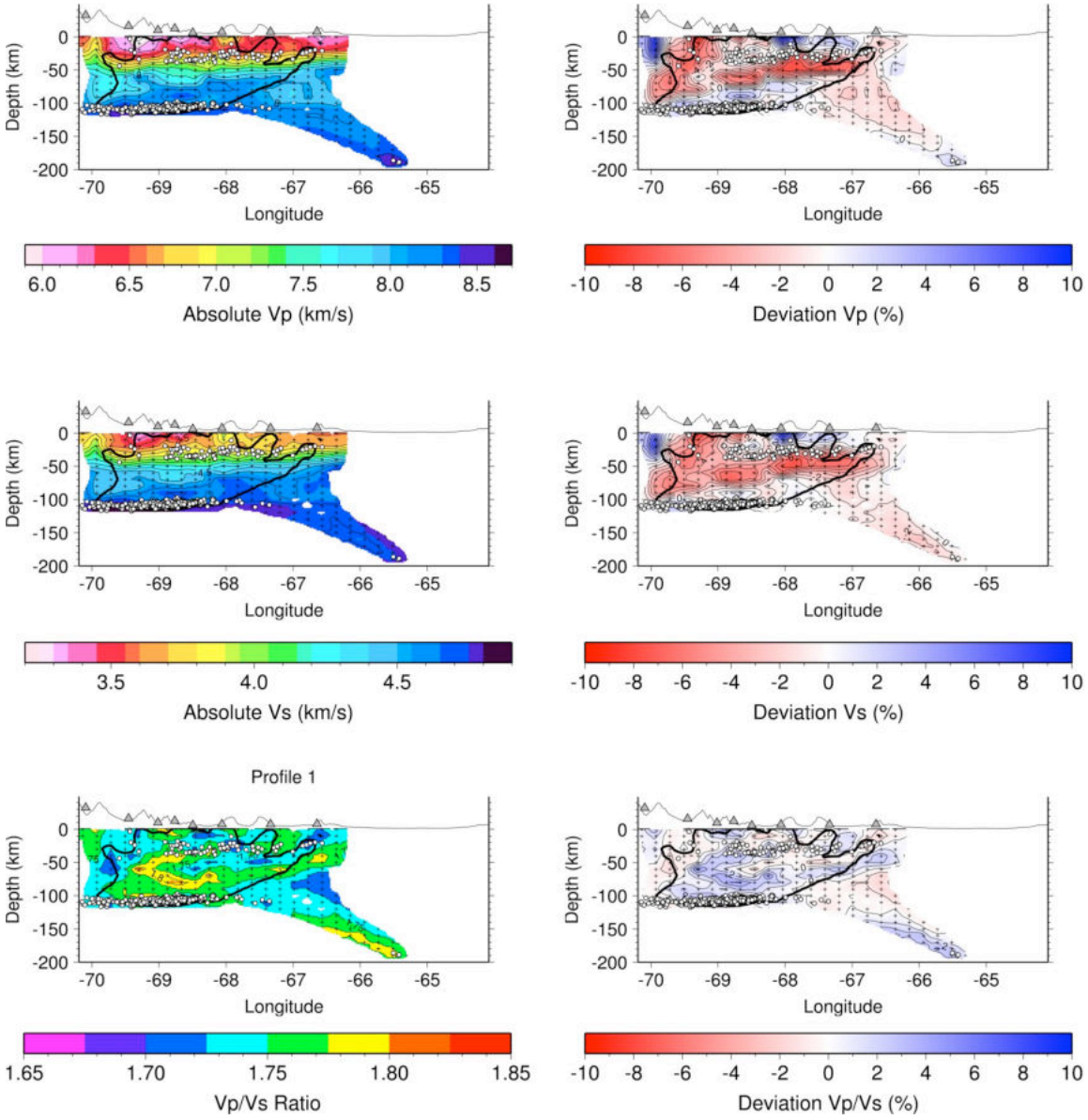

Figure S22. Vertical depth cross-section along Profile 1 through the Vp, Vs, and Vp/Vs models. Color scale is indicated below each plot. Location of profiles is indicated in Figure S18. Other symbols as in Figure 6.

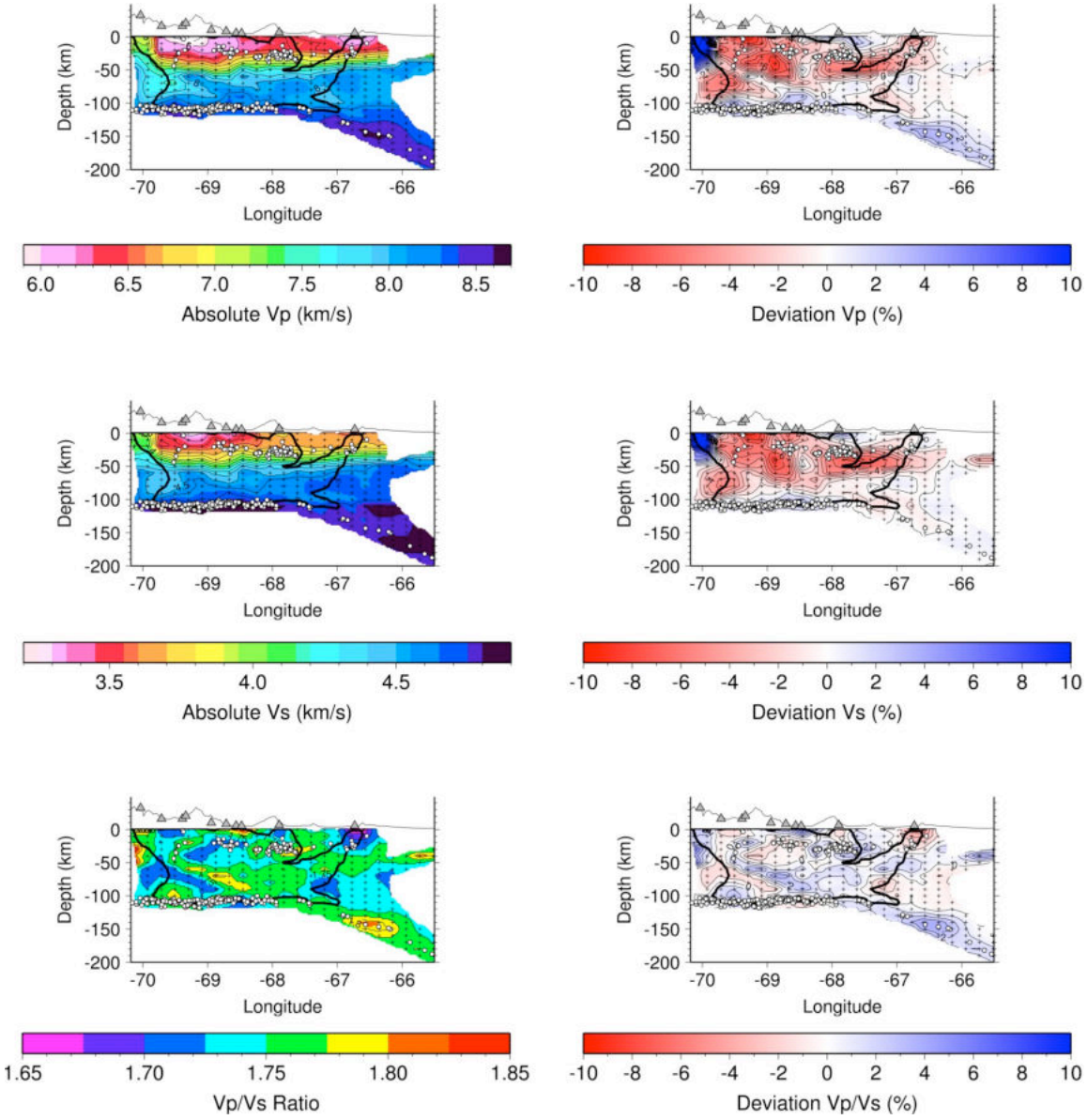

Figure S22. Vertical depth cross-section along Profile 2 through the Vp, Vs, and Vp/Vs models. Color scale is indicated below each plot. Location of profiles is indicated in Figure S18. Other symbols as in Figure 6.

APPENDIX C: GEOMETRY OF THE WADATI-BENIOFF ZONE AND DEFORMATION OF THE SUBDUCTING NAZCA PLATE IN THE PAMPEAN FLAT SLAB OF WEST-CENTRAL ARGENTINA

Lepolt Linkimer[1], Susan Beck[1], George Zandt[1], Patricia Alvarado[2], Megan Anderson[3], Hersh Gilbert[4], Kira Olsen[3]

[1]Department of Geosciences, University of Arizona

[2]Departamento de Geofísica y Astronomía, Universidad Nacional de San Juan-CONICET, Argentina

[3]Department of Geology, Colorado College

[4]Department of Earth and Atmospheric Sciences, Purdue University

Abstract

The descending Nazca Plate beneath west-central Argentina (latitude 30-33°S) has a sub-horizontal segment that extends ~300 km inland before resuming its descent into the mantle. This flat slab geometry is often explained as the result of the subduction of the incoming Juan Fernandez Ridge. We use data from the SIEMBRA (2007-2009) and ESP (2008-2010) broadband seismic deployments to study the geometry of the Wadati-Benioff Zone (WBZ) and the deformation of the subducting Nazca Plate in this region. We obtained high-quality earthquake locations using four different methods: a single event location, Minimum 1D model, double difference, and regional-scale double

difference tomography. Additionally, we present new contours for the slab seismicity and determined high-quality focal mechanism solutions from P-wave first motion polarities. Our new, more detailed contours show that the top of the WBZ of the Nazca Plate is nearly flat at ~100 km depth approximately within the region between latitude 28°S and 32°S and longitude 70°W and 68.5°W. Our earthquake locations show a 100 km-wide region of increased seismicity that coincides with the subducted path of the Juan Fernandez Ridge between longitude 70ºW and 68ºW, a seismicity gap along the projected path of Juan Fernandez Ridge to the northeast of longitude 68.5ºW, and two arms of descending seismicity on both sides of the seismicity gap. This non-uniform spatial distribution of the slab seismicity may reflect the variability in the hydration state of the subducting Nazca Plate with greater release of water from the subducted ridge region. We determine that the WBZ is a single layer of seismicity with thickness of 10-15 km and may correspond to dehydration of the oceanic mantle of the Nazca Plate. The abrupt decrease of earthquakes to the northeast of 68.5ºW may indicate that the upper mantle is completely de-serpentinized at this longitude perhaps after the Nazca Plate was intensively dehydrated in the region of the greatest concentration of seismicity. We found that the flat slab region is wider (~240 km) than the Juan Fernandez Ridge offshore (~100 km), and together with the shape of the slab contours may reflect the response of the geometry of the slab to the southward migration of the buoyant ridge. Focal mechanisms suggest that the slab is mostly under extension in the flat slab area. There is a region of mixed T-axis trends near where the slab descends abruptly to the south and northeast

which suggests that slab pull and ridge buoyancy may be important factors in the deformation of the slab.

1. Introduction and Tectonic Setting

The Wadati-Benioff Zone (WBZ) associated with the subducting Nazca Plate in the south-central Andes (latitude 28-36°S) exhibits strong variations in dip angle and down-dip length [Barazangi and Isacks, 1976; Cross and Pilger 1982; Jordan et al., 1983; Smalley and Isacks, 1987; Cahill and Isacks, 1992; Araujo and Suarez, 1994; Pardo et al., 2002a; Anderson et al., 2007]. North of 28°S and south of 33°S, the WBZ has a nearly constant ~25-30° dip towards the east under the South America Plate. North of 28°S, slab earthquakes are observed down to 600 km depth, whereas south of 33°S no seismicity below depths of 160 km is detected [Pardo et al., 2002a]. Between 30°S and 32°S, the WBZ dips ~30° near the trench, flattens for ~300 km at a depth of ~100 km, then inclines down to a maximum depth of ~200 km [Anderson et al., 2007; Pardo et al., 2002a]. In this study, we refer to this region of flat slab geometry as the Pampean flat slab (Fig. 1).

The northern (latitude ~28-30°S) and southern (latitude ~32-33°S) transition zones between normal and flat slab subduction are very different from one another [Pardo et al., 2002a]. The transition at 28°S is very gradual and is visible as the slab contours gradually widens until the flat slab reaches its broadest extent at ~32°S [e.g., Cahill and Isacks, 1992]. In contrast, the transition at 33°S is fairly abrupt, going from a very broad flat slab region to a normally dipping slab in less than 2° of latitude implying an abrupt flexure of the slab [e.g., Cahill and Isacks, 1992; Fuenzalida et al., 1992; Araujo and

Suarez, 1994]. Interestingly, no significant variation in the WBZ dip angle is observed for the shallow part of the subduction zone across central Chile below 45 km, even at places where major bathymetric features, such as the Juan Fernandez Ridge are subducted [Pardo et al., 2002a].

The Pampean flat slab is geographically correlated with the subduction of the aseismic Juan Fernandez Ridge; a ~100 km-wide chain of seamounts that extend for 900 km within the Nazca Plate [von Huene et al., 1997, Yáñez et al., 2001, 2002]. Much of the seismicity within the flat part of the subducting slab is clustered along the inferred extension of the Juan Fernandez Ridge into the subduction zone [Barazangi and Isacks 1976; Smalley and Isacks 1987; Yáñez et al., 2002; Anderson et al., 2007]. In addition, the region above the flat slab generates more crustal earthquakes and of a higher magnitude compared to adjacent segments, where the slab dips steeply [Gutscher et al., 2000; Alvarado et al., 2007]. Historically, three large (Mw > 6.8) damaging earthquakes have occurred in the crust above the flat slab segment in 1944, 1952, and 1977 [e.g., Langer and Hartzell, 1996; Alvarado and Beck, 2006]. In addition, this region is spatially correlated with the basement cored uplifts of the Sierras Pampeanas and the cessation of upper plate volcanism [e.g., Pilger, 1981; Ramos et al., 2002] and is relevant for understanding the geologic history of western United States as it is considered a modern analog of the Laramide deformation [Jordan and Allmendinger, 1986].

The flat slab geometry in the Pampean region is generally attributed to the subduction of over-thickened (13-19 km) oceanic crust of the Juan Fernandez Ridge, which may have provided the extra compositional buoyancy to cause slab flattening [e.g.,

Pilger, 1981; Yáñez et al., 2001; 2002; Espurt et a., 2008; Gans et al., 2011]. On the Nazca Plate, the Juan Fernandez Ridge strikes N80ºE, which results in a southward ridge migration of the ridge along the trench. The ridge-trench intersection point has moved only ~275 km in the last 12 Ma [Yáñez et al., 2001]. In contrast, during early Miocene a southward migration of the ridge-trench intersection was significantly faster, at a rate of ~200 km/Ma [Yáñez et al., 2001]. This southward migration correlates well with the eastward progression of deformation and arc volcanism, beginning between 20 and 18 Ma and increasing rapidly after 11 Ma [Kay and Abruzzi, 1996; Ramos et al., 2002]. Volcanism moved over 500 km east before ending completely between 5 and 1.9 Ma [Kay et al., 1988; Ramos et al., 2002; Kay and Mpodozis, 2002]. Currently, the modern active volcanic arc only occurs north of 28°S and south of 33°S where the subducting Nazca Plate dips steeply to the east [Kay and Abruzzi, 1996].

Additional detailed study of intermediate-depth seismicity in the Pampean flat slab region will help us refine previous slab contours of the subducting Nazca Plate and compute more high-quality focal mechanisms to better understand the deformation associated with slab earthquakes. With these goals in mind, we present new earthquake locations for intermediate-depth seismicity using data from the SIEMBRA and ESP broadband networks (Fig. 1), deployed in Pampean flat slab region between 2007 and 2010. These experiments are a follow-up to the CHile ARgentina Geophysical Experiment (CHARGE) that took place during 2000-2002 (Fig. 1) and two other temporary seismic networks: PANDA (1987-1988, Chiu et al. [1991]) and CHARSME (2002-2003, Pardo et al. [2002b]).

We obtained high quality earthquake locations from four different methods: single event location [Lienert et al., 1986], Minimum 1D model [Kissling et al., 1995], double difference [Waldhauser and Ellsworth, 2000], and a regional-scale double difference tomography [Zhang et al., 2004; Zhang and Thurber, 2006] and we compare our new determinations to the results from the CHARGE experiment [Anderson et al., 2007; Wagner et al., 2008]. Additionally, we determined high-quality focal mechanism solutions from P-wave first motion polarities. Our new locations are determined using a higher density network than previous studies, thus allows for a more thorough study of variations in depth of seismicity across the flat slab region. In addition, we have determined a larger number of higher quality focal mechanisms for understanding the deformation of the slab. Our earthquake locations confirm the WBZ observed from Cahill and Isacks [1992] and Anderson et al. [2007] and the resulting patterns from focal mechanisms are consistent with a buoyant ridge and slab pull hypothesis for the deformation of the slab in the flat region.

2. Data

We used data from two temporary broadband seismic deployments (Fig. 1): The SIerras pampeanas Experiment using a Multicomponent BRoadband Array (SIEMBRA) consisted of 40 broadband seismometers deployed between December 2007 and November of 2009 and the Eastern Sierras Pampeanas (ESP) experiment was deployed between August 2008 and August 2010 and consisted of 12 seismometers. Instrumentation for the SIEMBRA deployment was provided by the Program for Array

Seismic Studies of the Continental Lithosphere (PASSCAL) of the Incorporated Research Institutions for Seismology (IRIS) and for the ESP deployment by Purdue University and Colorado College.

We built an earthquake database from data recorded by SIEMBRA and ESP networks by using a short-term-average versus long-term-average (STA/LTA) trigger algorithm and by including all reported events from the catalogs of the Instituto Nacional de Prevención Sísmica (INPRES) and the Preliminary Determination Epicenter (PDE-NEIC) of the U.S. Geological Survey National Earthquake Information Center. Our database is composed of 1,562 earthquakes with a bimodal distribution in depth with hypocenters concentrated in the crust at depths of < 40 km and in the Nazca Plate at > 100 km depth (Fig 2). We handpicked P- and S-wave arrivals and polarities and weighted the picks based on the uncertainty caused by noise. The weighing scheme for phase reading ranges from quality 0, corresponding to a reading uncertainty of < 0.10 s to quality 4 which correspond to > 0.30 s. Phase readings were accomplished using the program MULPLT included in the software package SEISAN [Havskov and Ottemöeller, 1999; Ottemöeller et al., 2011]. More details about our database can be found in Linkimer et al. [2011].

3. Methods

Locating an earthquake is a typical inverse problem where the hypocentral parameters and origin time are the unknowns estimated from observed travel-times. Earthquake location algorithms are usually founded on Geiger [1912] and are based on

the linearization of the travel time equation in a first order Taylor series that relates the difference between the observed and predicted travel time to unknown adjustments in the hypocentral coordinates through the partial derivatives of travel time with respect to the unknowns. In this study, we obtained hypocentral parameters using four different methods (Figs. 2-7): single event location [Lienert et al., 1986], Minimum 1D model [Kissling et al., 1995], double difference [Waldhauser and Ellsworth, 2000], and regional-scale double difference tomography [Zhang et al., 2004; Zhang and Thurber, 2006]. To ensure well-constrained solutions, we applied these methods to 1,092 earthquakes with the following characteristics: an azimuthal gap of observations (GAP) $\leq$ 180°, have at least 10 P-wave and 6 S-wave arrival observations, and include at least one observation within a distance of 1.5 times the focal depth.

Initially, single event locations were determined with the program HYP [Lienert and Havskov 1995], a modified version of HYPOCENTER [Lienert et al., 1986], using a simple 1D velocity model based on the velocity models used by Smalley et al. [1993] and Anderson et al. [2007]. This preliminary 1D model has layers at 0, 50, and 110 km with corresponding velocities of 6.20, 8.00, and 8.11 km/s, and a Vp/Vs ratio of 1.75, 1.76, and 1.78, respectively. The program HYP uses the same adaptively-damped least-square solution for the hypocenter location problem from HYPOCENTER [Lienert et al., 1986], and additionally allows the use of azimuth data, weights outliers using the bi-square residual technique, forces the calculation of specific phases such as Pg and Pn, and can locate events at distances greater than 500 km.

The single event locations obtained from HYP, were used as starting locations to obtained a Minimum 1D Model using the program VELEST [Kissling et al., 1995]. The concept of the Minimum 1D model incorporates the iterative simultaneous inversion of velocity and hypocenter parameters, and is complemented by station corrections that account for lateral velocity heterogeneity [Kissling, 1988; Kissling et al., 1994]. A total of 39,112 P-wave observations were used to invert for the P-wave Minimum 1D Model. We first evaluated our earthquake dataset by performing several inversions using as starting velocity models, the velocity models presented by Smalley et al. [1993] and Anderson et al. [2007]. We found that the model that produces the minimum RMS has layers at 0, 20, 40, 60, and 100 km with resulting P-wave velocities of 6.25, 6.46, 7.19, 8.10, and 8.32 km/s, respectively. This resulting velocity model and station corrections were used to relocate the larger subset of 1,562 earthquakes that were used to generate WBZ contours in the regions outside the network coverage. More details about the Minimum 1D Model calculation can be found in Linkimer et al. [2011].

After performing the 1D inversion we relocated the events with a double difference algorithm by using the program HypoDD [Waldhauser, 2001]. One advantage of the double-difference algorithm is that if nearby events occur along a single structure, this multiple-event location method can better locate these events in relation to each other to more precisely resolve the shape of that structure [Waldhauser and Ellsworth, 2000]. HypoDD uses both absolute and differential travel times. The absolute arrival times correspond to the first arrival times directly picked on the seismograms. The differential times were obtained by directly subtracting travel times from event pairs with inter-event

distance of < 20 km at common stations located within 400 km from the earthquake cluster centroid. In our differential time catalogue, any event is linked to a maximum of 10 neighboring events by at least eight pair-wise observations, which resulted in an average separation between strongly linked events of ~9 km.

The resulting locations from the Minimum 1D model were also used as starting locations to use a regional-scale Double Difference (DD) tomography algorithm [tomoFDD; Zhang et al., 2004; Zhang and Thurber, 2006]. This program solves jointly for 3D velocity structure and earthquake locations using a combination of absolute arrival times and differential times, similar to the earthquake location program HypoDD. More details about the 3D inversion can be found in Linkimer et al. [2011].

There is a residual misfit improvement from the single event location to the 3D inversion (Fig. 5). As expected, the best fit occurs from the 3D inversion, for which travel time residuals are drastically reduced and sharply peaked symmetrically around zero. The RMS and variance of travel time residuals after the 1D inversion decreases from 0.430 s to 0.186 s, and from 0.202 s to 0.038 s, respectively. For the 3D inversion, the RMS and variance of travel time residuals decreases from 0.526 to 0.138 s, and from 0.3057 s to 0.0019 s, respectively.

In addition to earthquake locations, we determined first-motion focal mechanisms by using the program FOCMEC [Snoke et al., 1984] included in the SEISAN software package [Havskov and Ottemöeller, 1999; Ottemöeller et al., 2011]. The program uses P-wave polarity as input and take-off angles that were calculated using a layered medium resulted from the Minimum 1D model. The program makes a grid-search of the focal

sphere and finds how many polarities fit each possible solution. On average, 33 P-wave polarities were used per event and the search for solutions was controlled by a grid-search every five degrees to find zero polarity errors. The quality of the focal mechanisms has been classified according to the number of available polarities, their azimuthal distribution, the number of polarity errors, and number of the possible solutions. We interpreted results from the best quality focal mechanisms, which are characterized by well-constrained nodal planes and zero polarity errors. Figure 7 shows an example of a high-quality solution, where we observed there is good agreement between the nodal plane positions and emergent and impulsive P-wave arrivals.

4. Earthquake Locations

Unless noted, we describe the earthquake locations resulting from the regional-scale double difference tomography, which we consider the best locations based on the residual misfit improvement compared to the other methods used (Fig. 5). In map view, our recorded slab seismicity is mainly concentrated in three zones (Fig. 3a). The greatest concentration of slab seismicity occurs along the expected position of the Juan Fernandez Ridge, from longitude 70ºW to 68.5ºW and corresponds to a ~100 km-wide "finger" of earthquakes. Seismicity abruptly decreases to the northeast of this main cluster, at approximately longitude 68.5ºW. Two more clusters of slab earthquakes occur on both sides of the projected path of Juan Fernandez Ridge and we refer them as the northern and southern "arms" of seismicity. Unfortunately, part of the seismicity in the northern

arm occurs outside the region of network coverage; therefore we consider these locations of lower quality.

Between the two arms of seismicity there is an prominent gap. This seismicity gap is also visible in the earthquakes recorded during the CHARGE experiment (Fig. 3b) and in the PDE catalog from 1973-2010 (Fig. 3c). Given that we have several stations within the gap of seismicity, we performed a careful search for slab earthquakes in this region by tuning the STA/LTA trigger algorithm to detect smaller events. Surprisingly, we did not find any more slab earthquakes within the gap as we did for the two arms of seismicity (Fig. 3A).

Although our event locations obtained from four different methods are quite similar, there are some differences between them in detail (Fig. 4). Initial single event locations (Fig 4a) suggest that, within the flat slab region (longitude from 70°W to 68°W), there is a progressive shallowing of the seismicity towards the northeast, opposite to the direction of subduction. This feature has been widely observed in previous studies [e.g., Smalley and Isacks, 1987; Pujol et al., 1991; Reta, 1992; Anderson et al., 2007]. According Pujol et al. [1991], earthquakes located with a Joint Hypocenter Determination (JHD) method seem to be corrected to a flat plane and the anomalous updip in the WBZ was explained as the result of large velocity variations across the Precordillera. Similarly, Smalley and Isacks [1987] interpreted the westward dip as the result of velocity variations, but related to a dipping Moho about 6° to the west.

We found that when earthquakes are relocated by deriving a Minimum 1D Model, applying a double difference algorithm using the Minimum 1D model as a layered model,

or when applying a DD tomography using a 3D velocity model, earthquakes flatten out aligning more closely at ~100 km depth (Fig 4b, 4c, 4d). In these re-locations, earthquakes still retain a small westward dip, especially to the north of the projected path of Juan Fernandez Ridge. Even when the ‘‘reverse dip’’ is less obvious, events seem to have average deeper depths below the main cordillera and Precordillera (west of longitude 69ºW) than those located farther east below Pie de Palo (longitude ~68ºW). The slight westward dip still retained within our tomography locations likely reflects true variations in earthquake depth resolved by our study and may suggest that the subducted Nazca Plate has some slight “topography” due to the ridge buoyancy.

Using our earthquake locations, we present new contours to describe the shape of the subducting Nazca slab (Fig. 6). For calculating the slab contours, we used the high-quality locations resulted from the DD tomography in the area within network coverage. In addition, we performed single event locations for the earthquakes we detected in the region around the SIEMBRA and ESP networks, which we incorporated into the contour determinations to get a broader picture of the slab contours. We acknowledge that these locations have lower quality so we present them with different color and used dashed lines for the contours outside the networks (Fig. 6). We gridded the region every 0.2 degree in latitude and longitude and calculated both the mean and shallowest depth within each grid cell and generated the contours from these grid. In Figure 6 we show the contours to the shallowest depth of the WBZ.

Our new, more detailed contours show that the top of the WBZ of the Nazca Plate is nearly flat at ~100 km depth approximately within the region between latitude 28°S

and 32°S and longitude 70°W and 68.5°W. Overall, our relocated seismicity is in agreement with that obtained by Anderson et al. [2007] using multiple event locations and Wagner et al. [2008] from seismic tomography (Fig. 7). However, now with more stations in the region of latitude 29°S and 30°S we were able to detect slab events in this region at depths of ~100 km. During the CHARGE experiment, very few events were detected in this region; therefore, the 100 km contour has a shape of a "finger" [Anderson et al., 2007], similar to the region of abundant seismicity we also detected along the expected Juan Fernandez Ridge track. Our new slab contours show a broader flat region similar to the one inferred by Cahill and Isaacs [1992]. This wider flat slab region is consistent with receiver function observations by Gans et al. [2011] who tracked the flat slab across a broader region than that expected from the contours of Anderson et al. [2007].

In cross section, the slab earthquakes can be described in three segments (Fig. 6, 6). The westernmost segment dips 25-30° to the east and goes from an average depth of ~80 to ~100 km. In the central segment the dip of the WBZ drastically diminishes and gets almost flat for ~300 km. The easternmost segment dips again 25-30° to the east and varies from an average depth of ~100 to ~200 km. Across the region, our earthquake locations show a single plane of slab seismicity with a thickness of ~10-15 km (Fig. 6). This is thinner than the estimations of ~50 km by Pardo et al. [2002a] and ~20 km by Anderson et al. [2007] for the Pampean flat slab region.

5 Focal Mechanisms

We computed 411 high-quality focal mechanisms with an average of 33 polarities per event. Figure 9 shows the focal mechanisms classified by the rake angle in Normal, Normal Oblique, Strike-Slip, and Reverse-Oblique, illustrating the predominance of normal mechanisms (80 % of our solutions are normal) and indicating that the slab is mostly under extension. Locally, there is the occurrence of strike-slip faults and oblique faults with a reverse component. Very interestingly, the southern "arm" of seismicity exhibits mostly oblique solution but very few normal events that are abundant in the rest of the region.

Figure 10, shows the different trends in the T axes present in the area. We see that there is a region where all trends in T axes coexist near where the seismicity seems to be the shallowest. Also, the slab is abruptly descending to the NE and south of this region of mixed T axes. The majority of focal mechanisms are consistent with slab pull away from the subducted portion of the presumably more buoyant ridge.

A similar pattern in the slab focal mechanisms was found by Pardo et al. [2002a} and Anderson et al. [2007]. Pardo et al. [2002a] found that the intermediate depth seismicity that clusters along the subducted Juan Fernandez Ridge shows normal events with T-axis along the slab and also strike-slip mechanisms with T-axis with N-S orientation, which cannot be explained by only slab pull forces. According to these authors, these mechanisms might be related to reactivation of pre-existing faults in the thick oceanic crust, created near the trench and outer-rise by the interaction of the Juan Fernandez Ridge subduction. Pardo et al. [2002a] also concluded that the main force

acting over the slab in the sub-horizontal subduction region may be the result of the slab pull and a N-S extension related to the slab flattening due to buoyant forces.

Anderson et al. [2007] found that regionally, around the flat slab area, focal mechanism solutions have a tensional axis that is sub-perpendicular to the trench, indicating that the likely mechanism for deformation is slab pull, similar to conclusions from previous studies [Cahill and Isacks, 1992; Reta, 1992; Araujo and Suarez, 1994; Pardo et al., 2002a; Brudzinski and Chen, 2005]. However, Anderson et al. [2007] found that when pairing the focal mechanisms with the slab contours within the flat slab area, it reveals a consistent pattern for T-axes that are not oriented completely perpendicular to the trench. Between 33°S and 36°S, most sub-horizontal T-axes are trench-normal with a few exceptions, however, around 32°S, the predominant T-axis direction is no longer trench normal, but perpendicular to the local strike of the slab. This observation is still quite consistent with the slab pull mechanism because of the changing slab geometry.

6. Discussion

The mechanism responsible for intermediate-depth seismicity in the WBZ has been a subject of discussion ever since its discovery [Wadati et al., 1928; 1935; Benioff, 1955]. At depths greater than ~30 km, lithostatic pressure is so great that it should prevent brittle failure to occur so that intermediate-depth seismicity is commonly explained as the result of slab dehydration [Kirby et al., 1996, Hacker et al., 2003]. As the slab sinks, metamorphic reactions liberate fluids from hydrous phases. This dehydration increases pore pressure, reducing normal stress enough to bring the system into the brittle

regime. Earthquakes could be generated by dehydration embrittlement creating new faults [Zhang, J., et al., 2004] or reactivating pre-existing weak zones [Peacock, 2001; Warren et al., 2008]. The conceptual model of Ranero et al. [2005] for intermediate-depth seismicity proposes that it starts between 60-80 km, when dehydration of oceanic crust causes concentration of earthquakes on the upper part of slab. Deeper than ~100 km, eclogitization is completed; here or slightly deeper dehydration of slab mantle occurs generating seismicity within the upper slab mantle. Ranero et al. [2005], however, pointed out that this model might not be applicable to subduction of young lithosphere and broad aseismic ridges.

In the Pampean flat slab region, the slab seismicity is not uniformly distributed in map view or at depth (Fig. 3a, 4). The number of earthquakes is higher along the projected path of the Juan Fernandez Ridge where Pardo et al. [2002a] observed that the seismicity is more intense and the seismic moment released is larger than that relative to the adjacent segments. Anderson et al. [2007] also observed that the expected position of the Juan Fernandez Ridge within the subducted slab is coincident with the greatest concentration of seismicity in the flat slab region.

The spatial correlation between the projected path of the subducted Juan Fernandez Ridge and the greatest concentration of seismicity implies a possible connection. However, there are more earthquake clusters that are not located on the projected path of the ridge (Fig. 3). Additionally, the seismicity abruptly decreases along the projected path of subducted Juan Fernandez Ridge, to the northeast of longitude 68.5ºW. If the slab seismicity occurs as the result of dehydration embrittlement, then the

non-uniform spatial distribution of the slab seismicity may suggest that there is variability in the hydration state of the subducting Nazca Plate along the strike of the margin with greater release of water from the subducted ridge.

Ranero et al. [2005] statistically compared the strike of bending-related faults in the oceanic plate with that of the nodal planes of intermediate-depth earthquakes (> 70 km) along segments of the Chile subduction zone and attributed most of the intra-slab seismicity to reactivation of faults rather than formation of new ones. Ranero et al. [2005] also found higher rates of intra-slab seismicity associated with segments with more pervasive trench faulting, which supports the idea that the region of high slab seismicity may correspond to a more faulted (and hydrated) region compared to adjacent zones, prior subduction. Even though we do not have direct evidence for faults within the slab at ~100 km depth, the higher concentration of earthquakes may provide evidence for the reactivation of pre-existing faults within this segment of the slab. In fact, local seismic and high-resolution bathymetric surveys reveal the existence of a characteristic ridge-parallel seafloor fabric [von Huene et al., 1997; Kopp et al., 2004; Ranero et al., 2005], which has been interpreted as syngenetic normal faulting associated with the building of the seamounts [Yáñez et al., 2001; Kopp et al., 2004]. The alignment of aftershocks along planes extending down into the uppermost oceanic mantle in the outer rise, suggests that the fractures observed at the surface might be of lithospheric scale, hence acting as pathways for hydration of the oceanic mantle as inferred by Fromm et al. [2006] near the intersection of the Juan Fernandez Ridge and the Chilean trench.

Another possibility for explaining the non-uniform patterns of slab seismicity is by the variability in strain due to the bending of the slab along the buoyant part of the Juan Fernandez Ridge, tears or gaps in the slab, and/or the response of the slab geometry to the ridge migration through the geologic time. Pardo et al. [2002a], Anderson et al. [2007], and Olsen [2011] have hypothesized a small tear or a gap in the subducting slab to explain the pattern in P and T axis from focal mechanisms. The region of intense seismicity along the Juan Fernandez track is located north of an abrupt descend to the south in the slab contours. This abrupt flexure to the south may increase the stress in this region inducing more seismicity as opposed to regions where the plate only bends towards the northeast in the direction of subduction, which is the normal bend the plate has undergone since it started subducting beneath the South America Plate.

We did not observe a double plane of seismicity in the flat slab region as it has been observed in the inclined WBZ further west beneath the shallow part of the subduction zone in Chile, west of longitude 70ºW [Marot et al., 2010]. In this region, the lower seismic zone begins at ~50 km depth and extends to ~100 km depth, where it merges with the upper seismic zone. The separation between the two zones is ~30 km at the shallowest depth [Marot et al., 2010]. Our high quality locations, east of longitude 70ºW, show that WBZ is composed of only a single layer of seismicity with thickness of 10-15 km. Conceptual models for intermediate-depth seismicity [e.g., Ranero et al., 2005; Brudzinski et al., 2007] predict that a double plane of seismicity occurs if mantle dehydration starts at depth were crust dehydration is not completed. Analysis of our slab earthquake locations together with receiver function results [Gans et al., 2011]

suggest that the slab earthquakes appear to be occurring in the oceanic mantle of the slab rather than the crust. This may imply that in the Pampean flat slab region, the subducted oceanic crust is already dehydrated and that dehydration is mostly restricted to the serpentinized oceanic mantle.

What causes seismicity to decrease at 68.5ºW is intriguing. If slab earthquakes are occurring in the upper mantle of the subducting Nazca Plate, this abrupt decrease in seismicity may indicate that the upper mantle is completely de-serpentinized at this longitude perhaps after the plate is intensively dehydrated in the region of the greatest concentration of seismicity, between longitude 70ºW and 68ºW.

Even though there is a spatial correlation between the flat slab region and the projected path of Juan Fernandez Ridge, we found that the flat slab region is as wide as 240 km, which is broader than the width of Juan Fernandez Ridge offshore, which is only ~100 km [von Huene et al., 1997, Yáñez et al., 2001]. According to geological reconstructions, the Juan Fernandez Ridge has been migrating along the trench to the south, impacting the margin from latitude 25ºS during the Miocene [Yáñez et al., 2001]. Currently the ridge intersects the trench near 32º, which correlates with the southernmost part of the flat slab area. This southward migration of the ridge implies that it has disturbed the subduction zone further north of the current location. A wider flat slab region than that predicted by the width of the Juan Fernandez Ridge itself may show the response of the geometry of the slab to the passage of the buoyant ridge. In the northern part of the flat slab region (latitude ~28°-30°S) the Nazca Plate may be in the process of returning into a more steeply dipping subduction, therefore exhibit more gradual contours

as opposed to the southern flank (latitude ~32°-33°S) where slab contours suggest a sharper flexure more consistent with the current position of the ridge. This is also consistent with the gap in the active volcanic arc in the upper plate, which is also wider (~750 km) than the ridge itself.

Focal mechanism solutions and the orientation of P- and T-axes, coupled with the new slab contours from these events are consistent with a slab-pull model for this region. The sub-horizontal T-axes indicate that the slab pulls away from the Juan Fernandez Ridge, which is an indication of the buoyancy of the ridge. Inspection of T-axes orientations from focal mechanisms suggests that the slab is in extension. This extension is argued to result from a combination of buoyant forces of the subducted Juan Fernandez Ridge and the slab pulling away from the ridge to the north and south. If our contours indicate the true geometry of the subducting slab, our interpretation of sub-horizontal T-axes suggests that the slab pulls away from the Juan Fernandez Ridge cluster of seismicity both to the south and north. This would also be expected if the ridge were buoyant: the opposing forces of the buoyant ridge and the slab sinking around it would put the entire slab into extension perpendicular to the slab contours as interpreted by Anderson et al. [2007].

7. Conclusions

The most significant observations from the WBZ are: a 100 km-wide region of increased seismicity that coincides with the subducted path of the Juan Fernandez Ridge between longitude 70ºW and 68ºW, the seismicity gap along the projected path of Juan

Fernandez Ridge to the northeast of longitude 68.5ºW, and the two arms of descending seismicity on both sides of the seismicity gap. This non-uniform spatial distribution of the slab seismicity may suggest that there is variability in the hydration state of the subducting Nazca Plate across the strike of the margin with greater release of water from the subducted ridge region. What causes seismicity to decrease at 68.5ºW may indicate that the upper mantle is completely de-serpentinized at this longitude perhaps after the Nazca Plate was intensively dehydrated in the region of the greatest concentration of seismicity, between longitude 70ºW and 68ºW.

Initial single event locations suggest that, within the flat slab region there is a progressive shallowing of the seismicity towards the northeast, opposite to the direction of subduction. When earthquakes are relocated by deriving a Minimum 1D Model, applying a double difference algorithm, or when applying a DD tomography using a 3D velocity model, earthquakes flatten out aligning more closely at ~100 km depth. Even when the ‘‘reverse dip’’ is less obvious in these relocations, earthquakes seem to have average deeper depths below the main cordillera and Precordillera than those located farther east below Pie de Palo. The slight westward dip still retained within our tomography locations likely reflects true variations in earthquake depth resolved by our study and may suggest that the subducted Nazca Plate has some “topography” due to the ridge buoyancy.

We did not observe a double plane of seismicity in the flat slab region as it has been observed in the inclined WBZ further west beneath the shallow part of the subduction zone in Chile, west of longitude 70ºW [Marot et al., 2010]. We determine that

WBZ in the Pampean flat slab is a single layer of seismicity with thickness of 10-15 km. Analysis of our slab earthquake locations together with receiver function results [Gans et al., 2011] suggest that the slab earthquakes appear to be occurring in the oceanic mantle of the slab rather than the oceanic crust. This may imply that in the Pampean flat slab region, the subducted oceanic crust is already dehydrated and that dehydration is mostly restricted to the serpentinized oceanic mantle.

Our new, more detailed contours show that the top of the WBZ of the Nazca Plate is nearly flat ~100 km depth approximately within the region between latitude 28°S and 32°S and longitude 70°W and 68.5°W. Even though there is a spatial correlation between the flat slab region and the projected path of Juan Fernandez Ridge, we found that the flat slab region is as wide as 240 km, which is broader than the width of Juan Fernandez Ridge offshore, which is only ~100 km. A wider flat slab region that that predicted by the width of the Juan Fernandez Ridge itself may be the result of a still disturbed slab region after the passage of the buoyant ridge, which in the northern part of the flat slab is in the process of returning into a more steeply dipping subduction.

Focal mechanisms suggest that the slab is mostly under extension in the flat slab area. There is a region of mixed T-axes trends near where the slab descends abruptly to the south and northeast. Slab pull and ridge buoyancy may be key factors in the deformation of the slab.

8. Acknowledgments.

We are grateful to IRIS and people at the PASSCAL Instrument Center for their

help and support throughout the SIEMBRA deployment. The seismic instruments were provided by the Incorporated Research Institutions for Seismology (IRIS) through the PASSCAL Instrument Center (NSF Cooperative Agreement EAR-0552316). We also sincerely thank the Instituto Nacional de Prevención Sísmica, Argentina, for their help in logistics, as well as Noel Barstow (PASSCAL) for her invaluable assistance in the field. Special thanks to Ivonne Arroyo and C. Berk Biryol for helping with codes and comments. This research was supported by the National Science Foundation (EAR-0510966, EAR-0738935 and EAR-0739001). Maps were created using the Generic Mapping Tools (GMT) software [Wessel and Smith 1998].

9. References

Alvarado, P. & Beck, S., 2006. Source characterization of the San Juan (Argentina) crustal earthquakes of 15 January 1944 (Mw 7.0) and 11 June 1952 (Mw 6.8), *Earth Planet. Sci. Lett.*, doi:10.1016/j.epsl.2006.01.015.

Alvarado, P., Beck, S. & Zandt, G., 2007. Crustal structure of the south-central Andes Cordillera and backarc region from regional waveform modeling, *Geophys. J. Int.,* **170,** 858-875, doi:10.1111/j.1365-246X.2007.03452.x.

Anderson, M., Alvarado, P., Zandt, G. & Beck, S., 2007. Geometry and brittle deformation of the subducting Nazca Plate, Central Chile and Argentina, *Geophys. J. Int.,* **171,** 419-434, doi:10.1111/j.1365-246X.2007.03483.x.

Araujo, M. & Suárez, G., 1994. Geometry and state of stress of the subducted Nazca Plate beneath central Chile and Argentina: evidence from teleseismic data, *Geophys. J. Int.,*

116, 283-303, doi:10.1111/j.1365-246X.1994.tb01799.x.

Barazangi, M. & Isacks, B., 1976. Spatial distribution of earthquakes and subduction of the Nazca Plate beneath South America, *Geology,* **4,** 686-692, doi:10.1130/0091-7613(1976)4<686:SDOEAS>2.0.CO;2.

Benioff, H., 1955. Seismic evidence for crustal structure and tectonic activity, *Spec. Pap. - Geol. Soc. Am.,* **62,** 61-74.

Brudzinski, M.R. & Chen, W.-P., 2005. Earthquakes and strain in subhorizontal slabs, *J. Geophys. Res.,* **110,** B08303, doi:10.1029/2004jb003470.

Brudzinski, M.R., Thurber, C.H., Hacker, B.R. & Engdahl, E.R., 2007. Global Prevalence of Double Benioff Zones, *Science,* **316,** 1472-1474, doi:10.1126/science.1139204.

Cahill, T. & Isacks, B.L., 1992. Seismicity and shape of the subducted Nazca Plate, *J. Geophys. Res.,* **97,** 17503-17529, doi:10.1029/92JB00493.

Chiu, J.M., Steiner, G., Smalley, R., Jr. & Johnston, A.C., 1991. PANDA: A simple, portable seismic array for local- to regional-scale seismic experiments, *Bull. Seismol. Soc. Am.,* **81,** 1000-1014.

Cross, T.A. & Pilger, R.H., Jr., 1982. Controls of subduction geometry, location of magmatic arcs, and tectonics of arc and back-arc regions, *Geol. Soc. Am. Bull.,* **93,** 545-562, doi:10.1130/0016-7606(1982)93<545:COSGLO>2.0.CO;2.

Espurt, N., Funiciello, F., Martinod, J., Guillaume, B., Regard, V., Faccenna, C. & Brusset, S., 2008. Flat subduction dynamics and deformation of the South American plate: insights from analog modelling, *Tectonics,* **27**, doi:10.1029/2007TC002175.

Fromm, R., Alvarado, P., Beck, S. & Zandt, G., 2006. The April 9, 2001 Juan Fernandez

Ridge (Mw 6.7) Tensional Outer-Rise Earthquake and its Aftershock Sequence, *J. Seismol.,* **10,** 163-170, doi:10.1007/s10950-006-9013-3.

Fuenzalida, A., Pardo, M., Cisternas, A., Dorbath, L., Dorbath, C., Comte, D. & Kausel, E., 1992. On the geometry of the Nazca Plate subducted under Central Chile (32-34.5°S) as inferred from microseismic data, *Tectonophysics,* **205,** 1-11, doi:doi: 10.1016/0040-1951(92)90413-Z.

Gans, C.R., Beck, S.L., Zandt, G., Gilbert, H., Alvarado, P., Anderson, M. & Linkimer, L., 2011. Continental and oceanic crustal structure of the Pampean flat slab region, western Argentina, using receiver function analysis: new high-resolution results, *Geophys. J. Int.,* **186,** 45-58, doi:10.1111/j.1365-246X.2011.05023.x.

Geiger, L., 1912. Probability method for the determination of earthquake epicenters from the arrival time only, *Bull. St. Louis Univ.,* **8,** 60-71.

Gutscher, M.-A., Spakman, W., Bijwaard, H. & Engdahl, E.R., 2000. Geodynamics of flat subduction: Seismicity and tomographic constraints from the Andean margin, *Tectonics,* **19,** 814-833, doi:10.1029/1999tc001152.

Hacker, B.R., Peacock, S.M., Abers, G.A. & Holloway, S.D., 2003. Subduction factory 2. Are intermediate-depth earthquakes in subducting slabs linked to metamorphic dehydration reactions?, *J. Geophys. Res.,* **108,** 2030, doi:10.1029/2001jb001129.

Havskov, J. & Ottemoller, L., 1999. SeisAn Earthquake Analysis Software, *Seis. Res. Lett.,* **70,** 532-534, doi:10.1785/gssrl.70.5.532.

Jordan, T.E. & Allmendinger, R.W., 1986. The Sierras Pampeanas of Argentina; a modern analogue of Rocky Mountain foreland deformation, *Am. J. Sci.,* **286,** 737-764,

doi:10.2475/ajs.286.10.737.

Jordan, T.E., Isacks, B., Ramos, V.A. & Allmendinger, R.W., 1983. Mountain building in the central Andes, *Episodes,* **6,** 20-26.

Kay, S.M. & Abbruzzi, J.M., 1996. Magmatic evidence for Neogene lithospheric evolution of the central Andean "flat-slab" between 30°S and 32°S, *Tectonophysics,* **259,** 15-28, doi:10.1016/0040-1951(96)00032-7.

Kay, S.M. & Mpodozis, C., 2002. Magmatism as a probe to the Neogene shallowing of the Nazca Plate beneath the modern Chilean flat-slab, *J. South Am. Earth Sci.,* **15,** 39-57, doi:doi: 10.1016/S0895-9811(02)00005-6.

Kay, S.M., Maksaev, V., Moscoso, R., Mpodozis, C., Nasi, C. & Gordillo, C.E., 1988. Tertiary andean magmatism in Chile and Argentina between 28°S and 33°S: Correlation of magmatic chemistry with a changing Benioff zone, *J. South Am. Earth Sci.,* **1,** 21-38, doi:10.1016/0895-9811(88)90013-2|.

Kendrick, E., Bevis, M., Smalley, R., Jr., Brooks, B., Vargas, R.B., Lauría, E. & Fortes, L.P.S., 2003. The Nazca-South America Euler vector and its rate of change, *J. South Am. Earth Sci.,* **16,** 125-131, doi:10.1016/S0895-9811(03)00028-2.

Kirby, S., Engdahl, E.R. & Denlinger, R., 1996. Intermediate-depth intraslab earthquakes and arc volcanism as physical expressions of crustal and uppermost mantle metamorphism in subducting slabs (Overview), *in Subduction from Top to Bottom*, pp. 195-215, eds. Bebout, G. E., Scholl, D. W., Kirby, S. H. & Platt, J. P., American Geophysical Union Geophysical Monograph.

Kissling, E., 1988. Geotomography with local earthquake data, *Rev. Geophys.,* **26,** 659-698.

Kissling, E., Ellsworth, W.L., Eberhart-Phillips, D. & Kradolfer, U., 1994. Initial reference models in local earthquake tomography, *J. Geophys. Res.,* **99,** 19635-19646, doi:10.1029/93jb03138.

Kissling, E., Kradolfer, U. & Maurer, H., 1995. *VELEST User's Guide-short Introduction*, Institute of Geophysics & Swiss Seismological Service ETH Zurich.

Langer, C.J. & Hartzell, S., 1996. Rupture distribution of the 1977 western Argentina earthquake, *Phys. Earth Planet. Inter.,* **94,** 121-132, doi:doi: 10.1016/0031-9201(95)03080-8.

Lienert, B.R. & Havskov, J., 1995. A Computer Program for Locating Earthquakes Both Locally and Globally, *Seis. Res. Lett.,* **66,** 26-36, doi:10.1785/gssrl.66.5.26.

Lienert, B.R., Berg, E. & Frazer, L.N., 1986. HYPOCENTER: An earthquake location method using centered, scaled, and adaptively damped least squares, *Bull. Seismol. Soc. Am.,* **76,** 771-783.

Linkimer, L., Beck, S., Zandt, G., Alvarado, P., Anderson, M., Gilbert, H. & Zhang, H., 2011, in preparation. Lithospheric Structure of the Pampean Flat Slab Region from Double-Difference Tomography.

Marot, M., Monfret, T., Pardo, M. & Ranalli, G., 2010. A double seismic zone in the Nazca flat slab beneath central Chile (29°-34°S), *in EGU General Assembly 2010*, pp. EGU2010-11997, Vienna.

Olsen, K., 2011. *Dynamics of Flat Slab Subduction: Focal Mechanisms, Ridge Buoyancy, and Slab Tear in Central Argentina*, BSc thesis, Colorado College.

Ottemöller, L., Voss, P. & Havskov, J., 2011.*SEISAN: the Earthquake Analysis Software for*

Windows, Solaris, LINUX, and MACOSX, version 9.0.1, University of Bergen, pp. 361.

Pardo, M., Comte, D. & Monfret, T., 2002a. Seismotectonic and stress distribution in the central Chile subduction zone, *J. South Am. Earth Sci.,* **15,** 11-22, doi:doi: 10.1016/S0895-9811(02)00003-2.

Pardo, M., Monfret, T., Vera, E., Eisenberg, A., Gaffet, S., Lorca, E. & Perez, A., 2002b. Seismotectonic and Body-wave Tomography of Central Chile-NW Argentina Flat-slab Subduction Zone Using Local Earthquakes, *in EGS XXVII General Assembly*, Nice.

Peacock, S.M., 2001. Are the lower planes of double seismic zones caused by serpentine dehydration in subducting oceanic mantle?, *Geology,* **29,** 299-a-302, doi:10.1130/0091-7613(2001)029<0299:ATLPOD>2.0.CO;2.

Pilger, R.H.J., 1981. Plate reconstructions, aseismic ridges, and low-angle subduction beneath the Andes, *Geol. Soc. Am. Bull.,* **92,** 448-456, doi:10.1130/0016-7606(1981)92<448:PRARAL>2.0.CO;2.

Pujol, J., Chiu, J.M., Smalley, R., Jr., Regnier, M., Isacks, B., Chatelain, J.L., Vlasity, J., Vlasity, D., Castano, J. & Puebla, N., 1991. Lateral velocity variations in the Andean foreland in Argentina determined with the JHD method, *Bull. Seismol. Soc. Am.,* **81,** 2441-2457.

Ramos, V.A., Cristallini, E.O. & Pérez, D.J., 2002. The Pampean flat-slab of the Central Andes, *J. South Am. Earth Sci.,* **15,** 59-78, doi:10.1016/S0895-9811(02)00006-8.

Ranero, C.R., Villaseñor, A., Phipps Morgan, J. & Weinrebe, W., 2005. Relationship between bend-faulting at trenches and intermediate-depth seismicity, *Geochem., Geophys., Geosyst.,* **6,** Q12002, doi:10.1029/2005gc000997.

Reta, M.C., 1992. *High resolution view of the Wadati-Benioff zone and determination of the Moho depth in San Juan, Argentina*, MSc thesis, Memphis State University.

Smalley, R., Jr. & Isacks, B.L., 1987. A High-Resolution Local Network Study of the Nazca Plate Wadati-Benioff Zone Under Western Argentina, *J. Geophys. Res.,* **92,** 13903-13912.

Smalley, R., Jr., Pujol, J., Regnier, M., Chiu, J.-M., Chatelain, J.-L., Isacks, B.L., Araujo, M. & Puebla, N., 1993. Basement seismicity beneath the Andean precordillera thin-skinned thrust belt and implications for crustal and lithospheric behavior, *Tectonics,* **12,** 63-76, doi:10.1029/92tc01108.

Snoke, J.A., Munsey, J.W., Teague, A.C. & Bollinger, G.A., 1984. A program for focal mechanism determination by combined use of polarity and *SV-P* amplitude ratio data, *Earthquake Notes,* **55,** 15.

von Huene, R., Corvalán, J., Flueh, E.R., Hinz, K., Korstgard, J., Ranero, C.R., Weinrebe, W. & Scientists, C., 1997. Tectonic control of the subducting Juan Fernandez Ridge on the Andean margin near Valparaiso, Chile, *Tectonics,* **16,** 474-488, doi:10.1029/96tc03703.

Wadati, K., 1928. Shallow and deep earthquakes, *Geophys. Mag.,* **1,** 162-202.

Wadati, K., 1935. On the activity of deep-focus earthquakes in the Japan islands and neighbourhoods, *Geophys. Mag.,* **8,** 305-325.

Wagner, L.S., Anderson, M.L., Jackson, J.M., Beck, S.L. & Zandt, G., 2008. Seismic evidence for orthopyroxene enrichment in the continental lithosphere, *Geology,* **36,** 935-938, doi:10.1130/G25108A.1.

Waldhauser, F. & Ellsworth, W.L., 2000. A Double-Difference Earthquake Location

Algorithm: Method and Application to the Northern Hayward Fault, California, *Bull. Seismol. Soc. Am.,* **90,** 1353-1368, doi:10.1785/0120000006.

Waldhauser, F., 2001. HYPODD: A Computer Program to Compute Double-Difference Hypocenter Locations, *Open-File Rep. - U. S. Geol. Surv.,* **01-113,** 25.

Warren, L.M., Langstaff, M.A. & Silver, P.G., 2008. Fault plane orientations of intermediate-depth earthquakes in the Middle America Trench, *J. Geophys. Res.,* **113,** B01304, doi:10.1029/2007jb005028.

Wessel, P. & Smith, W.H.F., 1998. New, improved version of generic mapping tools released, *Eos Trans. Am. Geophys. Union,* **79,** 579.

Yáñez, G., Cembrano, J., Pardo, M., Ranero, C. & Selles, D., 2002. The Challenger-Juan Fernandez-Maipo major tectonic transition of the Nazca-Andean subduction system at 33-34°S: geodynamic evidence and implications, *J. South Am. Earth Sci.,* **15,** 23-38, doi:10.1016/S0895-9811(02)00004-4.

Yáñez, G.A., Ranero, C.R., von Huene, R. & Díaz, J., 2001. Magnetic anomaly interpretation across the southern central Andes (32°-34°S): The role of the Juan Fernandez Ridge in the late Tertiary evolution of the margin, *J. Geophys. Res.,* **106,** 6325-6345, doi:10.1029/2000jb900337.

Zhang, H. & Thurber, C., 2006. Development and Applications of Double-difference Seismic Tomography, *Pure Appl. Geophys.,* **163,** 373-403-403, doi:10.1007/s00024-005-0021-y.

Zhang, H., Thurber, C.H., Shelly, D., Ide, S., Beroza, G.C. & Hasegawa, A., 2004. High-resolution subducting-slab structure beneath northern Honshu, Japan, revealed by double-difference tomography, *Geology,* **32,** 361-364, doi:10.1130/G20261.2.

Zhang, J., Green, H.W., Bozhilov, K. & Jin, Z., 2004. Faulting induced by precipitation of water at grain boundaries in hot subducting oceanic crust, *Nature,* **428,** 633-636, doi:10.1038/nature02475.

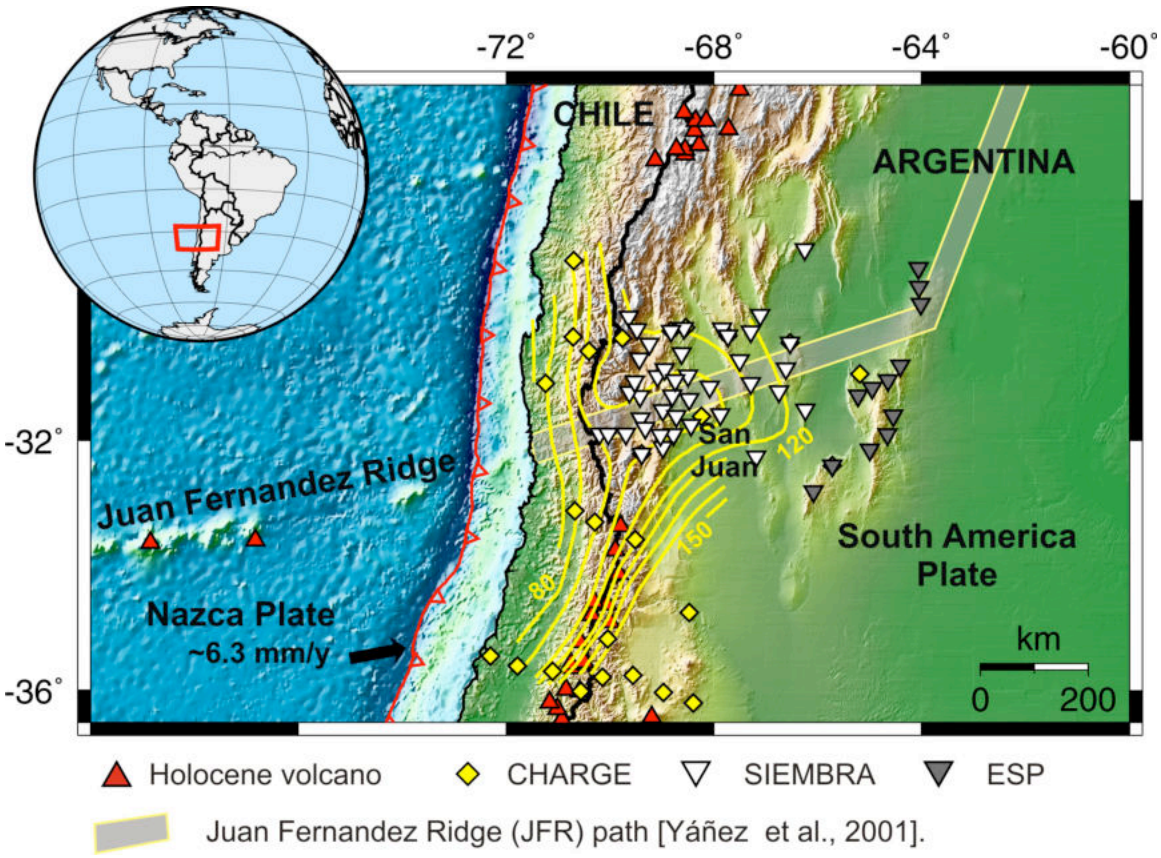

Figure 1. Location Map. Plate convergence velocity from Kendrick et al. [2003]. Slab contours from Anderson et al. [2007].

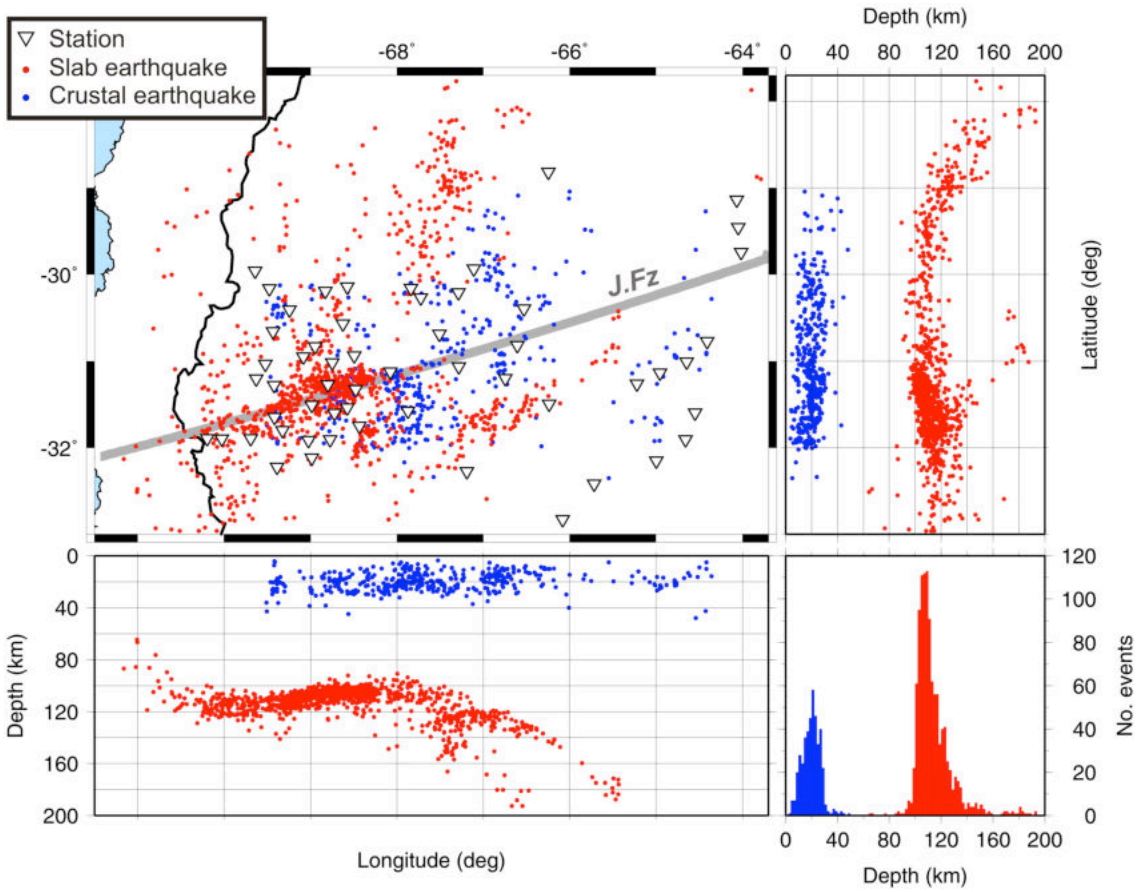

Figure 2. Distribution of the 1,562 earthquakes used in both map view and cross sections in E-W and N-S directions. These events were located with a single event location method using a preliminary velocity model based on Smalley et al. [1993] and Anderson et al. [2007].

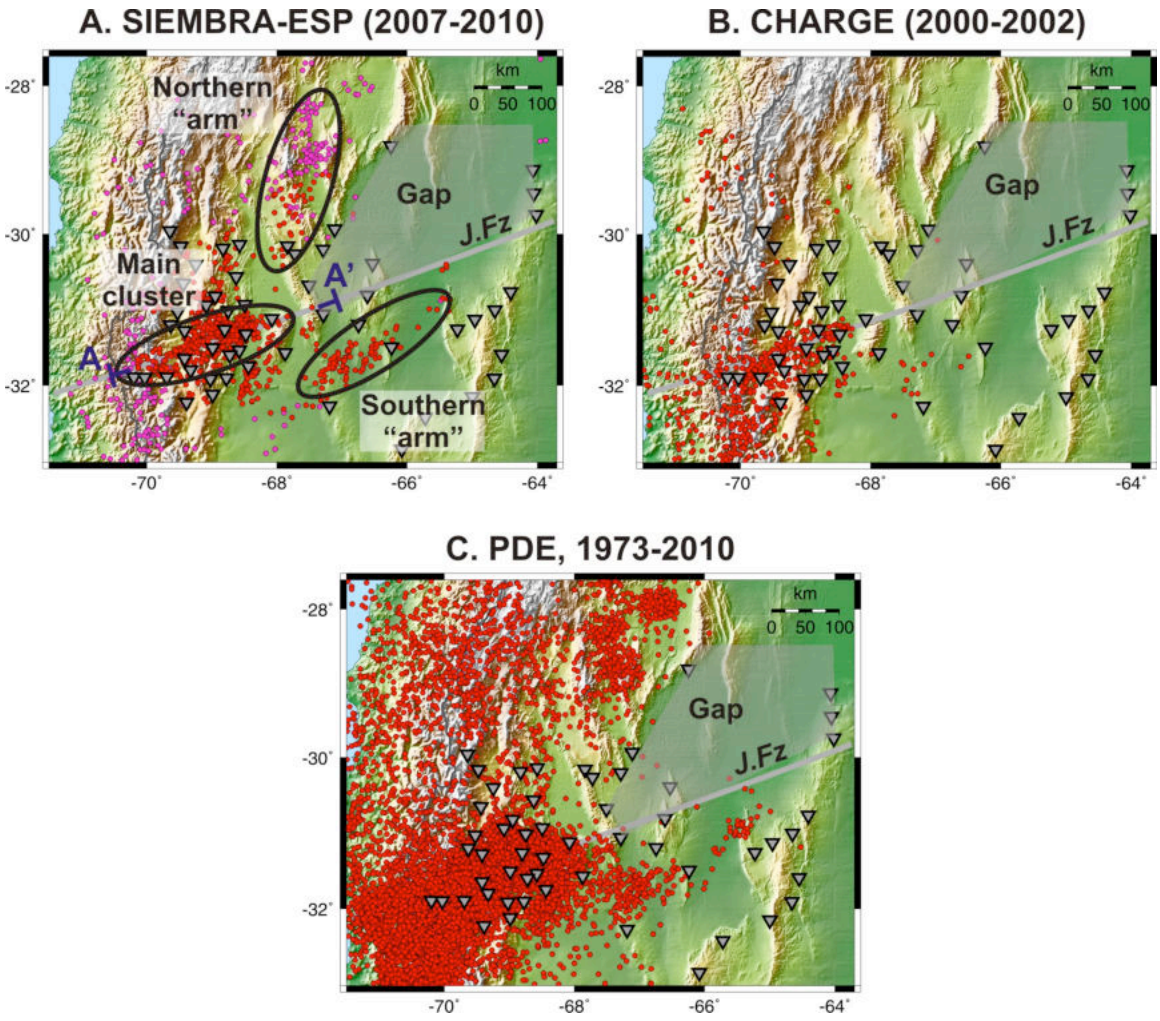

Figure 3. Slab seismicity from different earthquake catalogues. **A.** SIEMBRA-ESP earthquakes located with a regional-scale double difference algorithm in the area within network coverage (red) and with single-event location method in the region outside the networks (magenta). **B.** CHARGE earthquakes located using a multiple-event relocation method [Anderson et al., 2007]. **C.** PDE (1973-2010). The gray area denotes the gap region within network coverage where no earthquakes were recorded. Blue bars denote the location of A-A' cross section shown in Figure 4.

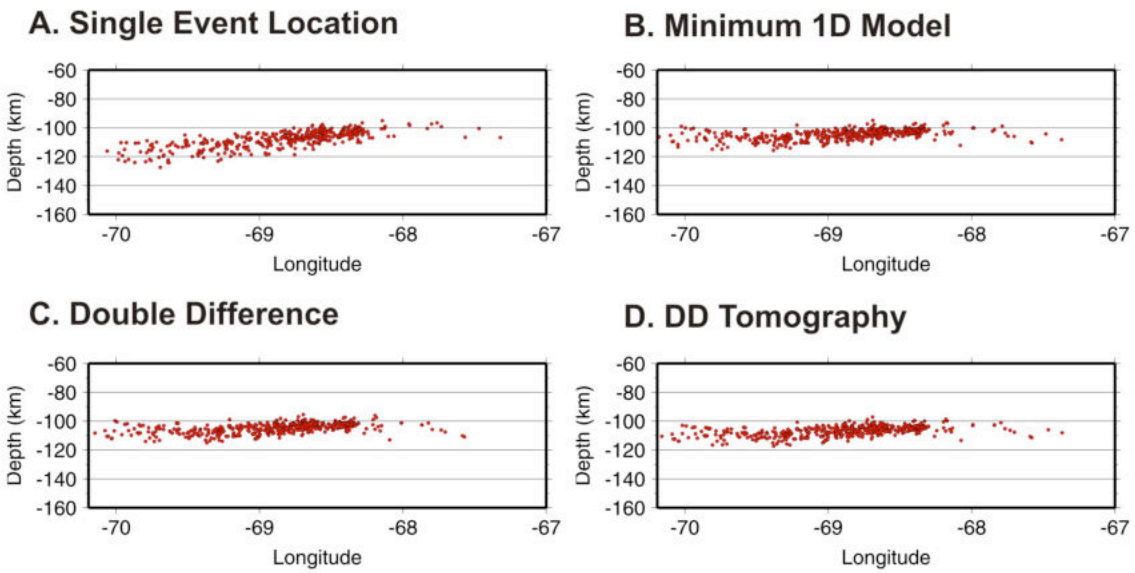

Figure 4. Earthquake locations obtained using different methods along a profile A-A' (Fig 3a). Events within 0.2 degree of the profile are shown. **A.** Single event location. **B.** Minimum 1D model. **C.** Double difference. **D.** Regional-scale double difference tomography.

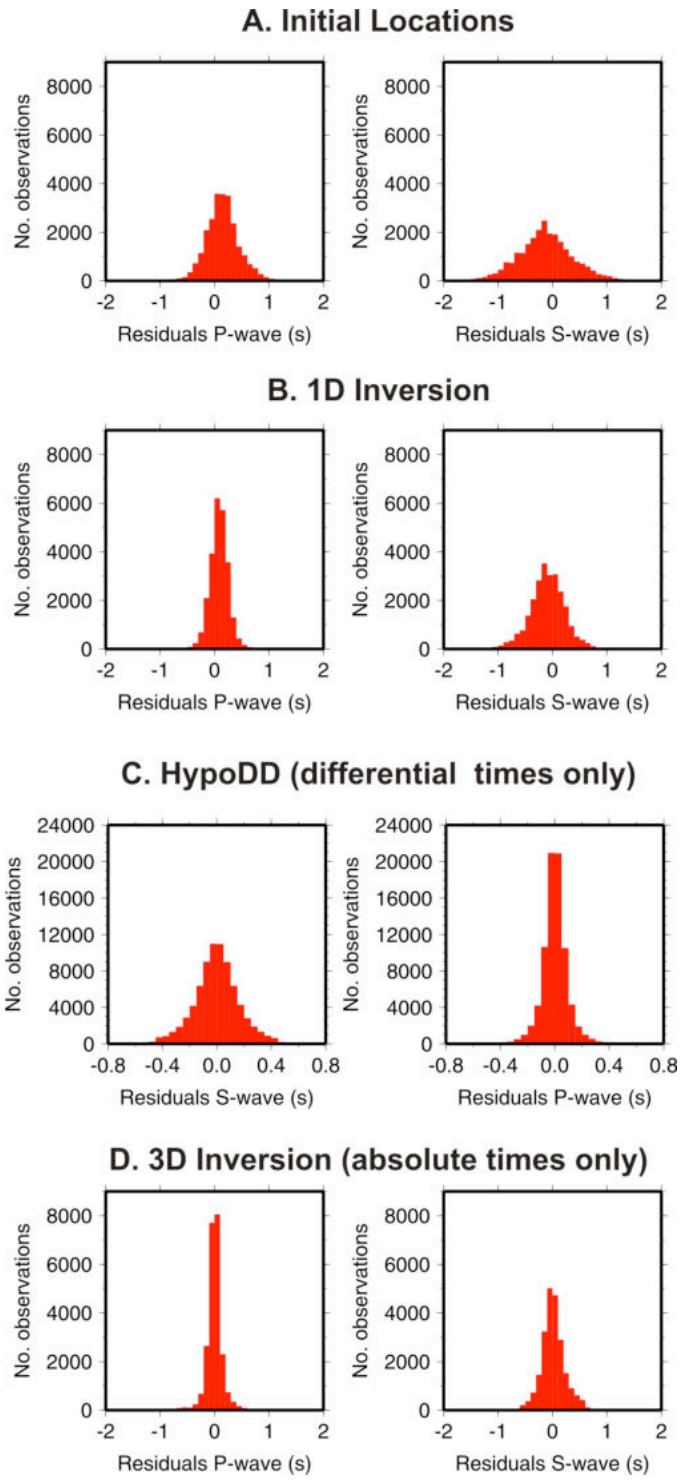

Figure 5. Residual misfit improvement for the 1,092 earthquakes used. **A.** Single event location. **B.** Minimum 1D Model. **C.** DD location. **D.** DD tomography.

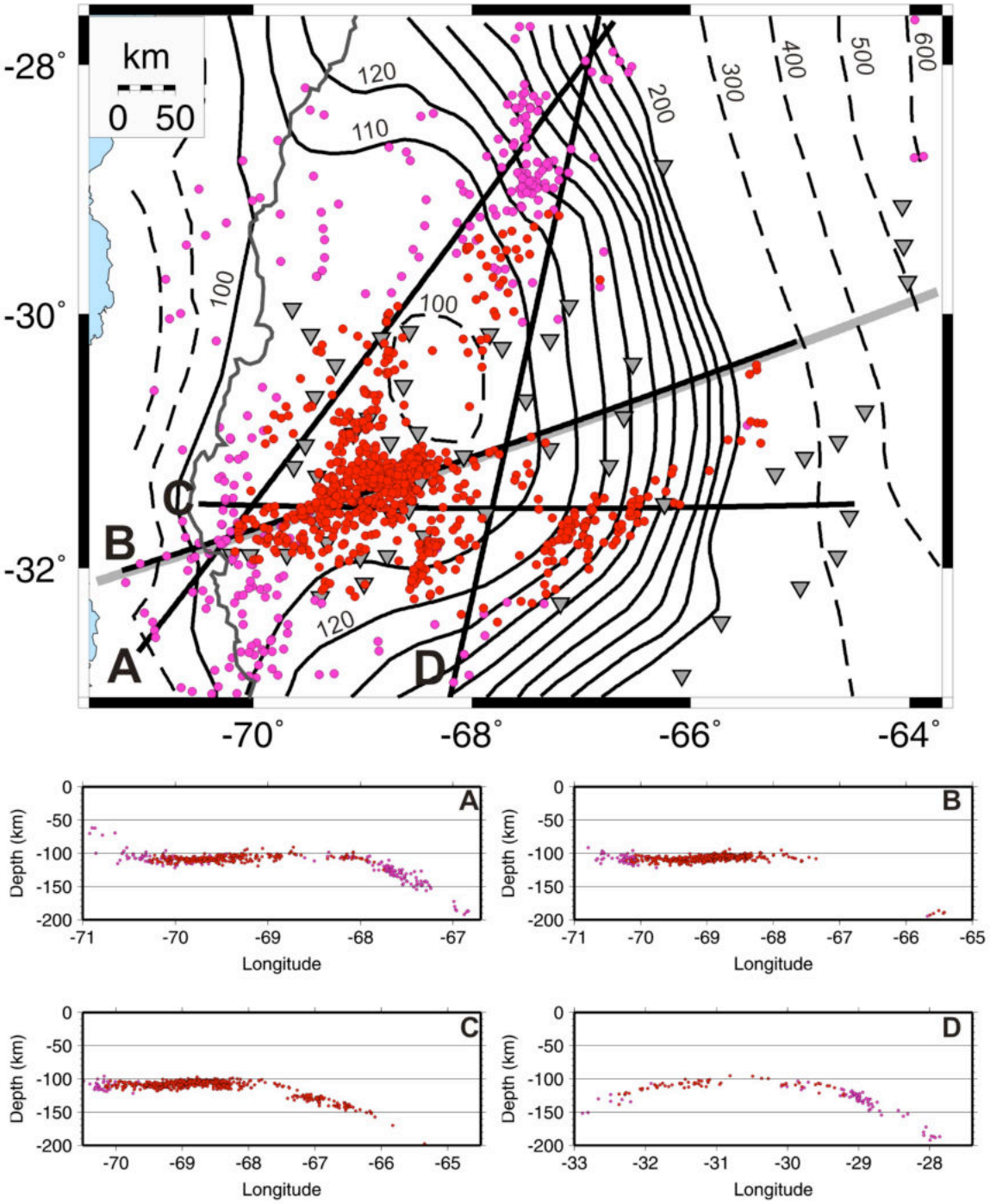

Figure 6. Contours (in km) to the top of the WBZ. These locations correspond to the earthquakes located with a regional-scale double difference algorithm in the area within network coverage (red) and with single-event location method in the region outside the networks (magenta). Black lines denote the location of cross sections. Earthquakes within 0.5 degree are projected onto each cross section.

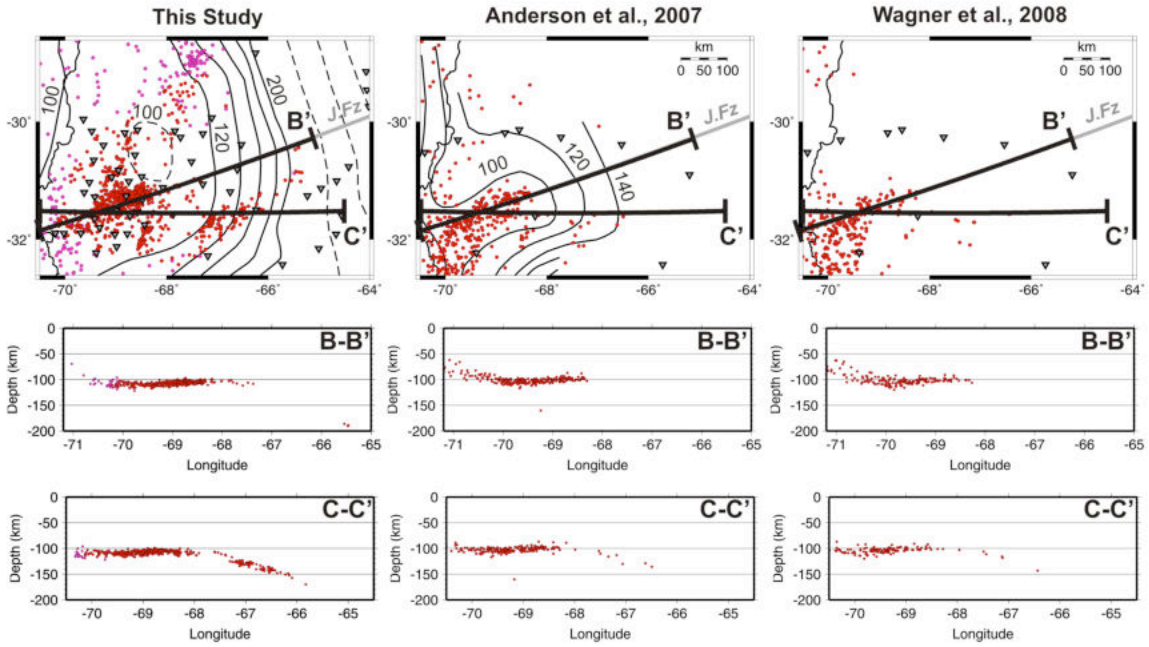

Figure 7. Comparison of earthquake locations from this study and those from Anderson et al. [2007] using a multiple-event location technique and Wagner et al. [2008] using seismic tomography.

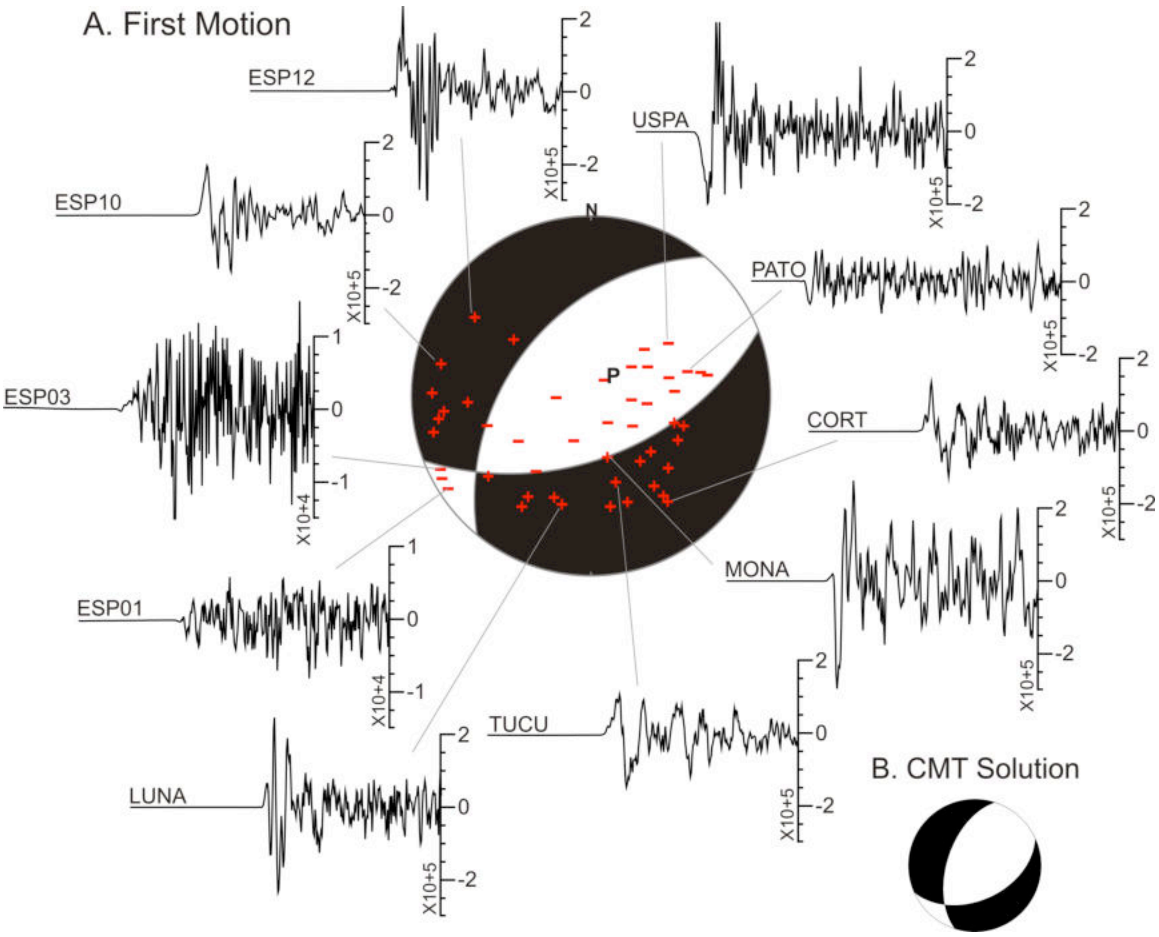

Figure 8. A) An example of a high-quality focal mechanism (lower hemisphere projection) of an earthquake that occurred on December 20, 2008 at 17:06 determined from the first motion polarity at 48 stations. Red positive signs indicate compression (up) arrivals and red negative signs tensional (down) arrivals. Nine seconds of waveform data is shown for the selected stations. A grid-search every five degrees of the focal sphere finds only one possible solution with zero polarity errors for this polarity pattern. **B)** Global CMT solution for the same event for comparison.

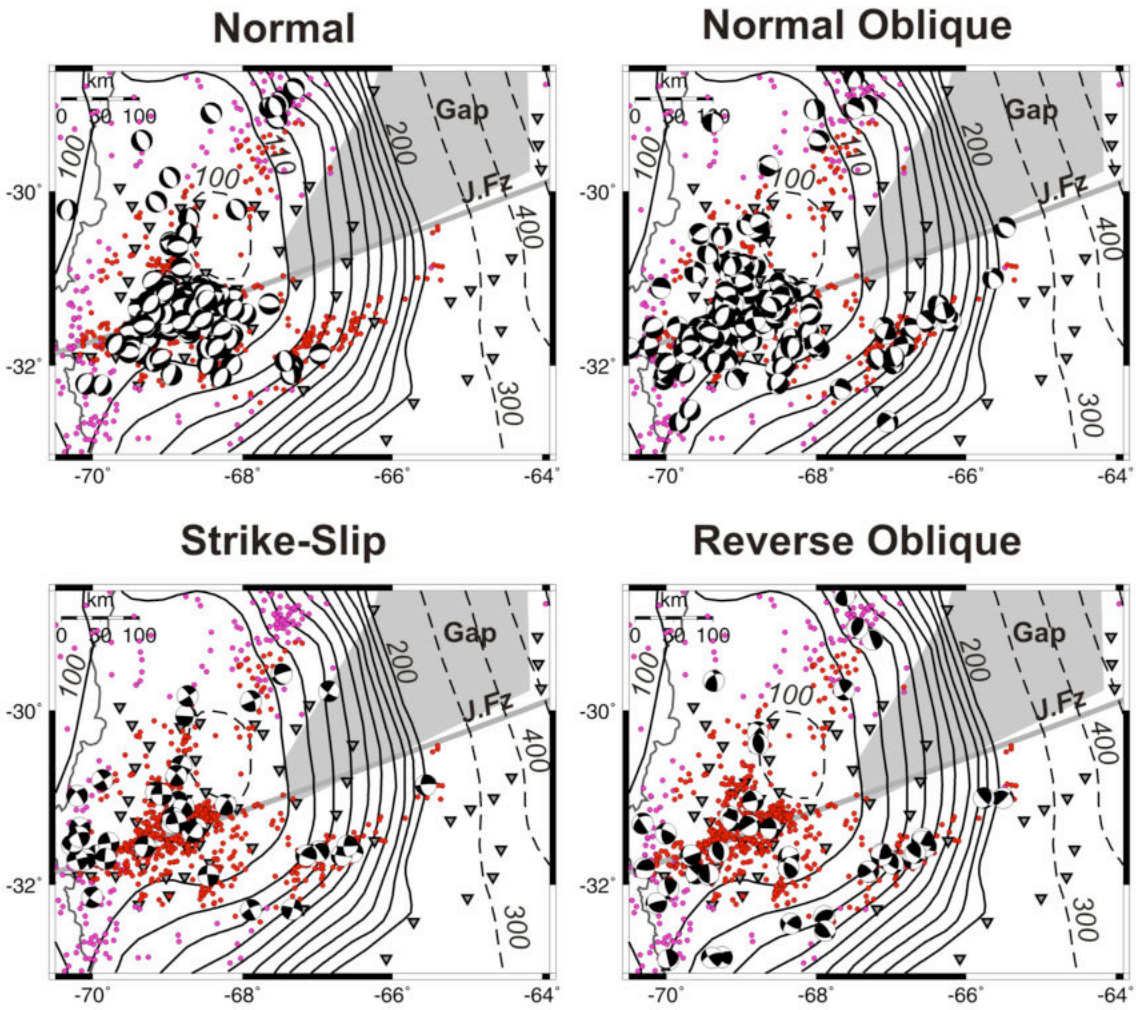

Figure 9. Focal mechanism solutions plotted as lower hemisphere projection. Slab contours are labeled in km. Other symbols like in Fig. 6.

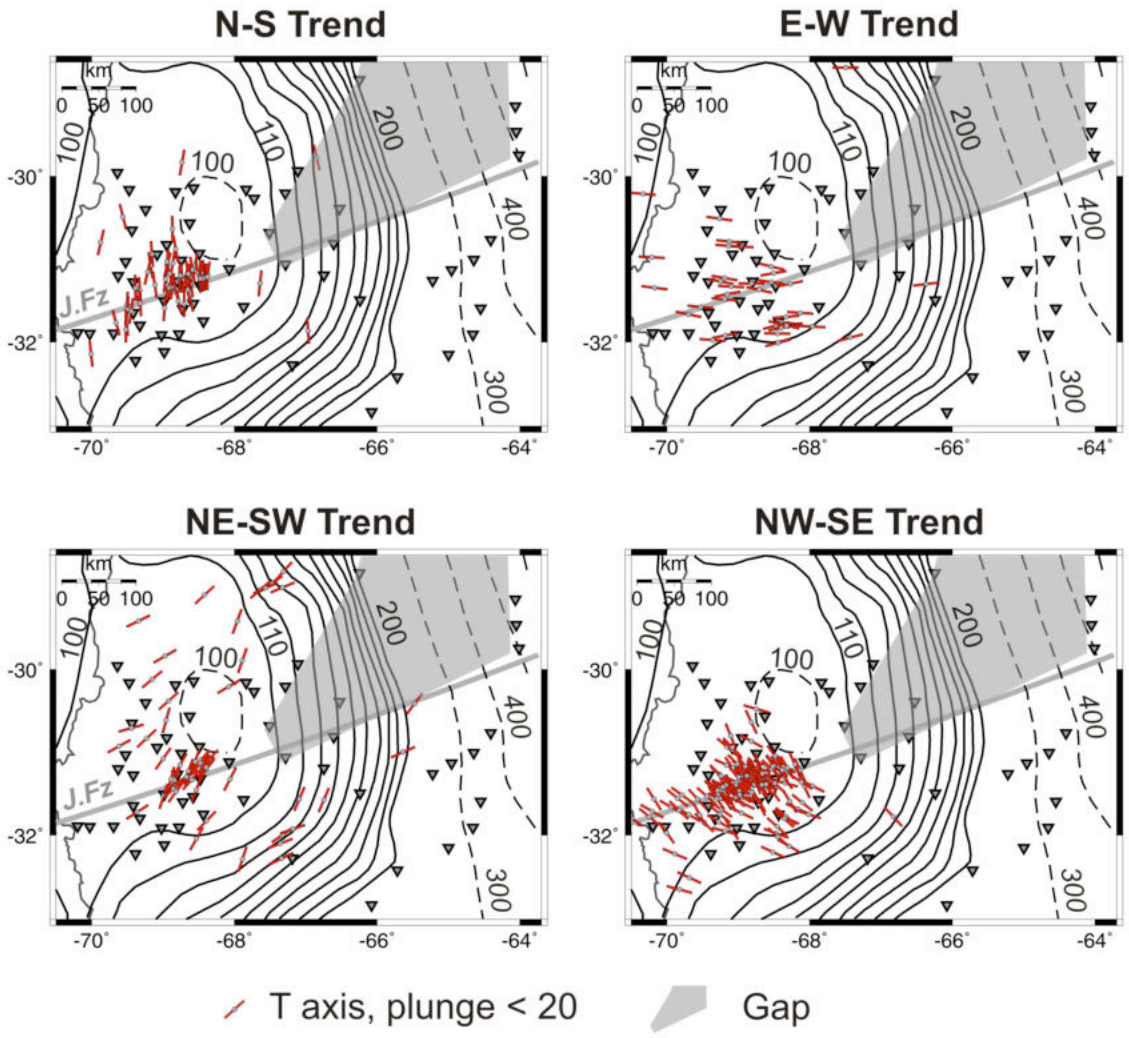

Figure 10. Sub-horizontal T axes determined from first motion data. Slab contours are labeled in km.

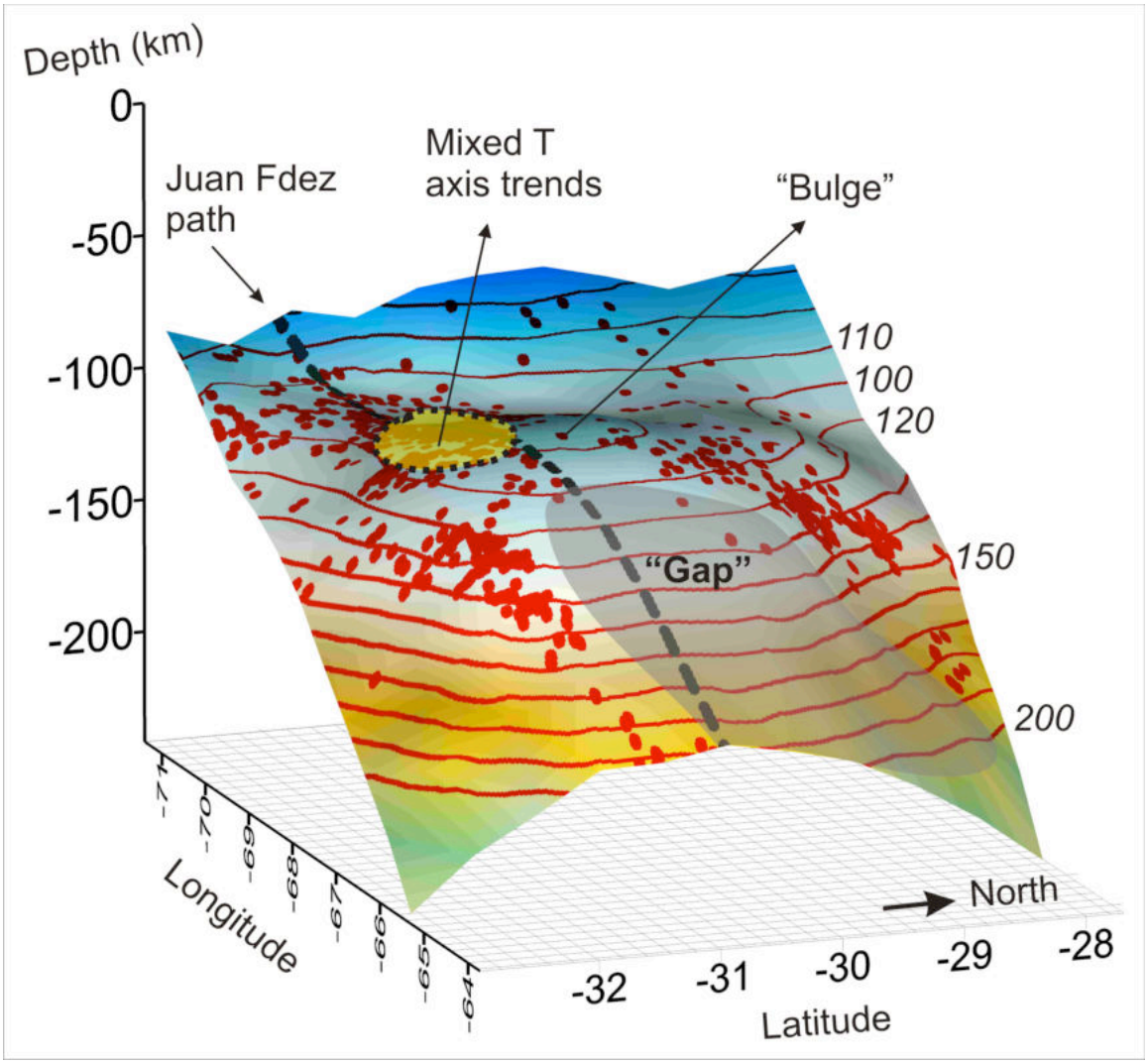

Figure 11. Summary diagram showing the surface of the top of the WBZ as viewed from the southeast.